



TRIS-CYCLOMETALATED IRIIDIUM COMPLEXES IN IMAGING AND
CATALYSIS

SUREEMAS MEKSAWANGWONG

A Thesis Submitted to the Graduate School of Naresuan University
in Partial Fulfillment of the Requirements
for the Doctor of Philosophy in (Chemistry)

2020

Copyright by Naresuan University

TRIS-CYCLOMETALATED IRIIDIUM COMPLEXES IN IMAGING AND
CATALYSIS



SUREEMAS MEKSAWANGWONG

A Thesis Submitted to the Graduate School of Naresuan University
in Partial Fulfillment of the Requirements
for the Doctor of Philosophy in (Chemistry)

2020

Copyright by Naresuan University

Thesis entitled "Tris-cyclometalated iridium complexes in imaging and catalysis"
By SUREEMAS MEKSAWANGWONG
has been approved by the Graduate School as partial fulfillment of the requirements
for the Doctor of Philosophy in Chemistry of Naresuan University

Oral Defense Committee

..... Chair
(Assistant Professor Nanthawat Wannarit, Ph.D.)

..... Advisor
(Assistant Professor Filip Kielar, Ph.D.)

..... Internal Examiner
(Assistant Professor Wikorn Punyain, Ph.D.)

..... Internal Examiner
(Assistant Professor Anchalee Sirikulkajorn, Ph.D.)

..... Internal Examiner
(Assistant Professor Uthai Wichai, Ph.D.)

Approved

.....
(Professor Paisarn Muneesawang, Ph.D.)

for Dean of the Graduate School

Title	TRIS-CYCLOMETALATED IRIDIUM COMPLEXES IN IMAGING AND CATALYSIS
Author	SUREEMAS MEKSAWANGWONG
Advisor	Assistant Professor Filip Kielar, Ph.D.
Academic Paper	Thesis Ph.D. in Chemistry, Naresuan University, 2020
Keywords	Cellular imaging, Iridium, Photoredox

ABSTRACT

A series of luminescent tris-cyclometalated iridium(III) complexes has been synthesized and characterized by ^1H -NMR, ^{13}C -NMR and MS spectroscopies. The photophysical properties of the complexes were investigated by using UV-Vis, steady state photoluminescence, and time-resolved photoluminescence techniques. Specifically, a group of derivatives of the prototypical complex *fac*-[Ir(ppy)₃] bearing various aminoalkyl sidechains, alkyl chain is terminated with a hydroxy group, and quarternary ammonium salts have been investigated with major focus on understanding the relationship between the structure, aggregation behavior, as a potential cellular imaging probe and photoredox catalysis. The complexes possess interesting properties including long luminescent lifetime in aqueous media. The length of the aminoalkyl sidechains and their nature (hydrophilic vs hydrophobic) affects the ability of the complexes to aggregate in the solutions with high content of water. The iridium(III) complexes with one and two 2-hydroxy ethyl groups on the nitrogen atom exhibit similar quantum yield to the parent complex *fac*-[Ir(ppy)₃] and the second of these also exhibits low cytotoxicity. The quarternary ammonium salts exhibits rapid photoreactivity, which can be used for the formation of new products. The complexes have been investigated as a potential cellular stain in NIH-3T3 cells. Tris-cyclometalated iridium(III) complex containing a single quarternary ammonium salt is less cytotoxic than aminoalkyl predecessor and shows lysosomal localization as its precursor. Finally, photoredox catalysis experiments carried out with the synthesized iridium(III) complexes show their ability to act as photoredox catalysts. Furthermore, iridium(III) complex immobilized on aminomethyl polystyrene shows

promise as heterogeneous catalyst, as it appears to be stable and active after recycling in organic synthesis reaction.



ACKNOWLEDGEMENTS

So many people have contributed to my thesis, to my education and to my life, and it is now my great pleasure to take this opportunity to thank them.

Firstly, I would like to gratefully thank my principal advisor, Asst. Prof. Dr. Filip Kielar for the unique opportunity to accomplish both B.Sc. and Ph.D degrees with him, his patience and knowledge and for offering several precious opportunities to attend and to make presentations in national and international academic conferences for every year. Thank you for taking me into your group and letting me witness the way you think. I deeply appreciate the opportunity. Thank you for all the guidance and support.

I would also like to thank Asst. Prof. Dr. Kittipong Chainok (Thammasat University) for help in collecting the data of single crystal X-ray and good sound advice.

I am very thankful to Asst. Prof. Dr. Wikorn Punyain (Naresuan University) for investigation and visualization DFT calculations.

I am extremely thankful to Asst. Prof. Dr. Robert Pal and Dr. Bhavini Gohil (Durham University) for investigation, and visualization cellular imaging.

I am grateful for father financial support provided from the National Research Council of Thailand (NRCT), administered by the Division of Research Administration at Naresuan University under grant No. R2560B098, a grant from the Thailand Research Fund No. RSA6080041, the National e-Science Infrastructure Consortium, S.M. also acknowledge scholarship support from the Science Achievement Scholarship of Thailand (SAST).

I also must thanks the Department of Chemistry, Naresuan University for the financial, facility and apace area for support this work.

A great thank to all the past and present members of the FK Group: Anusorn, Watcharapon, Winrawee, Pawittra, Sureerat, Tinnakorn, Pattarapon, Treerat, Petpailin, Jirayut, Attawit, and Wilaiwan for their help and suggestions with the laboratory work in synthesis and friendship.

I also have to thank my colleagues in the Department of Chemistry, Naresuan University especially Pilaipan, Meranee, Wasawat, Jantra, Juthathip, and Arnon for their support and the various extended relaxing lunch breaks.

Finally, I would like to thank my lovely family and the best friends for all their

continued support and endless encouragement over the years. I wish all of you the life of happiness and prosperity.

SUREEMAS MEKSAWANGWONG



TABLE OF CONTENTS

	Page
ABSTRACT.....	C
ACKNOWLEDGEMENTS.....	E
TABLE OF CONTENTS.....	G
LIST OF TABLES.....	M
LIST OF FIGURES	O
ABBREVIATIONS	Y
CHAPTER I.....	1
INTRODUCTION	1
CHAPTER II.....	4
PREVIEW OF RELATED LITERATURE AND RESEARCH.....	4
2.1 Photoactive cyclometalated iridium complexes	4
2.1.1 Structure and properties of iridium complexes	4
2.1.2 Cyclometalated iridium complexes	6
2.1.3 Photochemistry of luminescent transition metal complexes	9
1) Tuning the emission maximum	11
2.2 Use of cyclometalated iridium complexes in cellular imaging	13
2.3 Photoredox catalysis.....	29
2.3.1 Iridium(III) photocatalyst design.....	35
2.3.2 Immobilized catalysts on the solid support	45
CHAPTER III	47
METHODOGY.....	47
3.1 UV-Visible absorption spectroscopy.....	47
3.1.1 Absorption of radiation	47
3.1.2 Electromagnetic spectrum	47
3.1.3 Electronic transitions	48

3.2 Fluorescence spectroscopy	52
3.2.1 Fluorescence spectra.....	55
3.2.2 Fluorescence lifetime.....	57
3.3 Dynamic light scattering	58
3.4 DFT calculations	59
3.4.1 Kohn–Sham Theory	59
3.5 XRD.....	62
3.5.1 Crystallography	64
3.6 Cell imaging	65
3.7 Photoredox catalysis by LED.....	71
CHAPTER IV	73
EXPERIMENTAL PROCEDURES.....	73
4.1 Chemical reagents	73
4.2 Instruments	76
4.2.1 UV-visible spectroscopy	76
4.2.2 Photoluminescence spectroscopy	76
4.2.3 Dynamic light scattering.....	76
4.2.4 Thin layer chromatography	77
4.2.5 Mass spectroscopy.....	77
4.2.6 Nuclear magnetic resonance.....	77
4.2.7 Cell experiments.....	77
4.2.8 Density functional theory calculations	77
4.2.9 X-ray crystallography	78
4.2.10 Photoredox catalytic experiments	78
4.3 Experimental	78
4.3.1 Synthesis of Dimer (1)	78
4.3.2 Synthesis of <i>fac</i> -[Ir(ppy) ₂ (fppy)] (2)	79
4.3.3 Synthesis of <i>fac</i> -[Ir(ppy) ₂ (ppy-NHR)], R=C ₄ H ₉ (3).....	80
4.3.4 Synthesis of <i>fac</i> -[Ir(ppy) ₂ (ppy-NHR)], R=C ₆ H ₁₃ (4)	81

4.3.5 Synthesis of <i>fac</i> -[Ir(ppy) ₂ (ppy-NHR)], R=C ₈ H ₁₇ (5)	82
4.3.6 Synthesis of <i>fac</i> -[Ir(ppy) ₂ (ppy-N(R) ₂)], R=C ₄ H ₉ (6)	83
4.3.7 Synthesis of <i>fac</i> -[Ir(ppy) ₂ (ppy-NHR)], R=C ₁₀ H ₂₁ (7)	84
4.3.8 Synthesis of <i>fac</i> -[Ir(ppy) ₂ (ppy-NHR)], R=C ₁₂ H ₂₅ (8)	85
4.3.9 Synthesis of <i>fac</i> -[Ir(ppy) ₂ (ppy-NHR)], R=C ₂ H ₄ OH (9)	86
4.3.10 Synthesis of <i>fac</i> -[Ir(ppy) ₂ (ppy-NHR)], R=C ₃ H ₆ OH (10)	87
4.3.11 Synthesis of <i>fac</i> -[Ir(ppy) ₂ (ppy-NHR)], R=C ₄ H ₈ OH (11)	88
4.3.12 Synthesis of <i>fac</i> -[Ir(ppy) ₂ (ppy-NHR)], R=C ₆ H ₁₂ OH (12)	89
4.3.13 Synthesis of <i>fac</i> -[Ir(ppy) ₂ (ppy-NHR)], R=C ₂ H ₄ OH (13)	90
4.3.14 Synthesis of <i>fac</i> -[Ir(ppy) ₂ (ppy-N(R) ₂)], R=C ₂ H ₄ OH (14)	91
4.3.15 Synthesis of <i>fac</i> -[Ir(ppy) ₂ (ppy-N(CH ₃) ₂ R)], R=C ₄ H ₉ (15)	92
4.3.16 Synthesis of <i>fac</i> -[Ir(ppy) ₂ (ppy-N(CH ₃) ₂ R)], R=C ₆ H ₁₃ (16)	93
4.3.17 Synthesis of <i>fac</i> -[Ir(ppy) ₂ (ppy-N(CH ₃) ₂ R)], R=C ₈ H ₁₇ (17)	94
4.3.18 Synthesis of <i>fac</i> -[Ir(ppy) ₂ (ppy-N(CH ₃)R ₂)], R=C ₄ H ₉ (18)	95
4.3.19 Synthesis of <i>fac</i> -[Ir(ppy) ₂ (ppy-N(CH ₃) ₂ R)], R=C ₁₀ H ₂₁ (19)	96
4.3.20 Synthesis of <i>fac</i> -[Ir(ppy) ₂ (ppy-N(CH ₃) ₂ R)], R=C ₁₂ H ₂₅ (20)	97
4.3.21 Synthesis of Ir-SiO ₂ (21)	98
4.3.22 Synthesis of Ir-TEOS (22)	99
4.3.23 Synthesis of Ir-poly-L-lysine (23)	100
4.3.24 Synthesis of Ir-polystyrene powder (24)	101
4.3.25 Synthesis of Ir-polystyrene beads (25)	102
4.4 Study of the fundamental photophysical (UV-Vis, Fluorescence, Lifetime, DLS) properties of synthesized iridium complexes	103
4.5 Investigation of the relationship between the structure of the luminescent iridium complexes and their propensity to aggregate in aqueous solution	103
4.6 Investigation of the possibility to use the synthesized iridium complexes as cellular probes in fluorescence microscopy	103
4.6.1 Cell culture	103
1) Preparation for microscopy	103

2) Toxicity measurements	104
3) ICP-MS.....	105
4.6.2 Live cell imaging.....	105
1) Brightness analysis	105
4.7 Investigation of the possibility to utilize the synthesized iridium complexes as catalysts for photoredox reactions.....	106
4.7.1 α -Arylation of amines	106
4.7.2 Direct β -arylation of ketones.....	107
4.7.3 Direct allylic C-H arylation.....	107
4.7.4 Difluoromethylation	108
CHAPTER V	109
AMINOALKYL TRIS-CYCLOMETALATED IRIIDIUM COMPLEXES	109
5.1 Introduction	109
5.2 Results and discussion.....	110
5.3 Crystal structures	112
5.4 Photophysical properties in organic solvents	117
5.4.1 UV-vis spectra of complexes 3-14	117
5.4.2 Photoluminescence	118
5.4.3 Lifetime in organic solvent.....	122
5.4.4 Density Functional Theory Calculations	125
5.5 Photophysical properties in aqueous and mixed media.....	126
5.5.1 Photoluminescence	127
1) Photoluminescence in water and PBS	127
2) Photoluminescence in water and acetonitrile mixtures	129
5.5.2 Lifetime in water and acetonitrile mixtures	134
5.5.3 Dynamic light scattering.....	138
5.5.4 Effect of pH	140
5.6 Cellular experiments.....	145
5.6.1 Cytotoxicity	146

5.6.2 Brightness analysis	149
5.6.3 Microscopy studies	150
5.7 Conclusion	154
CHAPTER VI	155
QUATERNARY AMMONIUM TRIS-CYCLOMETALATED IRIDIUM COMPLEXES	155
6.1 Introduction	155
6.2 Result and discussion	157
6.2.1 Synthesis	157
6.2.2 Photophysical properties in organic solvents	161
1) UV-Vis spectrum	161
2) Photoluminescence	162
3) Lifetime	163
6.2.3 Photophysical properties in water and PBS	164
1) UV-vis and Photoluminescence spectra	164
2) Effect of pH	165
6.3 Density functional theory calculations	166
6.4 Photoreactivity	167
6.5 Cellular experiments	175
6.5.1 Cytotoxicity	175
6.5.2 Microscopy studies	176
6.6 Conclusion	178
CHAPTER VII	179
PHOTOREDOX CATALYSIS WITH TRIS-CYCLOMETALATED IRIDIUM COMPLEXES	179
7.1 Introduction	179
7.2 Results and discussion	179
7.2.1 Reactions with soluble complexes	179
1) α -Arylation of amines	180
2) β -Arylation of ketones	185

3) Direct allylic C-H arylation	188
4) Difluoromethylation	193
7.2.2 Attempts at immobilization	198
1) Synthesis.....	198
2) Photophysical properties	201
3) Stability	202
7.2.3 Photoredox catalyzed reactions with immobilized catalysts	207
1) α -Arylation of amines with immobilized catalysts	207
2) Difluoromethylation with immobilized catalysts	211
7.3 Conclusion.....	217
CHAPTER VIII	218
CONCLUSION.....	218
APPENDIX.....	220
REFERENCES	257
BIOGRAPHY	265

LIST OF TABLES

	Page
Table 1 Redox potentials and selected photophysical properties of the visible light photoredox catalysts.....	34
Table 2 The corresponding colors of the absorbed and observed wavelengths. ...	50
Table 3 UV absorbance range of different sample cells.....	52
Table 4 Manufacturer and purity of synthetic reagents.	73
Table 5 List of symbols R, R'	111
Table 6 Hydrogen-bond geometry (Å, °).	115
Table 7 Selected photophysical data in dichloromethane for complexes 2 to 14. 119	
Table 8 The emission maximum of all complexes in organic solvents (Toluene, DCM, THF, MeOH and ACN).	122
Table 9 Luminescence lifetime (μs) obtained for 10 μM solutions of complexes 3, 8, 9, and 14 various organic solvents ($\lambda_{ex} = 372$ nm) (values in brackets are for measurements in deaerated solutions).	124
Table 10 The emission maximum of complexes 3 to 14 in water and phosphate buffer (pH 7.4).	128
Table 11 The emission maximum of complexes 3 to 14 in water and acetonitrile mixtures. 131	
Table 12 Ratio luminescence intensity at 580/520 nm of complexes 3 to 14 in 0-100% water/acetonitrile solvent mixtures with varying amount of water (% v/v). Spectra were recorded with $\lambda_{ex} = 390$ nm.....	133
Table 13 Lifetime of complexes 3 to 14 in 0-100% water/acetonitrile for the monoexponential.....	135
Table 14 Lifetime of complexes 3 to 14 in 80-100% water/acetonitrile for the dominant lifetime for the biexponential.....	136
Table 15 % Value contribution of this dominant lifetime of complexes 3 to 14 in 80-100% water/acetonitrile for the biexponential.....	136
Table 16 Lifetime of complexes 3 to 14 in 80-100% water/acetonitrile for the secondary lifetime for the biexponential.....	137

Table 17	% Value contribution of this secondary lifetime of complexes 3 to 14 in 80-100% water/acetonitrile for the biexponential.....	137
Table 18	Dynamic Light Scattering Data of complexes 3-10 and 13-14 (10 μ M) in water/acetonitrile solvent mixtures with varying amount of water (60-100 % v/v), showing size-average by intensity distributions and Polydispersity Index (PDI).	139
Table 19	Ratio luminescence intensity at 580/520 nm of complexes 3 to 9 and 14 in various pH 5.5-10.0 from phosphate buffer.....	142
Table 20	Cytotoxicity and cell staining in NIH-3T3 cells of complex 9 at concentration 5 μ M.....	147
Table 21	Cytotoxicity and cell staining in NIH-3T3 cells of complex 9 at concentration 2 μ M.....	148
Table 22	IC ₅₀ values of complexes 5, 6, 9, and 14.....	149
Table 23	List of symbols R, R', R'' of the complexes discussed in this chapter..	157
Table 24	Photophysical properties of complex 15.	162
Table 25	Lifetime data for the complex 15 were obtained in aerated and deaerated organic solvents at room temperature (298 K) using TCSPC.....	163
Table 26	Structures and predicted masses for products formed during photochemical transformations of complex 15.....	173
Table 27	Conditions of photoredox catalyzed reaction of α -amino C–H arylation carried out with complexes 2, 3, and 15.	181
Table 28	Conditions of photoredox reaction of β -arylation carried out with complex 5.	187
Table 29	Conditions of photoredox reactions of allylic arylations carried out with complexes 2, 3, and 15.....	190
Table 30	Reaction conditions for photoredox catalyzed difluoromethylation using complexes 2, 3, and 15.....	194
Table 31	Structure of iridium immobilized on solid-support.....	200
Table 32	Relevant solid-state luminescence emission data of the immobilized iridium(III) complex.	201
Table 33	Conditions of photoredox reactions of allylic arylations carried out with immobilized complex 21.....	207
Table 34	Reaction conditions for photoredox catalyzed difluoromethylation using immobilized complexes 21, 22, 23, 24, and 25.	211



LIST OF FIGURES

	Page
Figure 1 Applications of cyclometalated iridium(III) complexes inspired from the attractive photophysical properties.	1
Figure 2 General structures of $[\text{Ir}(\text{ppy})_2(\text{bpy})]\text{PF}_6$, $\text{Ir}(\text{ppy})_3$, and $\text{Ir}(\text{ppy})_2(\text{ppy-NR}_1\text{R}_2)$. 2	2
Figure 3 Λ -(left-handed) and Δ -(right-handed) of enantiomers of octahedral complexes [2].	5
Figure 4 (a) Octahedral complex splitting. The changes in the energies of the electrons occupying the d orbitals when the latter is in an octahedral crystal field. (b) The energy changes are shown in terms of the orbital energies [3].	5
Figure 5 Stereochemical diagrams of representative archetypal cyclometalated Ir(III) complexes [8].	7
Figure 6 Structural formula of additional examples of cyclometalated Ir(III) complexes [8].	7
Figure 7 Structural formula of representative cyclometalated Ir(III) complexes comprising carbene ligands [8].	8
Figure 8 Stereochemical diagrams of representative cyclometalated Ir(III) complexes comprising tridentate ligands [8].	8
Figure 9 Orbital description of MC, MLCT and LC transitions; S is a substituent group capable of exerting electron withdrawing or donating effects (resulting in stabilization or destabilization, respectively, of the energy level of the filled d and π orbitals) [9].	9
Figure 10 Electronic transitions involving MC, MLCT and LC excited states; the MC levels are non-emissive (dashed arrows) [9].	10
Figure 11 Diagram showing in photophysical properties of luminescent iridium complexes [11].	10
Figure 12 Locations of the HOMO and LUMO on an ionic iridium(III) complex [14]. 11	11
Figure 13 Tuning of photophysical properties of cyclometalated iridium complexes through independent modulation of HOMO and LUMO orbitals [11].	11

Figure 14	Color versatility expressed by a series of six cationic iridium(III) luminophores [16].	12
Figure 15	Major organelles of an animal cell [24].	14
Figure 16	Chemical structures of iridium(III) complexes and their corresponding photoluminescence emission spectra in dichloromethane using 365 nm excitation wavelength. Prepared 10 mM of complexes 1 and 2 at room temperature [29].	15
Figure 17	Confocal luminescence (a and d) and brightfield images (b and e) of living HeLa cells incubated with 20 μ M of complexes 1 (top) and 2 (bottom). Samples are in DMSO/PBS (pH 7, 1:49, v/v) and were incubated with HeLa cells for 10 minutes at room temperature [29].	15
Figure 18	Structures of the iridium(III) Dpq and Dpqa Complexes. Fluorescence laser-scanning confocal microscopy images of fixed MDCK cells treated with the iridium(III) dpq and dpqa complexes (5 μ M) at room temperature for 30 min [30].	16
Figure 19	Chemical Structures of [Ir(bt) ₂ (acac)] (Ir-1), [Ir(bt) ₂ (bpy)]PF ₆ (Ir-2), and [Ir(bt) ₂ (CH ₃ CN) ₂]OTf (Ir-3). Luminescent photographs of Ir-1 at different pH values. Solution (a) and luminescence (b) color photographs of Ir-1 (40 μ M in CH ₃ CN solution) before (a ₁ and b ₁) and after (a ₂ and b ₂) addition of 1 equiv of Hg(II). Absorption (a) and emission spectra (b) of Ir-1, Ir-2, and Ir-3 in CH ₃ CN solution. Ratiometric phosphorescence images of Ir-1-incubated KB cells treated without or with Hg(II) [31].	17
Figure 20	The chemical structures of the biscarbene iridium(III) complexes. Absorption (A) and normalized emission (B) spectra of complexes 1-5 in acetonitrile solutions (40 mM, (λ_{ex} = 360 nm). Fluorescence images of HeLa cells incubated with complexes 1–5 for 2 hours at 37 °C [32].	18
Figure 21	Structures of the Ir-lyso. Absorption spectrum and emission spectrum of Ir-lyso (5 μ M) in disodium hydrogen phosphate/citric acid buffer solution (pH = 5.5). One-photon microscopy (OPM) and two-photon microscopy (TPM) images of HeLa cells colabeled with Ir-lyso (2 μ M, 0.5 h) and LTR (50 nM, 0.5 h). Scale bar: 20 μ m [34].	19
Figure 22	Tris-cyclometalated luminescent iridium(III) complex exhibiting selective staining of the lysosomes [35].	20
Figure 23	Confocal fluorescence images, brightfield images and their overlay of living HeLa cells incubated with 5 μ M Ir1 for 1 h at 37 °C. UV–Vis absorption spectra of Ir1 in hexane/ CH ₂ Cl ₂ mixture. Emission spectra of Ir1 in the different hexane/ CH ₂ Cl ₂ fraction solutions. The inset shows the change in the emission	

intensity of complex versus hexane fractions in CH_2Cl_2 . Images of the brightfield and room temperature luminescent emissions ($\lambda_{\text{ex}} = 365 \text{ nm}$) [36].21

Figure 24 Structures of the neutral iridium(III) complex pH-responsive probes. Luminescence microscopy images of HeLa-S3 cells stained with Ir complex (10 μM) and MitoTracker (10 nM) in MEM/DMSO (99/1, v/v) at 37 °C for 30 min. (a) brightfield image of HeLa-S3 cells, (b) emission images of Ir, (c) emission images of MitoTracker, and (d) overlay image of (c) and (d). λ_{ex} (b) = 377 nm, (c) = 540 nm [37]. 22

Figure 25 Structure of pH responsive luminescent iridium complex developed by Williams and co-worker. Corrected emission spectra of 1 and 2 in CH_2Cl_2 and the spectrum from CHO cells dosed with complex 1 (10 mM, 5 min incubation). Fluorescence microscopy images of live CHO cells co-stained Ir(III) complexes obtained without (a) and with (b) a 10 ns gate between excitation and imaging [38]. 23

Figure 26 (a) Schematic drawing of the structures of Ir1 and Ir2. (b) X-ray structures of the cations in Ir1 and Ir2 are showed in thermal ellipsoids at the 30% probability level. The hydrogen atoms and counterions are omitted for clarity. (c) UV/vis absorption and normalized photoluminescence (PL) spectra of Ir1 ($2 \times 10^{-5} \text{ M}$) and Ir2 ($2 \times 10^{-5} \text{ M}$) are measured in acetonitrile. $\lambda_{\text{ex}} = 405 \text{ nm}$ [39].24

Figure 27 (a) Representative confocal images of A549 cells exposed to Ir1/Ir2 (15 μM , 1 h) and MTDR (100 nM, 30 min). (b) Representative confocal images of A549 cells exposed to Ir1/Ir2 (15 μM , 1 h) and LTDR (50 nM, 30 min). Scale bars: 10 μm [39]. 25

Figure 28 Iridium complexes interacting with endoplasmic reticulum (ER) and mitochondria in live H9c2 cells [40].26

Figure 29 Iridium complex-peptide hybrid (IPH) induces a paraptosis-like cell death [41]. 27

Figure 30 Structures of complexes 1 and 2. Photograph of complexes 1 and 2 in various pH 5.5-9.5 (10 μM) was observed with the naked eye under 365 nm. Ratio of the emission intensity of complexes 1 and 2 at 580 nm and 520 nm as a function of pH [42]. 28

Figure 31 Fluorescence microscopy images of NIH-3T3 cells obtained with complex 1 (left) and 2 (right) (λ_{ex} 355 nm, λ_{em} 450–650 nm) (a), LysoTracker Red (λ_{ex} 543 nm HeNe laser, λ_{em} 600–650 nm) (b). Panel (c) shows the RGB overlay of panels (a) and (b); $P = 0.84(1)$ and $0.79(2)$, while panel (d) is the bright field image (scale bar: 20 μm) [42].28

Figure 32	The evolution of photoredox–transition metal catalysis. Number of publications per year in field of organic photoredox catalysis (data collected from Scopus, August 10, 2020).	29
Figure 33	Comparison of catalytic activation modes [47].	31
Figure 34	Multicatalytic activation modes of synergistic catalytic [47].	31
Figure 35	Quenching modes in photoredox catalysis [48].	32
Figure 36	Photoredox transformations using transition metal complexes as catalysts [49, 50]	33
Figure 37	Photoredox transformations using ruthenium complexes as catalysts [51, 52].	33
Figure 38	(a) Jablonski diagram of photophysical processes undertaken by the transition metal photocatalyst upon visible-light irradiation. (b) The redox transformations possible with Ir(ppy) ₃ photocatalyst [58].	35
Figure 39	Proposed catalytic cycle for metallaphotoredox C–H acylation [59].	36
Figure 40	Proposed catalytic cycle for β -sulfonation and aromatization of pyrrolidine derivatives using photoredox catalysis [62].	38
Figure 41	Proposed mechanism of the photoredox catalyzed arylation of α -amino C–H bonds [64].	40
Figure 42	Proposed mechanism for the direct β -arylation of ketones and aldehydes [65].	41
Figure 43	Proposed mechanism for the direct arylation of allylic C–H bonds via photoredox and organic catalysis [66].	42
Figure 44	Mechanism on the visible-light photoredox difluoromethylation [67]. ...	44
Figure 45	Structural of Ir-catalyzed aromatic C–H borylation [69].	46
Figure 46	The electromagnetic spectrum [75].	48
Figure 47	Illustration of different types of electronic transitions [76].	48
Figure 48	Typical optical layout of an absorption spectrophotometer. (A) Single beam spectrophotometer and (B) double beam spectrophotometer [81].	51
Figure 49	Perrin-Jablonski diagram showing the electronic processes occurring in a fluorescent molecule after excitation by light [82].	53
Figure 50	Mirror-image rule and Franck-Condon factors. The absorption and emission spectra are for anthracene (in Toluene). The numbers 0, 1, and 2 refer to vibrational energy levels [82].	56

Figure 51	Fluorescence lifetime measurements using the time-domain method and the frequency-domain method [84].	57
Figure 52	X-ray diffraction [109].	62
Figure 53	Constructive (on the left) and deconstructive (on the right) interferences in X-ray diffraction of a crystal sample [109].	63
Figure 54	The seven primitive crystal systems [110].	64
Figure 55	Leica SP5 II Confocal Laser Scanning Microscope is capable of Fluorescence Lifetime Imaging Microscopy and Fluorescence Cross Correlation Spectroscopy [111].	66
Figure 56	Confocal vs. Widefield illumination. Confocal: Light from the light-source (Ls) is focused through a pinhole for illumination (Pi) and subsequently into the sample (S) resulting in a relatively small volume. Widefield: The whole specimen volume is exposed to light [112].	67
Figure 57	Super-resolution optical microscopy enables imaging of such living viruses, proteins, small molecules, and other nanoscale structures [112].	67
Figure 58	Comparison of widefield (upper row) and laser scanning confocal fluorescence microscopy images (lower row) [112].	68
Figure 59	Comparison of axial (x-z) point spread functions for widefield (left) and confocal (right) microscopy [113].	69
Figure 60	Confocal microscope configuration and information flow schematic diagram [112].	69
Figure 61	The History of the light bulb (data from energy.gov, July 15,2020).	71
Figure 62	Standardization and Acceleration of photocatalytic reactions [118].	72
Figure 63	IC ₅₀ determination using linear regression.	105
Figure 64	Selected sample areas of cell incubated with luminescent Ir(III) compound for determination of mean grey values.	106
Figure 65	Structures of Iridium complexes 3 and 8.	110
Figure 66	A view of the molecular structures of the two independent cationic molecules of the complex 4, with the atom labelling. Displacement ellipsoids are drawn at the 35% probability level. Symmetry codes: (i) $x + 1, -y + 12, z + 12$; (ii) $-x + 2, -y + 1, -z + 1$; (iii) $x, -y + 12, z - 32$.	113
Figure 67	A perspective view of the complex 4, showing the intermolecular N-H...Cl hydrogen bonds (dotted lines) between the two independent molecules.	114

Figure 68	A perspective view showing the parallel fourfold phenyl embrace in the complex 4.	115
Figure 69	Normalized absorption spectrum of complex 4 (10 μ M) recorded in dichloromethane.	117
Figure 70	Normalized luminescence intensity of complex <i>fac</i> -[Ir(ppy) ₂ (ppy-NC ₆)] (4) (10 μ M) measured in dichloromethane. Emission spectra were recorded with λ_{ex} = 390 nm at room temperature.	118
Figure 71	Normalized luminescence intensity of complex 2 to 14 (10 μ M) measured in dichloromethane. Emission spectra were recorded with λ_{ex} = 390 nm at room temperature.	119
Figure 72	Normalized luminescence intensity of complex 2 to 14 (10 μ M) in toluene (a), tetrahydrofuran (b), methanol (c), and acetonitrile (d), respectively. Emission spectra were recorded with λ_{ex} = 390 nm at room temperature.	120
Figure 73	Plot emission intensity decay for complexes 9 and 14 in aerated dichloromethane solution.	123
Figure 74	Luminescence intensity of complexes 9 and 14 in dichloromethane aerated and deaerated. Emission spectra were recorded with λ_{ex} = 390 nm. Slit 2-2 nm.	123
Figure 75	The HOMO and LUMO orbitals of complex 9 calculated in dichloromethane.	125
Figure 76	The HOMO and LUMO orbitals of complex 14 calculated in dichloromethane.	126
Figure 77	Comparison of experimental and calculated (TD-DFT) spectra of 1 (complex 9) and 2 (complex 14) in dichloromethane.	126
Figure 78	Normalized luminescence intensity of complexes 3 to 14 in water (a) and phosphate buffer (pH 7.4) (b). Excitation spectra were recorded with λ_{ex} = 390 nm for the emission.	128
Figure 79	Normalized luminescence intensity of complexes 3 (a), 8 (b), 9 (c), and 14 (d) in water and acetonitrile mixtures. Excitation spectra were recorded with λ_{ex} = 390 nm for the emission.	130
Figure 80	Photograph of complexes 3 to 8 solutions (10 μ M) in 0-100% water/acetonitrile (left→right) was observed with the naked eye under 365 nm.	131

Figure 81	Ratio luminescence intensity at 580/520 nm of complex 3 to 8 (a) and 9 to 14 (b) in 0-100% water/acetonitrile solvent mixtures with varying amount of water (% v/v). Emission spectra were recorded with $\lambda_{\text{ex}} = 390$ nm.	132
Figure 82	Lifetime of series of aminoalkyl iridium complexes 3 to 8 (a) and 9 to 14 (b) 10 μM in water/acetonitrile solvent mixtures with varying amount of water (% v/v) for the monoexponential.	135
Figure 83	Z-Average size(nm) distribution by intensity of a series of aminoalkyl iridium complexes 3-10 and 13-14 in water/acetonitrile solvent mixtures with varying amount of water (%v/v).	139
Figure 84	Ratio luminescence intensity at 580/520 nm of complexes 3 to 9 and 14 in various pH 5.5-10.0 from phosphate buffer. Emission spectra were recorded with $\lambda_{\text{ex}} = 390$ nm.	141
Figure 85	Normalized luminescence intensity at 580/520 nm of complex 4 (a), 9 (b) and 14 (c) in various pH 5.5-10.0 from phosphate buffer. Emission spectra were recorded with $\lambda_{\text{ex}} = 390$ nm.	143
Figure 86	Photograph of complexes 3 to 8 solutions (10 μM) with different phosphate buffer from pH 5.5 to 9.5 (left→right) was observed with the naked eye under 365 nm.	144
Figure 87	Cyclometalated Ir(III) complexes to be investigated.	145
Figure 88	Viability of NIH-3T3 cells after 24 h exposure complexes 5, 6, 9, and 14.	146
Figure 89	Brightness analysis of microscopy image of cells incubated with complexes 5, 6, and 9 relative to control image of cell at a) 5 μM ,	149
Figure 90	LSCM microscopy images of NIH-3T3 cells obtained with complex 5 (λ_{ex} 355 nm, λ_{em} 450-650 nm) (a), lysotracker red (λ_{ex} 543 nm HeNe laser, λ_{em} 600-650 nm) (b). Panel c shows the RGB overlay of panels a and b, while panel d is the brightfield image. (Scale bar: 10 μm).	150
Figure 91	LSCM microscopy images of NIH-3T3 cells obtained with complex 6 (λ_{ex} 355 nm, λ_{em} 450-650 nm) (a), lysotracker red (λ_{ex} 543 nm HeNe laser, λ_{em} 600-650 nm) (b). Panel c shows the RGB overlay of panels a and b, while panel d is the brightfield image. (Scale bar: 10 μm).	151
Figure 92	LSCM microscopy images of NIH-3T3 cells obtained with complex 9 (λ_{ex} 355 nm, λ_{em} 450-650 nm) (a), lysotracker red (λ_{ex} 543 nm HeNe laser, λ_{em} 600-650 nm) (b). Panel c shows the RGB overlay of panels a and b; P = 0.68, while panel d is the brightfield image. (Scale bar: 20 μm).	152

Figure 93	LSCM microscopy images of NIH-3T3 cells obtained with complex 14 (λ_{ex} 355 nm, λ_{em} 450-650 nm) (a), lysotracker red (λ_{ex} 543 nm HeNe laser, λ_{em} 600-650 nm) (b). Panel c shows the RGB overlay of panels a and b; $P = 0.74$, while panel d is the brightfield image. (Scale bar: 20 μm)	153
Figure 94	Structural of quarternary ammonium salts iridium (III) complexes 15 to 20.	157
Figure 95	HRMS spectrum of the crude reaction mixture of complex 15.	158
Figure 96	HRMS spectrum of complex 15 after purification by column chromatography.	158
Figure 97	HRMS spectrum of complex 15 after purification by recrystallization.	159
Figure 98	Structure and precipitates image of complexes 15 to be investigated in this chapter.	159
Figure 99	^1H -NMR spectrum of complex 15 kept in light at ambient conditions (top) and <i>fac</i> -[Ir(ppy) ₂ (fppy)] (bottom) in DMSO- d_6 .	160
Figure 100	Absorption spectrum of complex 15 (10 μM) recorded in dichloromethane.	161
Figure 101	Normalized luminescence intensity spectrum of complex 15 (10 μM) recorded in dichloromethane.	162
Figure 102	Normalized absorption (a) and luminescence intensity (b) of complex 15 (10 μM) in water and phosphate buffer (pH 7.0).	164
Figure 103	Ratio luminescence intensity at 580/520 nm of complex 15 in various pH 5.5-10.0 from phosphate buffer. Emission spectra were recorded with $\lambda_{\text{ex}} = 390$ nm.	165
Figure 104	The HOMO and LUMO orbitals of complex 15 calculated in dichloromethane.	166
Figure 105	The HOMO and LUMO orbitals of the triplet state of complex 15 calculated in dichloromethane.	166
Figure 106	ES^+ HRMS spectrum of complex 15 kept in dark at ambient conditions in DMSO solution for 3 weeks.	168
Figure 107	ES^+ HRMS spectrum of complex 15 kept in light at ambient conditions in DMSO solution for 24 hours.	168
Figure 108	ES^+ HRMS spectrum of complex 15 kept in light at ambient conditions in DCM solution for 24 hours.	168

Figure 109 ES ⁺ HRMS spectrum of complex 15 kept in light at ambient conditions in MeOH solution for 24 hours.....	169
Figure 110 ES ⁺ HRMS spectrum of complex 15 kept in light at ambient conditions in ACN solution for 24 hours.....	169
Figure 111 ES ⁺ HRMS spectrum of reaction mixture containing complex 15 and benzylamine irradiated by and LED lamp for 72 hours.....	171
Figure 112 ES ⁺ HRMS spectrum of reaction mixture containing complex 15 and benzylalcohol irradiated by and LED lamp for 72 hours.....	172
Figure 113 ES ⁺ HRMS spectrum of reaction mixture containing complex 15 and octylamine irradiated by and LED lamp for 72 hours.	172
Figure 114 ES ⁺ HRMS spectrum of reaction mixture containing complex 15 and di-butylamine irradiated by and LED lamp for 72 hours.	172
Figure 115 Plot viability of NIH-3T3 cells versus concentration of complex 15.....	175
Figure 116 Fluorescence microscopy images of NIH-3T3 cells obtained with complex 15 (λ_{ex} 355 nm, λ_{em} 450-650 nm) (a), lysotacker red (λ_{ex} 543 nm HeNe laser, λ_{em} 600-650 nm) (b). Panel c shows the RGB overlay of panels a and b; P = 0.80, while panel d is the brightfield image. (Scale bar: 20 μm).....	176
Figure 117 Emission spectrum obtained from lysed cells loaded with complex 15.	177
Figure 118 Two photon microscopy image of NIH-3T3 cells incubated with complex 15 and acquired at 720 nm excitation, with emission collected using a 510 nm longpass filter.	177
Figure 119 Set up reaction of photoredox catalysis.....	180
Figure 120 ¹ H-NMR (top) and Mass spectrum (bottom) of 1a.....	182
Figure 121 ¹ H-NMR (top) and Mass spectrum (bottom) of 2a.....	183
Figure 122 ¹ H-NMR (top) and Mass spectrum (bottom) of 3a.....	184
Figure 123 ¹ H-NMR spectrum of 1b.	187
Figure 124 ¹ H-NMR spectrum of compound 1c.....	191
Figure 125 ¹ H-NMR spectrum of compound 2c.....	191
Figure 126 ¹ H-NMR spectrum of compound 3c.....	192
Figure 127 ¹ H-NMR (top) and ¹⁹ F-NMR (bottom) spectrum of 1d in CDCl ₃	195
Figure 128 ¹ H-NMR (top) and ¹⁹ F-NMR (bottom) spectrum of 2d in CDCl ₃	196
Figure 129 ¹ H-NMR spectrum of 3d in CDCl ₃	197

Figure 130 Structure of photoredox catalysts 21-25 immobilized on solid particles.
198

Figure 131 Normalized luminescence intensity in the solid state recorded for immobilized complexes 21 to 25 upon excitation the samples at 390 nm at room temperature. 201

Figure 132 Mass spectrum of complex 21_Dark 24 h.....202

Figure 133 Mass spectrum of complex 21_Light 24 h.202

Figure 134 Mass spectrum of complex 22_Dark 24 h.....203

Figure 135 Mass spectrum of complex 22_Light 24 h.203

Figure 136 Mass spectrum of complex 23_Dark 24 h.....204

Figure 137 Mass spectrum of complex 23_Light 24 h.204

Figure 138 Mass spectrum of complex 24_Dark 24 h.....205

Figure 139 Mass spectrum of complex 24_Light 24 h.205

Figure 140 Mass spectrum of complex 25_Dark 24 h.....206

Figure 141 Mass spectrum of complex 25_Light 24 h.206

Figure 142 Mass spectrum of 1e.....208

Figure 143 Mass spectrum of 1e_recycle.208

Figure 144 Mass spectrum of 2e.....209

Figure 145 Mass spectrum of 2e_recycle.209

Figure 146 ^1H -NMR spectrum of 2e in CDCl_3210

Figure 147 ^1H -NMR spectrum of 1f in CDCl_3212

Figure 148 ^1H -NMR spectrum of 1f_recycle in CDCl_3213

Figure 149 ^1H -NMR spectrum of 2f in CDCl_3213

Figure 150 ^1H -NMR spectrum of 2f_recycle in CDCl_3214

Figure 151 ^1H -NMR spectrum of 3f in CDCl_3214

Figure 152 ^1H -NMR spectrum of 4f in CDCl_3215

Figure 153 ^1H -NMR spectrum of 4f_recycle in CDCl_3215

Figure 154 ^1H -NMR spectrum of 5f in CDCl_3216

Figure 155 ^1H -NMR spectrum of 5f_recycle #1 in CDCl_3216

Figure 156 ^1H -NMR spectrum of 5f_recycle #2 in CDCl_3217



ABBREVIATIONS

ϕ	=	quantum yield
μ	=	micron
τ	=	excited state lifetime
λ	=	wavelength
Λ	=	left-handedness
Δ	=	right-handedness
ζ	=	spin-orbit coupling constant
δ	=	chemical shift
ε	=	extinction coefficient
ν	=	frequency
$^{\circ}\text{C}$	=	degrees Celsius
λ_{em}	=	emission wavelength
λ_{ex}	=	excitation wavelength
μg	=	microgram
μL	=	microliter
μmol	=	micromole
μs	=	microsecond
a.u.	=	arbitrary units
au	=	atomic units
azepane	=	hexamethyleneimine
b.p.	=	boiling point
C	=	carbon
C ^N	=	cyclometallating ligand
cm	=	centimeter
CT	=	charge transfer
d	=	day; doublet
DABCO	=	1,4-diazabicyclo[2.2.2]octane
DCM or CH ₂ Cl	=	dichloromethane
dd	=	doublet of doublets
ddd	=	doublet of doublets of doublets
DFT	=	density functional theory
dm	=	decimeter
DMA	=	<i>N,N</i> -dimethylacetamide
DMF	=	<i>N,N'</i> -dimethylformamide
DMPU	=	<i>N,N'</i> -dimethylprolineurea
DMSO	=	dimethylsulfoxid
dt	=	doublet of triplets
<i>E</i>	=	half-cell potential; energy

$E_{1/2}^{\text{ox}}$	=	half-cell oxidation
$E_{1/2}^{\text{red}}$	=	half-cell reduction
EDG	=	electron-donating group
equi.	=	equivalent
EWG	=	electron-withdrawing group
g	=	gram
GS	=	ground state
h	=	hour
h ν	=	visible light (unless stated otherwise)
HOMO	=	highest occupied molecular orbital
Ir	=	iridium
ISC	=	inter system crossing
J	=	coupling constant
K	=	Kelvin
k_{nr}	=	non-radiative decay rate constant
k_{r}	=	radiative decay rate constant
LC	=	ligand-center
LED	=	light-emitting diode
LLCT	=	ligand-to-ligand charge transfer
LUMO	=	lower unoccupied molecular orbital
m	=	meter; multiplet
M	=	molarity
m.p.	=	melting point
m/z	=	mass to charge ratio
MC	=	metal-center
Me or CH ₃	=	methyl
MeCN or CH ₃ CN	=	acetonitrile
mg	=	milligram
MHz	=	megahertz
min	=	minute
mL	=	milliliter
MLCT	=	metal to ligand charge transfer
mmol	=	millimole
MO	=	molecular orbital
mol	=	mole
MS	=	mass spectrometry
MW	=	molecular weight
N [^] N	=	ancillary ligand
nm	=	nanometer
NMR	=	nuclear magnetic resonance
ns	=	nanosecond

O	=	oxygen
OLEDs	=	organic light-emitting diodes
ppm	=	parts per million
ppy	=	2-phenylpyridine
Q-TOF	=	quadrupole-time-of-flight
Ru	=	ruthenium
s	=	second; singlet
S ₀	=	ground state
S ₁	=	first singlet state
S ₂	=	second singlet state
SET	=	single electron transfer
MC	=	metal charge transfer
LC	=	ligand charge transfer
lum.	=	luminescence
PBS	=	Phosphate buffer saline
t	=	triplet
T ₁	=	lowest-lying triplet state
THF	=	tetrahydrofuran
UV	=	ultraviolet
V	=	volts
Vis	=	visible
W	=	watts

CHAPTER I

INTRODUCTION

Cyclometalated iridium(III) complexes are compounds exhibiting a number of interesting properties, especially related to their photophysical behavior. Of note is their utilization in fields of cellular imaging, organic light emitting diodes (OLEDs), and photocatalysis. The beneficial properties of cyclometalated iridium(III) complexes, including efficient population of excited triplet states by intersystem crossing and their eventual radiative relaxation to the ground state, are related to efficient spin orbit coupling of the iridium(III) ion. In addition, cyclometalated iridium(III) complexes offer more rich photophysical properties than ruthenium(II) polypyridyl complexes, which makes it easier to tune their properties. For example, iridium(III) complexes exhibit photophysical properties based on a range of different types of electronic transitions, while the photophysical properties of ruthenium(II) complexes are almost exclusively based on metal to ligand charge transfer (MLCT) transitions. In addition, the localization of frontier orbitals of cyclometalated iridium(III) complexes facilitates the tuning of their emission colors.

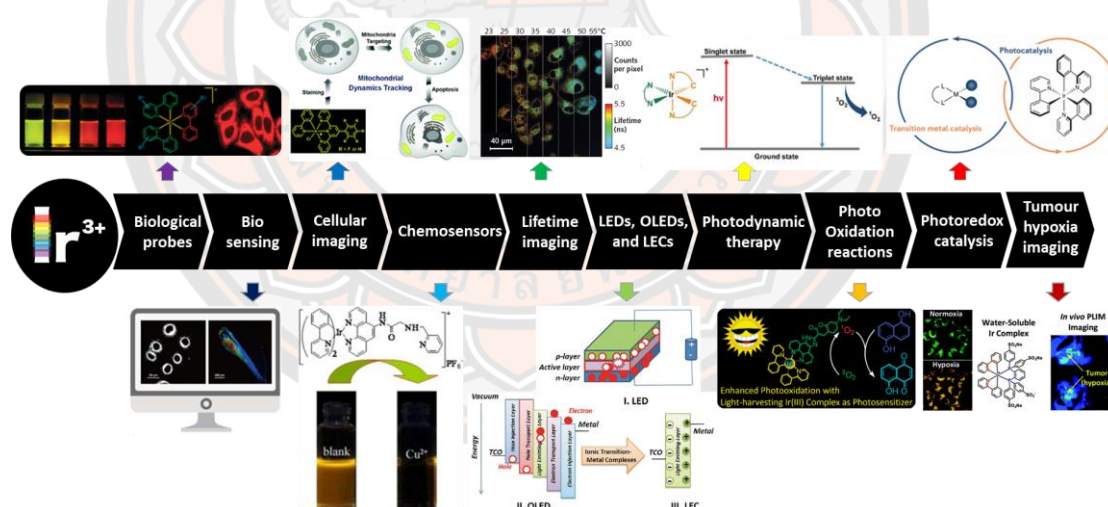


Figure 1 Applications of cyclometalated iridium(III) complexes inspired from the attractive photophysical properties.

Structurally, cyclometalated iridium(III) complexes can be divided into several classes with most of them falling in two categories: bis-cyclometalated or tris-cyclometalated. Both of these classes have been investigated as phosphorescent cellular probes, the initial area of our interest in these compounds. However, bis-cyclometalated iridium(III) complexes have been more widely investigated in this regard. We have recently identified and published several tris-cyclometalated iridium(III) complexes, which showed promise in terms of being used as cellular probes. We have hypothesized that these results could stem from the presence of an aminoalkyl group in the structure of our complexes, which can endow them with positive charge in cell imaging buffers. In fact, the positive charge of bis-cyclometalated iridium(III) complexes, in contrast to the charge neutral nature of triscyclometalated structures, is seen as a potential reason for their better performance in cellular imaging. These results have prompted us to study further derivatives from this class of compounds as potential cellular probes given the relative scarcity of tris-cyclometalated iridium(III) complexes being used in this regard. In addition, our previous report uncovered interesting aggregation behavior of these complexes in aqueous solutions. Therefore, a systematic study of the relationship between the structure of the complexes and their behavior in aqueous solution is also one of the goals of this work as they can lay ground for the development sensors for various species based on our luminescent materials.

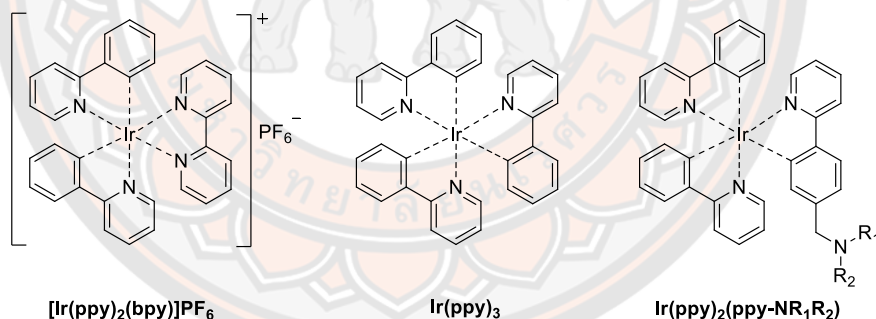
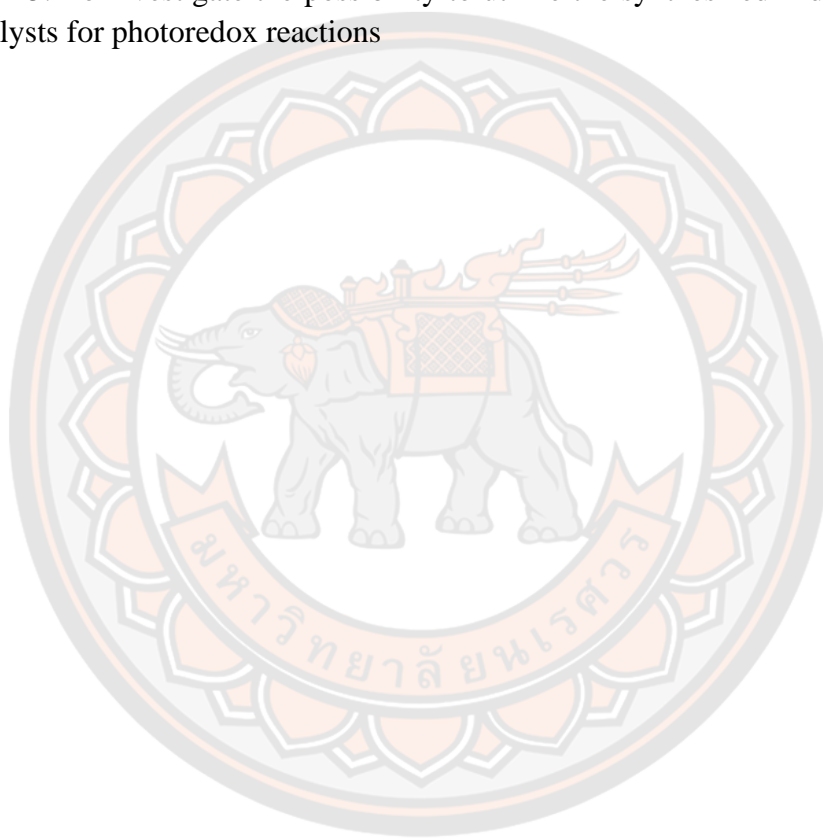


Figure 2 General structures of $[\text{Ir}(\text{ppy})_2(\text{bpy})]\text{PF}_6$, $\text{Ir}(\text{ppy})_3$, and $\text{Ir}(\text{ppy})_2(\text{ppy}-\text{NR}_1\text{R}_2)$.

In addition, photoredox chemistry has gained significant amount of interest in recent years as an alternative methodology in organic synthesis. Tris-cyclometalated iridium(III) complexes, due to their interesting photophysical properties and their ability to cause single-electrontransfer (SET) processes under mild conditions by irradiation of visible light (sunlight), have also been identified as potential catalysts for these reactions. One of the major challenges in the field of catalysis is the development of immobilized iridium(III) complexes to be utilized as recoverable and easier to separate catalysts in photoredox catalysis reaction.

Therefore, the aim of this work to study the tris-cyclometalated iridium(III) complexes synthesized in the course of this project for the following purposes:

1. To develop novel photoactive tris-cyclometalated iridium complexes
2. To study the fundamental photophysical (UV-Vis, Fluorescence, Lifetime, DLS) properties of synthesized iridium complexes
3. To investigate the relationship between the structure of the luminescent iridium complexes and their propensity to aggregate in aqueous solution
4. To investigate the possibility to use the synthesized iridium complexes as cellular probes in fluorescence microscopy
5. To investigate the possibility to utilize the synthesized iridium complexes as catalysts for photoredox reactions



CHAPTER II

PREVIEW OF RELATED LITERATURE AND RESEARCH

Photoactive cyclometalated iridium complexes exhibit a number of interesting photophysical properties. They might emit light upon photo excitation, which makes them interesting luminophores for spectroscopic and imaging purposes. The energy of the photoexcited states can also be utilized to drive chemical reactions, which are classified as photoredox transformations. Basic principles of fluorescence spectroscopy, fluorescence microscopy, and photoredox catalysis will be discussed below. This discussion will be followed by the discussion of properties of photoactive cyclometalated iridium complexes pertinent to these areas of interest.

2.1 Photoactive cyclometalated iridium complexes

One of the classes of luminescent and photoactive compounds that have received interest recently and that are the focus of this project are cyclometalated iridium complexes. These compounds offer specific benefits such as high luminescence quantum yields and the possibility to tune their emission wavelength. Luminescent iridium complexes can be classified into two main groups. Positively charged complexes made from two cyclometalating C^N ligands and a N⁺N ligand constitute the first group. Neutral complexes made either from three cyclometalating C^N ligands or two of such ligands and a negatively charged ligand such as picolinate form the second group. This work focuses on neutral tris-cyclometalated complexes as they are relatively underrepresented among luminescent iridium complexes used as probes in fluorescence microscopy.

2.1.1 Structure and properties of iridium complexes

Iridium has the ability to form compounds in many different oxidation states, starting with -3 (very rare) and all the states between -1 and +6. The most stable ones are +3 and +4 [1]. Iridium(III) has the [Xe] 5d⁶ electron configuration. Therefore, the geometrical arrangement of donor atoms around an iridium(III) metal center is normally octahedral [2]. A tris-chelate iridium complex in an octahedral environment is always chiral, yielding two enantiomers. To distinguish the two forms, the octahedron is viewed down a 3-fold axis. The enantiomer with left-handedness is labelled Λ , and that with right-handedness is Δ (**Figure 3**).

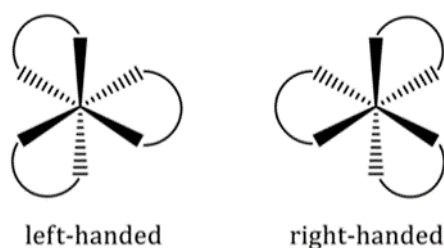


Figure 3 Λ -(left-handed) and Δ -(right-handed) of enantiomers of octahedral complexes [2].

In the free Ir^{3+} ion, the d orbitals are degenerate, i.e. in the gas phase ion with no ligand field. The orbitals are split in an octahedral ligand field by the amount of Δ_{oct} (**Figure 4**) [3]. In an O_h -symmetric complex, a d^6 electronic configuration can be low or high-spin, with a configuration of $t_{2g}^6 e_g^0$ or $t_{2g}^4 e_g^2$, respectively. Heavier metals have a larger splitting of the t_{2g} and e_g levels (i.e. large Δ_{oct} value) than 1st row metals. This leads to heavier metal ions invariably being low spin.

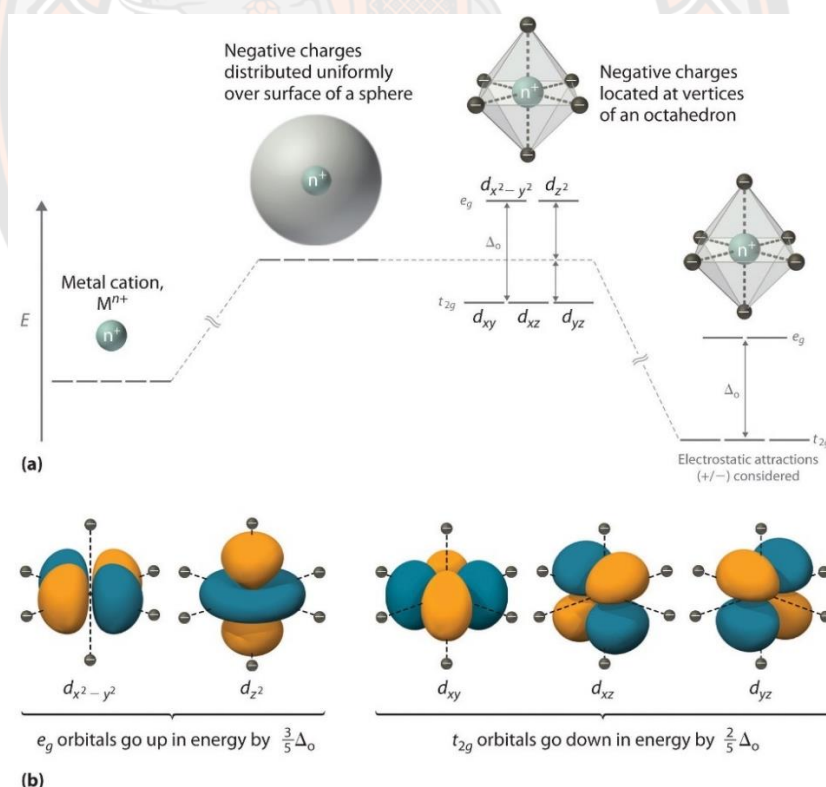


Figure 4 (a) Octahedral complex splitting. The changes in the energies of the electrons occupying the d orbitals when the latter is in an octahedral crystal field. (b) The energy changes are shown in terms of the orbital energies [3].

Thus the electrons in d^6 iridium(III) species are paired, leading to kinetically inert compounds with diamagnetic properties [4]. The amount of the splitting is dependent on the field strength exerted by the ligands.

2.1.2 Cyclometalated iridium complexes

In 1985, Watts and co-workers reported the synthesis of *fac*-Ir(ppy)₃ which was the first tris-cyclometalated complex of the ppy (ppy = 2-phenylpyridine) ligand [5]. This initial report led to a surge of research interest in the development of phosphorescent cyclometalated Ir(III) complexes. In 1999, Thompson, Forrest et al. demonstrated the first example of an organic light emitting diode (OLED) that incorporated *fac*-Ir(ppy)₃ as a phosphorescent dopant in the emitting layer [6].

Tris-bidentate Ir(III) complexes with asymmetric chelating ligands can adopt either a facial (*fac*) or meridional (*mer*) structure, which have *N,N*-cis and *N,N*-trans configurations respectively. The kinetic product, (*mer*) can be converted to the thermodynamic product (*fac*) both thermally and photochemically. Thompson et al. reported the first selective synthesis of *mer* and *fac* tris-cyclometalated Ir(III) complexes (**Figure 5**) and described the pronounced differences in the photophysical and electrochemical behavior of the facial and meridional isomers. The major differences found in this study include (i) the meridional complexes have oxidation potentials approximately 50-100 mV less positive than the corresponding facial complexes (ii) the MLCT absorption bands are less sharply defined in the meridional isomers and have lower extinction coefficients than those in the facial isomers and (iii) the meridional isomers display broader, more red-shifted emission in comparison to the facial isomers [7].

Ir(III) complexes bearing C[^]N and C[^]C: cyclometalated ligands possess impressive photophysical properties that make these compounds highly desirable for the optoelectronic and photonic applications. Stereochemical illustrations of representative archetypal Ir(III) cyclometalates are presented in **Figure 5** and structural formulae for additional examples are shown in **Figure 6**. In these structures, the C[^]N and C[^]C: bidentate ligands are monoanionic, and the negative charge is donated by a C atom occupying one coordination site. In the case of the C[^]C: cyclometalates, the second coordination site is occupied by the neutral C-donor (designated C:) of the carbene moiety (**Figure 7**). The :C[^]N and :C[^]C: types of carbene ligands are charge neutral and have been incorporated in heteroleptic complexes with monoanionic C[^]N or C[^]C: ligands. Examples of Ir(III) cyclometalates with tridentate ligands are shown in **Figure 8**. The Ir(III) complexes are generally obtained as racemic mixtures, and the structural diagrams in iridium complexes immobilize on solid support [8].

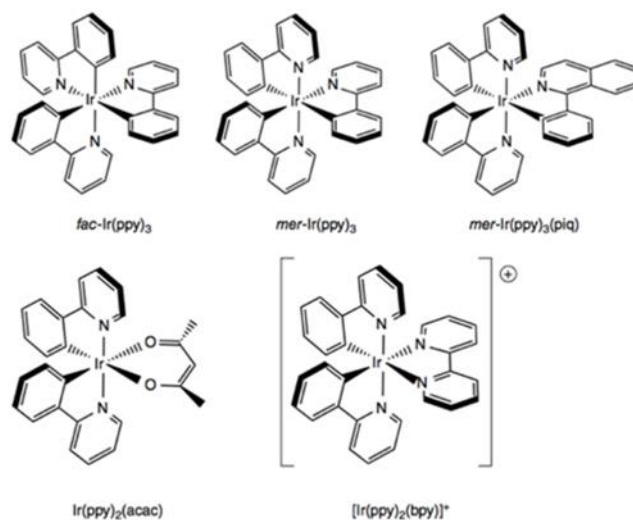


Figure 5 Stereochemical diagrams of representative archetypal cyclometalated Ir(III) complexes [8].

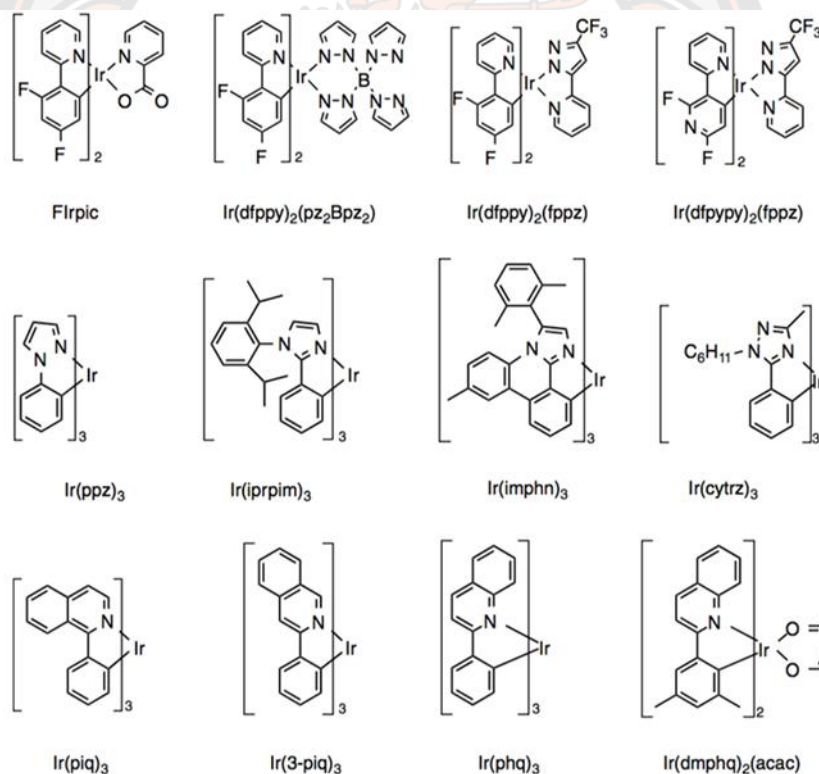


Figure 6 Structural formula of additional examples of cyclometalated Ir(III) complexes [8].

The cyclometalated Ir(III) compounds are highly emissive because the lowest energy excited states are a mixture of metal-to-ligand charge transfer (MLCT) and ligand centered (LC) $\pi-\pi^*$ states, not the non-radiative d-d states.

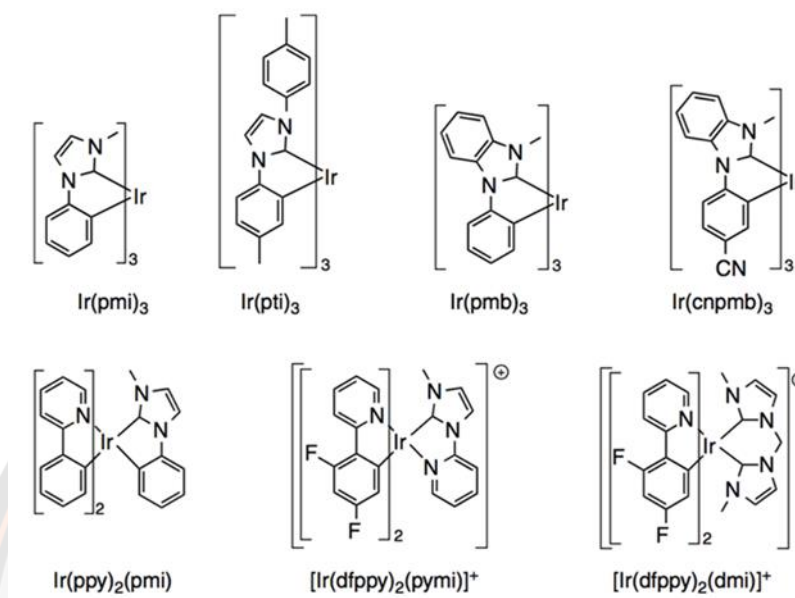


Figure 7 Structural formula of representative cyclometalated Ir(III) complexes comprising carbene ligands [8].

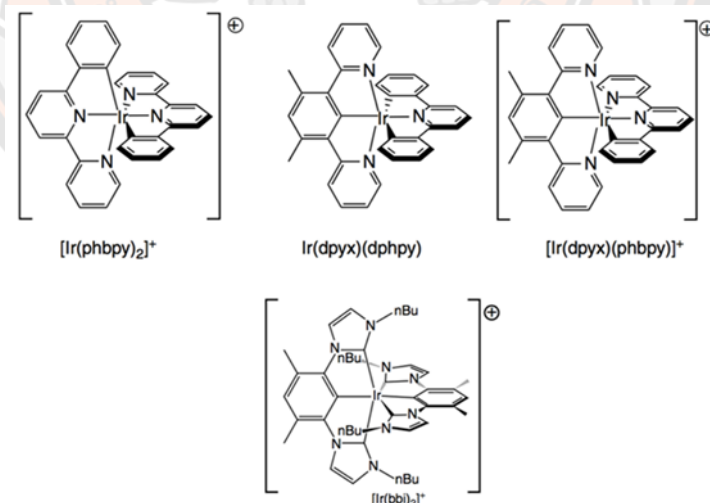


Figure 8 Stereochemical diagrams of representative cyclometalated Ir(III) complexes comprising tridentate ligands [8].

2.1.3 Photochemistry of luminescent transition metal complexes

Upon light absorption, the possible electronic transitions from the ground state (GS) are metal-centred (MC), ligand-centred (LC) or metal-to-ligand charge transfer (MLCT). These transitions are normally between singlet states, e.g. from the singlet GS to ^1LC , ^1MC , or $^1\text{MLCT}$. For ease of presentation, in **Figure 9** the metal and ligand orbitals are depicted separately.

According to the spin selection rule, d-d transitions are Laporte forbidden (e.g. MC transitions in **Figure 9**) [9]. Due to the high spin-orbit coupling in iridium, a singlet state mixes to some extent with a triplet state and thus, these spin-forbidden transitions become “allowed”, although they are still very weak.

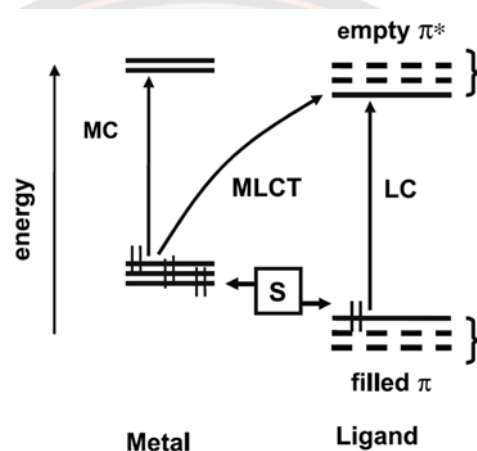


Figure 9 Orbital description of MC, MLCT and LC transitions; S is a substituent group capable of exerting electron withdrawing or donating effects (resulting in stabilization or destabilization, respectively, of the energy level of the filled d and π orbitals) [9].

Finally, the emission is normally from triplet states back to the ground state (**Figure 10**) [9]. This is due to the high spin-orbit coupling constant of iridium ($\zeta = 3909 \text{ cm}^{-1}$), which leads to an efficient intersystem crossing (ISC) from the singlet to the triplet excited state and inhibits non-luminescent pathways of electron-hole recombinations [10]. In addition, this combination of efficient ISC and less-forbidden nature of return to the ground state endows cyclometalating iridium complexes with photoluminescence lifetimes ranging from tens of nanoseconds to several microseconds.

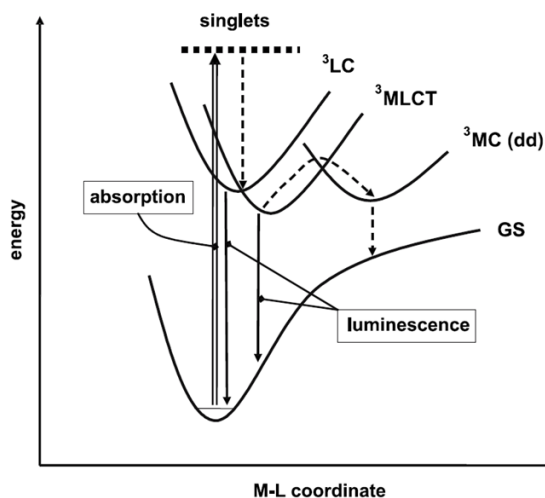


Figure 10 Electronic transitions involving MC, MLCT and LC excited states; the MC levels are non-emissive (dashed arrows) [9].

As the emission maximum of an iridium compound strongly depends on the energy of the triplet excited MLCT state ($^3\text{MLCT}$), this level may easily be modified by changing the ligands of the iridium compound (**Figure 11**) [11]. Therefore, in recent years, these properties of iridium compounds opened the field for using them in electroluminescence applications like organic light-emitting diodes (OLEDs) and light-emitting electrochemical cells (LECs) [12]. The emission maxima can be altered from the blue region ($\lambda_{\text{em}} = 452 \text{ nm}$), through the visible spectrum to the red region ($\lambda_{\text{em}} = 687 \text{ nm}$) and they offer high quantum efficiency [13].

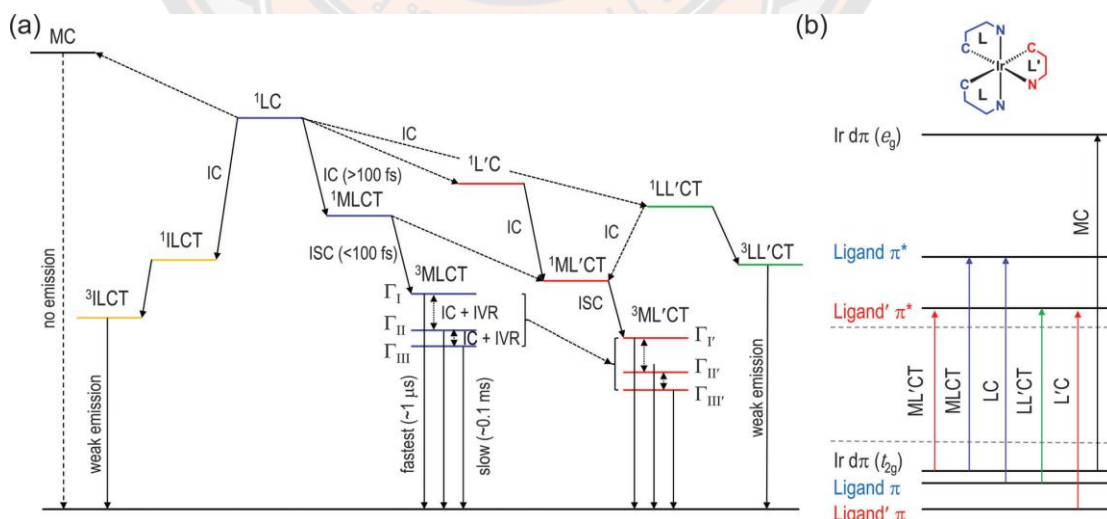


Figure 11 Diagram showing in photophysical properties of luminescent iridium complexes [11].

1) Tuning the emission maximum

Starting with the yellow emission of the first iridium(III) light emitting electrochemical (LEC), DFT calculations helped in understanding the localization of the HOMO and LUMO in these compounds [14]. The HOMO is usually center over the cyclometalating C^N ligands and the iridium atom, while the LUMO is localized on the ancillary N^N ligand (**Figure 12**). These are the two main points to change the environment of the iridium atom and therefore to alter the emission maximum of an iridium(III) complex.

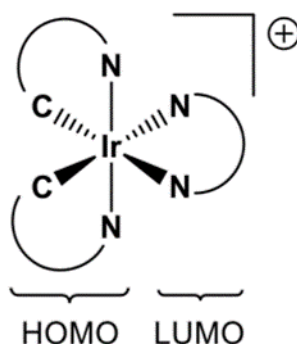


Figure 12 Locations of the HOMO and LUMO on an ionic iridium(III) complex [14].

Thus, the electronic transitions involve varying amounts of MLCT character mixed with other transition types (LLCT, IL, etc.). The mixed nature of the excited states results in one of the distinguishing features of cyclometalated iridium complexes, the possibility to systematically tune the energy difference between the ground and excited states resulting in tunable emission wavelength and excited state reactivity (**Figure 13**).

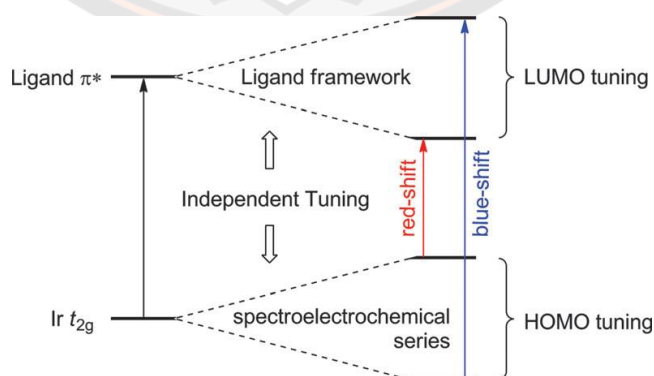


Figure 13 Tuning of photophysical properties of cyclometalated iridium complexes through independent modulation of HOMO and LUMO orbitals [11].

To increase the band gap between the HOMO and LUMO, the HOMO needs to be stabilized, thus lowering its energy level, and/or the LUMO needs to be destabilized, i.e. increasing its energy level. To stabilize the HOMO (electron-withdrawing substituents) such as -F or -CF₃ on the cyclometalating ligand are widely used. To destabilize the LUMO, electron-donating substituents (EDG) such as -N(CH₃)₂ are attached to the ancillary ligand [15]. Another possibility is the replacement of the π^* orbital ligand by more electron-rich ligand, strong-field ancillary ligands such as CO, isocyanides or carbenes are also effective in shifting the emission towards the blue.

With the reverse approach, compounds can be designed with emission maxima in the red region of the visible spectrum. A smaller band gap, and therefore a red shift, will be achieved by destabilizing the HOMO and/or stabilizing the LUMO. This can be achieved by attaching electron-withdrawing groups to the ancillary ligand or by increasing the conjugation length of the ligands [16]. The possibility to synthesize iridium complexes with different emission maxima can be further utilized by their mixing and matching. For example, combining red and blue emitting iridium (III) compounds may lead to a white emitting LEC device. This has been achieved by doping a small amount of a red emitting complex ($\lambda_{\text{em}} = 656 \text{ nm}$, QY = 0.20, 0.2-0.4% of weight), into a layer of a blue-green emitting complex ($\lambda_{\text{em}} = 497 \text{ nm}$, QY = 0.66) [17]. A series of heteroleptic, cationic iridium(III) complexes of color versatility, a broad range of excited-state lifetimes (from nanoseconds to several microseconds), and as well as phosphorescent yields approaching 1 have been achieved. (**Figure 14**) [18].

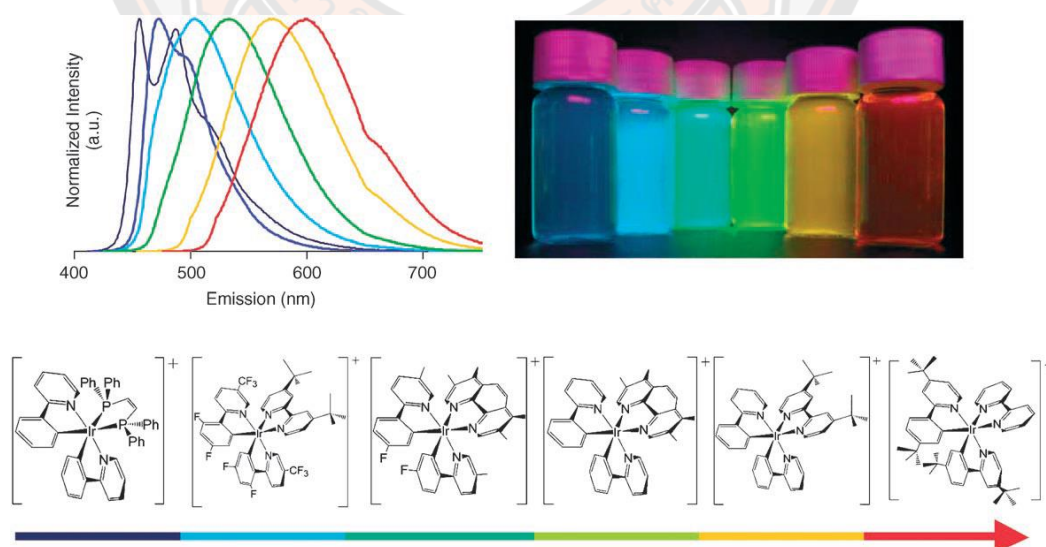


Figure 14 Color versatility expressed by a series of six cationic iridium(III) luminophores [16].

2.2 Use of cyclometalated iridium complexes in cellular imaging

One of key methods for cellular imaging is optical imaging or fluorescence microscopy imaging. This technique is based on the physical principles of excitation by a light source with detection of the fluorescence emission [19]. For fluorescence microscopy to be successful, the fluorophore needs to have a number of essential properties [20]. The fluorophores should have sufficient solubility in buffered aqueous solutions, be photostable, has the ability to reach the tissue (assisted by high lipophilicity), localize at a target site, and be non-toxic. In addition, the fluorophore has to be excited and emit light of long enough wavelengths in order to be in safe region and non-damaging to the cell. It should show a large Stokes shift to prevent self-quenching of the fluorophore, and have a long emission lifetime. Imaging agents should have a balance of lipophilicity and solubility in polar media [21]. Furthermore, cellular imaging technologies can be used contribute to a wide range of biological applications [22], including the drug discovery process [23].

Many research groups have reported the use of phosphorescent transition metal complexes in bioimaging. Due to their favourable optical and redox properties. In order for a luminophore to be suitable for cellular imaging it must be photostable, have a high quantum yield, reasonably non-toxic, cell permeable, have visible to near infrared emission and depending on the application, show a preference for localization within a certain organelle of the cell. Iridium complexes are the center of interest in this work to study their properties for cellular imaging and photoredox catalysis. Neutral tris-cyclometalated iridium complexes and positively charged bis-cyclometalate complexes are of particular interest for bio probe and photocatalytic applications.

Organelles are specialized subunits within cells that are usually separately enclosed by their own lipid bilayers. Major eukaryotic organelles include the nucleus, mitochondria, lysosomes, the endoplasmic reticulum, and the Golgi apparatus (**Figure 15**), with typical sizes from 20 to 1000 nm [24]. Each of these organelles plays a specific and indispensable role in cellular processes. For example, the nucleus regulates gene expression, mitochondria are responsible for aerobic metabolism, and lysosomes digest macromolecules for cell recycling.

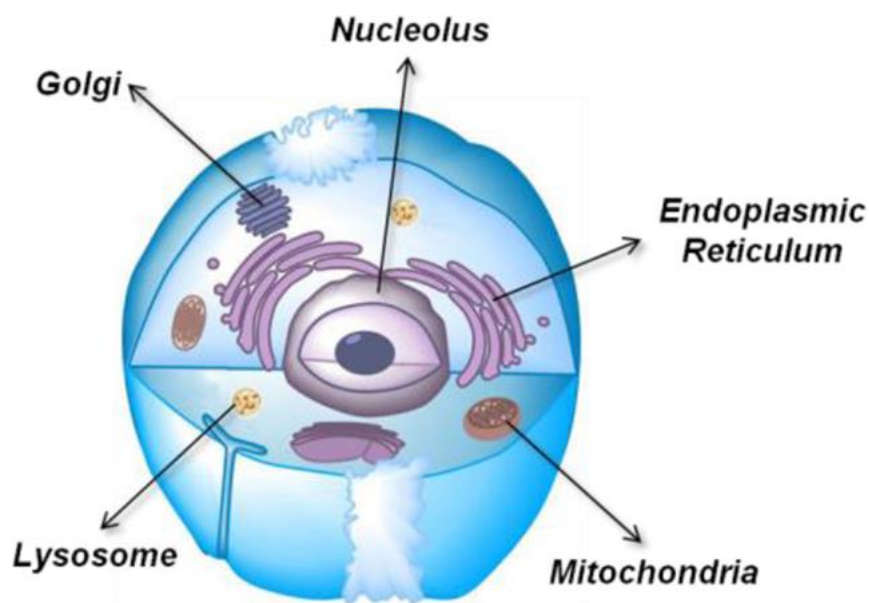


Figure 15 Major organelles of an animal cell [24].

Fluorescent probes are powerful molecular tools for both analytical sensing and optical imaging because of their high sensitivity, specificity, fast response, and technical simplicity. They can provide direct visualization and dynamic information concerning the localization and quantity of biomolecules of interest [25]. In addition, by taking advantage of the effect of the local environment on the fluorescence properties of fluorophores, highly environmentally sensitive fluorescent probes have been exploited to report on microenvironmental changes [26]. Confocal microscopy with increasing optical resolution has significantly facilitated the bioimaging applications of compartment specific fluorescent probes in live cells. Organelle-staining fluorescent probes are commercially available and can be used in biological investigations [27]. However, issues of cytotoxicity, photostability, short excitation and emission wavelengths, and fast fluorescence decay limit their applications in long-term fluorescence tracking of cellular events, tissue and body imaging with deep penetration and low autofluorescence, and time-resolved imaging. Cyclometalated iridium complexes exhibit properties that can address some of these issues.

In 2000, the first report of the application of *fac*-[Ir(ppy)₃] to OLEDs was published by Forrest and co-workers [28]. Due to their high phosphorescent quantum yield, long luminescent lifetimes, and visible tunable emission, iridium(III) complexes have become the most attractive class of phosphorescent transition metal complexes in biolabelling in recent years. In 2008, Yu and co-workers were the first research group to investigate luminescent staining of living cells using iridium(III) complexes. They reported the synthesis (**Figure 16**) and cellular uptake (**Figure 17**) of two difluorophenyl pyridine iridium(III) complexes that showed facile internalization

within HeLa cells [29]. The positively charged iridium(III) complexes transport through the membrane to reach the inside of the cell.

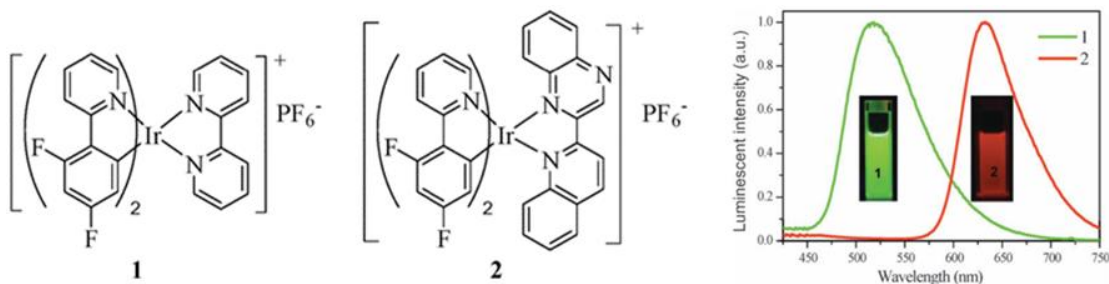


Figure 16 Chemical structures of iridium(III) complexes and their corresponding photoluminescence emission spectra in dichloromethane using 365 nm excitation wavelength. Prepared 10 mM of complexes 1 and 2 at room temperature [29].

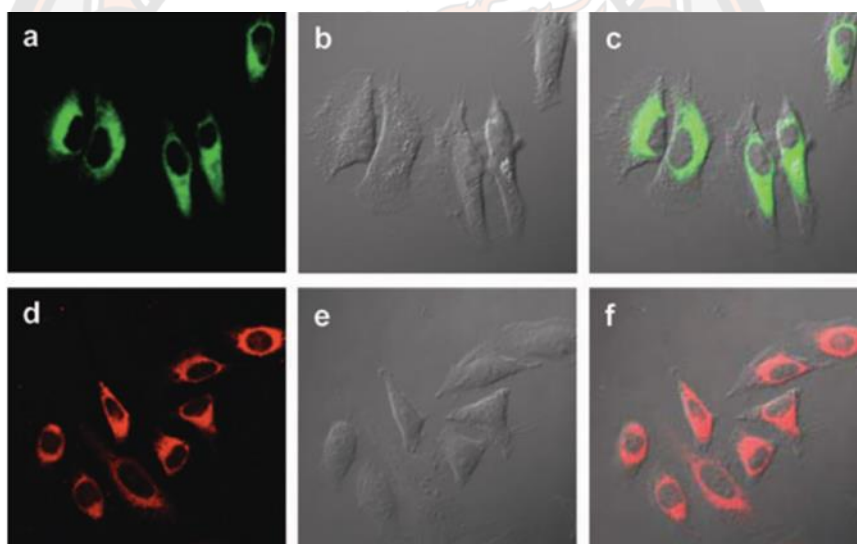


Figure 17 Confocal luminescence (a and d) and brightfield images (b and e) of living HeLa cells incubated with 20 μM of complexes 1 (top) and 2 (bottom). Samples are in DMSO/PBS (pH 7, 1:49, v/v) and were incubated with HeLa cells for 10 minutes at room temperature [29].

Cationic iridium(III) complexes have been reported for the staining of the nucleus. For example, in 2010 Lo and co-workers proposed a series of iridium(III) complexes containing dipyridoquinoxaline (dpq) ligands [30]. The modification of the structure of the cyclometalated ligand (1a-3a) and inclusion of a long chain on the dipyridoquinoxaline (dpqa) (1b-3b) (**Figure 18**) were investigated. In particular, it was proven that the complexes bind to the hydrophobic pocket of proteins and intercalate with DNA. The cytoplasm and the nucleus of the cell displayed very strong emission while the nucleoplasm emitted weakly. The positively charged iridium(III) complexes transport through the membrane to reach the inside of the cell.

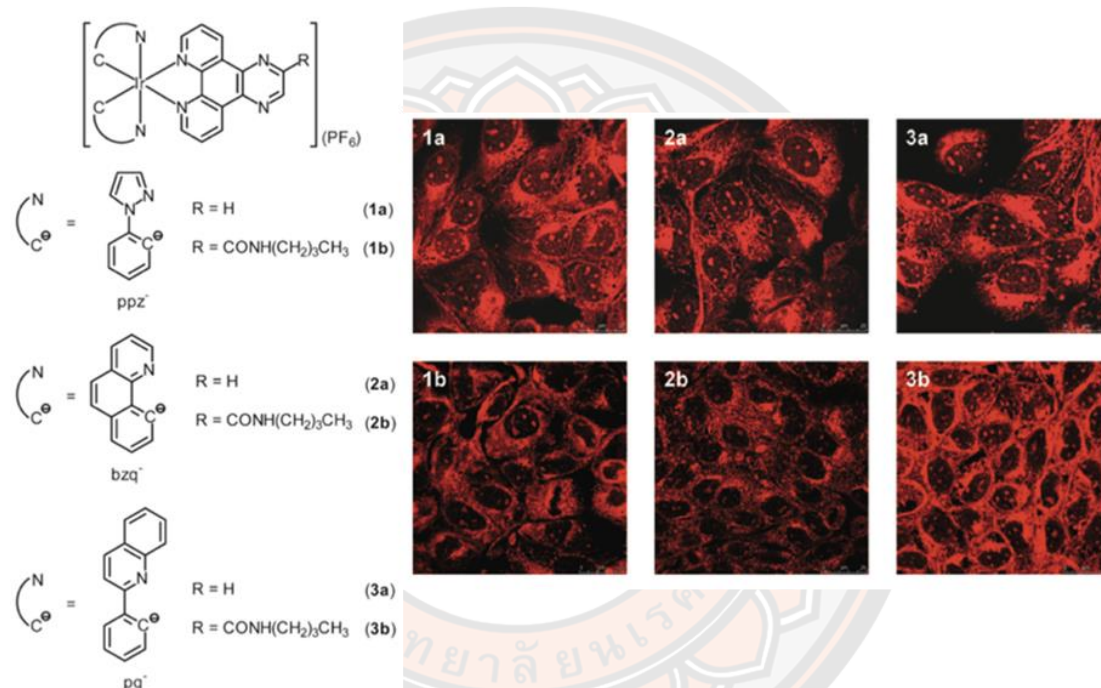


Figure 18 Structures of the iridium(III) Dpq and Dpqa Complexes.
Fluorescence laser-scanning confocal microscopy images of fixed MDCK cells treated with the iridium(III) dpq and dpqa complexes (5 μM) at room temperature for 30 min [30].

In 2011, Fuyou Li and co-worker demonstrated the internalization of a neutral iridium (III) complex **Ir-1** ($[\text{Ir}(\text{bt})_2(\text{acac})]$ (Hbt = 2-phenylbenzothiazole; Hacac = acetylacetonate)) into living cells and further selective detection of $\text{Hg}(\text{II})$ in cell samples by ratiometric measurement [31]. Compared with two cationic complexes **Ir-2** and **Ir-3**, complex **Ir-1** specifically responds to $\text{Hg}(\text{II})$ with an obvious change in phosphorescent emission color from yellow to green as shown in **Figure 19**. Outstandingly, cell imaging experiments have demonstrated that **Ir-1** is membrane absorbent and can readily reveal changes in intracellular $\text{Hg}(\text{II})$ concentration in a ratiometric way.

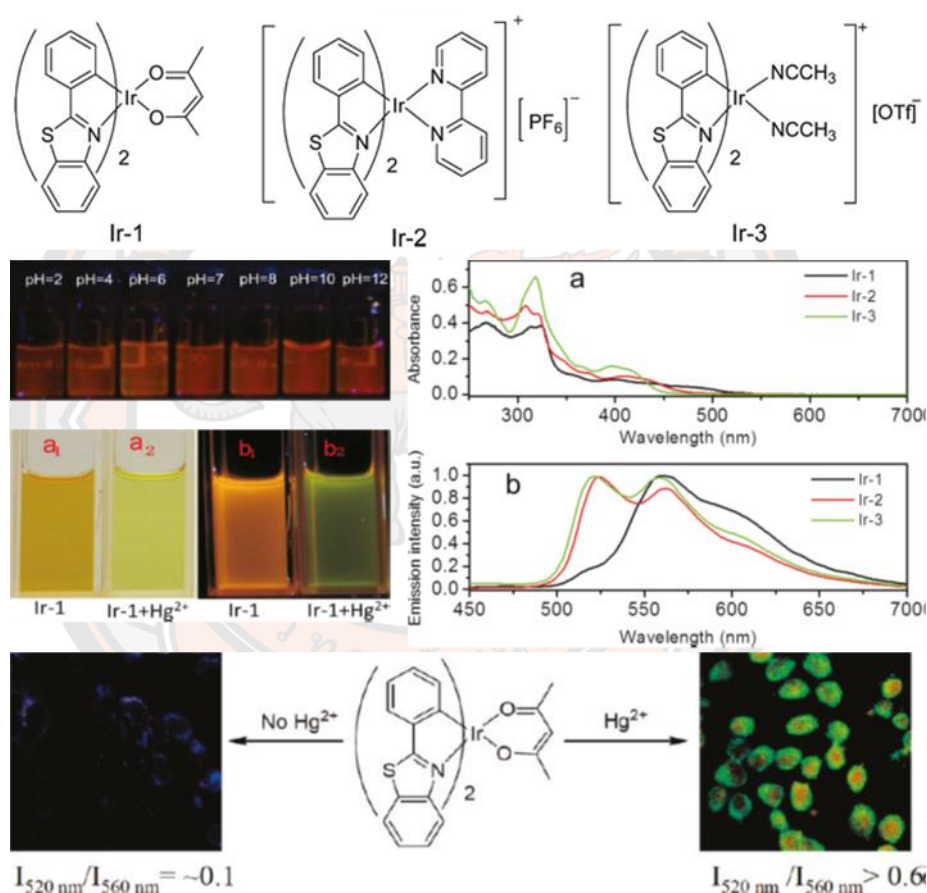


Figure 19 Chemical Structures of $[\text{Ir}(\text{bt})_2(\text{acac})]$ (**Ir-1**), $[\text{Ir}(\text{bt})_2(\text{bpy})]\text{PF}_6$ (**Ir-2**), and $[\text{Ir}(\text{bt})_2(\text{CH}_3\text{CN})_2]\text{OTf}$ (**Ir-3**). Luminescent photographs of **Ir-1** at different pH values. Solution (a) and luminescence (b) color photographs of **Ir-1** (40 μM in CH_3CN solution) before (**a**₁ and **b**₁) and after (**a**₂ and **b**₂) addition of 1 equiv of $\text{Hg}(\text{II})$. Absorption (a) and emission spectra (b) of **Ir-1**, **Ir-2**, and **Ir-3** in CH_3CN solution. Ratiometric phosphorescence images of **Ir-1**-incubated KB cells treated without or with $\text{Hg}(\text{II})$ [31].

In 2013, Zhou and co-workers presented three neutral iridium(III) complexes and two charged biscarbene complexes [32]. All the complexes display cytoplasmic localization (**Figure 20**).

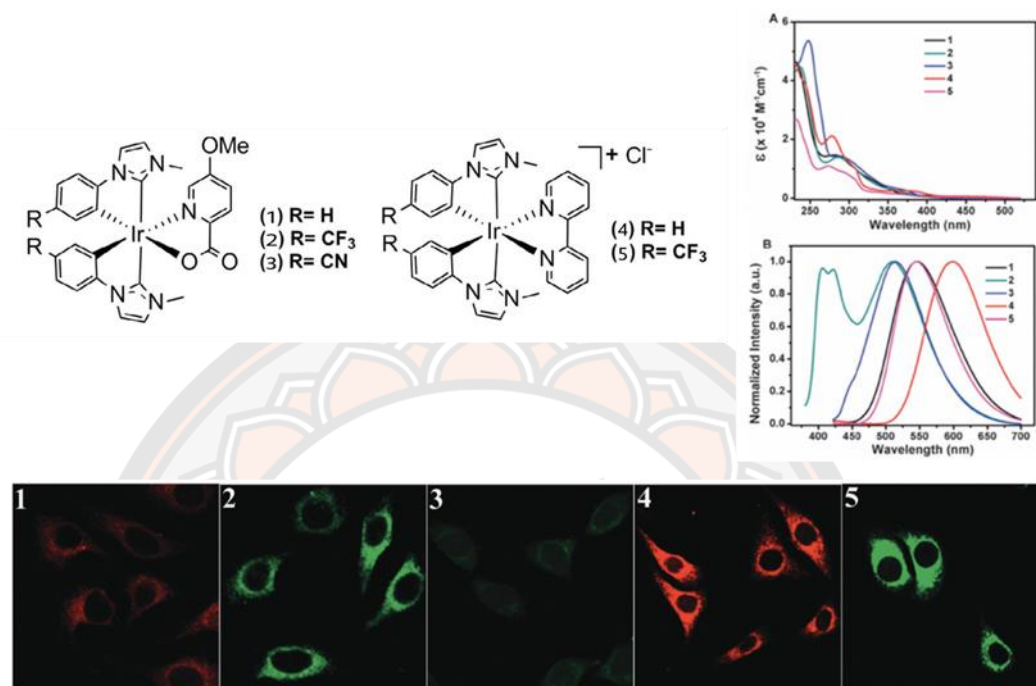


Figure 20 The chemical structures of the biscarbene iridium(III) complexes. Absorption (A) and normalized emission (B) spectra of complexes 1-5 in acetonitrile solutions (40 mM, $\lambda_{\text{ex}} = 360$ nm). Fluorescence images of HeLa cells incubated with complexes 1-5 for 2 hours at 37 °C [32].

The lysosome is the main digestive compartment of the cell, where all sorts of macromolecules are delivered for degradation. Lysosomes contain a high proton concentration and more than 50 hydrolases with an optimum pH below 6 [33]. Many research reports on amine-free lysosome targeting, pH-responsive lysosomal probes and the thermally activated delayed fluorescence of a fluorescein derivative that localizes in cell lysosomes have been published. Luminescent probes for the tracking of lysosome organelles need to possess resistance to degradation, low toxicity, high photostability, near-infrared or longer excitation wavelength. Lysosomes are acidic organelles containing a variety of hydrolytic enzymes. Examples of neutral and cationic iridium(III) complexes have been proposed for lysosome staining.

In 2016, Chao and co-workers published the neutral iridium(III) probes for long-term lysosome tracking [34]. The water-soluble tris-cyclometalated iridium(III) complexes are functionalized by morpholine, which can be protonated inside the lysosome. The pKa of morpholine is 5-6, and it can be protonated only in acidic lysosomes but not in other subcellular organelles or in the cytosol. The results indicate that Ir-lyso specifically localized in the lysosomes (**Figure 21**).

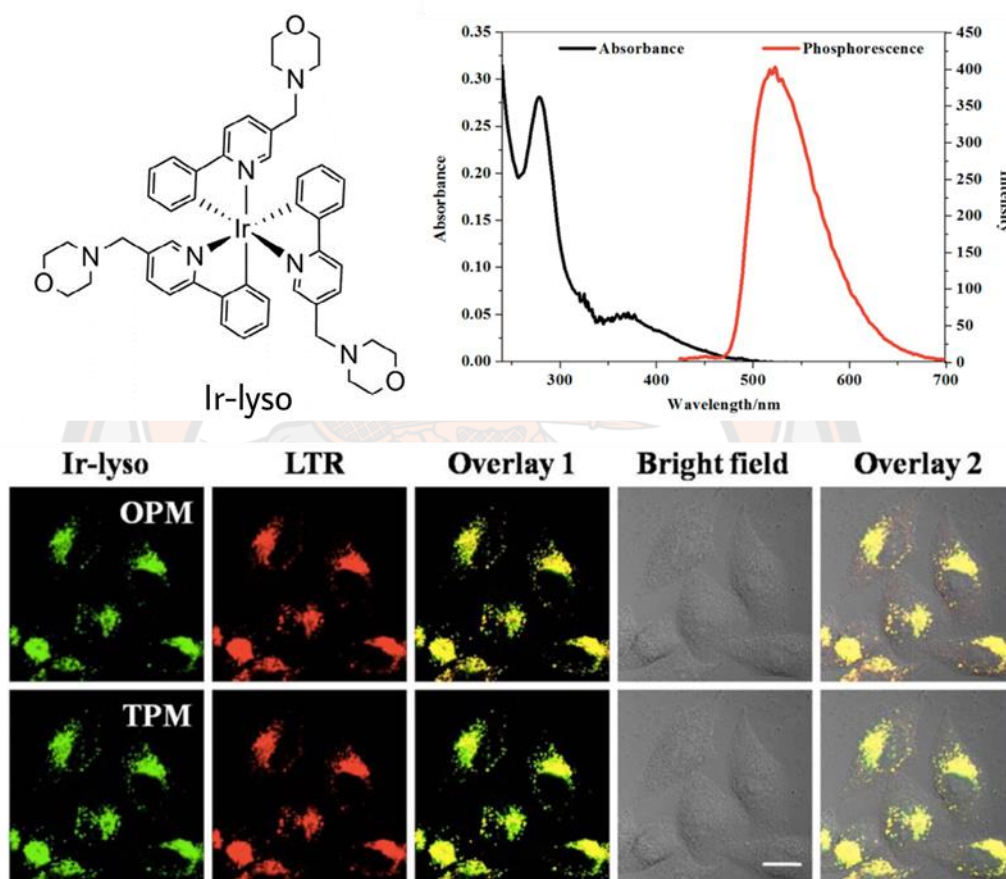


Figure 21 Structures of the Ir-lyso. Absorption spectrum and emission spectrum of Ir-lyso (5 μM) in disodium hydrogen phosphate/citric acid buffer solution (pH = 5.5). One-photon microscopy (OPM) and two-photon microscopy (TPM) images of HeLa cells colabeled with Ir-lyso (2 μM , 0.5 h) and LTR (50 nM, 0.5 h). Scale bar: 20 μm [34].

A further example of lysosomal staining by neutral iridium(III) probe was provided by Aoki and co-workers that can be used as luminescent pH-sensor and also a pH-dependent photosensitizer in live cells (**Figure 22**) [35]. This system contains an amino group, which can be protonated under acidic conditions. This structural feature is deemed crucial for the selective staining of the lysosomes in HeLa-S3 cells.

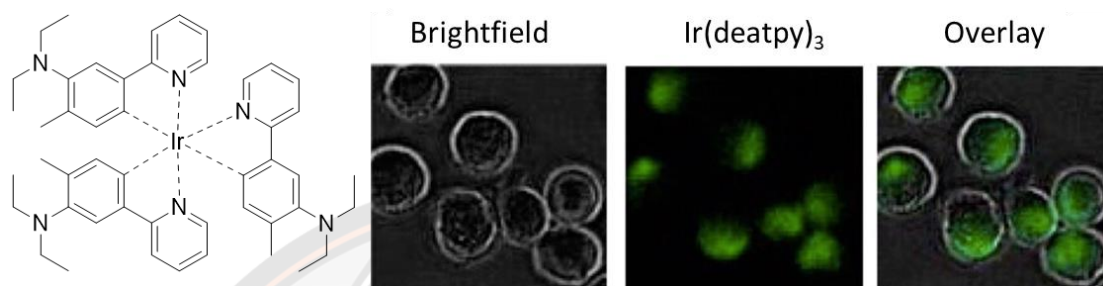


Figure 22 Tris-cyclometalated luminescent iridium(III) complex exhibiting selective staining of the lysosomes [35].

Mitochondria are rod-shaped organelles performing diverse functions, involving energy production via oxidative phosphorylation, calcium modulation, redox signaling, and apoptosis. For example Hui Chao and co-workers introduced new strategies for the development of imaging agents using cationic AIPE-active iridium(III) complexes, [Ir(btp)₂(PhenSe)]⁺ (**Ir1**), to be used as a phosphorescent agent for mitochondrial imaging and tracking in living cells as in 2011 [36]. In comparison to the commercial mitochondrial dye MTG, this **Ir1** possesses several advantages, such as not requiring culture medium replacement, maintaining specific mitochondrial staining in fixed cells, superior photostability, and high resistance to the loss of mitochondrial membrane potential as shown in **Figure 23**.

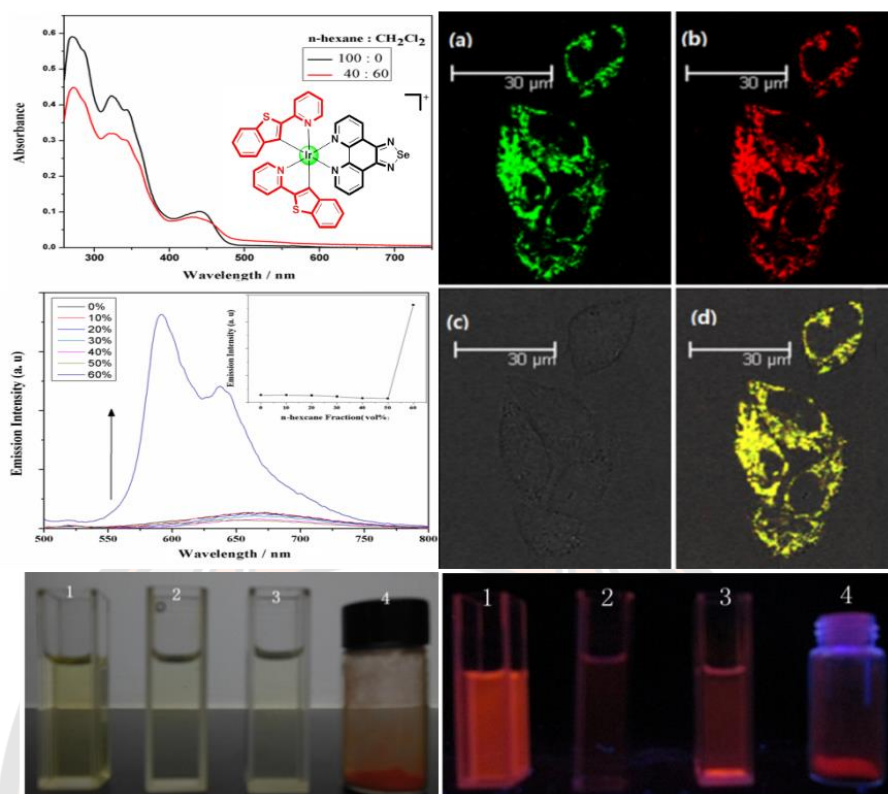


Figure 23 Confocal fluorescence images, brightfield images and their overlay of living HeLa cells incubated with 5 μ M Ir1 for 1 h at 37 $^{\circ}$ C. UV-Vis absorption spectra of Ir1 in hexane/ CH₂Cl₂ mixture. Emission spectra of Ir1 in the different hexane/ CH₂Cl₂ fraction solutions. The inset shows the change in the emission intensity of complex versus hexane fractions in CH₂Cl₂. Images of the brightfield and room temperature luminescent emissions ($\lambda_{\text{ex}} = 365$ nm) [36].

An interesting **Ir1** has the ability to localize and stain mitochondria in living cells. For example, it specifically stains the mitochondrial region in HeLa cells. The localization experiment with MTG suggests that the fluorescent images of MTG and **Ir1** are well merged and the correlation of the intensity distribution between the MTG signal and **Ir1** signal, is calculated to be 0.94, indicating that **Ir1** is localized selectively in mitochondria.

After their previous publication on pH-responsive probes [35], the group of Aoki synthesized a further neutral iridium(III) complexes containing three pyridyl groups at the 4'-position of the phenylpyridine ligand in 2013 [37]. Structure of the iridium(III) complex is shown in **Figure 24**. Ir(4Pyppy)₃ exhibits a reversible pH-dependent emission profile based on protonation and deprotonation on the pyridine rings with a weaker red emission in acidic pH and a green intense emission in neutral and basic condition.

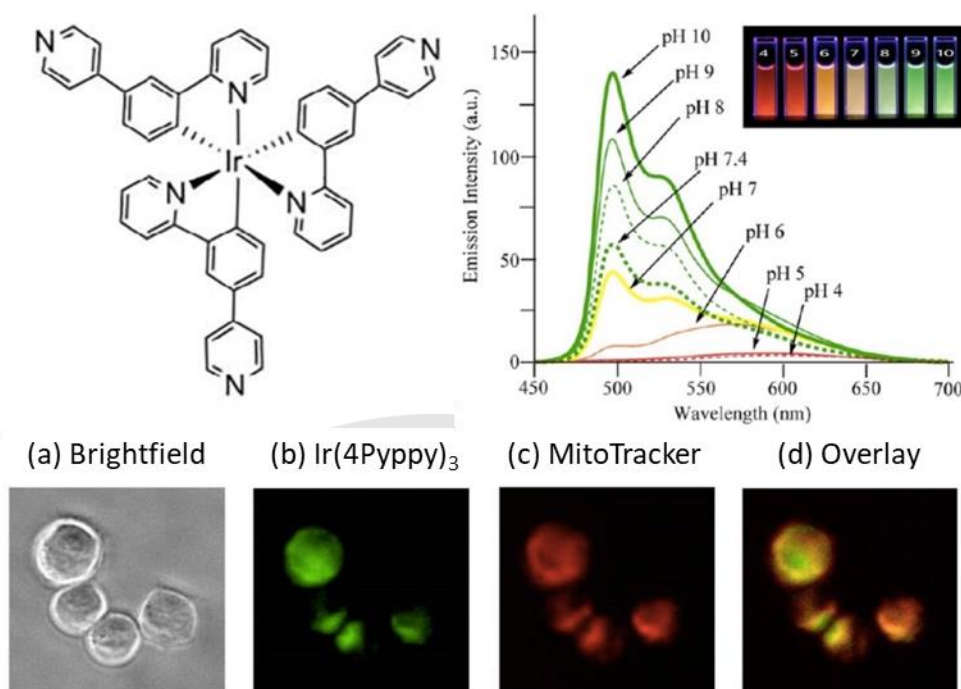


Figure 24 Structures of the neutral iridium(III) complex pH-responsive probes. Luminescence microscopy images of HeLa-S3 cells stained with Ir complex (10 μ M) and MitoTracker (10 nM) in MEM/DMSO (99/1, v/v) at 37 $^{\circ}$ C for 30 min. (a) brightfield image of HeLa-S3 cells, (b) emission images of Ir, (c) emission images of MitoTracker, and (d) overlay image of (c) and (d). λ_{ex} (b) = 377 nm, (c) = 540 nm [37].

In 2010, Williams and co-worker studied the potential of the long luminescence lifetimes of iridium complexes for time-resolved imaging [38]. Deoxygenated dichloromethane solution ($\tau = 3.2 \mu\text{s}$) but higher than the value in fully air-equilibrated solution (100 ns). The authors showed how the much longer lifetime of the iridium complex compared to a standard fluorophore could be exploited to allow independent imaging of two different probes within cells on the basis of the timescale of emission, rather than the usual requirement to emit in different regions of the spectrum. CHO cells were co-loaded with the iridium complex (10 μ M, 1 h) and Hoechst 33342, a well-known fluorescent nuclear stain (350 nM, 5 min). Imaging was carried out using a time-gated camera synchronised with a Q-switched Nd:YAG laser (ex = 355 nm, pulse length ~ 4 ns). In the image recorded with no time delay, bright emission in the nucleus dominates the image, emanating from the Hoechst stain (**Figure 25a**). The extra-nuclear staining of the Ir(III) complex is barely evident, being heavily outweighed by the Hoechst. In contrast, in the time-gated image obtained using a 10 ns delay between the laser pulse and image acquisition, no significant nuclear emission is detectable, but only bright emission from organelles

within the cytoplasmic region is observed. During the time delay, the emission from the Hoechst stain decays to a negligible level ($\tau = 3.6$ ns), whereas the emission from iridium complexes, with its long intracellular lifetime of around a microsecond, remains clear. The result shows how it is possible to selectively observe different subcellular compartments of the same sample, simply by setting a time delay between excitation and acquisition of the image.

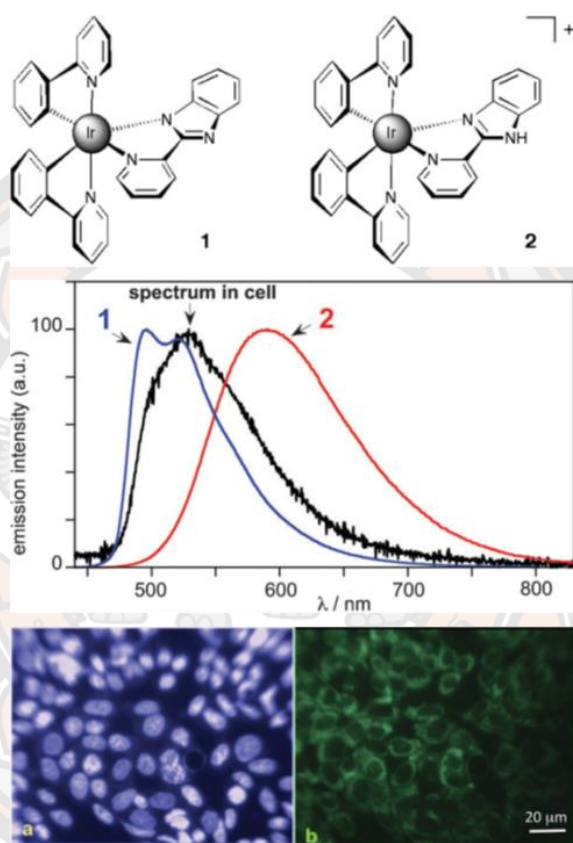


Figure 25 Structure of pH responsive luminescent iridium complex developed by Williams and co-worker. Corrected emission spectra of 1 and 2 in CH_2Cl_2 and the spectrum from CHO cells dosed with complex 1 (10 mM, 5 min incubation). Fluorescence microscopy images of live CHO cells co-stained Ir(III) complexes obtained without (a) and with (b) a 10 ns gate between excitation and imaging [38].

In 2017, Zong Wan Mao and co-workers developed two phosphorescent cyclometalated iridium(III) complexes, **Ir1** and **Ir2**, that can accumulate in mitochondria and induce mitophagy by depolarization of mitochondrial membrane potential (**Figure 26**) [39].

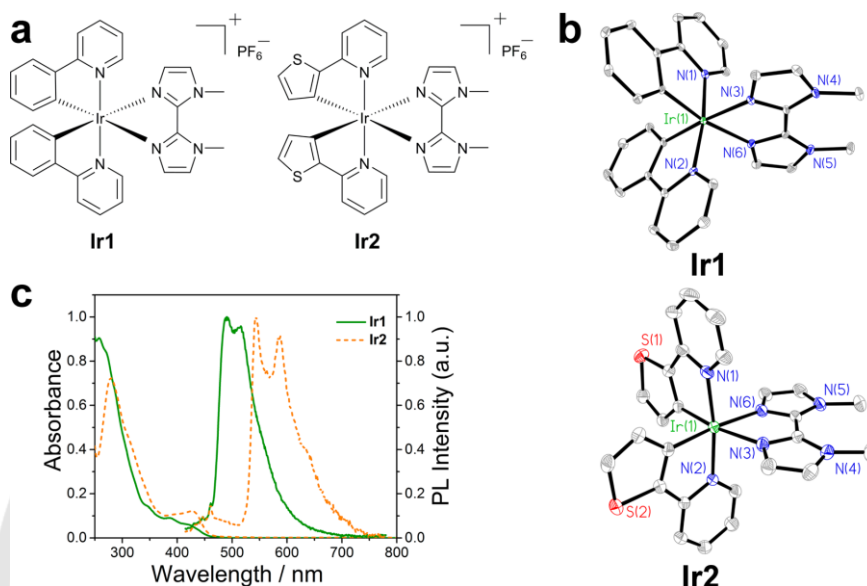


Figure 26 (a) Schematic drawing of the structures of Ir1 and Ir2. (b) X-ray structures of the cations in Ir1 and Ir2 are showed in thermal ellipsoids at the 30% probability level. The hydrogen atoms and counterions are omitted for clarity. (c) UV/vis absorption and normalized photoluminescence (PL) spectra of Ir1 (2×10^{-5} M) and Ir2 (2×10^{-5} M) are measured in acetonitrile. $\lambda_{\text{ex}} = 405$ nm [39].

Subcellular localization of phosphorescent Ir(III) complexes can be easily analyzed by confocal microscopy. After an incubation for 1 h, **Ir1** and **Ir2** can effectively enter A549 cells (**Figure 27**). The phosphorescence of the compounds is mainly retained in cytoplasm and displays an intense and punctate staining pattern. Colocalization experiments of Ir1/Ir2 with commercial MTDR (MitoTracker Deep Red) indicate that the complexes are capable of staining mitochondria specifically in A549 cells (**Figure 27a**). The Pearson's colocalization coefficients (PCC) of **Ir1** and **Ir2** with MTDR are 0.76 and 0.72, respectively. **Figure 27b**, very little overlap is observed for **Ir1** (PCC = 0.07) and **Ir2** (PCC = 0.09) with LTDR (LysoTracker Deep Red) at the same time.

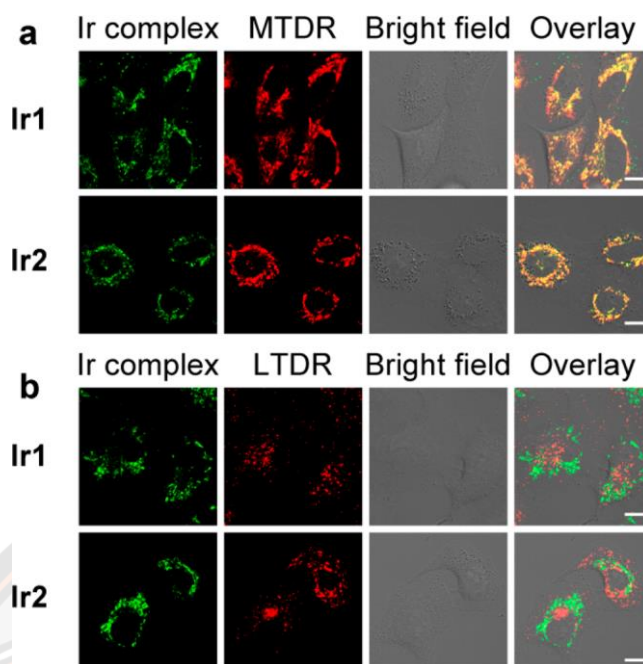


Figure 27 (a) Representative confocal images of A549 cells exposed to Ir1/Ir2 (15 μ M, 1 h) and MTDR (100 nM, 30 min). (b) Representative confocal images of A549 cells exposed to Ir1/Ir2 (15 μ M, 1 h) and LTDR (50 nM, 30 min). Scale bars: 10 μ m [39].

In 2017, Caporale and co-workers investigated intracellular localization for neutral and cationic iridium tetrazolato complexes in live cells [40]. The neutral complex $[\text{Ir}(\text{ppy})_2(\text{TzPyPhCN})]$ exhibit high iridium intracellular concentrations indicating good cellular internalization as shows in **Figure 28**. The methylated complex $[\text{Ir}(\text{ppy})_2(\text{MeTzPyPhCN})]^+$ localized in the cytoplasm and a staining pattern that is characteristic of mitochondrial association. MitoTracker Red CMXRos was confirmed this interaction. It is possible that the positive charge favours the transport across the mitochondrial membrane. Micrographs of H9c2 cells stained with the iridium complexes (green) and counter-stained with ER- and Mito-Tracker_Red (red). Yellow/orange colour in the merge indicates co-localization between markers. The iridium complexes were excited at 403 nm and the emission was collected in the region 525–644 nm; ER-Tracker and MitoTracker werre excited at 561 nm and the emission was collected in the region 570–620 nm. Scale bars: 10 μ m.

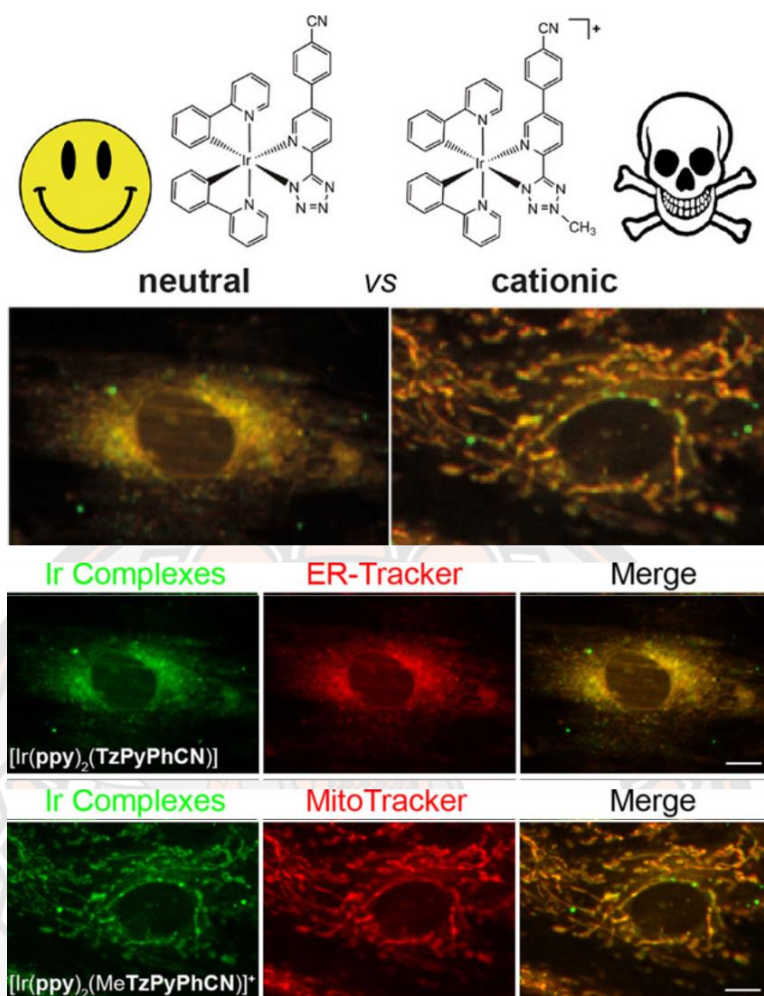


Figure 28 Iridium complexes interacting with endoplasmic reticulum (ER) and mitochondria in live H9c2 cells [40].

In 2020, Aoki and co-workers designed and synthesized a green-emitting iridium complex–peptide hybrid (**IPH**), which has an electron-donating hydroxyacetic acid (glycolic acid) moiety between the Ir core and the peptide part (**Figure 29**) [41]. These newly synthesized **IPH** exhibit a green emission, and their lifetimes are on the order of microseconds, due to phosphorescence from the excited triplet states. **IPH** is selectively cytotoxic against cancer cells, and the dead cells showed a green emission.

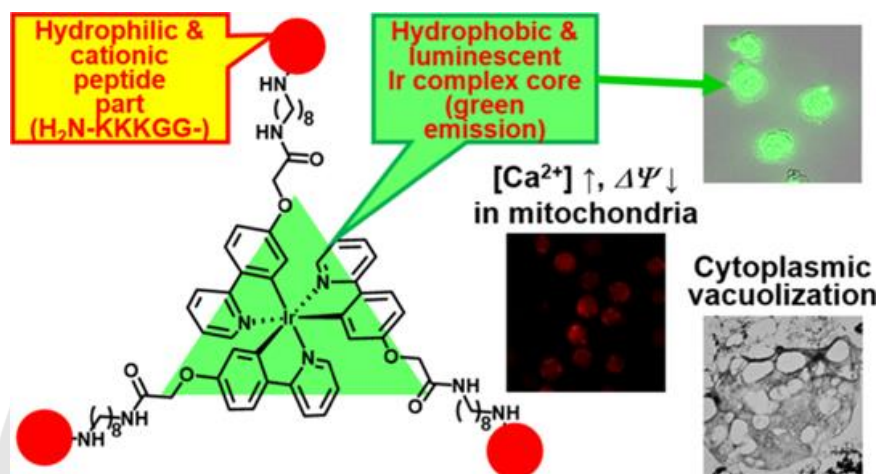


Figure 29 Iridium complex–peptide hybrid (IPH) induces a paraptosis-like cell death [41].

Mechanistic studies of cell death indicate that **IPH** induces a paraptosis-like cell death through the increase in mitochondrial Ca²⁺ concentrations via direct Ca²⁺ transfer from ER to mitochondria, the loss of mitochondrial membrane potential.

Our previous research resulted in the publication of a study of two novel aminoalkyl tris-cyclometalated iridium(III) complexes [42]. These complexes are relatively simple derivatives of the prototypical complex [Ir(ppy)₃]. These complexes exhibited interesting photophysical behavior in aqueous solutions, including ratiometric response to pH. More significant and abrupt change in the emission intensity ratio was observed for complex **1** (**Figure 30**), changing from a value of 0.8 at pH 5.5 to 5.0 at pH 9.5. In cell luminescence lifetimes of 0.97 and 1.17 μs have been calculated based on these decays for complexes **1** and **2**, respectively. The complexes have been shown to be taken up by NIH-3T3 cells, where they localize in the lysosomes (**Figure 31**).

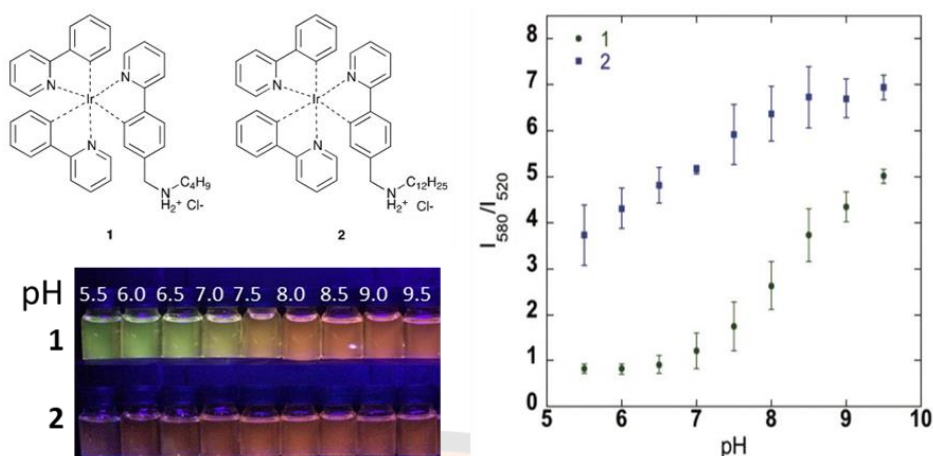


Figure 30 Structures of complexes 1 and 2. Photograph of complexes 1 and 2 in various pH 5.5-9.5 (10 μM) was observed with the naked eye under 365 nm. Ratio of the emission intensity of complexes 1 and 2 at 580 nm and 520 nm as a function of pH [42].

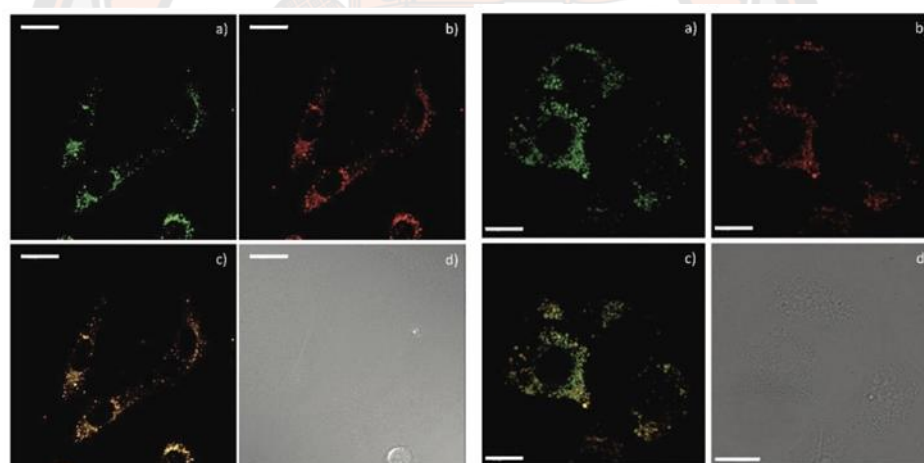


Figure 31 Fluorescence microscopy images of NIH-3T3 cells obtained with complex 1 (left) and 2 (right) (λ_{ex} 355 nm, λ_{em} 450–650 nm) (a), LysoTracker Red (λ_{ex} 543 nm HeNe laser, λ_{em} 600–650 nm) (b). Panel (c) shows the RGB overlay of panels (a) and (b); $P = 0.84(1)$ and $0.79(2)$, while panel (d) is the bright field image (scale bar: 20 μm) [42].

Luminescent cyclometalated iridium complexes serving both as stains for various organelles or as responsive probes have been prepared. Many research area iridium(III) complexes were initially screened as cellular markers for imaging. Most of the design of new iridium probes considerations of chemical nature such as charge, lipophilicity, solubility, and bioconjugation to specific biological vectors. The results

have clearly demonstrated the benefit of the long luminescent lifetime of cyclometalated iridium complexes to separate their signal from background and organic dyes. Consequently, design and development of fluorescence imaging probes are interesting to study.

2.3 Photoredox catalysis

Catalysis is a key to a number of important issues in chemical transformations. Catalysts allow chemical reactions to be performed under mild conditions to save energy, increase the product yields to reduce waste [43]. Chemical catalysts can be divided into two categories based on the phase they are in relative to the reaction mixture. The first class consists of catalysts in the same phase as the reactants (homogeneous), and the second class contains catalysts that are in a different phase from reactants and products (heterogeneous). Heterogeneous catalysts, such as metal oxides, zeolites, and supported metals, are among the most important catalytic systems and have wide applications in industry [44]. Normally catalysts are multi-sited and could be easily separated from the products. Homogeneous catalysts, such as mineral acids, metal-ligand complexes, are generally well-defined chemical compounds. They act under mild conditions and normally display very high activity and selectivity. Combining the advantages of homogeneous catalysts (high activity and selectivity, easy tunability) and heterogeneous catalysts (easy separation) leads to the development of immobilized molecular catalysts, which have attracted a lot of attention and developed into an important field in the catalysis research [45].

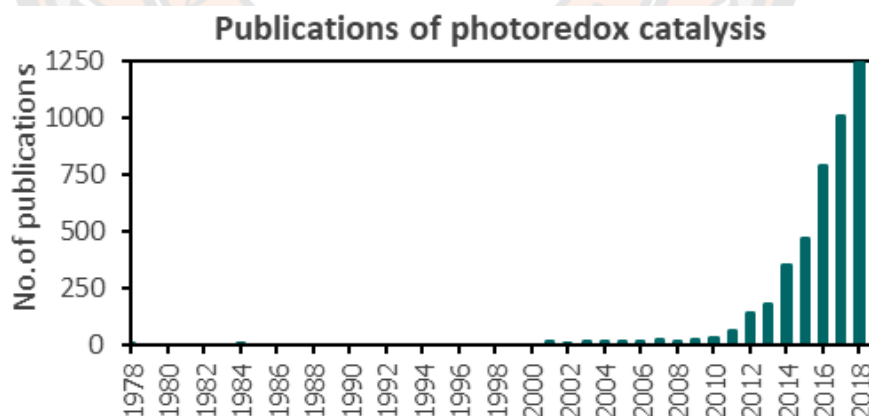


Figure 32 The evolution of photoredox–transition metal catalysis. Number of publications per year in field of organic photoredox catalysis (data collected from Scopus, August 10, 2020).

Photocatalysts provide a direct means to access the chemistry of reactive intermediates that often cannot be readily generated using visible light and have been

applied to a large range of important organic transformations, from simple oxidations and reductions to produce new bond formations with various functionalization.

Photoredox catalysis, one of the modes of photocatalysis, has recently gained large amount of attention. We have been drawn to this area as a means of further utilization of compounds developed in our group, cyclometalated iridium complexes, that we have originally developed for the purpose of cellular imaging. Cyclometalated iridium complexes are usually used as homogeneous catalysts. However, given the fact that our iridium complexes contain reactive functional groups that could facilitate their immobilization on surfaces, we have decided to develop such catalysts that could be regenerated and reused. The aim of this project is to assess the effect of these functional groups on the performance of the iridium complexes as catalysts prior to their attempted conjugation.

Over the last century, photoredox catalysis has found extensive application in the fields of carbon dioxide reduction, water splitting, and the development of novel solar cell materials. More recently, photoredox catalysis has also been gaining the interest of synthetic organic chemists. The motivation that brought this mode of catalysis to the attention of synthetic chemists in recent years was the 2008 report from the MacMillan group, which demonstrated the possibility to combine photoredox catalysis and organocatalysis to achieve synthesis of organic compounds. Another key factor in the recent and rapid growth of this activation platform has been the recognition that readily accessible metal polypyridyl complexes and organic dyes can facilitate the conversion of visible light into chemical energy under exceptionally mild conditions. Upon excitation, these molecules can engage in single-electron transfer (SET) events with organic (and organometallic) substrates, providing facile access to open-shell reactive species. Here, irradiation with visible light, at wavelengths where common organic molecules do not absorb, effects selective excitation of the photoredox catalyst. The resultant excited species can act as both a strong oxidant and a strong reductant simultaneously, thereby providing access to a reaction environment that is unique for organic chemistry. Indeed, this electronic duality contrasts directly with traditional redox reaction manifolds (e.g., electrochemistry) wherein the reaction medium can be either oxidative or reductive (but not both) and, in turn, provides access to previously inaccessible redox-neutral reaction platforms.

In addition, multicatalysis concepts have recently begun to emerge that allow access to many difficult or unattainable transformations. Synergistic catalysis is two catalysts and two catalytic cycles work in concert to create a single new bond [46]. The simplest form of synergistic catalysis involves the concurrent activation of both a nucleophile and an electrophile using distinct catalysts. This simultaneously creates two reactive species, one with a higher HOMO (highest occupied molecular orbital) and the other with a lower LUMO (lowest unoccupied molecular orbital), in comparison to the respective ground state starting materials. Multiple activation

approaches generally rely on a narrowing of the substrates HOMO-LUMO gap (ΔE) by lowering the LUMO of the electrophile and simultaneously raising the nucleophile of HOMO (Figure 33) [47].

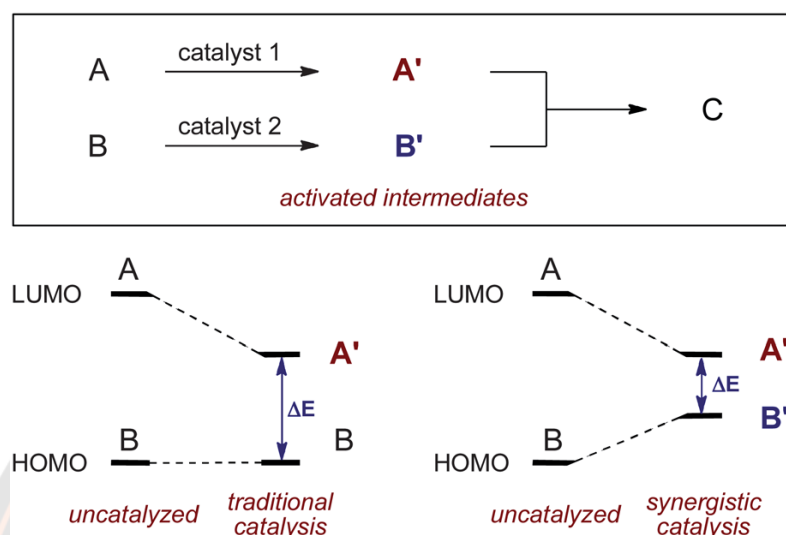


Figure 33 Comparison of catalytic activation modes [47].

Synergistic catalysis is prevalent in nature, as many enzymes function through the cooperation of two or more catalysts (or catalytic moieties within an active site) to afford a specific transformation (Figure 34).

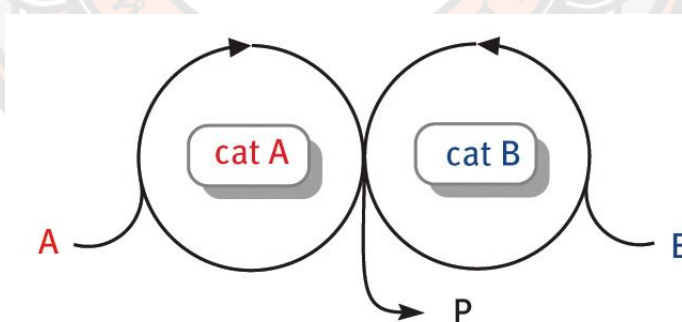


Figure 34 Multicatalytic activation modes of synergistic catalytic [47].

In general terms, an excited photoredox catalyst can either be quenched reductively or by oxidation via single electron transfer (SET) in the presence of a substrate. The resulting intermediate (ground state) catalyst species typically possesses high oxidative or reductive power depending on the nature of the prior quenching process and is ideally capable of performing a further SET to a different substrate or will undergo regeneration with a sacrificial electron acceptor or donor, respectively. Upon stepwise oxidation and reduction the photocatalyst mediates

electron transfer reactions between the different substrates and agents within a photoredox catalytic cycle **Figure 35** [48].

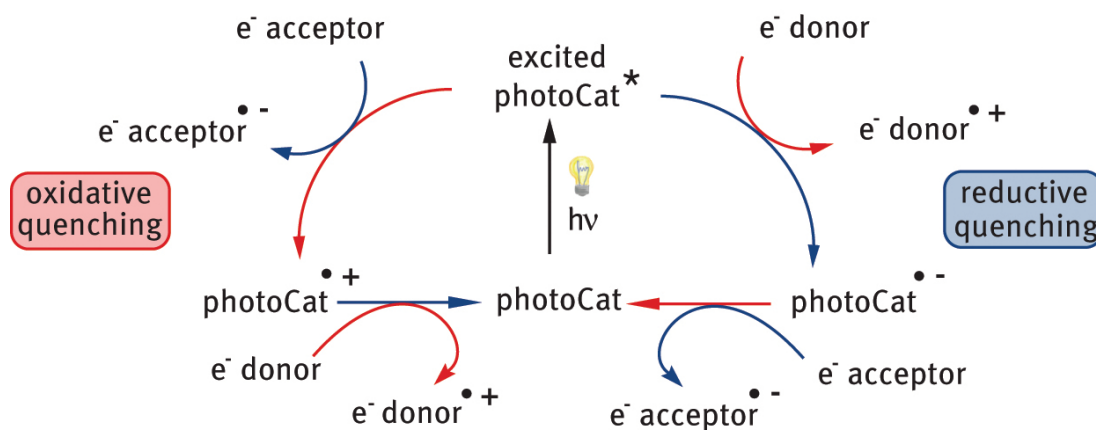


Figure 35 Quenching modes in photoredox catalysis [48].

In recent years, the field of photoredox catalysis has experienced rapid growth, resulting in the development of a wide array of novel synthetic methodologies. Recent advances offer synthetic chemists novel bond disconnections and can provide protocols for the direct derivatization of native functional groups, such as C–H bonds and carboxylic acids. In addition, photoredox-catalyzed reactions generally proceed under extremely mild reaction conditions and this feature renders these technologies amenable to a large range of structurally and functionally diverse molecules. As such, it is not surprising that these methodologies have found utility in the synthesis of natural products and medicinally relevant compounds. Initial reservations about the scalability of these protocols due to the inherent relationship between reaction efficiency and photon penetration have been addressed by the successful translation of batch photoredox-catalyzed reactions into large-scale flow protocols. Consequently, these technologies are now gaining considerable interest from industrial chemists both in the context of small scale synthetic applications, such as late stage functionalization in medicinal chemistry, and for large scale production of intermediates using flow. Herein, we will discuss key reports which highlight the utility of photoredox catalysis in the synthesis of complex molecular scaffolds and the application of this catalysis platform to medicinal chemistry.

Roughly 40 years ago, the first examples of visible light photoredox catalysis in organic synthesis applications were reported (**Figure 32**). In 1978, Richard Kellogg and co-workers used complex $[\text{Ru}(\text{bpy})_3]\text{Cl}_2$ ($\text{bpy} = 2,2'$ -bipyridine) with visible light irradiation in the presence of a dihydropyridine, which lead to the reductive desulfuration of sulfonium salts to corresponding alkanes [49]. In 1984, the first net oxidative photoredox-catalyzed reaction using aryldiazonium salts as the terminal oxidant for the conversion of benzylic alcohols to phenanthrene derivatives were

reported by Cano-Yelo and Deronzier by using $[\text{Ru}(\text{bpy})_3]\text{Cl}_2$ in photocatalytic Pschorr reaction (**Figure 36**) [50].

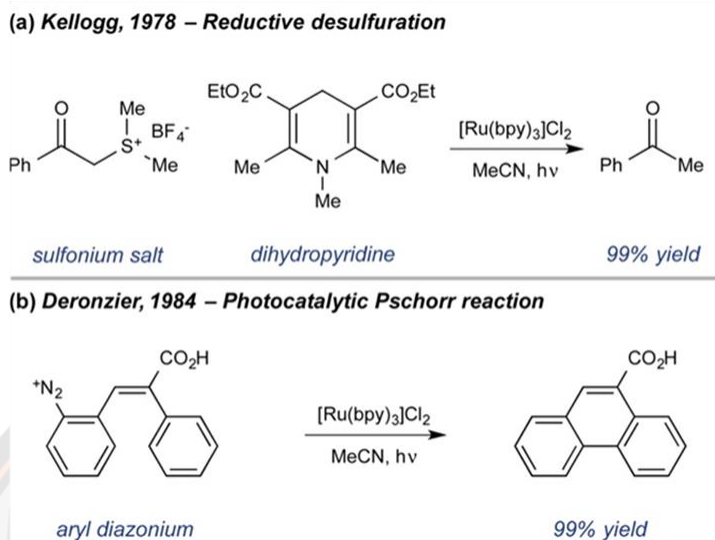


Figure 36 Photoredox transformations using transition metal complexes as catalysts [49, 50]

In 2003, Zen and co-workers demonstrated highly selective photochemical oxidation of sulfide to sulfoxide on a novel heterogeneous multicomponent naphthalene doped with a lead ruthenate pyrochlore (Pyc) catalyst and a $[\text{Ru}(\text{bpy})_3]^{2+}$ photosensitizer (**Figure 37**) [51]. In 2008, Yoon and co-workers developed an efficient method for crossed [2+2] cycloadditions of acyclic enones promoted by visible light photocatalysis [52].

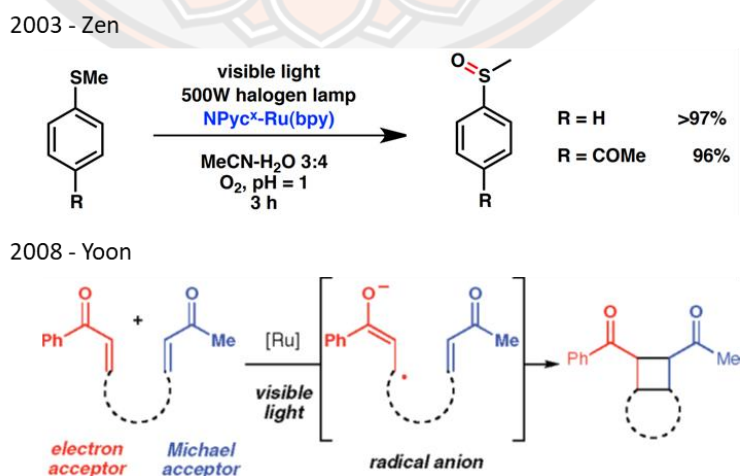



Figure 37 Photoredox transformations using ruthenium complexes as catalysts [51, 52].

During the last 3 years the number of publications on photoredox catalysis per year increased almost fourfold (**Figure 32**). Ruthenium and iridium polypyridyl complexes are used for a large part of light mediated chemical process [53]. These compounds have not seen much use in photocatalysis before 2004 when cationic and neutral iridium(III) complexes were used as photo-redox catalysts [54]. $[\text{Ir}(\text{ppy})_2(\text{dtbbpy})]^+$ (ppy = phenylpyridine, dtbbpy = 4,4'-di-*tert*-butyl-2,2'-bipyridine), *fac*- $[\text{Ir}(\text{ppy})_3]$ and $[\text{Ru}(\text{bpy})_3]^+$ (bpy = 2,2'-bipyridine) are most common commercially available photo-redox catalysts [55, 56]. Prominent properties of these three catalysts are their high oxidation and reduction potentials for single electron transfer and long lifetimes of their excited triplet states. Therefore, the most suitable catalyst has to be selected considering the reduction (E_{Red}) or oxidation (E_{Ox}) potential of the compounds that are desired to be transformed, either following a reductive or an oxidative quenching cycle. Moreover, the redox potentials of the photocatalysts can be further tuned by modification of the ligands [57]. Redox potentials for the oxidative quenching process [58], reductive quenching process, and other photophysical properties are shown in **Table 1**. All potentials are given in Volts (V) vs. saturated calomel electrode (SCE) in CH_3CN at ambient temperature.

Table 1 Redox potentials and selected photophysical properties of the visible light photoredox catalysts.



		$\text{Ir}(\text{ppy})_2(\text{dtbbpy})\text{PF}_6$	<i>fac</i> - $[\text{Ir}(\text{ppy})_3]$	$[\text{Ru}(\text{bpy})_3]\text{Cl}_2$
Oxidative	$E_{1/2} (\text{M}^+/\text{M}^*)$	-0.96	-1.71	-0.81
Oxidative	$E_{1/2} (\text{M}^+/\text{M})$	+1.21	+0.77	+1.29
Reductive	$E_{1/2} (\text{M}^*/\text{M}^-)$	+0.66	+0.31	+0.77
Reductive	$E_{1/2} (\text{M}/\text{M}^-)$	-1.51	-2.19	-1.33
	Excited-state lifetime τ (ns)	557	1900	1100
	Excitation(nm)		375	452
	Emission	581	494 ^a	615
	λ_{max} (nm)			

^aDetermined in 1:1 EtOH/MeOH mixture at 77 K.

2.3.1 Iridium(III) photocatalyst design

Photocatalytic methods have rapidly developed and have been widely applied to organic synthesis over the last decade. As the applications of Ru(II) photoredox catalysts emerged in organic synthesis, a clear need for stronger catalytic oxidants and reductants arose. Despite the fact that previous methods for synthesizing Ir(III) polypyridyl complexes, it was not until 2004 that neutral Ir(III) and cationic complexes were tested as photoredox catalysts. Ultimately, the measurable redox potentials and excited state lifetimes of these Ir(III) complexes suggested these complexes were capable of photoredox catalysis similar to $[\text{Ru}(\text{bpy})]^{2+}$. Most of the iridium(III) complexes absorb light in the near UV region around 400 nm and readily donate or accept an electron in their excited states thus enabling the activation of a broad range of substrates for synthetic transformations.

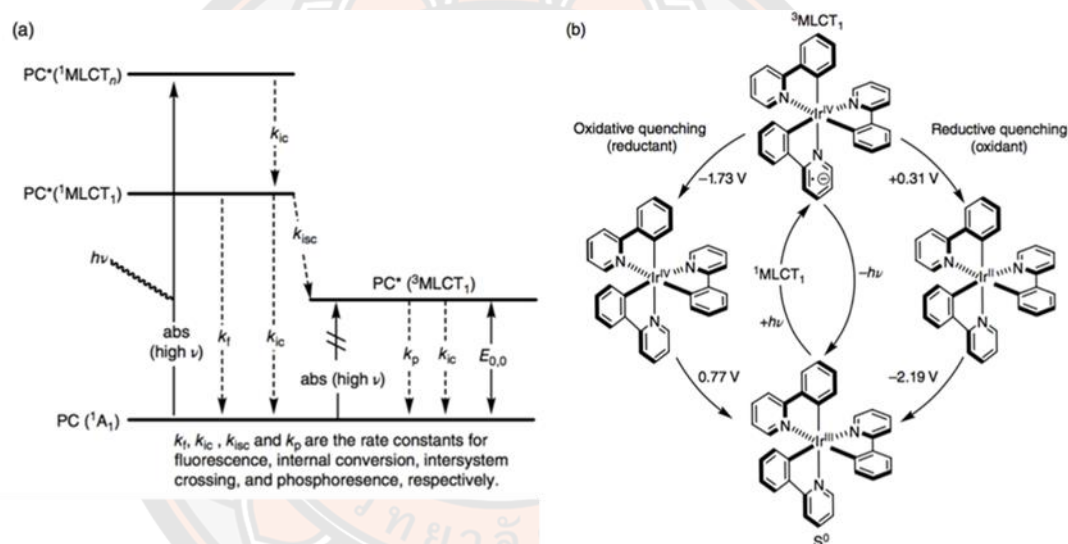


Figure 38 (a) Jablonski diagram of photophysical processes undertaken by the transition metal photocatalyst upon visible-light irradiation. (b) The redox transformations possible with $\text{Ir}(\text{ppy})_3$ photocatalyst [58].

Upon absorption of light of the appropriate wavelength (as shown in **Figure 38**), the photocatalyst in its excited state can either accept an electron from another molecule (reductive quenching) to give the reduced form of the sensitizer or transfer an electron to another molecule (oxidative quenching) yielding the oxidized sensitizer [58]. The reductive and the oxidative power of Ir(III) complexes in their excited state is determined by the energy difference between the photocatalytic active excited state and the reduced/oxidized form of the sensitizer.

The interest in the use of these complexes as catalysts for visible-light promoted photoredox catalysis started to appear after 2005. The properties of the tris-cyclometalated complex *fac*-[Ir(ppy)₃], a parent structure for the complexes investigated in this work, relevant to its use in photoredox catalysis are max absorption at 375 nm (visible light), long-lived excited state ($\tau = 1.9 \mu\text{s}$), single-electron transfer catalyst, the excited state of this complex possesses significant amount of energy (56 kcal/mol) and can act both as a reducing and oxidizing agent.

The recent progress of the most reaction types that were complex to operate by alternative methods and were extremely improved by the photocatalysis, which are functionalization, cycloaddition, and coupling reactions. In 2016, Doyle and co-worker reported α -amine functionalization reaction using nickel and photoredox catalysis, the direct functionalization of C(*sp*³)-H bonds of *N*-aryl amines by acyl electrophiles under mild conditions (**Figure 39**) [59].

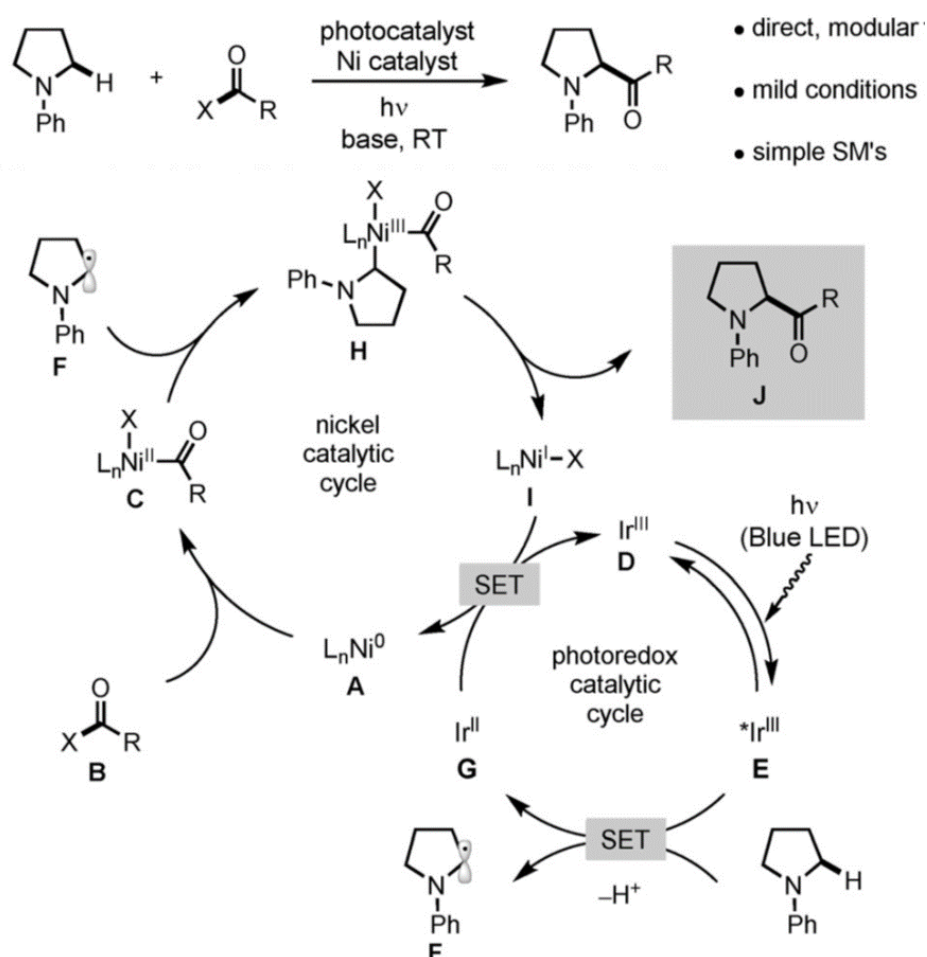


Figure 39 Proposed catalytic cycle for metallaphotoredox C-H acylation [59].

During the reaction optimization, the authors found that the reaction could not be promoted by the nickel catalyst alone due to its inability to activate the α -amino-(C–H) bond, instead, the nickel salt and the photoredox catalyst were both essential for the reaction to proceed. The C(sp³)–H acylation reaction in the catalytic cycle (**Figure 39**) is initiated by oxidative insertion of the nickel(0) catalyst **A** into the acyl-X **B** to afford the nickel(II)-acyl oxidative adduct **C** [60]. Concurrently, irradiation of the iridium photocatalyst, [Ir(ppy)₂(dtbbpy)]PF₆ (**D**) (ppy=2-phenylpyridine, dtbbpy=4,4'-di-*tert*-butyl-2,2'-dipyridyl), produces the long-lived excited state complex **E** ($\tau = 557$ ns). The complex **E** ($E_{1/2}^{\text{red}}[*\text{Ir}^{\text{III}}/\text{Ir}^{\text{II}}] = +0.70$ V vs. SCE in MeCN) can undergo SET with *N*-phenylpyrrolidine (**1**; $E_{1/2}^{\text{red}} = +0.70$ V) [61], which, upon deprotonation, generates the α -amino radical **F** and reduced iridium(II) species **G**. Interception of **F** by **C** likely affords the nickel(III) complex **H**. Subsequent reductive elimination forges the C–C bond, thus providing **J** with concomitant generation of the nickel(I) intermediate **I**. It is suggested that both catalytic cycles are closed by SET from the highly reducing **G** ($E_{1/2}^{\text{red}}[\text{Ir}^{\text{III}}/\text{Ir}^{\text{II}}] = -1.5$ V vs. SCE in MeCN) to **I** ($E_{1/2}^{\text{red}}[\text{Ni}^{\text{II}}/\text{Ni}^0] = -1.2$ V vs. SCE in DMF), thereby reconstituting the nickel(0) catalyst and the iridium(III) photocatalyst. The yield of reaction was strongly dependent on the nature of the base used.

The functionalization reactions at the β -position are difficult to achieve due to the complexity of generating active intermediates from *sp*³-carbon atoms that can undergo the desired transformations selectively. In 2018, Rueping and co-workers developed new visible-light photoredox-catalyzed synthesis of β -substituted pyrroles from unactivated pyrrolidines via an electron acceptor, metal-oxidant-free dehydrogenative aromatization reaction (**Figure 40**) [62].

Based on these observations a plausible mechanism for the oxidative dehydrogenation reaction is proposed (**Figure 40**). This discovery originated from observations made while working on functionalization of amines; the detection of the formation of a pyrrole derivate from pyrrolidine has led to further inquiries. The sulfonation of an N-substituted pyrrolidine **5a-e** derivate by sulfonyl chloride **2a**, surprisingly, afforded an aromatic β -sulfonation product **6a-e**, passing through a concerted dehydrogenative aromatization, with 14% yield. The optimal conditions found displayed the necessity of the PC, the base, and the light source.

The irradiation of photoredox catalyst $[\text{Ir}(\text{dF}(\text{CF}_3)\text{ppy}_2(\text{dtbbpy}))\text{PF}_6$ ($\text{dF}(\text{CF}_3)\text{ppy}$ = 2-(2,4-difluorophenyl)-5-trifluoro-ethylpyridine, dtbbpy = 4,4'-di-*tert*-butyl-2,2'-bipyridine, hereafter represented as Ir^{III}) promotes metal-to-ligand charge transfer (MLCT) followed by intersystem crossing (ISC) to generate excited $^*\text{Ir}^{\text{III}}$ by initial abstraction of a photon from visible light. This $^*\text{Ir}^{\text{III}}$ [$E_{1/2}^{\text{red}} = 1.21\text{ V}$ vs. SCE in CH_3CN] acts as an oxidant to oxidize the amine substrate via a single electron transfer (SET) mechanism. This single electron transfer step can generate a reduced iridium complex (Ir^{II}) with successive formation of the amine radical cation **A** and α -amino carbon radical **B** through deprotonation of the amino $\alpha\text{-C-H}$. The following SET provides iminium ion **C** which upon further tautomerization leads to the stable *endo* Z-enamine **D**. The reduced Ir^{II} acts as a reductant [$E_{1/2}^{\text{ox}} = -1.37\text{ V}$ vs. SCE in CH_3CN] to reduce 4-methylbenzenesulfonyl chloride **2a** [$E_{1/2} = -0.94\text{ V}$ vs. SCE in CH_3CN] [63] to corresponding sulfonyl radical (**2a'**) and regenerates Ir^{III} via SET. Regioselective sulfonyl radical addition to the enamine **D** provides the carbon-centered radical intermediate **E**, which gets further oxidized to form **6a-1**. Finally, aromatization and product formation of **6a** occurs in sequence analogous to the formation **6a-1** form **1**. To fulfill the catalytic cycle arylsulfonyl chloride acts additionally as a sacrificial electron acceptor to form isolatable S-(*p*-tolyl) 4-methylbenzenesulfonothioate **2a-1** and 1,2-di-*p*-tolylidisulfane **2a-2** (see reduction cycle). However, the exact mechanism for formation of **2a-1** and **2a-2** from **2a** needs to be established.

In 2011, Macmillan and co-workers discovered a photoredox-catalyzed α -amino C-H arylation reaction for the construction of benzylic amines [64]. The group also proposed mechanistic explanation of the C-H arylation process is described in **Figure 41**. The mechanism of the reaction proposed by the authors, uses *N*-aryl pyrrolidine as the amine and $[\text{Ir}(\text{ppy})_3]$ as the catalyst.

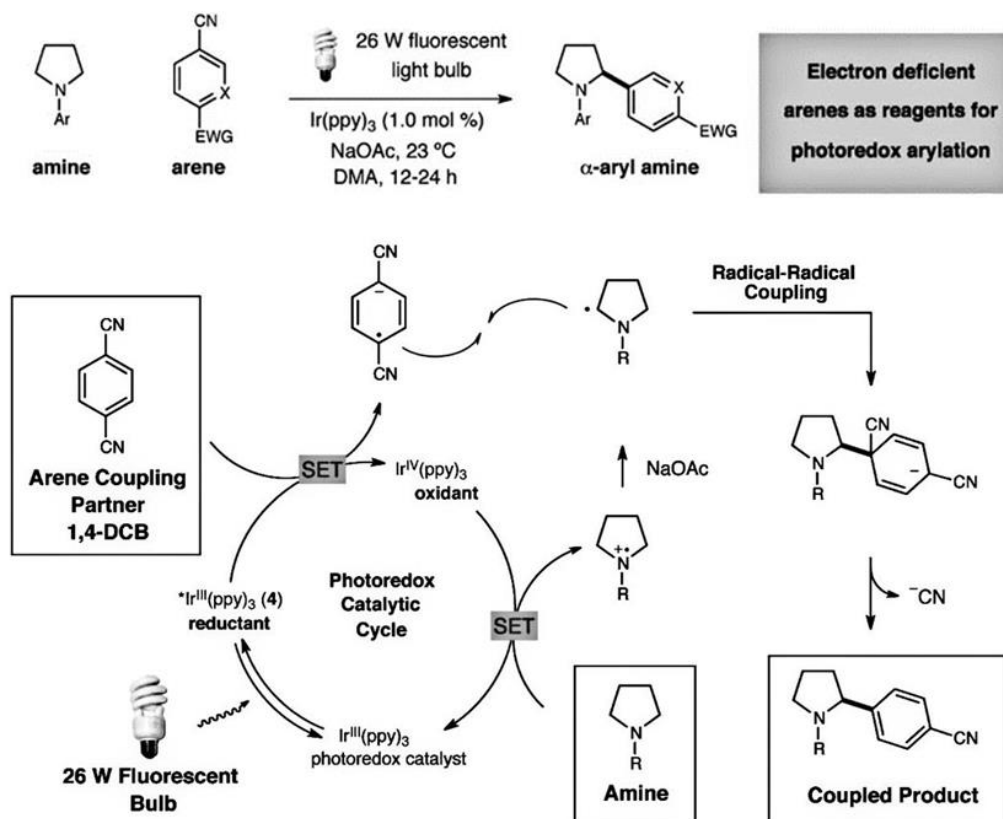


Figure 41 Proposed mechanism of the photoredox catalyzed arylation of α -amino C-H bonds [64].

Proposed mechanistic explanation for C-H arylation process of triscyclometalated Ir(III) complexes, $\text{Ir}(\text{ppy})_3$, is reversibly promoted to its excited state from $^*\text{Ir}(\text{ppy})_3$ upon absorption of a photon from the 26-W light source. $^*\text{Ir}^{\text{III}}(\text{ppy})_3$ is a strong reductant ($E_{1/2}^{\text{ox}} = -1.73$ V versus saturated calomel electrode (SCE) in CH_3CN) and acts as one electron reducing agent for the 1,4-DCB ($E_{1/2}^{\text{red}} = -1.61$ V vs SCE in CH_3CN). This single electron transfer results in the formation of the arene radical anion. The resulting $\text{Ir}^{\text{IV}}(\text{ppy})_3$ is a strong oxidant ($E_{1/2}^{\text{ox}} = +0.77$ V vs SCE in CH_3CN) and should be capable of undergoing a single-electron transfer event with amine, generating amine radical cation, as well as re-forming $\text{Ir}^{\text{III}}(\text{ppy})_3$ and thereby completing the photoredox cycle. The C-H bonds adjacent to the nitrogen atom are weakened by about 40 kcal/mol and so could undergo deprotonation by NaOAc (where OAc is an acetoxy group) to give α -aminoradical. A radical-radical coupling reaction could then unite intermediates, the key bond-forming step. Elimination of CN^- would then form the aromatized benzylic amine product.

In 2013, the same group published β -arylation of ketones and aldehydes [65]. The catalysis activation mode arises from the combination of photoredox and amine catalysis to enable the direct arylation of cyclic and acyclic carbonyls at the β -methylene position (**Figure 42**).

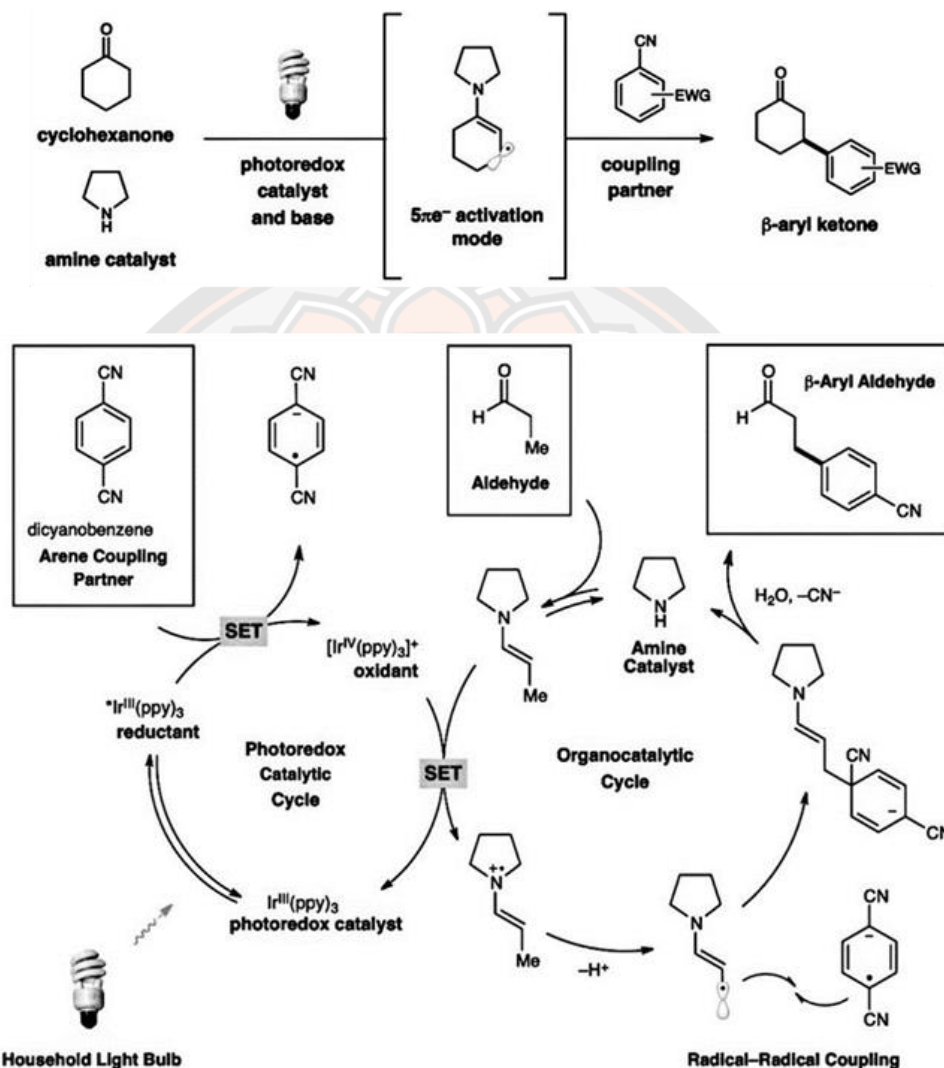


Figure 42 Proposed mechanism for the direct β -arylation of ketones and aldehydes [65].

The detailed mechanism of the reaction proposed by the authors, uses *N*-aryl pyrrolidine as the amine and $[\text{Ir}(\text{ppy})_3]$ as the catalyst. The iridium complex $[\text{Ir}(\text{ppy})_3]$ is known to undergo a metal to ligand charge transfer and intersystem crossing to generate the long-lived excited state Ir^{III} , which is a strong reductant ($E_{1/2}^{\text{ox}} = -1.73$ V versus saturated calomel electrode (SCE) in CH_3CN) acts as a one electron reducing agent for the 1,4-dicyano benzene ($E_{1/2}^{\text{red}} = -1.61$ V vs SCE in CH_3CN). This single electron transfer results in the formation of the radical ion of

1,4-dicyanobenzene and oxidation of the iridium complex from oxidation state +III to oxidation state +IV. The oxidized iridium complex ($E_{1/2}^{\text{red}} = +0.77$ V vs SCE in CH_3CN) is a relatively strong oxidizing agent that undergoes a second single electron transfer reaction with the enamine reagent resulting in the return of the iridium complex to its ground state and oxidation state +III. The reaction also forms a radical cation from the enamine, which is subsequently deprotonated by acetate present in the reaction mixture on the β -carbon. The resulting radical and the radical anion originally formed from 1,4-dicyanobenzene undergo a radical-radical recombination to form an anion, which finally aromatizes by eliminating a cyanide and forms the desired product.

In 2015, the same group found that photoredox catalysis allylic sp^3 C–H bonds [66]. The mechanism of the reaction proposed by the authors, uses 4-cyanopyridines as the alkene and $[\text{Ir}(\text{ppy})_3]$ as the catalyst (**Figure 43**).

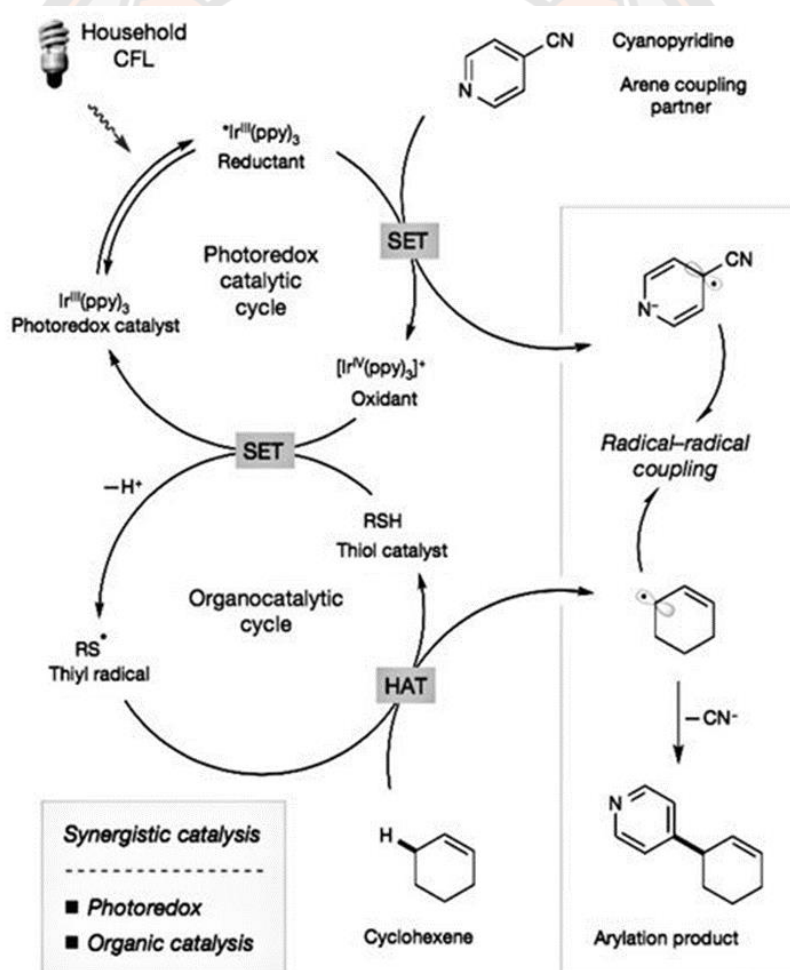


Figure 43 Proposed mechanism for the direct arylation of allylic C–H bonds via photoredox and organic catalysis [66].

Ir(ppy)_3 is a strong reductant (oxidation potential $E_{1/2}^{\text{ox}} = -1.73$ V versus saturated calomel electrode (SCE) in CH_3CN) acts as one electron reducing agent for the 1,4-dicyanobenzene (reduction potential $E_{1/2}^{\text{red}} = -1.61$ V vs SCE) to generate an arene radical anion. This single electron transfer results in the formation of the radical ion of 1,4-dicyanobenzene and oxidation of the iridium complex from oxidation state +III to oxidation state +IV. The oxidized iridium complex ($E_{1/2}^{\text{red}} = +0.77$ V vs SCE in CH_3CN) is not likely to be sufficiently oxidizing agent that undergoes a second single electron transfer reaction with the thiol ($E_{1/2}^{\text{red}} = +1.12$ V vs SCE for butanethiol in CH_3CN). The weakly acidic thiol is deprotonated to thiolate anion ($E_{1/2}^{\text{xred}} = -0.85$ V vs SCE in CH_3CN) is readily oxidized by the photocatalyst. The thiyl radical is then expected to abstract an allylic hydrogen atom from the alkene substrate to provide allylic radical with regenerated organocatalyst. An intermolecular radical coupling would serve to forge the new C–C bond, with the resulting pyridienyl or cyclohexadienyl anion undergoing rapid rearomatization via elimination of cyanide. Given the fact that the first reaction discussed above worked, it can be concluded that the issue in this reaction is either due to the organocatalytic cycle or the stability of the allylic radical.

In 2017, Difluoromethylation of phenols and thiophenols with commercially available difluorobromoacetic acid [67]. The mechanism of the reaction proposed by the authors $[\text{Ir}(\text{ppy})_3]$ as the catalyst (**Figure 44**).

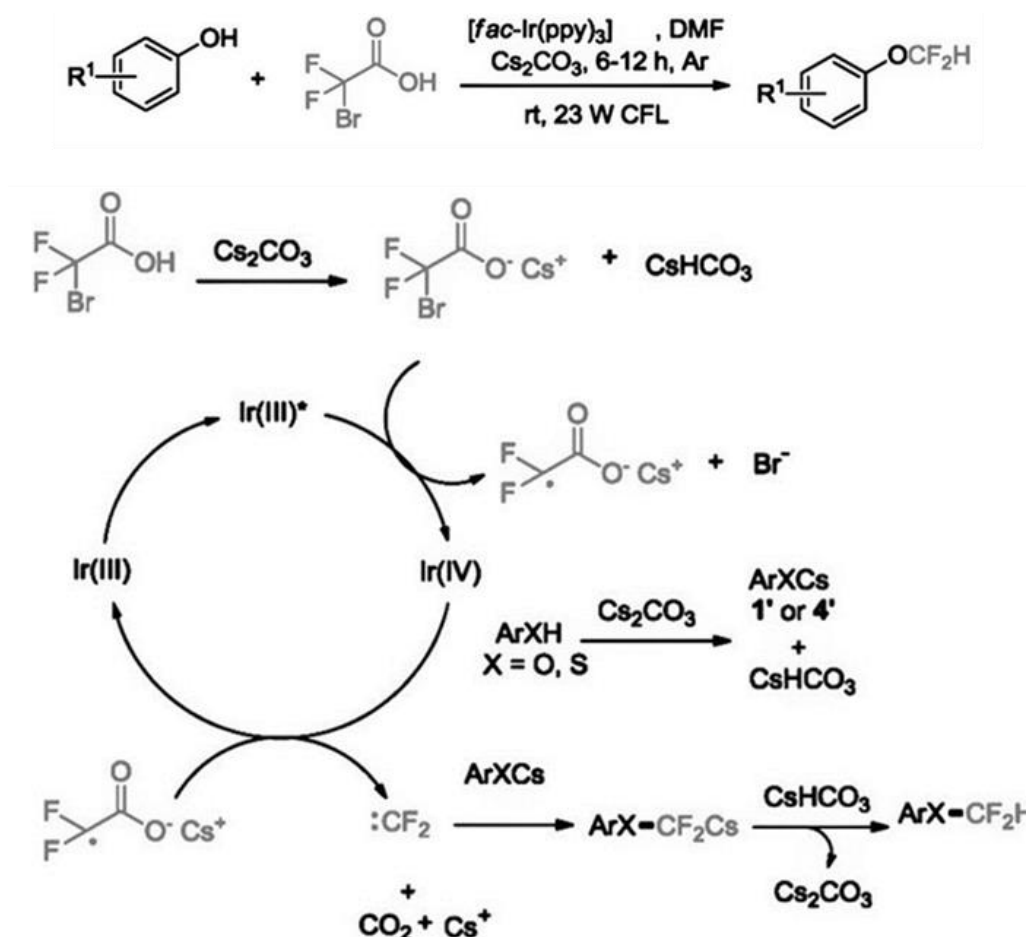


Figure 44 Mechanism on the visible-light photoredox difluoromethylation [67].

The photoexcited iridium complex ($E_{1/2}^{\text{ox}} = -1.73$ V versus saturated calomel electrode (SCE) in CH_3CN) acts as a one electron reducing agent for the difluorobromoacetic acid leading to its reductive dehalogenation ($E_{1/2}^{\text{red}} = -1.29$ V vs SCE in CH_3CN), which leads to the formation of radical anion. This single electron transfer also results in the oxidation of the iridium complex from oxidation state +III to oxidation state +IV. The oxidized iridium complex then undergoes a single electron transfer with radical anion, which leads to the original state of the catalyst and also forms difluorocarbene. This carbene then reacts with the Cs salt of the phenol and the intermediate is finally protonated by CsHCO_3 to give the product.

Consequently, design and development of iridium(III) complexes for photoredox catalysis organic molecule are interesting to study possibility of their complexes.

2.3.2 Immobilized catalysts on the solid support

In particular, the iridium-based metal complexes exhibited the superior catalytic performances because of their strong visible light absorption, long luminescence lifetime of the excited species, high quantum yield, and well defined molecular structure. These are more expensive price, limited amount of available on Earth associated with difficult product isolation and recycle block its future application. Thus, the immobilization of the homogeneous iridium complex onto solid supports without any loss of catalytic activity needs to be developed. Immobilization techniques can be attached by adsorption, covalent bonding, entrapment, cross-linking and cell aggregation. Compared to homogeneous catalysts, it is always much easier to separate immobilized catalysts (filtration, centrifuge, magnetic separation, etc.), making it more realistic to reuse the catalysts. It is also more efficient for the product isolation and purification as well as removal of the catalyst residues.

Silicas, aluminas, zeolites, metal oxides, clays, and polymeric support are also widely used for the catalyst immobilization. Materials with high surface areas and large pore sizes would lead to the improved catalytic performance. The immobilization of iridium(III) complexes in solids support allows the easy, clean separation of catalysts and improved catalytic performance due to the presence of a solid support. The efficiency of this separation process depends on a strong metal–support interaction. The materials used for immobilization of iridium complex use for recyclic catalysts have been investigated.

In 1996, Gaetano Di Marco and co-worker studied immobilized in polymeric matrices by using advantage of active luminescent iridium(III) cyclometallated $[\text{Ir}(\text{ppy})_2(\text{dpt-NH}_2)](\text{PF}_6)$ immobilized in pPEGMA [68]. The design of Ir-doped/pPEGMA having suitable excited state redox properties. In 2001, Yutaka Amao and co-worker developed $[\text{Ir}(\text{ppy})_3]$ immobilized in polystyrene, poly(styrene-co-TFEM), pPEGMA film and etc. There reported sensors using the $[\text{Ir}(\text{ppy})_3]$ in polystyrene film is highly oxygen-sensitive and photostability device. In 2014, Fengshou Wu and co-workers describes a new silica-supported iridium complex for C–H borylation catalysis [69]. They have developed an immobilized bipyridine-iridium system recycled catalyst (**Figure 45**) prepared from a silica-supported for direct C–H borylation of arenes.

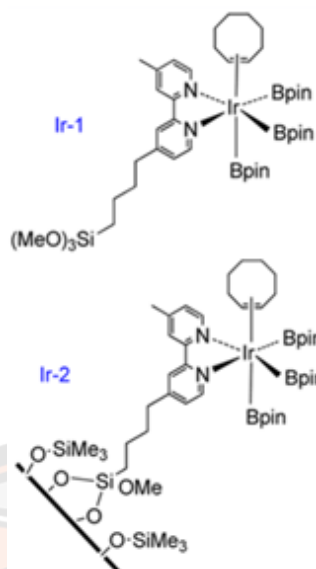


Figure 45 Structural of Ir-catalyzed aromatic C–H borylation [69].

When iridium complexes are immobilized to the surface of the solid supports, the catalyst normally will experience a different local environment compared to the homogeneous analogues in an organic solvent. Instance, the surface of polystyrene materials have a hydrophobic surface. While the silica surface is normally quite polar and hydrophilic, which would have an influence on the activity of the catalyst.

Glass slides coated with polylysine amino acids have been studied in 1975 by Mazin and co-workers [70]. The attachment of cells to the polylysine surfaces. The adhesion behaviors of cells interact between interfacial adsorption of cationic polylysine onto the surface of an anionic of cell. In 2010, Moriuchi Toshiyuki and co-worker reported luminescence from electrostatic interaction between cationic β -sheeted of poly-L-lysine and anionic of dicyanoaurate. poly- L-lysine-coated slides can be purchased commercially [71]. For attach iridium(III) complex to poly-L-lysine will use reductive amination. Proposed mechanism for the reductive amination of aldehydes converted into 1°, 2° and 3° amines takes place in two steps. The first step is the nucleophilic addition of the carbonyl group to form an imine. The second step is the reduction of the imine to an amine using a reducing agent.

CHAPTER III

METHODOGY

3.1 UV-Visible absorption spectroscopy

3.1.1 Absorption of radiation

The UV light can be considered as electromagnetic radiation with a wavelength. The visible light ranges between 400 nm and 700 nm [72] and the UV light which is defined as electromagnetic radiation, has a wavelength between 10 and 400 nm. Energy absorbed in the UV or visible region causes a change in the electronic distribution of the molecule. The energy of a photon absorbed or emitted during a transition from one molecular energy level to another level is given by the Planck law shown in **equation (1)**

$$E = h \cdot \nu = \frac{h \cdot c}{\lambda} \quad (1)$$

Where:

h is Plank's constant;
 ν is the frequency;
 c is the velocity of the light;
 λ is the wavelength.

3.1.2 Electromagnetic spectrum

Ultraviolet-visible spectroscopy or ultraviolet-visible spectrophotometry (UV-vis) is an absorption or reflectance spectroscopy in the ultraviolet and visible ranges. The UV-vis absorption spectroscopy has been in general used to study optical properties of compounds, which can absorb energy in the UV-visible region. Ultraviolet and visible spectrometers have become important analytical instruments due to their simplicity, versatility, speed, accuracy, and cost-effectiveness [73]. The analysis by using UV-vis absorption spectrometer relates to the absorption of energy in the range of near UV and visible parts of the electromagnetic spectrum [74], which have wavelength range as shown in **Figure 46** [75].

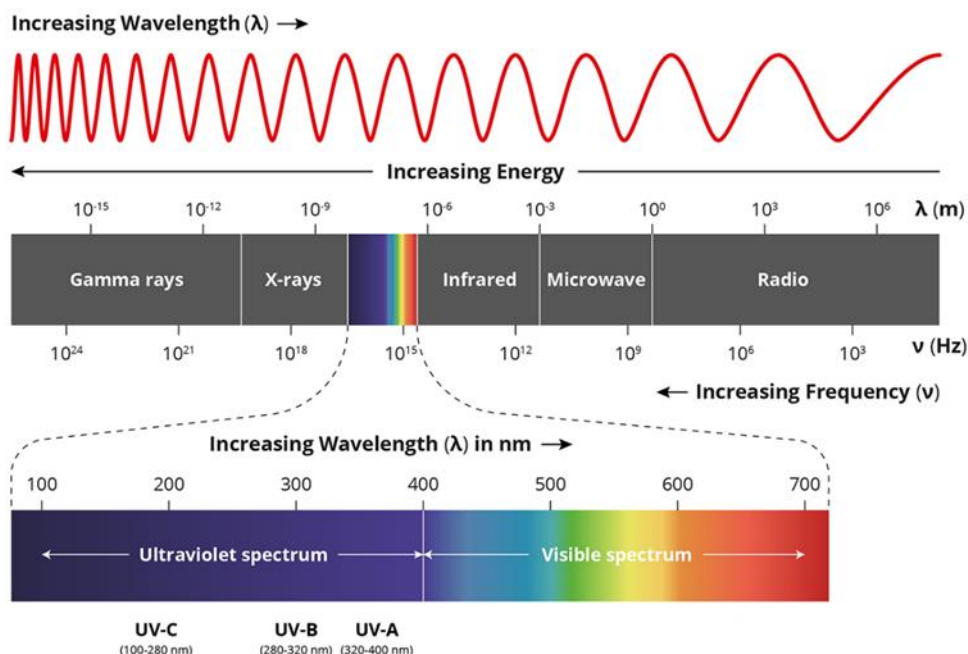


Figure 46 The electromagnetic spectrum [75].

3.1.3 Electronic transitions

Molecules containing π -electrons or non-bonding electrons can absorb the energy in the form of ultraviolet or visible light to excite these electrons to higher anti-bonding molecular orbitals. Organic compounds absorb the light in the UV or visible region. The electron transition from bonding orbital π to antibonding orbital π^* is the most common transition for conjugated organic molecules. The UV-vis spectra for organic material are generally very complex with broad spectral bands as shown in **Figure 47** [76].

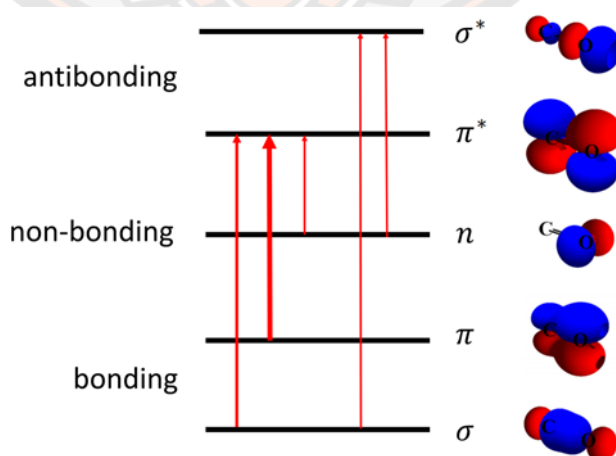


Figure 47 Illustration of different types of electronic transitions [76].

When photons of UV-vis light are absorbed by molecules and atoms, the valence electrons are excited from a lower energy level to higher energy level. The transitions normally involve the $n \rightarrow \pi^* < \pi \rightarrow \pi^* < n \rightarrow \sigma^* < \sigma \rightarrow \pi^* < \sigma \rightarrow \sigma^*$ transitions. Theoretically, the electronic transitions of atoms should result in very narrow absorption spectra at specific wavelengths, relating to the characterization of the differences in energy levels of each absorbing species [73].

The Beer-Lambert law states that the absorbance of a solution is directly proportional to the concentration of the absorbing species in the solution and the path length [77] UV-visible spectrometers usually display the relationship between absorbance and concentration is known as Beer-Lambert's law [78]. It is described by the **equation (2)**

$$A = \varepsilon \cdot b \cdot c \quad (2)$$

Where: A is the absorbance of the solution (no units);
 ε is the molar absorptivity ($\text{L mol}^{-1} \text{cm}^{-1}$);
 b is the path length of radiation through the absorbing medium (cm);
 c is the concentration (mol L^{-1}).

An absorption spectrum shows us the wavelength at which a molecule can absorb light and thus provides information about electronic state energies. From the magnitude of $A(\lambda)$ we can obtain information about sample composition or the probability of an electronic transition. When monochromatic radiation passes through a homogeneous solution in a sample cell, the intensity of UV-vis light depends on the thickness and the concentration of the solution. Depending on the nature of the ground and excited state orbitals this probability can be very different [79]. **Table 2** shows the relationship between the range of absorbed wavelengths and the colors which are observed by human eyes [80].

Table 2 The corresponding colors of the absorbed and observed wavelengths.

Wavelength (nm)	Color absorbed	Color observed
390–420	Violet	Green-yellow
420–440	Violet-blue	Yellow
440–470	Blue	Orange
470–500	Blue-green	Red
500–520	Green	Purple
520–550	Yellow-green	Violet
550–580	Yellow	Violet-blue
580–620	Orange	Blue
620–680	Red	Blue-green
680–780	Purple	Green

An absorption spectrophotometer is a device used to measure absorbed light intensity as a function of wavelength. In UV–visible spectrophotometers, a beam of light from a suitable UV and/or visible light source is passed through a prism or diffraction grating monochromator. The light then passes through the sample to be analyzed before reaching the detector (**Figure 48**). UV–visible spectrophotometers have five main components: the light source, monochromator, sample holder, detector, and interpreter [81]. The standard light source consists of a deuterium arc (190–330 nm) and a tungsten filament lamp (330–800 nm), which together generates a light beam across the 190–800 nm spectral range. The monochromator produces a compact optical path and reduces optical aberrations. Modern instruments use grating monochromators in reflection mode as the dispersing element.

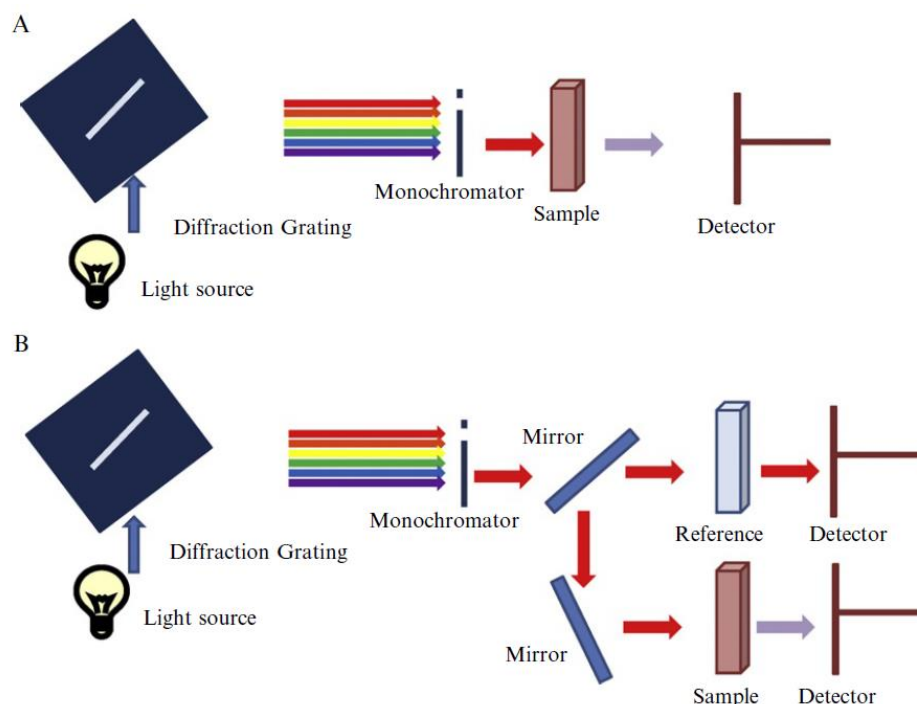


Figure 48 Typical optical layout of an absorption spectrophotometer. (A) Single beam spectrophotometer and (B) double beam spectrophotometer [81].

There are two major classes of spectrophotometers used to collect UV-Visible spectra: single beam spectrometer and double beam spectrometer. The single beam instrument (**Figure 48A**) requires a reference sample to be measured separately from the test sample. A single beam spectrophotometer should always be switched on some time before use to allow the lamp to reach a constant temperature. This instrument is cheaper to build and easy to use and maintain. In a double beam instrument, the light from the source is split into two separate beams after passing through the monochromator (**Figure 48B**). One beam is used for the sample, while the other one is used for reference determination. This configuration is advantageous because sample and reference reading can be conducted simultaneously so that the measurement becomes independent from variations in the intensity and spectral composition of the light source.

Sample cells are available in a wide variety of materials and pathlengths, with most routine measurements being made using 10 mm rectangular cell. These are conventionally being fabricated using materials such as fused quartz, glass, and plastic [79]. Quartz has an advantage over the other materials in that they can be used to measure absorbance below 380 nm. For specialized experiments, numerous designs and sizes of sample (0.2–4.0 ml) cuvettes/cells are available.

Table 3 UV absorbance range of different sample cells.

Material	Wavelength range (nm)
Fused quartz	Below 380
Glass	380-780
Plastic	380-780

3.2 Fluorescence spectroscopy

When a molecule is promoted to an electronically excited state by the absorption of ultraviolet, visible, or near infrared radiation, luminescence or the emission of light from this state can occur when this excited molecule decays back to the ground state, or to a lower-lying excited electronic state [82]. Luminescent processes are subdivided into fluorescence and phosphorescence.

Fluorescence and phosphorescence are alike in that excitation is brought about by the absorption of photons. As a consequence, the two phenomena are often referred to by the more general term photoluminescence. Fluorescence differs from phosphorescence in that the electronic energy transitions responsible for fluorescence do not involve a change in electron spin. Because of this, the excited states involved in fluorescence are short-lived ($<10^{-5}$ s). In contrast, a change in electron spin accompanies phosphorescence, and the lifetimes of the excited states are much longer, often on the order of seconds or even minutes. In most instances, photoluminescence, be it fluorescence or phosphorescence, occurs at wavelengths longer than that of excitation radiation.

Luminescence can be considered as a three-stage process that is best illustrated by a Perrin-Jablonski diagram (**Figure 49**) [82]. Here the singlet ground state, first and second excited states are depicted as S_0 , S_1 , and S_2 respectively. Each electronic energy level has a number of vibrational energy levels, depicted by 0, 1, 2 etc. Rotational energy levels are omitted from the diagram for clarity. The transitions between states are depicted as vertical lines to indicate the instantaneous nature of light absorption.

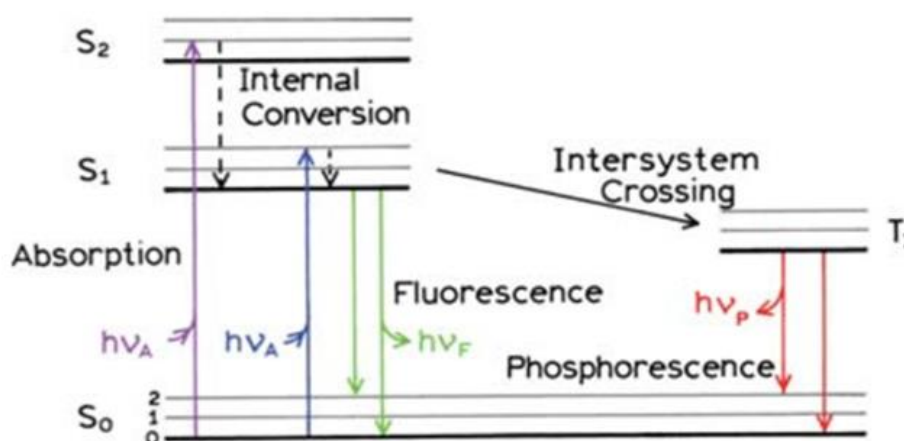


Figure 49 Perrin-Jablonski diagram showing the electronic processes occurring in a fluorescent molecule after excitation by light [82].

Stage 1: Excitation

Following light absorption, a photon of given energy $h\nu_{ex}$ is supplied from an outside source such as a laser or a lamp. An electron is excited from the ground state (S_0) to one of the vibrational levels of an upper excited electronic state (S_1 or S_2). The process of excitation is fast and occurs on femtosecond timescale. This is shown as a vertical transition which occurs in a femtosecond (10^{-15} sec) time frame, too short to significantly displace the nuclei (the Frank-Condon principle) or change the electronic spin-state from that of the ground state configuration. The Frank-Condon principle is equally applied to the transitions from higher to lower energy states as well.

Stage 2: Excited-State Transitions

The S_1 or S_2 excited states exist for a finite amount of time with a subsequent partial dissipation of energy in the form of heat by rapid relaxation to the lowest vibrational level of S_1 , yielding a relaxed singlet excited state (S_1) from which fluorescence emission originates. This process is called internal conversion and occurs in 10^{-12} s or less. Since fluorescence lifetimes are typically near 10^{-9} s, internal conversion is generally complete prior to emission. Not all the molecules initially excited by absorption (Stage 1) return to the ground state (S_0) by fluorescence emission, instead returning to the ground state by non-radiative transitions. Internal conversion from S_1 to S_0 is also possible but is less efficient than conversion from S_2 to S_1 , because of the larger energy gap between S_1 and S_0 . Under certain conditions such as heavy atom spin-orbit coupling, molecules in the S_1 state can undergo a spin conversion to the first excited triplet state T_1 via the process of intersystem crossing. Emission from this state is termed phosphorescence and is typically of a much longer timescale than fluorescence due to $T_1 \rightarrow S_0$ transitions being spin forbidden (or highly improbable) by the spin selection rule for electronic transitions ($\Delta S = 0$).

Stage 3: Fluorescence Emission

Fluorescence emission usually occurs from the lowest vibrational level of the S1 state and can return the molecule to different vibrational levels of the ground state. The emission of a photon is as fast as the absorption ($\approx 10^{-15}$ s), but excited molecules stay in the S1 state for a certain time (from 10^{-12} to 10^{-6} s depending on the type of molecule and the medium used) before emitting a photon or undergoing other excited state transitions. This characteristic time is called the fluorescence lifetime. Unless the fluorophore is irreversibly destroyed in the excited state (a phenomenon known as photobleaching), the same fluorophore can be repeatedly excited and detected. The fact that a single fluorophore can cycle between the ground and excited states many thousands of times (estimates of 10,000 to 40,000 cycles have been given) is fundamental to the high sensitivity of fluorescence detection techniques [83]. A photon of energy $h\nu_{em}$ is emitted, returning the fluorophore to its ground state S_0 . Due to energy dissipation during the excited-state lifetime, the energy of this photon is lower, and therefore of longer wavelength, than the excitation photon $h\nu_{ex}$. The difference in energy or wavelength represented by $(h\nu_{ex}-h\nu_{em})$ is called the Stokes' shift. The Stokes shift is fundamental to the sensitivity of fluorescence techniques because it allows emission photons to be detected against a low background, isolated from excitation photons. In contrast, absorption spectrophotometry requires measurement of transmitted light relative to high incident light levels at the same wavelength. The fluorescence quantum yield (ϕ), which is the ratio of the number of fluorescence photons emitted (Stage 3) to the number of photons absorbed (Stage 1), is a measure of the relative extent to which these processes occur.

As mentioned above, a key characteristic of fluorescence spectroscopy is its high sensitivity, achieving limits of detection several orders of magnitude lower than many other analytical techniques. Limits of detection of 10^{-10} M or lower are possible for intensely fluorescent molecules. Under controlled conditions, single molecule (the ultimate limit of detection) may be reached. Because of the low detection limits, fluorescence is widely used for quantification of trace constituents of biological and environmental samples. Also the use of fluorescent molecules or markers to detect non-fluorescent molecules is widespread and has numerous applications (such as molecular imaging and DNA sequencing) [84]. However, luminescence methods are less widely applicable for quantitative analyses than absorption methods because many more molecules absorb ultraviolet and visible radiation than exhibit photoluminescence when radiation is absorbed in this region of the spectrum.

UV-vis spectroscopy has been used in this work to investigate the photophysical properties of the synthesized compounds. The UV-vis absorption spectra can provide information about effects of structural modifications on the photophysical properties of newly synthesized iridium(III) complexes.

3.2.1 Fluorescence spectra

As shown in **Figure 50**, when a photon of excitation light is absorbed by an electron of a fluorescent molecule this results in the movement of this electron to an excited state [82]. Ultimately, within a short period of time, the electron relaxes back to its original position in the ground state. During this short time period, some of the energy is dissipated by molecular collisions or transferred to a proximal molecule, and then the remaining energy is emitted as a photon release relaxes the electron back to the ground state. Therefore, the emitted photon usually carries less energy and thus the emitted light has a longer wavelength than the excitation light. The phenomenon of fluorescence emission displays a number of general characteristics. As energy is lost due to internal conversion, the emitted photon is of lower energy and this results in a difference between the maximum of the first absorption band and the maximum of the fluorescence emission, called the Stokes' shift. For single fluorophores, thermal relaxation usually leads to the lowest vibrational energy level of the S_1 state, and because of this, the same emission spectrum is generally observed irrespective of the excitation wavelength. This phenomenon is known as Kasha's rule. Because the differences between the vibrational levels are similar in the ground and excited states, and due to the Frank-Condon principle, the emission spectrum is typically a mirror image of the absorption spectrum of the $S_0 \rightarrow S_1$ transition. Also, if a particular transition to a vibrational level of an excited state is of higher probability or intensity, then the reciprocal transition will also have the highest probability. The absorption and emission spectra of Anthracene, a typical aromatic hydrocarbon present in crude oil are shown in **Figure 50**. Incident photons of varying wavelength (and energies) initiate transitions to varying vibrational energy levels of S_1 , giving rise to multiple peaks. As the photons absorbed have a large number of vibrational and rotational energy levels, the discrete electronic transitions represented in **Figure 50** are replaced by rather broad energy spectra called the fluorescence excitation spectrum and fluorescence emission spectrum, respectively.

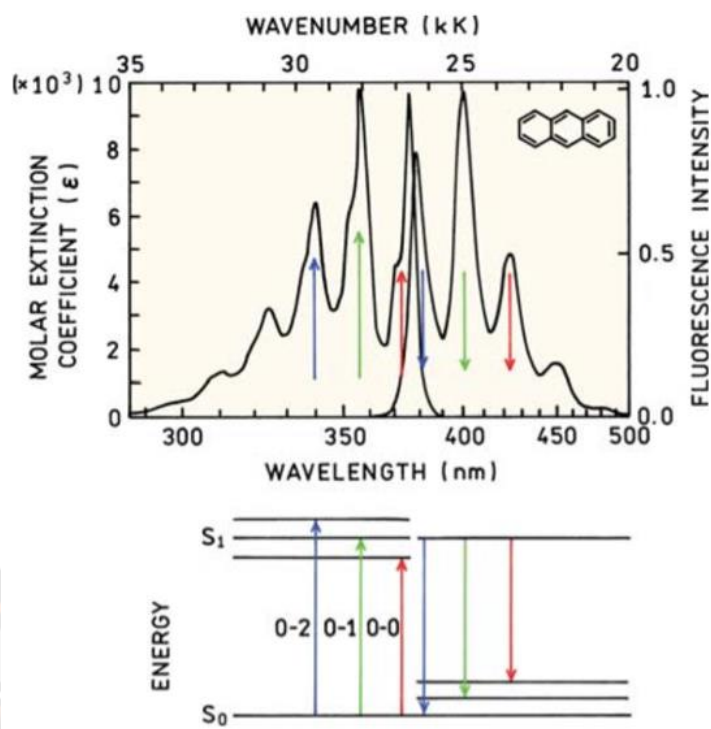


Figure 50 Mirror-image rule and Franck-Condon factors. The absorption and emission spectra are for anthracene (in Toluene). The numbers 0, 1, and 2 refer to vibrational energy levels [82].

The peaks in the absorption spectrum correspond to transitions from the lowest vibrational level of the electronic ground state to different vibrational levels of the first electronic excited state, while the peaks observed in the fluorescence spectrum arise from transitions from the lowest vibrational level of the excited electronic state to the different vibrational levels of the ground state [82]. As shown in **Figure 50**, there is some overlap of the absorption and emission spectra because at room temperature a small fraction of the molecules in a vibrational level higher than 0. At cryogenic temperatures, this overlap would be reduced.

Larger molecules will typically have more complex electronic spectra, emitting at longer wavelengths. For example, in large PAH's, the degree of conjugation increases, the number of delocalized p-orbitals increases. Increased delocalization reduces the energy gap between the highest occupied molecular orbital (HOMO) and the lowest unoccupied molecular orbital (LUMO). Since the absorption energy is reduced, a shift of the absorption and emission to longer wavelengths occurs.

Fluorescence spectroscopy has been used in the course of this work to investigate the photophysical properties of the synthesized iridium(III) complexes. The acquisition of this information was crucial given the intended purpose of the synthesized compounds in their use for cellular imaging.

3.2.2 Fluorescence lifetime

Fluorescence measurements can be broadly classified into two types: Steady-State and Time-Resolved. For steady-state measurements, the sample is illuminated with a continuous beam of light and the intensity of the emission spectrum is recorded. This fluorescence emission spectrum represents an average of the time-resolved processes occurring during an intensity decay. Temporal information such as lifetime can be recovered by using a pulsed or modulated light source, the essence of a time-resolved fluorescence measurement. Fluorescence lifetime is an intrinsic property of a fluorophore, and it does not depend on fluorophore concentration, absorption by the sample, sample thickness, method of measurement, fluorescence intensity, photo-bleaching, or excitation intensity. It is affected by external factors, such as temperature, polarity, and the presence of fluorescence quenchers. Fluorescence lifetime is sensitive to internal factors that are dependent on fluorophore structure.

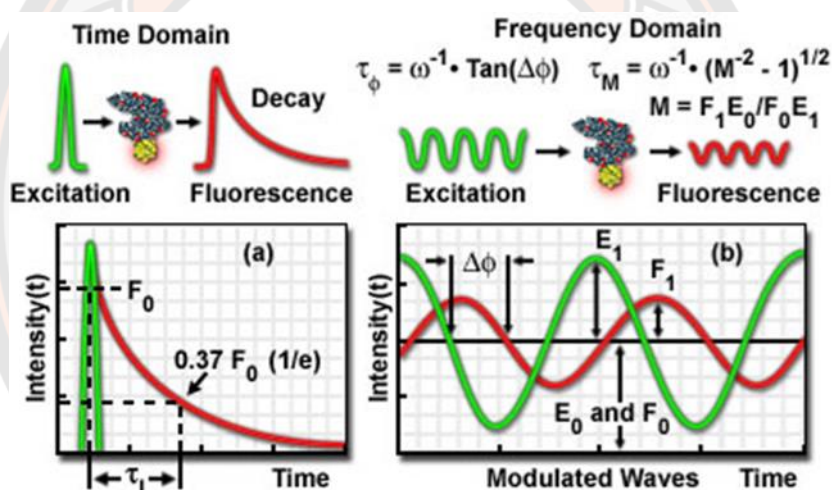


Figure 51 Fluorescence lifetime measurements using the time-domain method and the frequency-domain method [84].

Two different time-resolved fluorescence techniques, Pulse fluorometry and Phase Modulation fluorometry, are commonly used to measure the fluorescence lifetimes (**Figure 51**) [84]. In pulse fluorometry, one measures the sample emission following excitation by a short pulse of light and works in the Time-Domain (TD). TD measurements are usually performed using the Time Correlated Single Photon Counting (TCSPC) method. In Phase-Modulation fluorometry, one measures the emission phase angle lag and modulation attenuation relative to the sinusoidally modulated excitation. This method works in the Frequency-Domain (FD). Both TD and FD methods provide lifetime values, which will be the same for simple homogeneous fluorophores.

Fluorescence lifetime measurements can give information about collisional deactivation processes, about energy transfer rates, and about excited-state reactions. Lifetime measurement can also be used analytically to provide additional selectivity in the analysis of mixtures containing luminescent species. The measurement of luminescence lifetimes was initially restricted to phosphorescent systems, where decay times were long enough to permit the easy measurement of emitted intensity as a function of time. By now, equipment is offered by several instrument manufacturers for studying rates of luminescence decay on a fluorescence time scale (10^{-5} to 10^{-9} s).

Measurement of the luminescence lifetimes of the synthesized iridium(III) complexes by the TCSPC technique was a crucial part of description of the photophysical properties of these compounds. The luminescence lifetimes of iridium complexes reaching the microsecond regime are one of their key benefits and therefore required investigation as part of this work

3.3 Dynamic light scattering

The Zetasizer Nano series performs size measurements of dispersed particles by a process called Dynamic Light Scattering (DLS) (also called Photon Correlation Spectroscopy (PCS)). This technique measures the random changes in the intensity of light scattering based on Brownian motion and relates this to the size of the particles. DLS used to determine the size distribution of small particle in suspension or polymers in solution [85]. The instrument performs the measurement by illuminating the particles with a laser and analyzing the intensity fluctuations in the scattered light.

In practice, particles suspended in a liquid are never stationary. The particles are constantly moving due to Brownian motion. Brownian motion is the movement of particles due to the random collision with the molecules of the liquid that surrounds the particle. An important feature of Brownian motion for DLS is that small particles move quickly and large particles move more slowly. The relationship between the size of a particle and its speed due to cc is defined in the Stokes-Einstein **equation (3)**.

$$D = \frac{k_B T}{6 \pi \eta r} \quad (3)$$

Where:

- D is the diffusion constant;
- k_B is the Boltzmanns constant;
- T is the absolute temperature;
- π is the ratio of a circle's circumference to its diameter;
- η is the viscosity of the liquid;
- r is the radius of the Brownan particle.

As the particles are constantly in motion the speckle pattern will also appear to move. The particles move around, the constructive and destructive phase addition of the scattered light will cause the bright and dark areas to grow and diminish in intensity or to put it another way, the intensity at any particular point appears to fluctuate. The Zetasizer Nano system measures the rate of the intensity fluctuation and then uses this to calculate the size of the particles.

Significant portion of this work has been devoted to investigating the effects of changes in the structure of the developed iridium(III) complexes on their photophysical properties in aqueous media. One of the key assumption in this regard, was that this behavior is linked to changes in the aggregation status of these compounds in regards to structural change or changes in the solution composition. DLS was therefore utilized as a supporting technique to provide evidence for this hypothesis.

3.4 DFT calculations

The Density Functional Theory (DFT) [86] based electronic states of atoms, molecules, and materials in terms of the three dimensional electronic density of the system. DFT calculations involve a 3N-dimensional antisymmetric wave function for a system with N electrons [87]. The first attempts to use the electron density rather than the wave function for obtaining information about atomic and molecular systems are almost as old as is quantum mechanics itself and date back to the early work of Thomas in 1926 and Fermi in 1927 [88]. The main idea of DFT is to describe a many-body interacting system via its particle density and not via its many-body wavefunction. DFT was introduced in two publications in 60's, the first with Pierre Hohenberg-Kohn in 1964 [89] and the second Walter Kohn and Lu Jeu Sham in 1965 [90], including its spin-polarized extension. The basic quantity in DFT is the many-electron spin density, ρ . The spin density is ρ is the sum of ρ_α and ρ_β , the spin density ρ_α is the 3-dimensional electron density of all spin-up electrons, and ρ_β is the same for spin-down electrons. In a many-electron system comprised of both spin-up and spin-down electrons, the term spin-density is the measure of the probability of an electron also sometimes used to refer to the position-dependent difference between the up and down spin densities [91] Density functional theory (DFT) become the method for electronic structure theory for complex chemical systems. The advantages of DFT such as spin state in organic, metals, especially transition metals compound.

3.4.1 Kohn–Sham Theory

Kohn–Sham spin-orbitals, $\Psi_{j\sigma}$ where σ is α or β and j is the other quantum numbers, are obtained by a self-consistent field calculation and are formally functions of the exact density of the system. The Hohenberg–Kohn theorem [89] shows in the **equation (4)**.

$$\rho_{\sigma} = \sum_j^{\text{occ}} |\psi_{j\sigma}|^2 \quad (4)$$

Where σ is the spin component (α or β), the spin-orbitals are normalized, and the sum is over occupied orbitals of a given spin component. The electronic energy of the system is approximated as a sum of four terms, T_n , ϵ_{ne} , ϵ_{ee} , and ϵ_{xc} . T_n is the kinetic energy of a system of noninteracting electrons with the same spin densities as the real system; ϵ_{ne} is the interaction of the electron distribution with the nuclear framework; ϵ_{ee} is the classical Coulomb energy of the spin densities interacting with each other and with themselves; and ϵ_{xc} , called the exchange–correlation energy, is everything else (everything except T_n , ϵ_{ne} , and ϵ_{ee}). Therefore ϵ_{xc} includes the interaction correction to T_n . The Kohn–Sham spin-orbitals are functions of the spin-densities, ϵ_{xc} can depend explicitly on the spin densities and also implicitly on them by depending on the spin-orbitals. Direct dependence on the spin-densities can also include a dependence on their derivatives. The density functional is usually written as the sum of an “exchange” part and a “correlation” part. In particular, DFT correlation includes only dynamic correlation, and DFT exchange includes not only exchange but also some static correlation, although the latter is present in an unspecified and uncontrolled way [92].

The oldest approximation to a density functional is the Dirac–Slater approximation to exchange [93, 94]. This must be renormalized for use with Kohn–Sham theory. This is usually called the local spin density approximation (**LSDA**) since it depends only on spin densities. The next level of complexity in density functionals is to add a dependence on the gradients of the spin densities; in particular the functional depends on the unitless reduced spin-density gradients. Such functionals are called generalized gradient approximations (**GGAs**).

Popular **GGAs** include **BP86**, where **B** denotes Becke’s 1988 exchange functional (usually abbreviated as **B88** or just **B**) [95], and **P86** denotes Perdew’s 1986 correlation functional [96]; **BLYP**, where **LYP** denotes the Lee–Yang–Parr correlation functional [97]; **PW91**, from Perdew and Wang in 1991 [98]; and a functional of Perdew, Burke, and Ernzerhof (**PBE**) [99]. The modified Perdew–Wang functional of Adamo and Barone [100], called **mPWPW**, is very similar to **PBE**. Notice that **GGAs** may combine an exchange functional from one source with a correlation functional from another, or they may both be from the same source. Thus **BP86** and **BLYP** combine **B88** exchange with **P86** or **LYP** correlation, respectively; **PW91** combines **PW91** exchange with **PW91** correlation; **PBE** combines **PBE** exchange with **PBE** correlation; **mPWPW** combines **mPW** exchange with **PW91** correlation; **SLYP** combines the Slater **LSDA** exchange with **LYP** correlation; and **PBELYP** combines **PBE** exchange with **LYP** correlation.

The density functionals that perform best for main-group chemistry are not the same as those that perform best for transition metals [101]. Whereas in solid-state chemistry local functionals are often chosen, partly because they are easier to apply to

extended systems, in organic chemistry hybrid functionals are the more typical choice because of their demonstrated superior predictions of energetics; by far the most popular such hybrid functional is **B3LYP** [102], which is a hybrid GGA put together by Stephens et al [103]. On the basis of earlier work by Becke and others especially a hybrid **GGA** called **B3PW91**. The correlation functionals of **B3PW91** and **B3LYP** are based on **PW91** and **LYP**, respectively.

The Gaussian program [104] is based on Gaussian basis sets. It is the most widely used program for isolated molecules, but it also supports periodic boundary conditions, as well as calculations with continuum solvation. Molecular calculations with local functionals can employ density fitting.

The utility of Ir(III) cyclometalated complexes in organic light-emitting diodes has given rise to many TD-DFT studies of their electronic spectral properties. More relevant to catalysis, recent studies have appeared employing DFT (usually **B3LYP**) to study the mechanistic details of iridium-catalyzed allylic etherification [105], alkene hydrolization [106], and C–H bond activation [107]. Ghosh et al. [108] successfully rationalized carbon–carbon bond forming reductive elimination rates in pincer PCP–Ir complexes having various degrees of steric bulk, noting the critical importance of non-bonded interactions (as opposed to electronic effects) affecting ligand rotations required to bring eliminating alkyl fragments into reactive conformations.

The application of DFT to transition metal systems has become well established, even though many studies have been carried out with less than fully reliable density functionals. Given the rapid pace of ongoing functional development and the ever increasing scope of applications, the field must be regarded as still in its infancy. There remains considerable room for improvement, and the future is likely to be exciting.

DFT calculations have been used as part of this work for the purpose of theoretically verifying and rationalizing the observed photophysical properties of the synthesized iridium(III) complexes.

3.5 XRD

X-ray diffraction (XRD) represents the most contributive experimental method for structure resolution in structural biology. In order to present the possible improvements that can be introduced to the preparation procedures and the quality of collected data during crystallography experiments, the principles of this method and the different experimental methodologies are introduced.

X-ray wavelength is adapted to observe atomic details, as inter-atomic dimensions are about 1 to 2 Å and X-ray wavelength is in the range of 0.1 to 1000 Å. Nevertheless, using X-ray for direct observation at the atomic scale is not possible, considering that the refractive index of X-ray is so small that an optic lens for X-ray microscope is impossible to make. Therefore, analysis of the atomic structure of macromolecules requires another method. An alternative solution is to collect the X-ray diffraction measurements from a single crystal (**Figure 52**). By processing these collected data, we are able to deduce the atomic structure of the crystallized macromolecule.

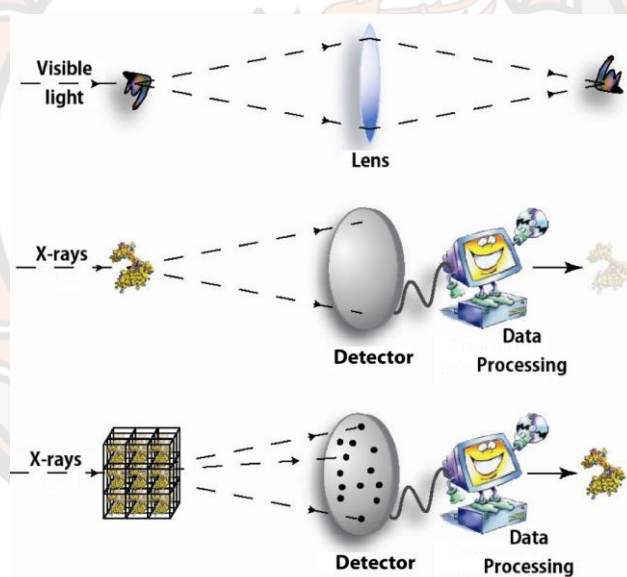


Figure 52 X-ray diffraction [109].

X-ray diffraction is considered as a scattering technique. X-ray photons from an incident beam are reflected when encountering atoms of the exposed sample, giving birth to a scattered beam. As mentioned before, over 99% of the X-rays pass through the molecule without being scattered. So to emphasize the scattering signals, a large number of same molecules should be arranged in a well known spatial configuration, which is called a crystal. In 1912, Bragg [109] discovered that precious information could be revealed by measuring the intensity and the angle of the scattering beam on a crystalline sample. Bragg law relates the incident wavelength to the scattering angle and the distance between atomic planes of a crystal lattice

(equation (5)). A discrete atomic model of a crystal in equation (5) shows the distance d , and the θ angle as half of the angle between the incident and the scattered beam.

$$n\lambda = 2d \sin \theta \quad (5)$$

Where: n is an integer determined by the order given,
 λ is the wavelength of x-rays, and moving electrons, protons and neutrons,
 d is the spacing between the planes in the atomic lattice, and
 θ is the angle between the incident ray and the scattering planes.

The reflected photons from the incident beam could interfere constructively (overlapping one another producing a more intense scattered wave) or unconstructively (neutralizing one another or decreasing the intensity of the wave) (Figure 53). The results of these interferences of scattered beam form the spots observed on diffraction patterns [109]. Crystals, as a three-dimensional periodic repetition of molecules, allow increasing the constructive interferences to give more intense spots and thus generate usable information for structure resolution.

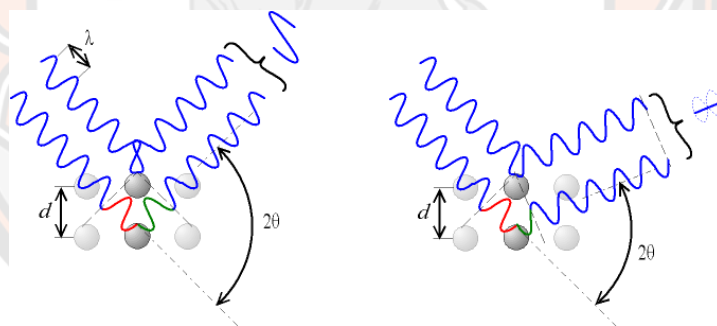


Figure 53 Constructive (on the left) and deconstructive (on the right) interferences in X-ray diffraction of a crystal sample [109].

The scattered X-ray from the crystal allows the measurement of a large number of Bragg reflections in a single exposure. A crystal lattice is three-dimensional, only a fraction of the crystal lattice points are in diffracting position at any given orientation of the crystal. Therefore, the crystal is also rotated through an angle of 0.1 to 2° during the exposure to bring more reflections to diffracting position. A diffraction pattern represents an instant image of the crystal. Thus, in order to be able to reconstruct the three-dimensional structure of the crystal, exposures at different orientations of the crystal are required. The crystal lattice has a rotational symmetry allowing limited orientation in diffraction data collection. Thus, crystals

with higher symmetry require fewer diffraction images to cover the entire crystal lattice.

3.5.1 Crystallography

Crystallography is the experimental science of the arrangement of atoms in solids. A crystal is any solid material in which the component atoms are arranged in a definite pattern and whose surface regularity reflects its internal symmetry. Unit cell is the smallest unit of volume that permits identical cells to be stacked together to fill all space. By repeating the pattern of the unit cell over and over in all directions, the entire crystal lattice can be constructed. The crystal systems are a grouping of crystal structures according to the axial system used to describe their lattice. Each crystal system consists of a set of three axes in a particular geometrical arrangement. There are seven unique crystal systems. The simplest and most symmetric, the cubic (or isometric) system, has the symmetry of a cube, that is, the three axes are mutually perpendicular and of equal length. The other six systems, in order of decreasing symmetry, are hexagonal, tetragonal, rhombohedral (also known as trigonal), orthorhombic, monoclinic and triclinic (**Figure 54**) [110].

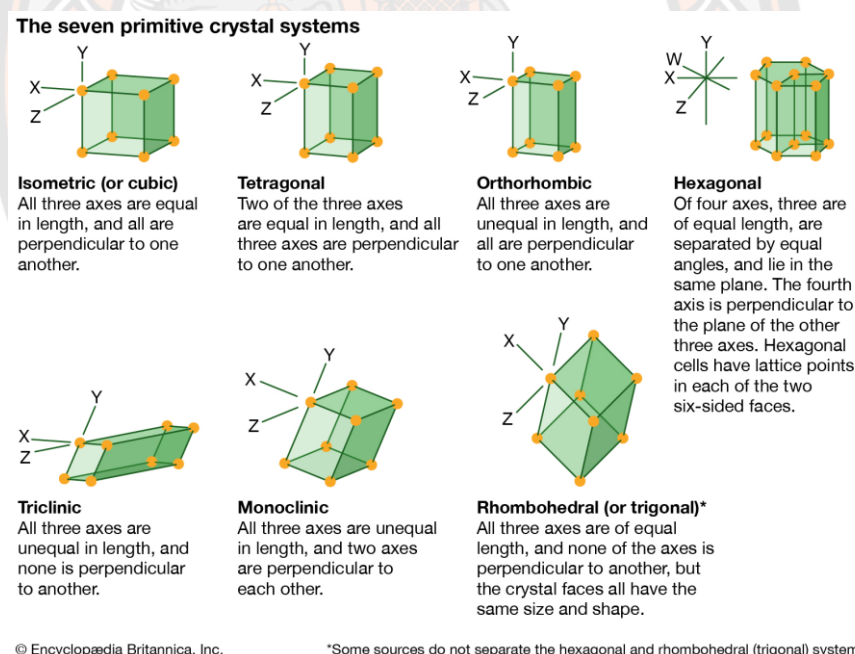


Figure 54 The seven primitive crystal systems [110].

The cubic (isometric) crystal system is characterized by its total symmetry. The cubic system has three crystallographic axes that are all perpendicular to each other, and equal in length. The cubic system has one lattice point on each of the cube's four corners. The hexagonal crystal system has four crystallographic axes consisting of three equal horizontal or equatorial (x, y, and w) axes at 120° , and one vertical (z)

axis that is perpendicular to the other three. The (z) axis can be shorter, or longer than the horizontal axes. A tetragonal crystal is a simple cubic shape that is stretched along its (z) axis to form a rectangular prism. The tetragonal crystal will have a square base and top, but a height which is taller. By continuing to stretch the body-centered cubic, one more Bravais lattice of the tetragonal system is constructed. A rhombohedron (trigonal system) has a three-dimensional shape that is similar to a cube, but it has been skewed or inclined to one side making it oblique. Its form is considered prismatic because all six crystal faces are parallel to each other. Any faces that are not squared at right angles are called rhombi. A rhombohedral crystal has six faces, 12 edges, and 8 vertices. If all of the non-obtuse internal angles of the faces are equal (flat sample, below), it can be called a trigonal-trapezohedron. Minerals that form in the orthorhombic (aka rhombic) crystal system have three mutually perpendicular axes, all with different, or unequal lengths. Crystals that form in the monoclinic system have three unequal axes. The (x) and (z) crystallographic axes are inclined toward each other at an oblique angle, and the (y) axis is perpendicular to a and c. The (y) crystallographic axis is called the ortho axis. Crystals that form in the triclinic system have three unequal crystallographic axes, all of which intersect at oblique angles. Triclinic crystals have a 1-fold symmetry axis with virtually no discernible symmetry, and no mirrored or prismatic planes.

With molecules exposed to X-rays, the scattered radiation contains precious information on molecules structure. Nevertheless, over 99% of the X-rays pass through the molecule without being scattered. So to emphasize the scattering signals, a large number of same molecules should be arranged in a well known spatial configuration. This arrangement of molecules constitutes what is called a crystal. The science related to the arrangement of molecules is called crystallography. It defines a crystal as a unique form of arrangement of molecules or a three-dimensional repetition of molecules creating a lattice.

XRD has been used in this project as an ultimate verification of the structure of the synthesized iridium complexes. Specifically, it has been used to demonstrate that the complexes have the expected *fac* geometry.

3.6 Cell imaging

Live-cell imaging is an important analytical tool in laboratories studying biomedical research disciplines, such as cell biology, neurobiology, pharmacology, and developmental biology. Imaging of fixed cells and tissues (for which photobleaching is the major issue) usually requires a high illumination intensity and long exposure time; however, these must be avoided when imaging living cells. Live-cell microscopy usually involves a compromise between obtaining image quality and maintaining healthy cells. Therefore, to avoid a high illumination intensity and long exposure time, spatial and temporal resolutions are often limited in an experiment. Imaging live cells involves a wide range of contrast-enhanced imaging methods for

optical microscopy. Most investigations use one of the many types of fluorescence microscopy, and this is often combined with transmitted light techniques. Continual advances in imaging techniques and design of fluorescent probes improve the power of this approach (**Figure 55**), ensuring that live-cell imaging will continue to be an important tool in biology [111].



Figure 55 Leica SP5 II Confocal Laser Scanning Microscope is capable of Fluorescence Lifetime Imaging Microscopy and Fluorescence Cross Correlation Spectroscopy [111].

Biological systems are typically three dimensional structures. When the fluorophore labeled sample is flooded with excitation laser light like in conventional widefield microscopy, the resulting image is usually highly disturbed by out-of-focus fluorescent light. This leads to blurring of the image and results in a significant decrease in contrast. Confocal microscopy is a technique to reduce this unwanted out of focus light. In this technique, the excitation light is tightly focused in the sample. The emission light from the focus is collected by the same objective, after which it is focused through a small pinhole and directed towards a photodetector (**Figure 56left**) [112]. The out of focus emission light will be largely blocked by the pinhole (**Figure 56right**).

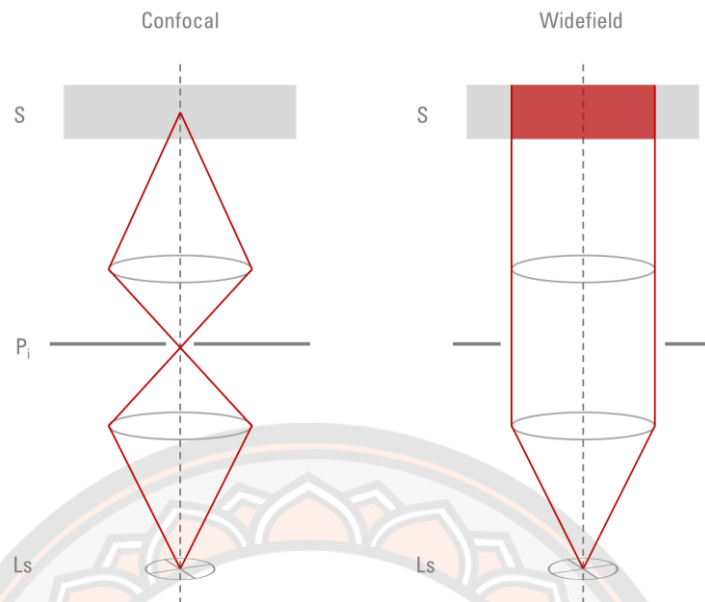


Figure 56 Confocal vs. Widefield illumination. Confocal: Light from the light-source (Ls) is focused through a pinhole for illumination (Pi) and subsequently into the sample (S) resulting in a relatively small volume. Widefield: The whole specimen volume is exposed to light [112].

Confocal microscopy offers several advantages over conventional optical microscopy, including shallow depth of field, elimination of out-of-focus glare, and the ability to collect serial optical sections from thick specimens. In the biomedical sciences, a major application of confocal microscopy involves imaging either fixed or living cells and tissues that have usually been labeled with one or more fluorescent probes.

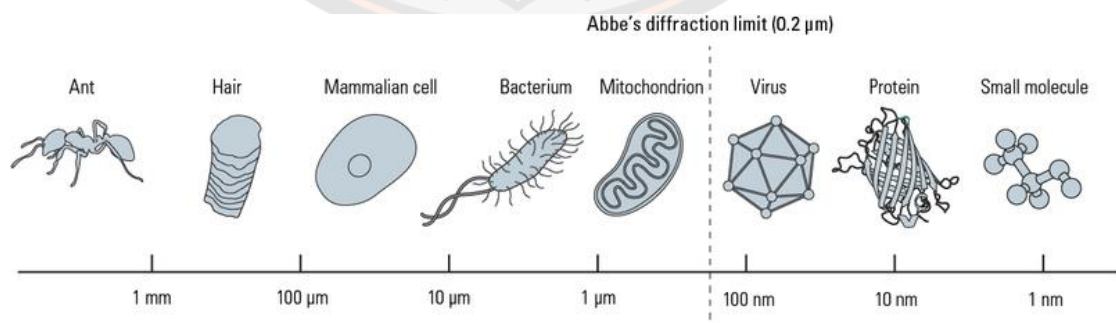


Figure 57 Super-resolution optical microscopy enables imaging of such living viruses, proteins, small molecules, and other nanoscale structures [112].

The resolution of a microscope is simply the ability to distinguish detail in a specimen. The resolution is determined by the numerical aperture (NA) and the wavelength of light. In light microscopy, the limit of resolution is around 200 nm (**Figure 57**) [112]. In a perfectly aligned microscope system with the highest NA optics, the limit of resolution is roughly half of the wavelength of light used to image the specimen (or excite the fluorophores). In comparing widefield to confocal microscopy, the theoretical limits of resolution are similar in both methods. The actual resolution achieved by a widefield microscope is exacerbated by background fluorescence. In a confocal system, the pinhole (within the scan head) is used to block any out-of-focus light from reaching the PMT detectors (**Figure 58**).

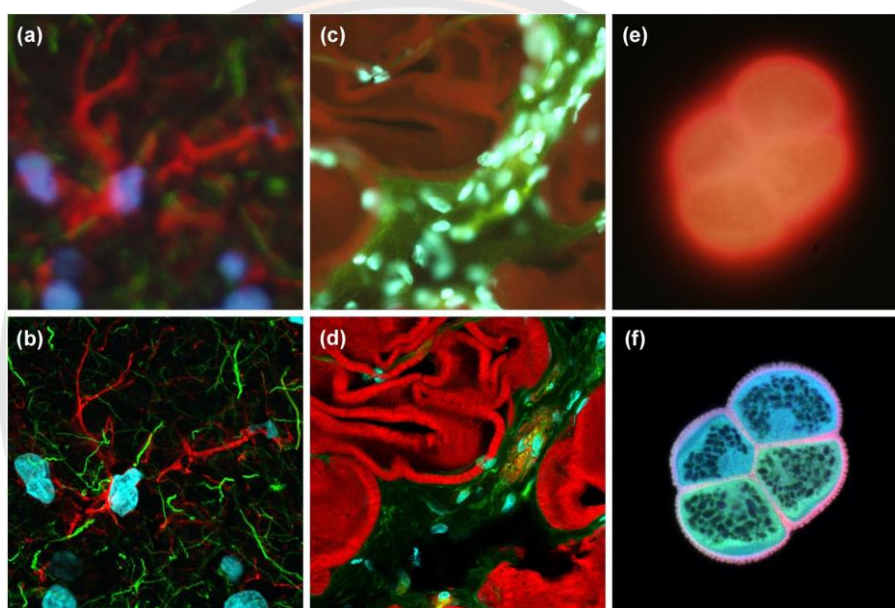


Figure 58 Comparison of widefield (upper row) and laser scanning confocal fluorescence microscopy images (lower row) [112].

The significant amount of signal in the widefield images from fluorescent structures located outside of the focal plane (**Figure 58**). (a) and (b) Mouse brain hippocampus thick section treated with primary antibodies to glial fibrillary acidic protein (GFAP; red), neurofilaments H (green), and counterstained with Hoechst 33342 (blue) to highlight nuclei. (c) and (d) Thick section of rat smooth muscle stained with phalloidin conjugated to Alexa Fluor 568 (targeting actin; red), wheat germ agglutinin conjugated to Oregon Green 488 (glycoproteins; green), and counterstained with DRAQ5 (nuclei; blue). (e) and (f) Sunflower pollen grain tetrad autofluorescence.

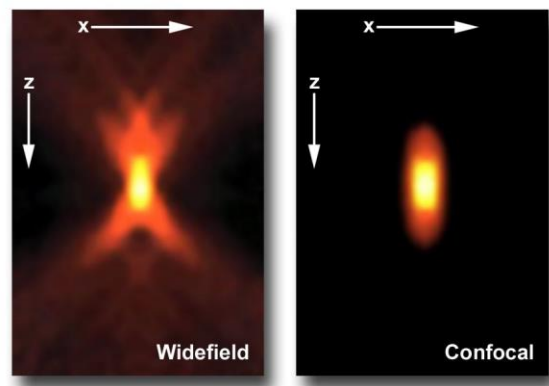


Figure 59 Comparison of axial (x-z) point spread functions for widefield (left) and confocal (right) microscopy [113].

The resolution is of primary interest in discussing resolution and contrast, although the axial extent of the microscope intensity point spread function is similarly reduced in the confocal arrangement as compared to the widefield fluorescence configuration [114]. Reasonable contrast between point-like objects lying on the optical axis occurs when they are separated by the distance between the central maximum and the first minimum of the axial point spread function component. Presented in **Figure 57** are the axial intensity distributions for a typical widefield (**Figure 57left**) and confocal (**Figure 59right**) fluorescence microscope [118].

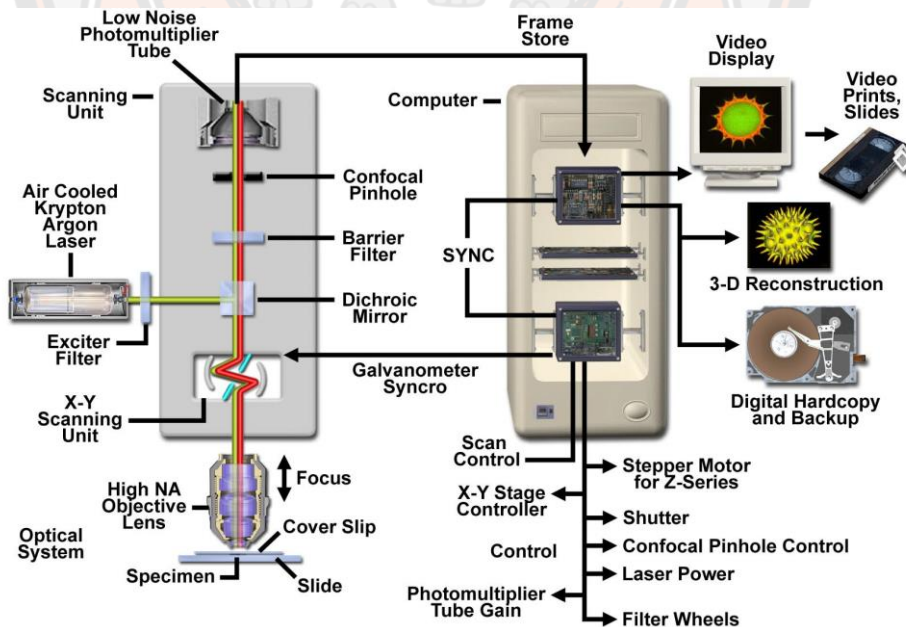


Figure 60 Confocal microscope configuration and information flow schematic diagram [112].

In a confocal system, the pinhole (within the scan head) is used to block any out-of-focus light from reaching the photomultiplier tubes (PMT) detectors (**Figure 60**). Although this has the advantage of producing a sharply focussed image by blocking background and auto-fluorescence, some of the out of focus photons may have originated from the focal plane. This means that some of the information could potentially be lost due to the pinhole. There is a balance between the sharp images produced on a confocal system and inadvertently collecting out of focus light with a widefield microscope [112].

As mentioned above imaging using fluorescence microscopy is critically dependent both on the development of instrumentation and fluorescent probes. A wide array of probes is available and can be roughly divided into four groups: 1) small molecule organic fluorophores, 2) fluorescent proteins, 3) nanoscale luminophores, and 4) luminescent metal complexes. Luminophores in each of these classes offer their unique strengths and weaknesses making them complementary and suitable for varied tasks. The multitude of targets, tasks, and experiments, which can be performed with fluorescent probes calls for a continued effort to develop novel and improved ones. Metal-based luminophores, which are the focus of the presented study, offer long luminescence lifetimes and large Stokes' shift as their main benefits. These are beneficial properties for imaging as they present an opportunity to discriminate between signal and the probe through time-gating. Furthermore, the large Stokes' shift helps to prevent self-quenching and can be useful in FRET based experiments as it can provide a better separation of the donor and acceptor signals.

The photophysical properties of tris-cyclometalated iridium complexes have led to increased interest in their development into sensors for bio-sensing and cellular imaging. Imaging probes must be able to specifically reach the target of interest in live-cell. The beneficial properties of cyclometalated iridium complexes are their large Stokes' shifts, long luminescence lifetimes (in contrast to organic fluorophores), and good photostability. For many recent years, these complexes consist an iridium(III) center bound to two cyclometalated ligands and on bidentate ligand. The chemical nature of the complexes can be easily tuned by chemical variations of coordinated ligands for their potential application as cellular markers. Complexes can be bioconjugated to target localization within a specific organelle such as cytoplasm, nucleus, lysosomes, endosomes, mitochondria, endoplasmic reticulum and Golgi apparatus.

Conducting cellular imaging experiments using fluorescence microscopy has been a crucial part of this work as utilization of the synthesized iridium(III) complexes for the purpose of fluorescence microscopy has been one of the key goals of this work. Therefore, it was important to investigate and evaluate their properties and performance for this purpose.

3.7 Photoredox catalysis by LED

Photoredox catalysis offers an alternative method in two ways the first of catalytic cycle is light-activated and second the catalyst is not directly involved as an intermediate in the coupling process. Typically, light from the visible spectrum is used to excite a photosensitizer into an excited state, which acts as a reducing or oxidizing agent for the chosen substrate. The substrate undergoes a one electron addition or removal to generate an open shell reactive intermediate that can independently engage with other species to perform many different organic transformations. The photosensitizer is replenished by a late stage intermediate to turn over its cycle and repeat the process. Throughout the last twenty years, the development of novel photoredox protocols for organic synthesis has grown exponentially. When the photocatalyst is promoted by light source to its excited state, whether it be singlet or triplet, it becomes a better electron donor and acceptor compared to its ground state. The excited photocatalyst can then be quenched by a variety of electron donors or acceptors in solution.

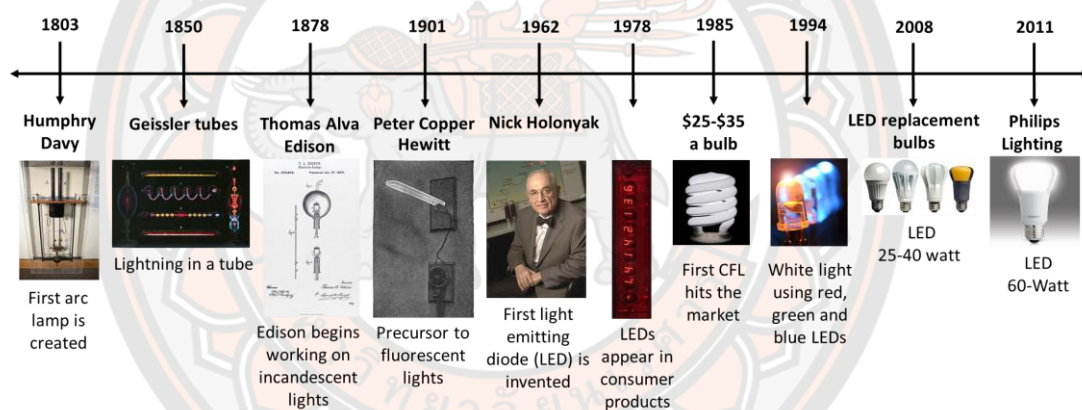


Figure 61 The History of the light bulb (data from energy.gov, July 15,2020).

The first light bulb fabricated in the 19th century, developed to use a tungsten filament as bright white light [115]. In 1803, Humphry Davy created the first electric streetlights of arc lamp it marked the beginning of the history of light. First constant electric light was discovery by James Bowman Linsay in 1835 only 10 % of energy incandescent bulb used into light starting focus their energy other lighting solutions. In 1878, Thomas Alva Edison and his researchers begins study on incandescent lights focused on improving the filament. The first patent for the incandescent bulb with a carbonized filament was created in 1880. Lifetime of lamps up to 1,200 hours. In 1901, blue-green light by passing an electric current through mercury vapor invented by Peter Copper Hewitt. The reported emission of silicon carbide diodes in 1927 by Oleg Losev now known as the light emitting diode or the LED. The lights had few suitable uses because of the color but were one of the precursors to fluorescent lights.

In 1951, fluorescent lamps were produced by research in the U.S. First compact fluorescent light (CFL) was figured out by Edward Hammer. One of the fastest developing lighting technologies today is the light-emitting diode (or LED) invented by Nick Holonyak in 1962. A type of solid-state lighting, LEDs use a semiconductor to convert electricity into light, are often small in area (less than 1 square millimeter) and emit light in a specific direction, reducing the need for reflectors and diffusers that can trap light. The first visible-spectrum LED in the form of red diodes. While yellow and green diodes were invented next. LED is a semiconductor, diode based, light emitting electronic circuit element.

Photoexcitation can be performed using natural sunlight, a LED lamp, a Xe lamp, fluorescent light bulb, or laser. The light emitting diode (LED) light sources have been used to photocatalytic. LED light sources have continuous source for a long time (different from sunlight), are inexpensive and exhibit a high current-to-light conversion efficiency with warm light [116]. Over the past 10 years there has been growth in the organic synthesis. MacMillan group designed of new an integrated small-scale photoreactor as show in **Figure 62** for photoredox catalytic reaction [117].

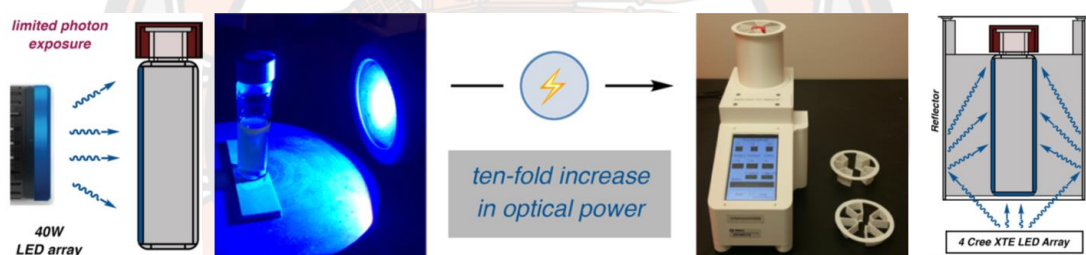


Figure 62 Standardization and Acceleration of photocatalytic reactions [118].

As mention above, many studies employ the use of directional lamps with cylindrical vials, a great deal of photonic energy is lost due to reflection. Limited of reaction are low photon penetration relative to vessel width and diminished photon capture arising from poor surface area exposure [118]. The standard setup with 40 W Kessil blue LEDs and cutaway view to show limited photon exposure as show in the **Figure 62left**. The **Figure 62right** show new LED setup with cutaway view to show high photon exposure to the reaction vessel. This reflective chamber ensures that 360 degree of the vial surface area can be subjected to photon exposure.

Utilizing the synthesized iridium(III) complexes for the purpose of photoredox catalysis has been the second area of their application explicitly investigated in this work. Performing photoredox reactions catalyzed by these compounds was, therefore, an integral part of this project.

CHAPTER IV

EXPERIMENTAL PROCEDURES

4.1 Chemical reagents

Chemicals and reagents were purchased from any supplier follow **Table 4** and were used without any further purification unless otherwise stated. All reactions were performed in nitrogen atmosphere unless otherwise stated.

Table 4 Manufacturer and purity of synthetic reagents.

Compound Name	Manufacturer	Purity
(1,4-Diazabicyclo[2.2.2]octane)	Acros Organics	97.0%
(Aminomethyl)polystyrene	Sigma-Aldrich	-
(<i>N,N</i> -Dimethylproleneurea)	Sigma-Aldrich	≥99.0%
1,3-Dimethyl-3,4,5,6-tetrahydro-2(1H)-pyrimidinone	Acros Organics	97.0%
1,4-Dicyanobenzene	Acros Organics	98.0%
2-(2-Aminoethoxy)ethanol	Acros Organics	98.0%
2-Ethoxyethanol	Carlo Erba	99.0%
2-Phenylpyridine	Fluorochem	-
3-(Triethoxysilyl)propyl isocyanate	Sigma-Aldrich	95.0%
3-Amino-1-propanol	Acros Organics	99.0%
3-Aminopropyltriethoxysilane	Acros Organics	99.0%
4-(2-Pyridyl)benzaldehyde	Acros Organics	97.0%
4-Amino-1-butanol	Acros Organics	98.0%
4-Dimethylaminopyridine	Acros Organics	99.0%
4-Nitrophenol	Acros Organics	99.0%
6-Amino-1-hexanol	Acros Organics	94.0%
Acetic acid	Carlo Erba	99.8%
Acetone	Carlo Erba	99.8%
Acetone- <i>d</i> ₆	CIL	99.9%
Acetonitrile	Carlo Erba	99.5%
Ammonia solution 30%	Carlo Erba	28.0-30.0%
Aniline	Panreac	99.0%
Benzalkonium chloride (trimethylbenzylammonium chloride)	Sigma-Aldrich	≥95.5%
Benzyl alcohol	Acros Organics	99.0%
Benzyl mercaptan	Sigma-Aldrich	99.0%
Benzylamine	Acros Organics	99.0%
Bromodifluoroacetic acid	Fluorochem	98.0%

Table 4 (cont.)

Compound Name	Manufacturer	Purity
Cesium carbonate	Sigma-Aldrich	99.0%
Chloroform- <i>d</i>	CIL	99.8%
Cyclohexanone	Carlo Erba	99.9%
Cyclohexene	Acros Organics	99.0%
Decanoic acid	Acros Organics	99.0%
Deuterium oxide	CIL	99.9%
Dichloromethane	Carlo Erba	99.9%
Di-ethanolamine	Carlo Erba	99.0%
Diethylaniline	Acros Organics	99.0%
Diethylether	Panreac	99.7%
Dimethyl sulfoxide	Carlo Erba	99.9%
Dimethyl sulfoxide- <i>d</i> ₆	CIL	99.9%
Dimethylacetamide	Sigma-Aldrich	99.5%
Dimethylformamide	Carlo Erba	99.9%
Di- <i>n</i> -butylamine	Acros Organics	99.0%
Dioxane	Sigma-Aldrich	99.0%
Dodecylamine	Acros Organics	98.0%
Ethanol absolute anhydrous	Carlo Erba	99.9%
Ethanolamine	Carlo Erba	99.0%
Ethyl acetate	Carlo Erba	99.8%
Glycolic acid	Acros Organics	99.0%
Hexamethyleneimine(azepane)	Acros Organics	99.0%
Hexane	Carlo Erba	96.0%
Hydrochloric acid	RCI Labscan	37.0%
Iridium(III) chloride trichydrate	Acros Organics	53.0-56.0%
L-Phenylalanine	Sigma-Aldrich	98.5%
L-phenylalanine methyl ester hydrochloride	Sigma-Aldrich	98.0%
Magnesium sulfate anhydrous	QReC	98.0%
Methanol	Carlo Erba	99.9%
Methanol- <i>d</i> ₄	CIL	99.8%
Methyl glycolate	Sigma-Aldrich	98.0%
Methyl iodide (iodomethane)	Merck	≥99.0%
Methyl octanoate	Acros Organics	99.0%
Morpholine	Sigma-Aldrich	99.0%
<i>N,N</i> -Diethylaniline	Acros Organics	99.0%
<i>N,N</i> -Dimethylformamide	Carlo Erba	99.9%
<i>n</i> -Butylamine	Acros Organics	99.0%

Table 4 (cont.)

Compound Name	Manufacturer	Purity
<i>n</i> -Decylamine	Acros Organics	99.0%
<i>n</i> -Hexylamine	Acros Organics	99.0%
Nitrogen gas	PGP	99.9%
<i>n</i> -Octylamine	Acros Organics	99.0%
Oxalyl chloride	Acros Organics	98.0%
Piperazine	Acros Organics	99.0%
Piperidine	Sigma-Aldrich	99.0%
Poly-L-lysine coated glass slides	Sigma-Aldrich	-
Potassium carbonate	UNILAB	99.0%
Pyrrolidine	Sigma-Aldrich	99.0%
SilicaFlash G60	SILICYCLE	-
Silver trifluoromethanesulfonate	Acros Organics	99.0%
Sodium acetate	Carlo Erba	99.0%
Sodium borohydride powder	Sigma-Aldrich	≥98.0%
Sodium carbonate	Merck	99.9%
Sodium cyanoborohydride	Acros Organics	95.0%
Tetraethyl orthosilicate	Acros Organics	98.0%
Tetrahydrofuran	Carlo Erba	99.5%
Toluene	Carlo Erba	99.8%
Triethylamine	Carlo Erba	99.5%
Triisopropylsilane thiol	Sigma-Aldrich	97.0%

4.2 Instruments

4.2.1 UV-visible spectroscopy

UV-visible absorption spectra were recorded using Analytik Jena 210 plus diode array spectrophotometer. All samples were contained in quartz cuvettes of 1 cm pathlength, and run against a reference of pure solvent contained within a matched cuvette. Extinction coefficients were determined by dilution technique and graphical application of the Beer-Lambert law.

4.2.2 Photoluminescence spectroscopy

All emission spectra were recorded using Fluoromax-4 spectrofluorometer from Yvon Horiba. Excitation and emission slit widths were usually set to 5 nm, 4 nm, and 2 nm, but 4 nm slits were also used, depending on the condition required. Room temperature measurements were performed at 293K. Quantum yield measurements were carried out by the optically dilute method by comparison with $[\text{Ir}(\text{ppy})_2(\text{ppy-NC}_4)]$ [42] in aerated/deaerated dichloromethane.

The lifetime measurements were carried out using a DeltaFlexTM instruments, Time Correlated Single Photon Counting (TCSPC), with a blue LED excitation source of wavelength 372 nm. Deaeration was done using freeze-pump-thaw method.

Degassing is done very efficiently using the freeze pump thaw method. The sample solution was first taken in a glass apparatus having a special cuvette at one end and a glass bulb attached to it. The solution was kept in the glass bulb which is connected to the apparatus. A bowl of liquid methanol and dryice were placed under the glass bulb in order to freeze the solution. The freeze pump thaw procedure was repeated 3 times, so that all dissolved gases were removed.

4.2.3 Dynamic light scattering

Dynamic Light Scattering of the colloidal system were analysed using a Nanoparticle Sizing and Zeta Potential Analyzer (Malvern Zetasizer). The systems measure size using dynamic light scattering. Zetasizer Nano ZS 90 Nanoparticle Size Analyzer is used for routine measurements of particle size distributions from about 0.3 nm (diameter) to about 5 μm any liquid by using Dynamic Light Scattering (DLS). In this technique, random intensity fluctuations arising from the Brownian motion of colloidal particles are analyzed by autocorrelation to give both a simple mean size and polydispersity (distribution width) or more complete distribution data even for multimodal distributions.

4.2.4 Thin layer chromatography

Thin layer chromatography (TLC) was performed on SilicaPlate TLC Plates, Aluminium-Backed (SLILCYCLE, 200 μm thickness, 20 x 20 cm). These were then immersed in a TLC tank containing mobile phase of interest and analyzed under UV light (at 254 and 365 nm).

4.2.5 Mass spectroscopy

Mass spectra were taken with an Agilent Technologies UHD Accurate-Mass Q-TOF LC/MS instrument model 6540 (Agilent Technologies, Singapore). The instrument analysis of each sample was performed in positive ionization mode of electrospray ionization (ESI) to provide abundant information for structural identification. The injection volume was 5 μL for each sample. The mass range was set at m/z 100-1200 with a 250 ms/spectrum. All the acquisition of the data was controlled by Agilent LCMS-QTOF MassHunter Data Acquisition Software version B.05.01 and Agilent MassHunter Qualitative Analysis Software B 06.0 for analysis (Agilent Technologies, USA).

4.2.6 Nuclear magnetic resonance

^1H -NMR, ^{13}C -NMR, and ^{19}F -NMR spectra were measured on a Bruker Avance III-400 (400, 100, and 362 MHz) spectrometers. Referencing chemical of both nucleus are referenced to residual solvent signal with tetramethylsilane $\delta(\text{TMS}) = 0$ ppm

4.2.7 Cell experiments

Cell viability was determined using the Chemmetec NucleoCounter3000 cell analyzer. Microscopy images were obtained using laser scanning confocal microscopy (LSCM) with Leica SP5 II LSCM confocal microscope with a HCX APO x63/1.4 NA Lambda-Blue objective. The instrument was enhanced with PhMoNa to improve resolution. Toxicity was then measured using a ChemoMetec A/S NucleoCounter3000-Flexicyte instrument using Via1-cassette cell viability cartridges (using DAPI to identify non-viable cells, and Acridine Orange for cell detection).

4.2.8 Density functional theory calculations

Density Functional Theory (DFT) calculations were carried out with the Gaussian09 software package at the DFT level, using the hybrid functional B3LYP and the double-zeta basis set LANL2DZ [119]. The calculations were carried out for a vacuum environment as well as acetonitrile ($\epsilon = 35.688$) and dichloromethane ($\epsilon = 8.93$) using the polarizable continuum model. The molecular orbitals were visualized using the Gabeit program package.

4.2.9 X-ray crystallography

X-ray diffraction data were collected using a Bruker D8 QUESST CMOS operating at $T = 296$ K. Data were measured using ω and ϕ scans of 0.5 (d, scan_width) $^\circ$ per frame for 30 (d, scan_rate) seconds using $\text{Cu } K\alpha$ radiation (50 kV, 30 mA). The total number of runs and images was based on the strategy calculation from the program APEX2. The maximum resolution achieved was $\theta = 25.825^\circ$.

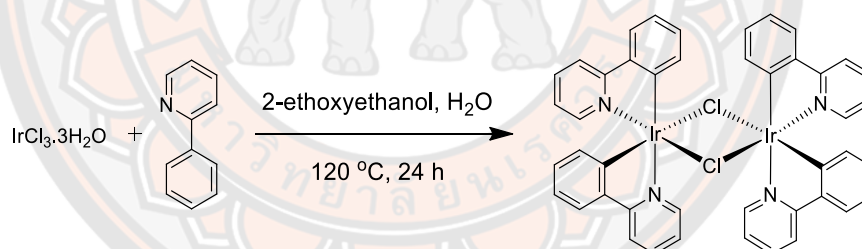
4.2.10 Photoredox catalytic experiments

The photo catalytic experiments were performed under nitrogen atmosphere as follows. For the photolysis reaction in solvent, the septa capped deoxygenated photolysis reaction schlenk tube. The solutions were photolysed using BIO-LED MR16-E27-7W light source for photoredox reaction. Color Daylight. Color temperature 6500K. Lumen 560lm. Voltage 220~240V.

4.3 Experimental

Development of novel photoactive tris-cyclometalated iridium complexes by modification on phenyl ring of parent $\text{Ir}(\text{ppy})_3$ with amino alkyl hydrophilic and hydrophobic groups. Using amination reaction after synthesis *fac*- $[\text{Ir}(\text{ppy})_2(\text{fppy})]$.

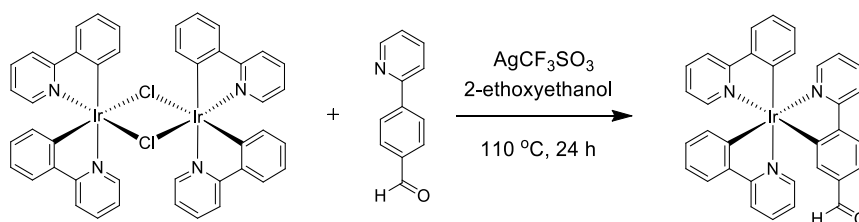
4.3.1 Synthesis of Dimer (1)



Scheme 1 Synthesis of Dimer, $[(\text{ppy})_2\text{Ir}(\mu\text{-Cl})]_2$ (1).

The compound was prepared according to the literature [120]. Briefly, a mixture of 2-ethoxyethanol-water (3:1) mixture (40 mL) was stirred for 1 h at room temperature under nitrogen gas. Iridium(III) chloride trihydrate (2.8359 mmol, 1.0 g) was added and the mixture was heated to 60 $^\circ\text{C}$ for 10 min. 2-phenylpyridine (8.5077 mmol, 1.3189 g) was added to the mixture using the Nanoyama reaction to produce chloro-bridged dimers, and the mixture was heated to 120 $^\circ\text{C}$ for 24 h. After cooling to room temperature water (10 mL) was added and the precipitate was filtered and thoroughly washed with water-methanol (1:1). The product was isolated as a yellow solid.

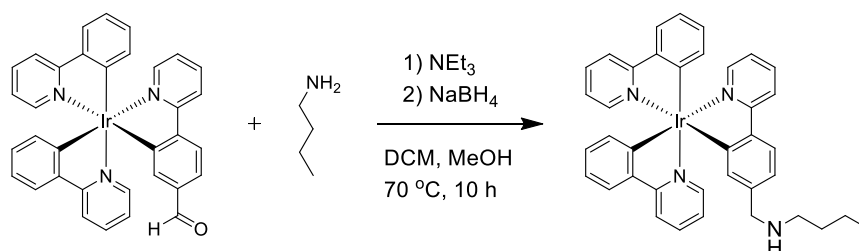
4.3.2 Synthesis of *fac*-[Ir(ppy)₂(fppy)] (2)



Scheme 2 Synthesis of *fac*-[Ir(ppy)₂(fppy)] (2).

2-ethoxyethanol 10 mL was degassed for 10 minutes with N₂. Ir(ppy)₂(μ-Cl)₂ (0.1586 mmol, 170 mg), 4-(2-pyridyl)benzaldehyde (1.586 mmol, 289 mg), and silver trifluoromethanesulfonate (0.3172 mmol, 81.5 mg) were dissolved in the solvent [121]. The reaction mixture was heated at 110 °C with continuous stirring in dark for 24 h. A dark orange-red solution was obtained. The solution was allowed to cool to room temperature and water was added. The solvent was completely removed under reduced pressure and the residue was dissolved in dichloromethane and purified by column chromatography on silica using dichloromethane as the eluent. The pure product was isolated as a red solid (0.1996 mmol, 136.3 mg, 59.83%). ¹H NMR (400 MHz, DMSO-*d*₆, δ) 9.61 (*s*, 1H), 8.32 (*d*, *J* = 8.4 Hz, 1H), 8.16 (*m*, 2H), 8.01 (*d*, *J* = 8 Hz, 1H), 7.90–7.86 (*m*, 1H), 7.83–7.75 (*m*, 4H), 7.58–7.56 (*m*, *J* = 5.6 Hz, 1H), 7.47–7.46 (*m*, 2H), 7.34–6.65 (*m*, 1H), 7.27–7.23 (*m*, 1H), 7.18–7.11 (*m*, 3H), 6.86–6.79 (*m*, 2H), 6.75–6.64 (*m*, 3H), 6.55 (*m*, 1H). HRMS (ES⁺) calculated for C₃₄H₂₅IrN₃ (684.1621); found (684.1706).

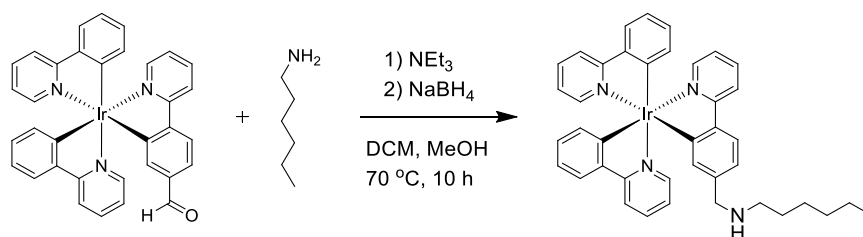
4.3.3 Synthesis of *fac*-[Ir(ppy)₂(ppy-NHR)], R=C₄H₉ (3)



Scheme 3 Synthesis of *fac*-[Ir(ppy)₂(ppy-NHR)], R=C₄H₉ (3).

fac-[Ir(ppy)₂(fppy)] (2) (1.3181 mmol, 0.900 g), *n*-butylamine (1.9772 mmol, 1.4460 g), and triethylamine (1.3181 mmol, 133.4 mg) were suspended in dichloromethane-methanol (1:1) mixture (24 mL) [42]. The reaction mixture was then refluxed under nitrogen atmosphere for 10 h. The solution was left to cool to room temperature, and NaBH₄ (2.6362 mmol, 0.0997 g) was added. The reaction mixture was stirred at room temperature for 20 h. The solvent was removed under reduce pressure and the residue was dissolved in dichloromethane (20 mL). The dichloromethane solution was washed with water (3 × 15 mL) and filtered. The residue was dissolved in dichloromethane, dried over anhydrous sodium sulfate, and filtered. The solvent was completely removed under reduced pressure and the residue was dissolved in dichloromethane and purified by column chromatography on silica using gradient of methanol (up to 5%) in dichloromethane as the eluent. The pure product was isolated as an yellow solid (1.3006 mmol, 962.4 mg, 97.37%). ¹H NMR (400 MHz, DMSO-*d*₆, δ) 8.73 (*s*, 2H), 8.20 (*d*, *J* = 8.0 Hz, 1H), 8.14 (*d*, *J* = 8.0 Hz, 2H), 7.87 (*d*, *J* = 8.0 Hz, 1H), 7.83–7.75 (*m*, 5H), 7.49 (*d*, *J* = 5.2 Hz, 1H), 7.45 (*t*, *J* = 6.0 Hz, 2H), 7.18 (*d*, *J* = 6.8 Hz, 1 H), 7.15–7.10 (*m*, 2H), 7.05 (*d*, *J* = 8.4 Hz, 1H), 6.85–6.79 (*m*, 2H), 6.73–6.61 (*m*, 5H), 3.74 (*s*, 2H), 2.68–2.64 (*m*, 2H), 1.48 (*q*, *J* = 7.2 Hz, 2H), 1.25–1.21 (*m*, 2H), 0.84 (*t*, *J* = 7.2 Hz, 3H). ¹³C (100 MHz, DMSO-*d*₆, δ) 165.5, 165.5, 164.8, 161.4, 160.1, 160.0, 146.9, 146.8, 146.7, 144.8, 143.7, 137.6, 137.0, 136.2, 131.7, 129.2, 129.0, 124.3, 124.2, 123.2, 122.8, 120.7, 119.8, 119.7, 119.4, 119.1, 115.6, 114.4, 50.2, 45.6, 27.0, 19.3, 13.4. HRMS (ES⁺) calculated for C₃₈H₃₆IrN₄ (741.2564); found (741.2591).

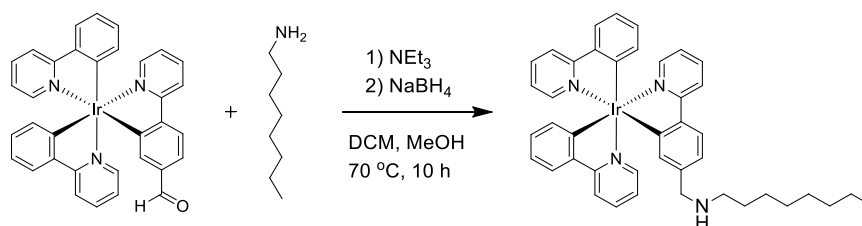
4.3.4 Synthesis of *fac*-[Ir(ppy)₂(ppy-NHR)], R=C₆H₁₃ (4)



Scheme 4 Synthesis of *fac*-[Ir(ppy)₂(ppy-NHR)], R=C₆H₁₃ (4).

fac-[Ir(ppy)₂(fppy)] (2) (0.1465 mmol, 100.0 mg), *n*-hexylamine (0.2197 mmol, 34.6 mg), and triethylamine (0.1465 mmol, 14.8 mg) were suspended in dichloromethane-methanol (1:1) mixture (14 mL). The mixture was heated at reflux under nitrogen for 10 h. The solution was left to cool to room temperature, and NaBH₄ (0.2929 mmol, 11.1 mg) was added. The reaction mixture was stirred at room temperature for 20 h. The solvent was removed under reduced pressure and the residue was dissolved in dichloromethane (20 mL). The mixture was extracted with dichloromethane, washed with water (3 × 15 mL), dried over sodium sulphate, filtered, and evaporated to dryness. The solvent was completely removed under reduced pressure and the residue was dissolved in dichloromethane and purified by column chromatography on silica using gradient of methanol (up to 5%) in dichloromethane as the eluent. The pure product was isolated as a yellow solid (1.5882 mmol, 108.0 mg, 91.83%). ¹H NMR (400 MHz, DMSO-*d*₆, δ) 8.18 (*d*, *J* = 8.2 Hz, 1H), 8.13 (*d*, *J* = 8.0 Hz, 2H), 7.85–7.70 (*m*, 6H), 7.40–7.50 (*m*, 3H), 7.15–7.06 (*m*, 3H), 7.05 (*d*, *J* = 7.8 Hz, 1H), 6.75–6.85 (*m*, 2H), 6.70–6.65 (*m*, 5H), 3.67 (*s*, 2H), 2.52–2.65 (*m*, 2H), 1.47 (*m*, 2H), 1.32–1.21 (*m*, 6H), 0.85 (*t*, *J* = 6.7 Hz, 3H). ¹³C NMR (100 MHz, DMSO-*d*₆, δ) 165.5, 165.0, 161.2, 160.1, 146.8, 144.5, 143.7, 137.5, 137.0, 136.2, 133.0, 129.0, 124.2, 123.1, 122.8, 120.6, 119.7, 119.4, 119.1, 130.2, 130.0, 125.0, 124.1, 122.6, 122.4, 122.2, 122.1, 121.7, 120.4, 120.1, 119.3, 119.0, 118.8, 50.6, 46.1, 30.7, 25.8, 25.5, 21.9, 13.8. HRMS (ES⁺) calculated for C₄₀H₄₀IrN₄ (769.2877); found (769.3010).

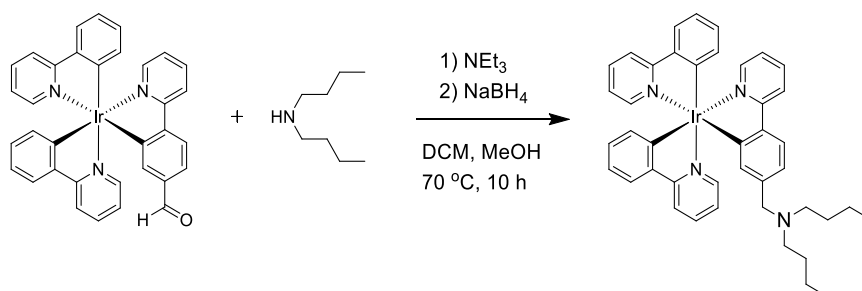
4.3.5 Synthesis of *fac*-[Ir(ppy)₂(ppy-NHR)], R=C₈H₁₇ (5)



Scheme 5 Synthesis of *fac*-[Ir(ppy)₂(ppy-NHR)], R=C₈H₁₇ (5).

fac-[Ir(ppy)₂fppy] (**2**) (0.1465 mmol, 100.0 mg), *n*-octylamine (0.2197 mmol, 28.4 mg), and triethylamine (0.1465 mmol, 14.8 mg) were suspended in dichloromethane-methanol (1:1) mixture (14 mL). The mixture was heated at reflux under nitrogen for 10 h. The solution was left to cool to room temperature, and NaBH₄ (0.2929 mmol, 11.1 mg) was added. The reaction mixture was stirred at room temperature for 20 h. The solvent was removed under reduced pressure and the residue was dissolved in dichloromethane (20 mL). The mixture was extracted with dichloromethane, washed with water (3 × 15 mL), dried over sodium sulphate, filtered, and evaporated to dryness. The solvent was completely removed under reduced pressure and the residue was dissolved in dichloromethane and purified by column chromatography on silica using gradient of methanol (up to 5%) in dichloromethane as the eluent. The pure product was isolated as a yellow solid (0.1389 mmol, 110.6 mg, 88.27%). ¹H NMR (400 MHz, DMSO-*d*₆, δ) 8.12 (*d*, *J* = 8.4 Hz, 3H), 7.79–7.73 (*q*, *J* = 8 Hz, 6H), 7.45 (*t*, *J* = 5.6 Hz, 3H), 7.12–7.08 (*m*, 3H), 6.88–6.86 (*m*, 1H), 6.82–6.67 (*m*, 2H), 6.67–6.66 (*m*, 4H), 6.60 (*d*, *J* = 1.6 Hz, 1H), 3.46 (*s*, 2H), 2.50 (*t*, *J* = 2 Hz, 2H), 1.28–1.19 (*m*, 12H), 0.85 (*t*, *J* = 6.8 Hz, 3H). ¹³C NMR (100 MHz, DMSO-*d*₆, δ) 165.6, 165.6, 165.3, 160.8, 160.6, 160.5, 146.8, 146.7, 146.7, 143.8, 143.7, 143.1, 136.8, 136.5, 136.3, 129.0, 129.0, 124.2, 124.1, 124.1, 124.1, 122.8, 122.8, 122.8, 122.7, 122.7, 122.6, 120.0, 119.6, 119.6, 119.5, 119.1, 119.0, 52.3, 47.6, 31.2, 28.7, 28.6, 27.9, 26.6, 22.0, 13.9. HRMS (ES⁺) calculated for C₄₂H₄₄IrN₄ (797.3190); found (797.3227).

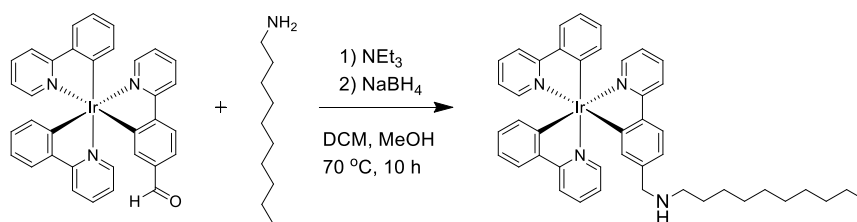
4.3.6 Synthesis of *fac*-[Ir(ppy)₂(ppy-N(R)₂)], R=C₄H₉ (6)



Scheme 6 Synthesis of *fac*-[Ir(ppy)₂(ppy-N(R)₂)], R=C₄H₉ (6).

fac-[Ir(ppy)₂(fppy)] (2) 0.1465 mmol, 100.0 mg), di-*n*-butylamine (0.2167 mmol, 28.4 mg), and triethylamine (0.1465 mmol, 14.8 mg) were suspended in dichloromethane-methanol (1:1) mixture (14 mL). The mixture was heated at reflux under nitrogen for 10 h. The solution was left to cool to room temperature, and NaBH₄ (0.2929 mmol, 11.1 mg) was added. The reaction mixture was stirred at room temperature for 20 h. The solvent was removed under reduced pressure and the residue was dissolved in dichloromethane (20 mL). The mixture was extracted with dichloromethane, washed with water (3 × 15 mL), dried over sodium sulphate, filtered, and evaporated to dryness. The solvent was completely removed under reduced pressure and the residue was dissolved in dichloromethane and purified by column chromatography on silica using gradient of methanol (up to 5%) in dichloromethane as the eluent. The pure product was isolated as a yellow solid (0.0525 mmol, 41.8 mg, 35.84%). ¹H NMR (400 MHz, DMSO-*d*₆, δ) 8.12–8.05 (*m*, 3H), 7.79–7.65 (*m*, 5H), 7.66 (*d*, *J* = 4 Hz, 1H), 7.47–7.44 (*m*, 3H), 7.71–7.05 (*m*, 3H), 6.80–6.77 (*m*, 2H), 6.73–6.61 (*m*, 6H), 2.27 (*t*, *J* = 8 Hz, 2H), 2.18 (*t*, *J* = 8 Hz, 4H), 1.36–1.20 (*m*, 8H), 0.77 (*t*, *J* = 8 Hz, 6H). ¹³C NMR (100 MHz, DMSO-*d*₆, δ) 165.7, 165.6, 161.0, 160.7, 160.4, 146.7, 146.7, 143.8, 143.7, 142.2, 137.2, 136.8, 136.7, 136.7, 136.4, 136.3, 128.9, 128.9, 124.1, 124.0, 123.8, 122.7, 122.6, 122.3, 120.6, 119.5, 119.4, 119.0, 118.9, 118.8, 52.7, 46.9, 20.0, 28.7, 28.2, 19.9, 19.4, 13.9, 13.5. HRMS (ES⁺) calculated for C₄₂H₄₄IrN₄ (797.3190); found (797.3227).

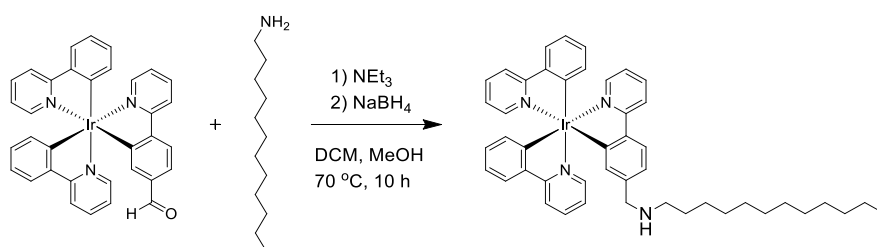
4.3.7 Synthesis of *fac*-[Ir(ppy)₂(ppy-NHR)], R=C₁₀H₂₁ (7)



Scheme 7 Synthesis of *fac*-[Ir(ppy)₂(ppy-NHR)], R=C₁₀H₂₁ (7).

fac-[Ir(ppy)₂(fppy)] (**2**) (0.0732 mmol, 50.0 mg), *n*-decylamine (0.1098 mmol, 17.3 mg), and triethylamine (73.229 μ mol, 7.4 mg) were suspended in dichloromethane-methanol (1:1) mixture (14 mL). The mixture was heated at reflux under nitrogen for 10 h. The solution was left to cool to room temperature, and NaBH₄ (0.1465 mmol, 5.5 mg) was added. The reaction mixture was stirred at room temperature for 20 h. The solvent was removed under reduced pressure and the residue was dissolved in dichloromethane (20 mL). The mixture was extracted with dichloromethane, washed with water (3 \times 15 mL), dried over sodium sulphate, filtered, and evaporated to dryness. The solvent was completely removed under reduced pressure and the residue was dissolved in dichloromethane and purified by column chromatography on silica using gradient of methanol (up to 5%) in dichloromethane as the eluent. The pure product was isolated as an yellow solid (0.0502 mmol, 41.4 mg, 68.60%). ¹H NMR (400 MHz, DMSO-*d*₆, δ) 8.12 (*d*, *J* = 3.2 Hz, 1H), 8.09 (*m*, 2H), 7.79–7.77 (*d*, *J* = 7.6 Hz, 3H), 7.75–7.71 (*m*, 2H), 7.70–7.68 (*d*, *J* = 7.6 Hz, 1H), 7.47–7.44 (*t*, *J* = 6.4 Hz, 3H), 7.12–7.06 (*m*, 3H), 6.80–6.77 (*m*, 3H), 6.67–6.66 (*d*, *J* = 4 Hz, 4H), 6.58 (*d*, *J* = 1.6 Hz, 1H), 3.35 (*s*, 2H), 2.65 (*t*, *J* = 7.2 Hz, 2H), 1.46–1.41 (*m*, 4H), 1.24 (*s*, 12H), 0.85–0.83 (*m*, 3H). ¹³C NMR (100 MHz, DMSO-*d*₆, δ) 165.6, 165.6, 165.6, 160.8, 160.8, 160.5, 146.7, 146.7, 146.7, 143.8, 143.7, 143.7, 142.3, 140.7, 136.8, 136.8, 136.3, 136.0, 136.0, 129.0, 129.0, 128.9, 124.1, 124.1, 122.7, 122.7, 122.4, 119.6, 119.5, 119.4, 119.0, 119.0, 118.8, 53.2, 48.3, 31.3, 30.3, 28.9, 28.9, 28.7, 26.8, 26.0, 22.1, 13.9. HRMS (ES⁺) calculated for C₄₄H₄₈IrN₄ (825.3503); found (825.3547).

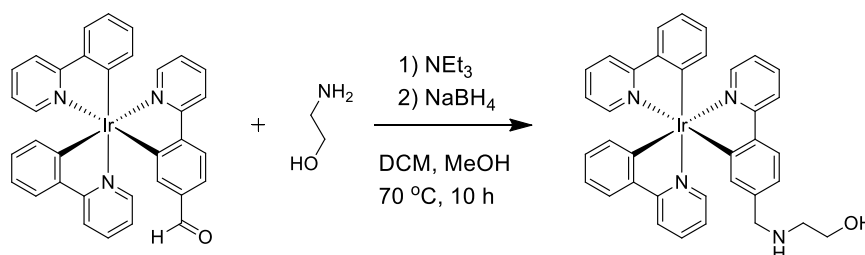
4.3.8 Synthesis of *fac*-[Ir(ppy)₂(ppy-NHR)], R=C₁₂H₂₅ (8)



Scheme 8 Synthesis of *fac*-[Ir(ppy)₂(ppy-NHR)], R=C₁₂H₂₅ (8).

fac-[Ir(ppy)₂(fppy)] (**2**) (0.1465 mmol, 100.0 mg), dodecylamine (0.2197 mmol, 40.7 mg), and triethylamine (0.1465 mmol, 14.8 mg) were suspended in dichloromethane-methanol (1:1) mixture (16 mL). The mixture was heated at reflux under nitrogen for 10 h. The solution was left to cool to room temperature, and NaBH₄ (0.2929 mmol, 11.1 mg) was added. The reaction mixture was stirred at room temperature for 20 h. The solvent was removed under reduced pressure and the residue was dissolved in dichloromethane (20 mL). The mixture was extracted with dichloromethane, washed with water (3 × 15 mL), dried over sodium sulphate, filtered, and evaporated to dryness. The solvent was completely removed under reduced pressure and the residue was dissolved in dichloromethane and purified by column chromatography on silica using gradient of methanol (up to 5%) in dichloromethane as the eluent. The pure product was isolated as a yellow solid (0.1218 mmol, 103.8 mg, 77.23%). ¹H NMR (400 MHz, CDCl₃, δ) 9.35 (*s*, 1H), 9.25 (*s*, 1H), 7.87 (*d*, *J* = 8.4 Hz, 1H), 7.84 (*d*, *J* = 8.4 Hz, 2H), 7.70–7.61 (*m*, 3H), 7.60–7.52 (*m*, 5H), 7.48 (*d*, *J* = 5.2 Hz, 1H), 7.25 (*m*, 1H), 6.91–6.76 (*m*, 7H), 7.00 (*d*, *J* = 5.2 Hz, 1H), 6.62 (*d*, *J* = 5.2 Hz, 1H), 6.53 (*s*, 1H), 3.79 (*m*, 2H), 2.42–2.54 (*m*, 2H), 1.64 (*m*, 2H), 1.32–1.21 (*m*, 18H), 0.87 (*t*, *J* = 6.8 Hz, 3H). ¹³C (100 MHz, CDCl₃, δ) 166.7, 166.7, 165.9, 161.8, 160.8, 160.6, 147.3, 147.2, 145.1, 143.8, 143.7, 139.2, 137.0, 137.0, 136.3, 136.2, 136.2, 130.7, 130.2, 130.0, 125.0, 124.1, 122.6, 122.4, 122.2, 122.1, 121.7, 120.4, 120.1, 119.3, 119.0, 118.8, 50.3, 44.9, 32.1, 29.8, 29.7, 29.5, 29.2, 27.1, 25.8, 22.8, 14.2. HRMS (ES⁺) calculated for C₄₆H₅₂IrN₄ (853.3816); found (853.3838).

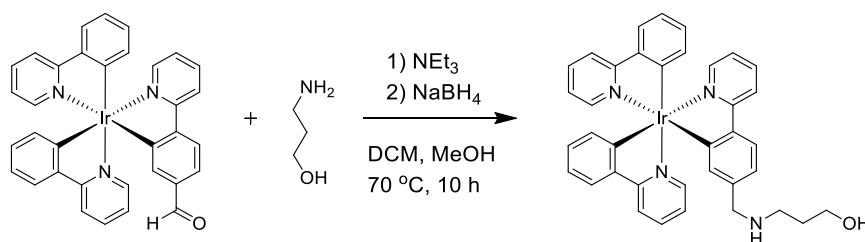
4.3.9 Synthesis of *fac*-[Ir(ppy)₂(ppy-NHR)], R=C₂H₄OH (9)



Scheme 9 Synthesis of *fac*-[Ir(ppy)₂(ppy-NHR)], R=C₂H₄OH (9).

fac-[Ir(ppy)₂(fppy)] (**2**) (0.2199 mmol, 150 mg), ethanolamine (0.4399 mmol, 27 μ L), and triethylamine (0.2200 mmol, 31 μ L) were suspended in dichloromethane-methanol (1:1) mixture (20 mL). The mixture was heated at reflux under nitrogen for 10 h. The solution was left to cool to room temperature, and NaBH₄ (0.4399 mmol, 16.6 mg) was added. The reaction mixture was stirred at room temperature for 20 h. The solvent was removed under reduced pressure and the residue was dissolved in dichloromethane (20 mL). The mixture was extracted with dichloromethane, washed with water (3 \times 15 mL), dried over sodium sulphate, filtered, and evaporated to dryness. The solvent was completely removed under reduced pressure and the residue was dissolved in dichloromethane and purified by column chromatography on silica using gradient of methanol (up to 5%) in dichloromethane as the eluent. The pure product was isolated as a yellow solid (0.1003 mmol, 73.0 mg, 45.48%). ¹H NMR (400 MHz, CD₃OD, δ) 8.01–7.98 (*q*, *J* = 4.4 Hz, 2H), 7.95 (*d*, *J* = 8.4 Hz, 1H), 7.78 (*d*, *J* = 8 Hz, 1H), 7.71–7.59 (*m*, 5H), 7.58 (*m*, 1 H), 7.53 (*m*, 2H), 6.98–6.89 (*m*, 4H), 6.86–6.80 (*m*, 3H), 6.77–6.71 (*m*, 2H), 6.69–6.67 (*m*, 2H), 3.84–3.76 (*q*, *J* = 12.8 Hz, 2H), 3.64–3.61 (*m*, 2H), 2.85–3.81 (*m*, 2H). ¹³C NMR (100 MHz, CD₃OD, δ) 165.7, 165.7, 165.5, 161.0, 160.8, 160.6, 146.9, 146.9, 146.8, 143.9, 143.9, 143.2, 138.4, 137.1, 137.0, 136.6, 136.4, 136.4, 129.2, 124.4, 124.3, 123.0, 122.9, 122.9, 122.8, 122.8, 122.8, 120.0, 119.8, 119.7, 119.3, 119.2, 119.1, 59.1, 52.6, 50.3. HRMS (ES⁺) calculated for C₃₆H₃₂IrN₄ (729.2200); found (729.2142).

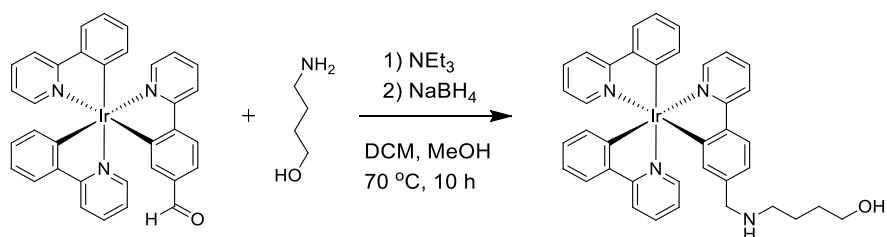
4.3.10 Synthesis of *fac*-[Ir(ppy)₂(ppy-NHR)], R=C₃H₆OH (10)



Scheme 10 Synthesis of *fac*-[Ir(ppy)₂(ppy-NHR)], R=C₃H₆OH (10).

fac-[Ir(ppy)₂(fppy)] (**2**) (0.2929 mmol, 200 mg), 3-amino-1-propanol (0.5858 mmol, 45 μ L), and triethylamine (0.2929 mmol, 41 μ L) were suspended in dichloromethane-methanol (1:1) mixture (14 mL). The mixture was heated at reflux under nitrogen for 10 h. The solution was left to cool to room temperature, and NaBH₄ (0.5858 mmol, 22.2 mg) was added. The reaction mixture was stirred at room temperature for 20 h. The solvent was removed under reduced pressure and the residue was dissolved in dichloromethane (20 mL). The mixture was extracted with dichloromethane, washed with water (3 \times 15 mL), dried over sodium sulphate, filtered, and evaporated to dryness. The solvent was completely removed under reduced pressure and the residue was dissolved in dichloromethane and purified by column chromatography on silica using gradient of methanol (up to 5%) in dichloromethane as the eluent. The pure product was isolated as an yellow solid (0.2034 mmol, 150.9 mg, 60.36%). ¹H NMR (400 MHz, CD₃OD, δ) 8.11 (*s*, 1H), 8.09 (*d*, *J* = 7.2 Hz, 2H), 7.78–7.70 (*m*, 6H), 7.46–7.44 (*t*, *J* = 5.2 Hz, 3H), 7.11–7.06 (*m*, 3H), 6.85–6.77 (*m*, 3H), 6.68–6.67 (*m*, 4H), 6.58 (*d*, *J* = 1.2 Hz, 1H), 3.38 (*t*, *J* = 6.8 Hz, 5H), 2.50–2.49 (*m*, 2H), 2.49–2.46 (*d*, *J* = 6.4 Hz, 1H), 1.53–1.46 (*m*, 2H). ¹³C NMR (100 MHz, CD₃OD, δ) 165.7, 165.7, 165.5, 160.8, 160.8, 160.7, 146.9, 146.8, 146.8, 143.9, 143.9, 143.8, 142.8, 139.6, 139.6, 137.0, 137.0, 136.9, 136.4, 136.4, 136.3, 129.2, 124.3, 124.2, 122.8, 122.8, 122.6, 119.8, 119.7, 119.7, 119.2, 119.1, 119.0, 59.5, 53.1, 45.9, 31.8. HRMS (ES⁺) calculated for C₃₇H₃₄IrN₄O (743.2356); found (743.2475).

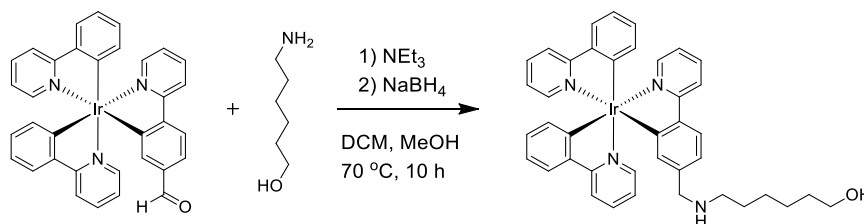
4.3.11 Synthesis of *fac*-[Ir(ppy)₂(ppy-NHR)], R=C₄H₈OH (11)



Scheme 11 Synthesis of *fac*-[Ir(ppy)₂(ppy-NHR)], R=C₄H₈OH (11).

fac-[Ir(ppy)₂(fppy)] (**2**) (0.2197 mmol, 150 mg), 4-amino-1-butanol (0.4394 mmol, 41 μ L), and triethylamine (0.0222 mmol, 31 μ L) were suspended in dichloromethane-methanol (1:1) mixture (14 mL). The mixture was heated at reflux under nitrogen for 10 h. The solution was left to cool to room temperature, and NaBH₄ (0.2197 mmol, 8.3 mg) was added. The reaction mixture was stirred at room temperature for 20 h. The solvent was removed under reduced pressure and the residue was dissolved in dichloromethane (20 mL). The mixture was extracted with dichloromethane, washed with water (3 \times 15 mL), dried over sodium sulphate, filtered, and evaporated to dryness. The solvent was completely removed under reduced pressure and the residue was dissolved in dichloromethane and purified by column chromatography on silica using gradient of methanol (up to 5%) in dichloromethane as the eluent. The pure product was isolated as a yellow solid (0.1248 mmol, 94.4 mg, 53.24%). ¹H NMR (400 MHz, CD₃OD, δ) 8.07 (*d*, *J* = 8 Hz, 1H), 8.03 (*d*, *J* = 8.4 Hz, 1H), 8.00 (*d*, *J* = 8 Hz, 1H), 7.81 (*d*, *J* = 8 Hz, 1H), 7.74–7.65 (*m*, 5H), 7.60 (*d*, *J* = 5.6 Hz, 1H), 7.53 (*t*, *J* = 6.4 Hz, 2H), 7.03–6.93 (*m*, 4H), 6.87–6.81 (*m*, 3H), 6.76–6.66 (*m*, 4H), 3.88–3.80 (*m*, 2H), 3.54 (*t*, *J* = 6 Hz, 2H), 2.84–2.79 (*m*, 2H), 1.67–1.60 (*m*, 2H), 1.54–1.48 (*m*, 2H). ¹³C NMR (100 MHz, CD₃OD, δ) 167.8, 166.9, 166.9, 163.9, 161.8, 161.4, 148.6, 148.5, 148.3, 147.3, 147.3, 145.4, 139.3, 138.0, 137.9, 137.8, 137.8, 132.5, 130.5, 130.3, 125.7, 125.6, 125.2, 125.2, 125.2, 124.0, 123.4, 123.3, 121.9, 121.1, 120.5, 120.1, 120.0, 62.0, 52.6, 30.7, 30.5, 24.0. HRMS (ES⁺) calculated for C₃₈H₃₆IrN₄O (757.2513); found (757.2519).

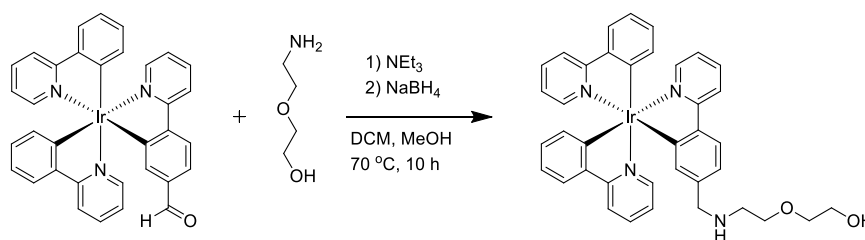
4.3.12 Synthesis of *fac*-[Ir(ppy)₂(ppy-NHR)], R=C₆H₁₂OH (12)



Scheme 12 Synthesis of *fac*-[Ir(ppy)₂(ppy-NHR)], R=C₆H₁₂OH (12).

fac-[Ir(ppy)₂(fppy)] (**2**) (0.2490 mmol, 170 mg), 6-amino-1-hexanol (0.4980 mmol, 61 μ L), and triethylamine (0.2490 mmol, 35 μ L) were suspended in dichloromethane-methanol (1:1) mixture (14 mL). The mixture was heated at reflux under nitrogen for 10 h. The solution was left to cool to room temperature, and NaBH₄ (0.0498 mmol, 18.8 mg) was added. The reaction mixture was stirred at room temperature for 20 h. The solvent was removed under reduced pressure and the residue was dissolved in dichloromethane (20 mL). The mixture was extracted with dichloromethane, washed with water (3 \times 15 mL), dried over sodium sulphate, filtered, and evaporated to dryness. The solvent was completely removed under reduced pressure and the residue was dissolved in dichloromethane and purified by column chromatography on silica using gradient of methanol (up to 5%) in dichloromethane as the eluent. The pure product was isolated as a yellow solid (0.0159 mmol, 124.5 mg, 63.09%). ¹H NMR (400 MHz, CD₃OD, δ) 8.03–7.98 (*m*, 3H), 7.75–7.68 (*m*, 6H), 7.59–7.54 (*m*, 3H), 6.99–6.95 (*m*, 3H), 6.88–6.82 (*m*, 3H), 6.77–6.67 (*m*, 5H), 3.63 (*m*, 2H), 3.53 (*t*, *J* = 6.4 Hz 2H), 2.59–2.54 (*m*, *J* = 7.6 Hz, 2H), 1.54–1.44 (*m*, 4H), 1.34–1.28 (*m*, 4H). ¹³C NMR (100 MHz, CD₃OD, δ) 167.9, 163.3, 163.3, 162.2, 161.8, 161.8, 148.5, 148.4, 148.3, 145.4, 138.6, 138.0, 137.9, 137.7, 137.6, 130.5, 130.4, 130.4, 130.3, 130.3, 130.3, 125.4, 125.1, 125.1, 123.5, 123.4, 123.2, 121.5, 120.9, 120.9, 120.2, 120.0, 119.9, 62.8, 53.5, 33.4, 30.5, 28.7, 27.9, 26.6. HRMS (ES⁺) calculated for C₄₀H₄₀IrN₄O (785.2826); found (785.2836).

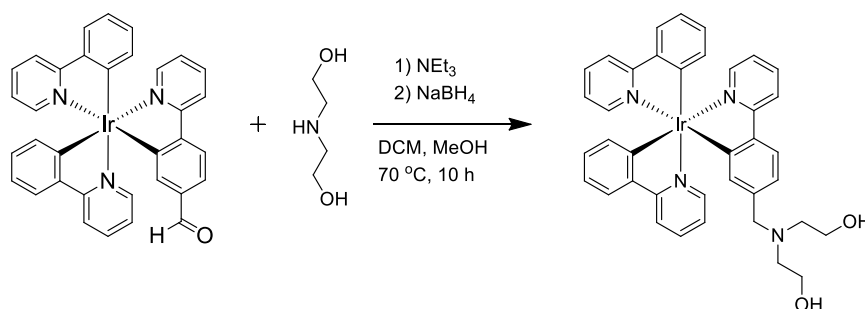
4.3.13 Synthesis of *fac*-[Ir(ppy)₂(ppy-NHR)], R=C₂H₄OH (13)



Scheme 13 Synthesis of *fac*-[Ir(ppy)₂(ppy-NHR)], R=C₂H₄OH (13).

fac-[Ir(ppy)₂(fppy)] (**2**) (0.0732 mmol, 50 mg), 2-(2-Aminoethoxy)ethanol (0.1465 mmol, 15 μ L), and triethylamine (0.0732 mmol, 11 μ L) were suspended in dichloromethane-methanol (1:1) mixture (14 mL). The mixture was heated at reflux under nitrogen for 10 h. The solution was left to cool to room temperature, and NaBH₄ (0.1465 mmol, 5.5 mg) was added. The reaction mixture was stirred at room temperature for 20 h. The solvent was removed under reduced pressure and the residue was dissolved in dichloromethane (20 mL). The mixture was extracted with dichloromethane, washed with water (3 \times 15 mL), dried over sodium sulphate, filtered, and evaporated to dryness. The solvent was completely removed under reduced pressure and the residue was dissolved in dichloromethane and purified by column chromatography on silica using gradient of methanol (up to 5%) in dichloromethane as the eluent. The pure product was isolated as an yellow solid (0.0704 mmol, 54.2 mg, 90.86%). ¹H NMR (400 MHz, CD₃OD, δ) 8.01 (*d*, *J* = 8.4 Hz, 3H), 7.72–7.66 (*m*, 6H), 7.56 (*t*, *J* = 6.4 Hz, 3H), 6.97–6.93 (*m*, 3H), 6.87–6.80 (*m*, 3H), 6.75–6.65 (*m*, 5H), 3.62 (*t*, *J* = 4.4 Hz, 2H), 3.54 (*d*, *J* = 8 Hz, 2H), 3.49–3.43 (*m*, 4H), 2.68–2.66 (*m*, 4H). ¹³C NMR (100 MHz, CD₃OD, δ) 165.6, 165.6, 165.1, 161.2, 160.5, 160.3, 146.9, 146.8, 146.8, 146.8, 144.1, 143.9, 143.8, 137.1, 137.0, 137.0, 137.0, 136.4, 136.3, 129.2, 129.2, 124.4, 124.3, 124.3, 124.2, 123.1, 122.9, 120.4, 119.8, 120.4, 119.8, 119.8, 119.7, 119.3, 119.2, 72.2, 66.6, 60.1, 51.4, 46.4. HRMS (ES⁺) calculated for C₃₈H₃₆IrN₄O₂ (773.2462); found (773.2586).

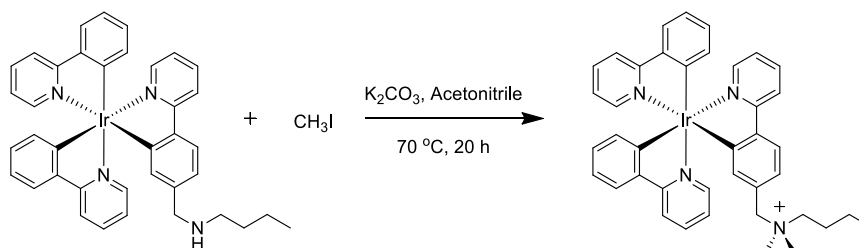
4.3.14 Synthesis of *fac*-[Ir(ppy)₂(ppy-N(R)₂)], R=C₂H₄OH (14)



Scheme 14 Synthesis of *fac*-[Ir(ppy)₂(ppy-N(R)₂)], R=C₂H₄OH (14).

fac-[Ir(ppy)₂(fppy)] (**2**) (0.0776 mmol, 53 mg), diethanolamine (0.1164 mmol, 12 μ L), and triethylamine (0.0776 mmol, 11 μ L) were suspended in dichloromethane-methanol (1:1) mixture (14 mL). The mixture was heated at reflux under nitrogen for 10 h. The solution was left to cool to room temperature, and NaBH₄ (0.0776 mmol, 2.9 mg) was added. The reaction mixture was stirred at room temperature for 20 h. The solvent was removed under reduced pressure and the residue was dissolved in dichloromethane (20 mL). The mixture was extracted with dichloromethane, washed with water (3 \times 15 mL), dried over sodium sulphate, filtered, and evaporated to dryness. The solvent was completely removed under reduced pressure and the residue was dissolved in dichloromethane and purified by column chromatography on silica using gradient of methanol (up to 5%) in dichloromethane as the eluent. The pure product was isolated as an yellow solid (0.0399 mmol, 30.8 mg, 51.42%). ¹H NMR (400 MHz, CD₃OD, δ) 8.07 (*d*, *J* = 8.4 Hz, 1H), 8.03–8.00 (*q*, *J* = 4.8 Hz, 2H), 7.81–7.79 (*d*, *J* = 8 Hz, 1H), 7.75–7.67 (*m*, 5H), 7.64–7.62 (*m*, 1H), 7.60–7.56 (*q*, *J* = 5.6 Hz, 2H), 7.05–7.02 (*m*, 1H), 7.00–6.95 (*m*, 3H), 6.88–6.82 (*m*, 2H), 6.78 (*d*, *J* = 2 Hz, 1H), 6.74–6.73 (*m*, 2H), 6.69–6.67 (*m*, 1H), 6.64 (*m*, 1H), 4.10 (*s*, 2H), 3.82–3.69 (*m*, 4H), 3.19–3.09 (*m*, 4H). ¹³C NMR (100 MHz, CD₃OD, δ) 167.8, 167.7, 166.6, 164.0, 161.8, 161.3, 148.7, 148.5, 147.8, 145.4, 145.4, 141.0, 138.0, 137.9, 137.9, 137.8, 137.7, 130.6, 130.4, 129.8, 125.5, 125.3, 125.3, 124.2, 123.6, 123.5, 123.3, 121.2, 121.1, 120.6, 120.1, 120.0, 58.4, 56.5, 56.4, 55.5, 54.8. HRMS (ES⁺) calculated for C₃₈H₃₆IrN₄O₂ (773.2462); found (773.2470).

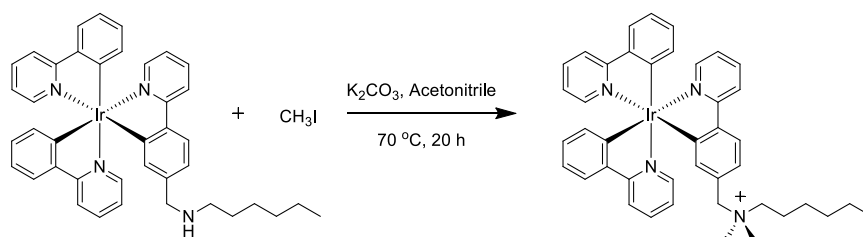
4.3.15 Synthesis of *fac*-[Ir(ppy)₂(ppy-N(CH₃)₂R)], R=C₄H₉ (15)



Scheme 15 Synthesis of *fac*-[Ir(ppy)₂(ppy-N(CH₃)₂R)], R=C₄H₉ (15).

fac-[Ir(ppy)₂(ppy-NHC₄H₉)] (**3**) (0.7917 mmol, 300 mg), methyl iodide (2.3752 mmol, 148 μ L), and potassium carbonate (0.7917 mol, 109.4 mg) was added in acetonitrile 20 mL. The reaction mixture was heated to reflux under nitrogen for 20 h. The reaction mixture was allowed to cool down and the solvent was completely removed under reduced pressure. The residue was recrystallized using dichloromethane and hexane. The pure product was isolated as a yellow solid (0.3231 mmol, 248.5 mg, 79.70%). ¹H NMR (400 MHz, DMSO-D₆, δ) 8.25 (*d*, *J* = 4.8 Hz, 1H), 8.15–8.13 (*m*, 2H), 7.91–7.87 (*m*, 1H), 7.86–7.75 (*m*, 5H), 7.55 (*d*, *J* = 4.8 Hz, 1H), 7.49–7.48 (*m*, 2H), 7.23–7.19 (*m*, 1H), 7.16–7.12 (*m*, 2H), 6.98–6.96 (*m*, 1H), 6.85–6.80 (*t*, *J* = 17.2 Hz, 2H), 6.72–6.62 (*m*, 4H), 6.56 (*d*, *J* = 7.6 Hz, 1H), 4.21–4.09 (*m*, 2H), 2.99–2.88 (*m*, 2H), 2.82 (*d*, *J* = 4.8 Hz, 5H), 1.56–1.48 (*m*, 2H), 1.19–1.13 (*m*, 2H), 0.86 (*t*, *J* = 7.2 Hz, 3H). ¹³C NMR (100 MHz, DMSO-D₆, δ) 165.4, 165.4, 164.5, 161.4, 160.0, 159.8, 147.1, 146.9, 146.8, 146.2, 143.9, 143.7, 140.1, 137.2, 137.1, 136.0, 135.9, 129.7, 129.2, 129.2, 127.8, 124.3, 124.2, 123.7, 123.7, 122.9, 122.9, 119.9, 119.8, 119.1, 119.1, 119.0, 67.3, 62.0, 49.4, 23.6, 19.2, 13.4. HRMS (ES⁺) calculated for C₄₀H₄₀IrN₄ (769.2877); found (769.2846).

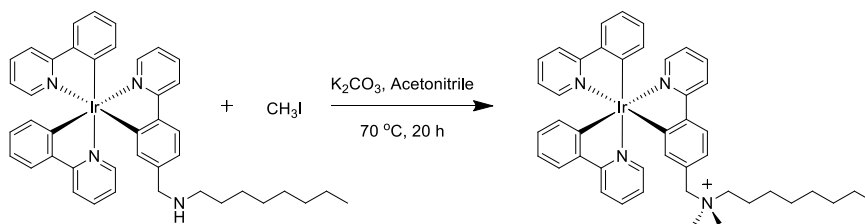
4.3.16 Synthesis of *fac*-[Ir(ppy)₂(ppy-N(CH₃)₂R)], R=C₆H₁₃ (16)



Scheme 16 Synthesis of *fac*-[Ir(ppy)₂(ppy-N(CH₃)₂R)], R=C₆H₁₃ (16).

fac-[Ir(ppy)₂(ppy-NHC₆H₁₃)] (**4**) (0.7917 mmol, 70 mg), methyl iodide (0.2735 mmol, 17 μ L), and potassium carbonate (0.0911 mol, 30 mg) was added in acetonitrile 10 mL. The reaction mixture was heated to reflux under nitrogen for 20 h. The reaction mixture was allowed to cool down and the solvent was completely removed under reduced pressure. The residue was recrystallized using dichloromethane and hexane. The product was isolated as a yellow solid (0.0760 mmol, 60.6 mg, 77.10%). ¹H NMR (400 MHz, DMSO-D₆, δ) 8.25 (*d*, *J* = 8 Hz, 1H), 7.13 (*t*, *J* = 7.2 Hz, 2H), 7.90–7.86 (*m*, 2H), 7.84–7.74 (*m*, 5H), 7.55 (*m*, *J* = 4.8 Hz, 2H), 7.48 (*d*, *J* = 4.4 Hz, 2H), 7.23–7.19 (*m*, 1H), 7.14 (*t*, 2H), 6.98–6.96 (*m*, 1H), 6.84–6.79 (*m*, 2H), 6.72–6.66 (*m*, 3H), 6.61 (*d*, *J* = 6.8 Hz, 1H), 6.55 (*d*, *J* = 6.8 Hz, 1H), 3.04 (*s*, 1H), 2.83 (*s*, 3H), 2.80 (*s*, 3H), 1.57–1.50 (*m*, 2H), 0.84 (*t*, *J* = 6.4 Hz, 3H). HRMS (ES⁺) calculated for C₄₂H₄₄IrN₄ (797.3190); found (797.3241).

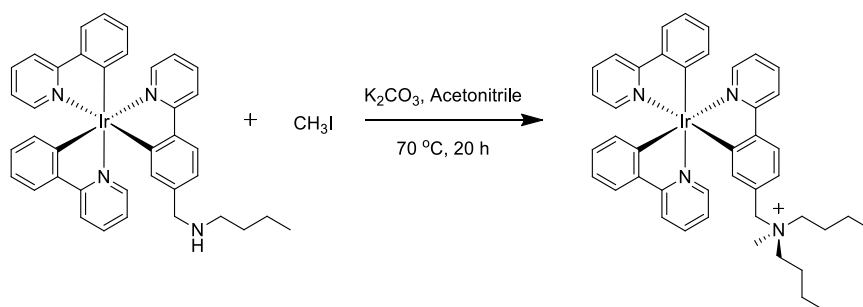
4.3.17 Synthesis of *fac*-[Ir(ppy)₂(ppy-N(CH₃)₂R)], R=C₈H₁₇ (17)



Scheme 17 Synthesis of *fac*-[Ir(ppy)₂(ppy-N(CH₃)₂R)], R=C₈H₁₇ (17).

fac-[Ir(ppy)₂(ppy-NHC₈H₁₇)] (**5**) (0.0754 mmol, 60 mg), methyl iodide (0.2261 mmol, 14 μ L), and potassium carbonate (0.0754 mol, 11 mg) was added in acetonitrile 10 mL. The reaction mixture was heated to reflux under nitrogen for 20 h. The reaction mixture was allowed to cool down and the solvent was completely removed under reduced pressure. The residue was recrystallized using dichloromethane and hexane. The product was isolated as a yellow solid (0.0843 mmol, 69.6 mg, 35.51%). ¹H NMR (400 MHz, DMSO-D₆, δ) 8.25 (*d*, *J* = 8.4 Hz, 1H), 8.14 (*t*, *J* = 8 Hz, 2H), 7.90–7.74 (*m*, 6H), 7.56–7.54 (*m*, 1H), 7.49–7.47 (*m*, 2H), 7.23–7.13 (*m*, 3H), 6.97–6.95 (*m*, 1H), 6.84–6.79 (*m*, 2H), 2.02–1.97 (*m*, 2H), 1.23 (*s*, 10H), 0.85 (*m*, 8H). HRMS (ES⁺) calculated for C₄₄H₄₈IrN₄ (825.3503); found (825.3524).

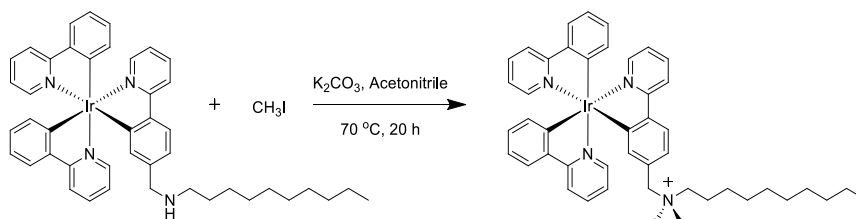
4.3.18 Synthesis of *fac*-[Ir(ppy)₂(ppy-N(CH₃)R₂)], R=C₄H₉ (18)



Scheme 18 Synthesis of *fac*-[Ir(ppy)₂(ppy-N(CH₃)R₂)], R=C₄H₉ (18).

fac-[Ir(ppy)₂(ppy-N(C₄H₉)₂)] (**6**) (0.0565 mmol, 45 mg), methyl iodide (0.1696 mmol, 11 μ L), and potassium carbonate (0.0563 mol, 8 mg) was added in acetonitrile 15 mL. The reaction mixture was heated to reflux under nitrogen for 20 h. The reaction mixture was allowed to cool down and the solvent was completely removed under reduced pressure. The residue was recrystallized using dichloromethane and hexane. The product was isolated as a yellow solid (0.0440 mmol, 35.7 mg, 76.44%). ¹H NMR (400 MHz, DMSO-D₆, δ) 8.14–8.09 (*m*, 3H), 7.80–7.71 (*m*, 6H), 7.47–7.42 (*m*, 3H), 7.13–7.07 (*m*, 3H), 6.83–6.77 (*m*, 3H), 6.69–6.64 (*m*, 4H), 6.60 (*d*, *J* = 1.2 Hz, 1H), 4.80 (*d*, *J* = 5.6 Hz, 1H), 4.20–4.09 (*m*, 2H), 2.02–1.93 (*m*, 1H), 0.97–0.91 (*m*, 1H), 0.85 (*t*, 1H). HRMS (ES⁺) calculated for C₄₃H₄₆IrN₄ (811.3346); found (811.3347).

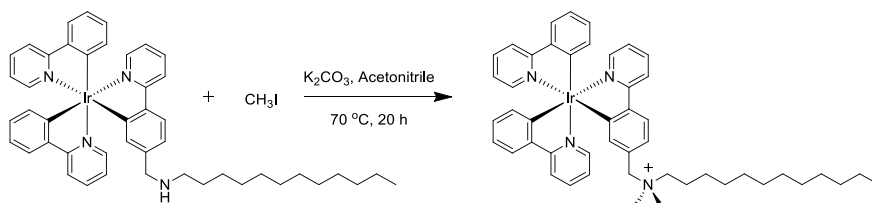
4.3.19 Synthesis of *fac*-[Ir(ppy)₂(ppy-N(CH₃)₂R)], R=C₁₀H₂₁ (19)



Scheme 19 Synthesis of *fac*-[Ir(ppy)₂(ppy-N(CH₃)₂R)], R=C₁₀H₂₁ (19).

fac-[Ir(ppy)₂(ppy-NHC₁₀H₂₁)] (7) (0.0607 mmol, 50 mg), methyl iodide (0.1820 mmol, 12 μ L), and potassium carbonate (0.0607 mol, 8 mg) was added in acetonitrile 15 mL. The reaction mixture was heated to reflux under nitrogen for 20 h. The reaction mixture was allowed to cool down and the solvent was completely removed under reduced pressure. The residue was recrystallized using dichloromethane and hexane. The product was isolated as a yellow solid (0.0305 mmol, 26 mg, 43.01%). ¹H NMR (400 MHz, DMSO-D₆, δ) 8.24 (*d*, *J* = 7.6 Hz, 1H), 8.13 (*t*, *J* = 7.6 Hz, 2H), 7.90–7.74 (*m*, 6H), 7.56 (*d*, *J* = 5.2 Hz, 1H), 7.49–7.47 (*m*, 1H), 7.14 (*t*, *J* = 6.8 Hz, 2H), 6.97 (*d*, *J* = 7.2 Hz, 1H), 6.84–6.79 (*m*, 2H), 6.72–6.62 (*m*, 5H), 6.55 (*d*, *J* = 7.2 Hz, 1H), 5.36–5.31 (*m*, 2H), 4.20–4.07 (*m*, 2H), 2.82 (*d*, *J* = 8 Hz, 4H), 2.02–1.96 (*m*, 5H), 1.69–1.62 (*m*, 7H), 0.87–0.83 (*m*, 14H). HRMS (ES⁺) calculated for C₄₆H₅₂IrN₄ (853.3816); found (853.3843).

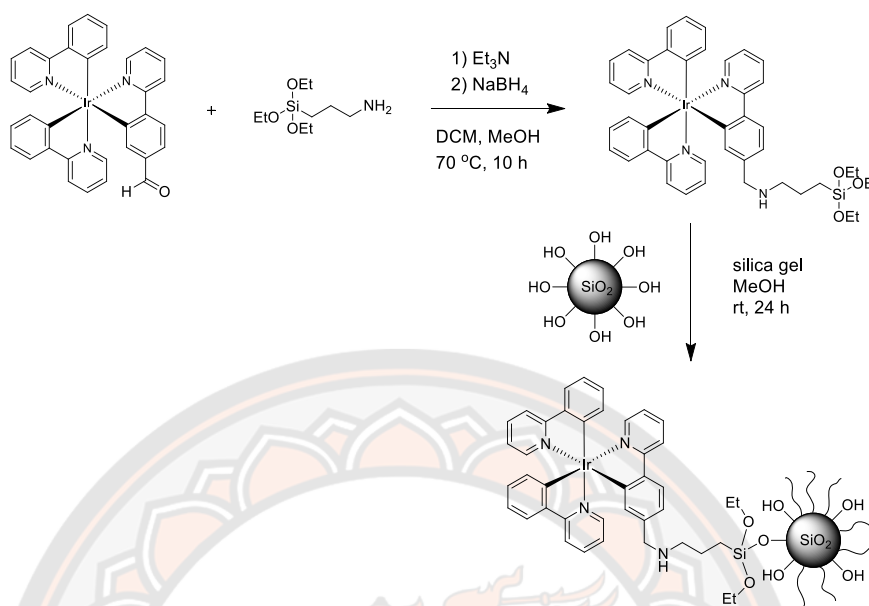
4.3.20 Synthesis of *fac*-[Ir(ppy)₂(ppy-N(CH₃)₂R)], R=C₁₂H₂₅ (20)



Scheme 20 Synthesis of *fac*-[Ir(ppy)₂(ppy-N(CH₃)₂R)], R=C₁₂H₂₅ (20).

fac-[Ir(ppy)₂(ppy-NHC₁₂H₂₅)] (**8**) (0.0586 mmol, 50.0 mg), methyl iodide (0.1759 mmol, 11 μ L), and potassium carbonate (0.0586 mol, 8.1 mg) was added in acetonitrile 15 mL. The reaction mixture was heated to reflux under nitrogen for 20 h. The reaction mixture was allowed to cool down and the solvent was completely removed under reduced pressure. The residue was recrystallized using dichloromethane and hexane. The product was isolated as a yellow solid (0.0556 mmol, 47.4 mg, 95.90%). ¹H NMR (400 MHz, DMSO-D₆, δ) 8.24 (*d*, *J* = 8.4 Hz, 1H), 8.13 (*t*, *J* = 7.6 Hz, 2H), 7.88 (*t*, *J* = 8.4 Hz, 2H), 7.84–7.73 (*m*, 6H), 7.56 (*d*, *J* = 5.6 Hz, 1H), 7.49–7.47 (*m*, 2H), 7.23–7.10 (*m*, 5H), 6.97–6.95 (*m*, 1H), 6.84–6.78 (*m*, 3H), 6.72–6.62 (*m*, 6H), 6.54 (*d*, *J* = 7.6 Hz, 1H), 5.37–5.30 (*m*, 1H), 4.20–4.07 (*m*, 2H), 2.82 (*d*, *J* = 6.4 Hz, 4H), 2.02–1.90 (*m*, 4H), 1.69–1.62 (*m*, 7H), 0.85 (*m*, *J* = 6.4 Hz, 14H). HRMS (ES⁺) calculated for C₄₈H₅₆IrN₄ (881.4129); found (881.4151).

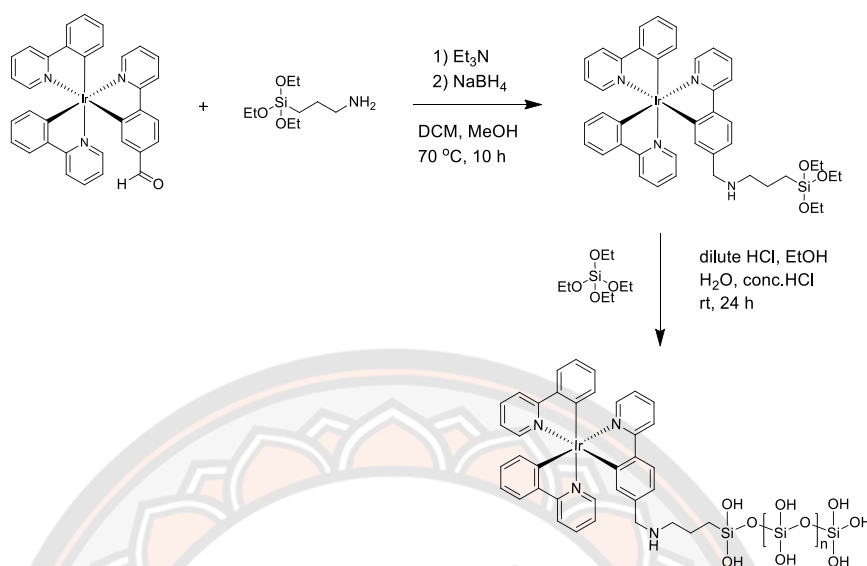
4.3.21 Synthesis of Ir-SiO₂ (21)



Scheme 21 Synthesis of [Ir(ppy)₂(ppy-SiO₂)] (21).

[Ir(ppy)₂(ppy-SiO₂)] (21) has been synthesized in two steps. Firstly, *fac*-[Ir(ppy)₂(fppy)] (**2**) (0.0732 mmol, 50.0 mg), 3-aminopropyltriethoxysilane (0.1464 mmol, 32.4 mg), and triethylamine (0.0732 mmol, 7.4 mg) were suspended in methanol:dichloromethane 1:1 mixture (8:8 mL). The reaction mixture was then refluxed under nitrogen atmosphere for 10 h. The solution was left to cool to room temperature, and NaBH_4 (0.1464 mmol, 5.5 mg) was added. The reaction mixture was stirred at room temperature for 20 h. The solution was removed under vacuum. Finally, the crude was dissolved in methanol. Silica gel (214.7 g) was added in the solution. The reaction mixture was stirred under nitrogen atmosphere for 24 h at room temperature. The solution was filtered through filter paper. Rinse the Ir-SiO₂ with a small amount of methanol 2-3 times for reduce impurity and dried at room temperature.

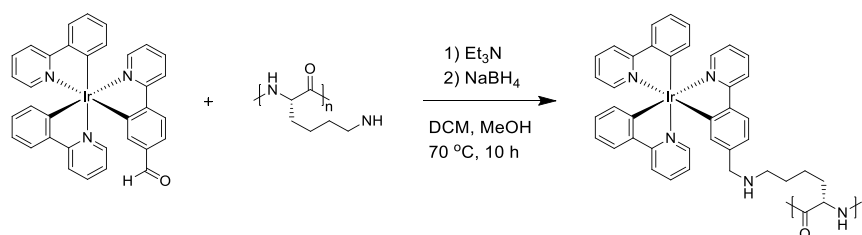
4.3.22 Synthesis of Ir-TEOS (22)



Scheme 22 Synthesis of [Ir(ppy)₂(ppy-TEOS)] (22).

[Ir(ppy)₂(ppy-TEOS)] (22) have been synthesized in two steps. Firstly, *fac*-[Ir(ppy)₂(fppy)] (2) (0.0732 mmol, 50.0 mg), 3-aminopropyltriethoxysilane (0.1464 mmol, 32.4 mg), and triethylamine (0.0732 mmol, 7.4 mg) were suspended in methanol:dichloromethane 1:1 mixture (8:8 mL). The reaction mixture was then refluxed under nitrogen atmosphere for 10 h. The solution was left to cool to room temperature, and NaBH₄ (0.1464 mmol, 5.5 mg) was added. The reaction mixture was stirred at room temperature for 20 h. The solution was removed under vacuum. Finally, the crude was dissolved in water (10 mL). Tetraethylorthosilicate (TEOS) (500 μL), dilute hydrochloric acid (500 μL), ethanol (500 μL) were added in the solution mixture and then added conc. HCl 5 drops in the solution. The reaction mixture was stirred under nitrogen atmosphere for 24 h at room temperature. The solution was filtered through vacuum pump and washed with ethanol. Ir-TEOS was taken to dryness at room temperature.

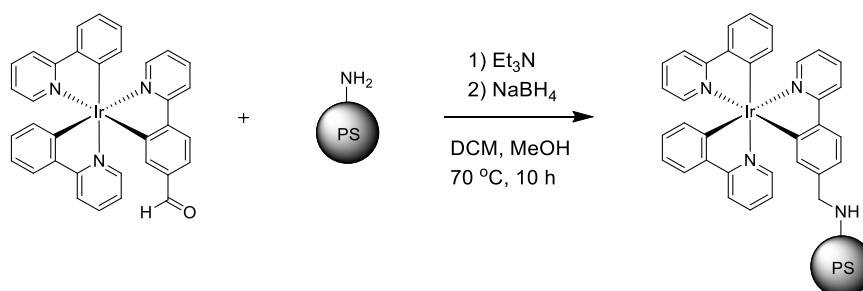
4.3.23 Synthesis of Ir-poly-L-lysine (23)



Scheme 23 Synthesis of [Ir(ppy)₂(ppy-poly-L-lysine)] (23).

The poly-L-lysine coated glass slides was broken up into small pieces (2.1428 g) and suspended in methanol:dichloromethane 1:1 mixture (12:12 mL) in round bottom flask. *fac*-[Ir(ppy)₂(fppy)] (2) (0.0811 mmol, 0.0554 g), and triethylamine (0.0811 mmol, 8.2 mg) were added in the solution. The reaction mixture was then refluxed under nitrogen atmosphere for 10 h. The solution was left to cool to room temperature, and NaBH₄ (0.1622 mmol, 6.1 mg) was added. The reaction mixture was stirred at room temperature for 20 h. The solution was filtered through filter paper. Rinse the Ir-poly-L-lysine glasses with a small amount of dichloromethane 2-3 times for reduce impurity and the slides are dried at room temperature.

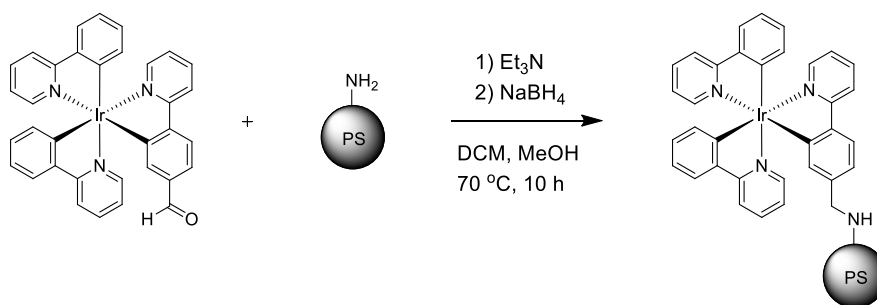
4.3.24 Synthesis of Ir-polystyrene powder (24)



Scheme 24 Synthesis of [Ir(ppy)₂(ppy-polystyrene)] powder (24).

fac-[Ir(ppy)₂(fppy)] (2) (0.0732 mmol, 50.0 mg) and (Aminoethyl)polystyrene (0.0366 mmol, 24.4 mg) were added in the solution. The reaction mixture was stirred (high speed) and then refluxed under nitrogen atmosphere for 10 h. The solution was left to cool to room temperature, and NaBH₄ (0.0146 mmol, 5.5 mg) was added. The reaction mixture was stirred at room temperature for 20 h. The solvent was removed under reduce pressure and the residue was dissolved in dichloromethane (20 mL). The dichloromethane solution was washed with water (2 × 15 mL) and filtered solid product from organic layer. Ir-polystyrene was taken to dryness at room temperature. The result of product observed solid powder because high rotational speed to break beads of polystyrene.

4.3.25 Synthesis of Ir-polystyrene beads (25)



Scheme 25 Synthesis of [Ir(ppy)₂(ppy-polystyrene)] beads (25).

fac-[Ir(ppy)₂(fppy)] (2) (0.0439 mmol, 30.0 mg) and (Aminoethyl) polystyrene (0.0219 mmol, 14.6 mg) were added in the solution. The reaction mixture was stirred (low speed) and then refluxed under nitrogen atmosphere for 10 h. The solution was left to cool to room temperature, and NaBH₄ (0.0439 mmol, 1.6 mg) was added. The reaction mixture was stirred at room temperature for 20 h. The solvent was removed under reduce pressure and the residue was dissolved in dichloromethane (20 mL). The dichloromethane solution was washed with water (2 × 15 mL) and filtered solid product from organic layer. Ir-polystyrene was taken to dryness at room temperature. The result of product observed solid beads of Ir-polystyrene.

4.4 Study of the fundamental photophysical (UV-Vis, Fluorescence, Lifetime, DLS) properties of synthesized iridium complexes

Stock solutions (0.5 mM) were prepared by weighing a calculated amount of the sample and dissolving it in DMSO (1-3 mL). The stock solution was then diluted with the chosen solvent to a final concentration of 10 μ M (toluene, tetrahydrofuran (THF), methanol (MeOH), and acetonitrile (ACN)). Samples for DLS measurements were prepared with solvents that were filtered before the dilution step. UV-Vis, fluorescence, lifetime and DLS measurements were carried out with these dilute solutions.

4.5 Investigation of the relationship between the structure of the luminescent iridium complexes and their propensity to aggregate in aqueous solution

Stock solutions (0.5 mM) were prepared by weighing a calculated amount of the sample and dissolving it in DMSO (1-3 mL). The stock solution was then diluted with either water or buffer (PBS, pH 7.4) to a final concentration of 10 μ M. Fluorescence, lifetime and DLS measurements were carried out with these dilute solutions.

4.6 Investigation of the possibility to use the synthesized iridium complexes as cellular probes in fluorescence microscopy

4.6.1 Cell culture

Mouse skin fibroblast (NIH-3T3) and human breast cancer (MCF7) cell lines were maintained in exponential growth in Dulbecco's Modified Eagle Medium (DMEM) supplemented with 10% foetal bovine serum in 75 cm³ cell culture flasks with no prior surface treatment. The cultures were incubated in average humidity, 5% CO₂ at 37 °C. Cells were harvested by treatment with 0.25% trypsin solution at 37 °C for 5 minutes. Cell suspensions were pelleted by centrifugation at 1000 rpm and re-suspended by repeated aspiration with a sterile plastic pipette in fresh media.

1) Preparation for microscopy

Cells for microscopy were seeded into 24-well plates on 13 mm 0.17 mm thick glass coverslips and allowed to reach 50-60% confluence in 5% CO₂ at 37 °C at which stage the medium was changed to DMEM without phenol red (referred to as LCM). These cells were then dosed with the appropriate amount of stock solution of the complexes to give the desired final loading concentration in the LCM and incubated over a desired loading time at 5% CO₂ at 37 °C. A co-stain of either LTR or propidium iodide was added in the last 30 min of this loading time at final concentrations of 75 nM and 15 nM respectively in LCM. After the incubation period the coverslips were washed with PBS and mounted onto a glass slide, and sealed with clear nail polish to prevent drying out of the sample.

2) Toxicity measurements

Cells were seeded in 6-well plates and allowed to reach 80-90% confluence at normal humidity, 5% CO₂ at 37 °C at which stage the cells were counted assuming the media was replaced such that samples with final loading concentrations of 0.5, 1, 2, 5, 10, 25 and 50 µM, plus a control, were made up for complexes **15**. The cells were then incubated for the appropriate loading time at 37 °C, and then harvested with 0.25% trypsin solution. Toxicity was then measured using a ChemoMetec A/S NucleoCounter3000-Flexicyte instrument using Vial-cassette cell viability cartridges (using DAPI to identify non-viable cells, and Acridine Orange for cell detection).

Proliferation of cells is a process resulting in an increase in live cell numbers due to division and growth of cells. As a result, the recorded %viability is an overestimate requiring correction. This was achieved by first determining the theoretical maximum number of cells in a sample but multiplying the controlled % viability by live cell number. A correction factor for the viability recorded at each concentration was then calculated by dividing the recorded live cell number by the theoretical maximum. The recorded %viability was then corrected for by multiplication with the correction factor.

Dose response curves were generated by plotting the logarithm of analyte concentration against cell viability, and then fitting this data to a function modelled by a four parameters sigmoidal function of the form **equation (6)**:

$$\% Viability = A + \frac{B}{1 + e^{\left(\frac{C - \log[Analyte]}{D}\right)}} \quad (6)$$

where A, B, C and D are parameters to be found and optimized to best fit the data. Parameters unique to variable analytes and incubation times were determined using the Matlab Curve Fitting application. IC₅₀ values were extrapolated using a logarithmic function as opposed to a linear one (outlined in **Figure 63**) due to a more even spread of across the series such that the shape of the curve was better defined and hence, a better quality of fit could be achieved.

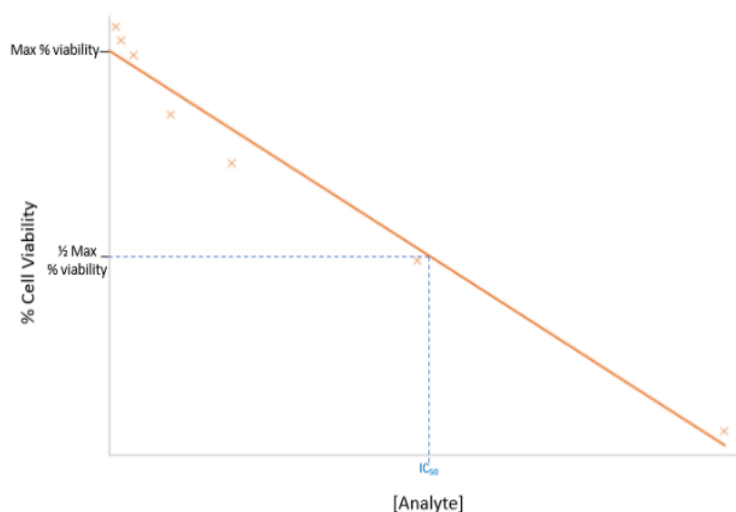


Figure 63 IC₅₀ determination using linear regression.

3) ICP-MS

Cells were seeded in 6-plate wells and allowed to reach 80-90% confluence in normal humidity, 5% CO₂ at 37 °C, at which point the media was changed such that it contained the desired final loading concentration of complexes **15**. Cells were incubated for the appropriate amount of time at 37 °C, after which the total intracellular Ir concentration was determined by ICP-MS.

4.6.2 Live cell imaging

Microscopy images were obtained using laser scanning confocal microscopy (LSCM) with Leica SP5 II LSCM confocal microscope with a HCX APO x63/1.4 NA Lambda-Blue objective. The instrument was enhanced with PhMoNa to improve resolution.

1) Brightness analysis

The brightness of the compounds *in cellulo* was determined relative to a control sample image of an untreated cell; this was necessary to account for cellular autofluorescence. Images of cells incubated with compounds with incubation times of 24 h was obtained, keeping the laser power consistent throughout acquisition. Using the image processing software ImageJ, 5 sample areas of about 25 μm² of a cell in each experiment (**Figure 64**), plus a control, were then selected and the mean grey value of each area was determined. These values were averaged. As the localisation profile of the compounds *in cellulo* was determined to be lysosomal, the sample areas were selected such that at least 70% of it contained lysosomes. The average mean grey value of the control sample was treated as 100% relative brightness and hence, the % brightness of subsequent experiments was determined relative to this.

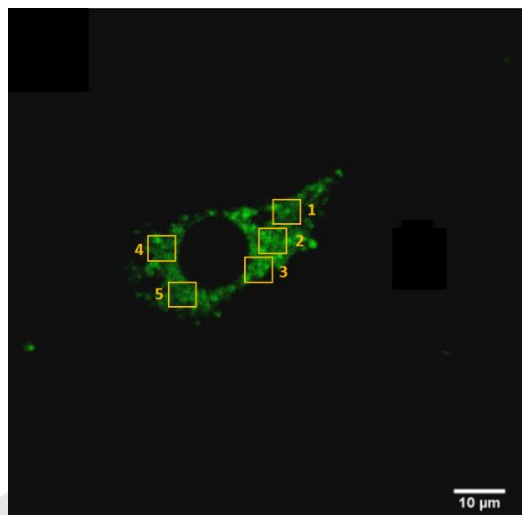


Figure 64 Selected sample areas of cell incubated with luminescent Ir(III) compound for determination of mean grey values.

4.7 Investigation of the possibility to utilize the synthesized iridium complexes as catalysts for photoredox reactions

4.7.1 α -Arylation of amines

4-(1-(ethyl(phenyl)amino)ethyl)benzonitrile: An oven-dried schlenk tube with sleeve stopper septa was charged with the photocatalyst of tris-cyclometalated iridium(III) complexes (4 mg, 5.0 μmol , 0.005 equiv.), 1,4-dicyanobenzene (150 mg, 1.17 mmol, 1.00 equiv.), sodium acetate (192 mg, 2.34 mmol, 2.0 equiv.), *N,N*-diethylaniline (457 μL , 3.51 mmol, 3.0 equiv.) and 4.0 mL of DMA were added in the reaction. The schlenk tube of reaction mixture was then degassed via three cycles of vacuum evacuation with freeze-pump-thaw (15 min), backfilled with nitrogen (via nitrogen balloon), and warmed to room temperature. After the reaction was thoroughly degassed, the schlenk tube was sealed with parafilm and placed approximately 1 cm from a 7W LED daylight lamp. After 24 h, the reaction mixture was diluted with ethyl acetate and added to a separated funnel containing 20 mL of a saturated aqueous solution of Na_2CO_3 . The layers were separate and the aqueous layer was extracted with EtOAc (3 x 10 mL). The combined organic extracts were washed with brine, dried (MgSO_4) and concentrated with rotary evaporation. The residue of product was characterized by ^1H -NMR spectroscopy using indicated the desired alpha-arylation of amine product.

4.7.2 Direct β -arylation of ketones

4-(3-Oxocyclohexyl)benzonitrile: An oven-dried schlenk tube with sleeve stopper septa was charged with the photocatalyst of tris-cyclometalated iridium(III) complexes (5 mg, 7.8 μ mol, 0.01 equiv.), terephthalonitrile (150 mg, 0.78 mmol, 1.00 equiv.), 438 mg of DABCO (3.90 mmol, 5.00 equiv.), 26.67 μ L of azepane (0.156 mmol, 0.20 equiv.), 403.78 μ L of cyclohexanone (3.90 mmol, 5.00 equiv.), 282 μ L of water (15.60 mmol, 20.00 equiv.), 9 μ L of acetic acid (0.156 mmol, 0.20 equiv.) and 2.0 mL of DMPU were added in the reaction. The schlenk tube of reaction mixture was then degassed via three cycles of vacuum evacuation with freeze-pump-thaw (5 min), backfill with nitrogen (via nitrogen balloon), and warmed to room temperature. After the reaction was thoroughly degassed, the schlenk tube was sealed with parafilm and placed approximately 1 cm from a 7W LED daylight lamp. After 24 h, the reaction mixture was diluted with ethyl acetate and added to a separatory funnel containing 20 mL of a saturated aqueous solution of NaCl. The layers were separated and the aqueous layer was extracted with EtOAc (3 x 10 mL). The combined organic extracts were dried over MgSO₄ and concentrated with rotary evaporation. The residue of product was characterized by ¹H-NMR spectroscopy using indicated the desired β -arylated ketone product.

4.7.3 Direct allylic C-H arylation

1',2',3',4'-Tetrahydro-[1,1'-biphenyl]-4-carbonitrile: An oven-dried schlenk tube with sleeve stopper septa was charged with the photocatalyst of tris-cyclometalated iridium(III) complexes (5 mg, 7.8 μ mol, 0.01 equiv.), terephthalonitrile (100 mg, 0.78 mmol, 1.00 equiv.), potassium carbonate (5 mg, 0.039 mmol, 0.05 equiv.), cyclohexene (395 μ L, 3.90 mmol, 5 equiv.), triisopropylsilanethiol (9 μ L, 0.039 mmol, 0.05 equiv.) and acetone 7.5 mL were added. The schlenk tube of reaction mixture was then degassed via three cycles of vacuum evacuation with freeze-pump-thaw (5 min), backfill with nitrogen (via nitrogen balloon), and warmed to room temperature. After the reaction was thoroughly degassed, the schlenk tube was sealed with parafilm and placed approximately 1 cm from a 7W LED daylight lamp. After 24 h, the reaction mixture was then concentrated with rotary evaporation. The residue of product was characterized by ¹H-NMR spectroscopy using indicated the desired the allylic arylation product.

4.7.4 Difluoromethylation

1-(Difluoromethoxy)-4-nitrobenzene: An oven-dried schlenk tube with sleeve stopper septa was charged with the photocatalyst of tris-cyclometalated iridium(III) complexes (5 mg, 7.8 μmol , 0.01 equiv.), nitrophenol (100 mg, 0.72 mmol, 1 equiv.), difluorobromoacetic acid (125.7 mg, 0.72 mmol, 1 equiv.), Cs_2CO_3 (468.4 mg, 1.44 mmol, 2 equiv.) and DMF 4 mL were added in the reaction. The schlenk tube of reaction mixture was then degassed via three cycles of vacuum evacuation with freeze-pump-thaw (5 min), backfill with nitrogen (via nitrogen balloon), and warmed to room temperature. After the reaction was thoroughly degassed, the schlenk tube was sealed with parafilm and placed approximately 1 cm from a 7W LED daylight lamp. After 24 h, 5 mL of 1M HCl was added to the tube, and the aqueous solution was extracted twice by ethyl acetate (2 x 10 mL). The combined organic phase was washed with saturated brine twice (2 x 5 mL), dried over anhydrous Na_2SO_4 , then filtered and concentrated with rotary evaporation. The residue of product was characterized by ^1H -NMR spectroscopy using indicated the desired difluoromethylation product.

CHAPTER V

AMINOALKYL TRIS-CYCLOMETALATED IRIIDIUM COMPLEXES

5.1 Introduction

Tris-cyclometalated iridium complexes are interesting photoactive compounds finding applications in various fields (e.g. imaging OLED, etc.). The work reported herein has been inspired by the previous results from our group [42], which reported the synthesis, stability studies, and photophysical properties of these compounds. Furthermore, the work investigated the compounds as potential cellular imaging probes. The two complexes are derivatives of *fac*-[Ir(ppy)₃] bearing aminoalkyl groups on one of the phenylpyridine rings (**Figure 65**). These compounds have initially been synthesized as parts of efforts in our group to develop responsive luminescent iridium complexes. These have been based on monocationic bis-cyclometalated and neutral tris-cyclometalated structures. The two tris-cyclometalated complexes shown in **Figure 65** were derived from two different amines, namely butyl amine (C₄) and dodecyl amine (C₁₂). The complexes were synthesized by using Noanoyama reaction followed with reductive amination of the aldehyde to the final aminoalkyl side chain. The interesting luminescent properties of these complexes include structured emission bands in aqueous media, which depended on the length of the alkyl chain. Their efficient emission properties in aqueous media have also prompted us to investigate these complexes as potential luminescent probes for cellular imaging. The interesting results obtained with these complexes in terms of both photoluminescent properties and cellular imaging lead us to synthesize further derivatives described herein. The aim of this work was to systematically investigate the effect of structure of the complexes on photophysical properties in aqueous media, which were believed to be related to aggregation, and to study these compounds as potential cell imaging agents given the relative scarcity of tris-cyclometalated iridium(III) complexes used for this purpose. For this work was to lay ground for the potential future development of new responsive probes and cell imaging agents.

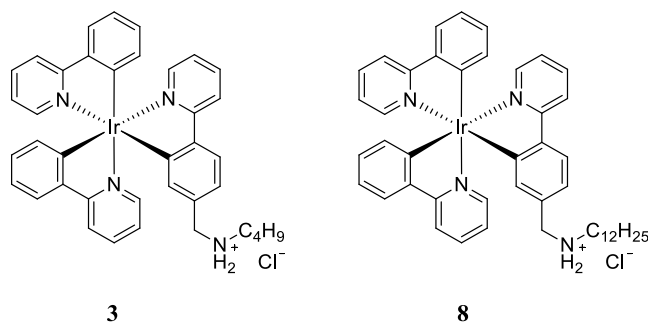
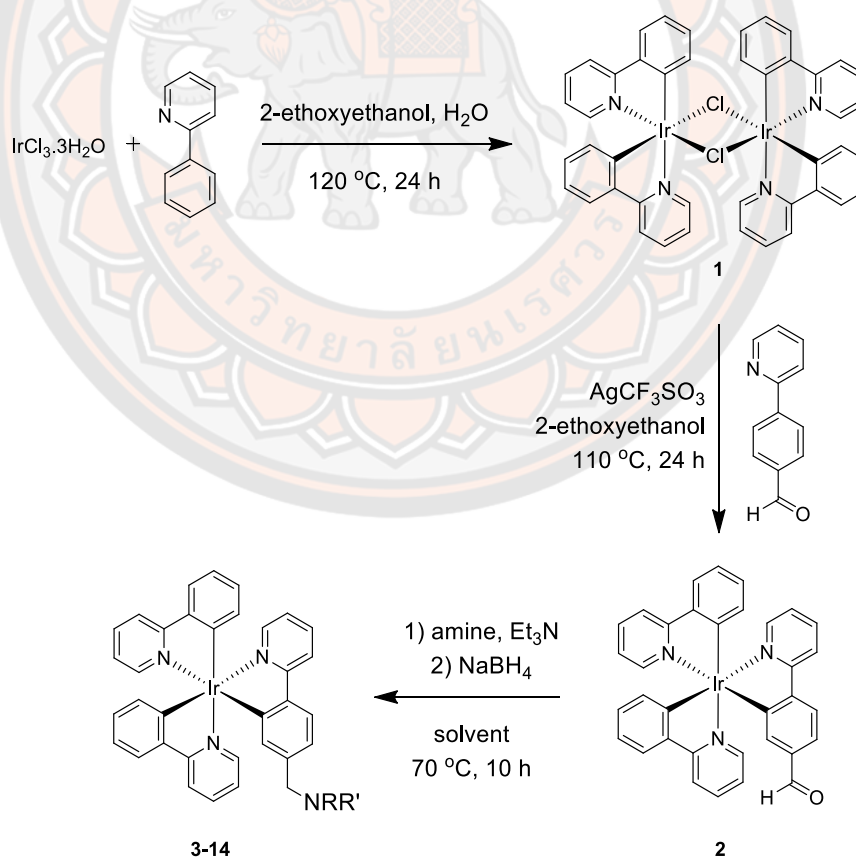


Figure 65 Structures of Iridium complexes 3 and 8.

5.2 Results and discussion

For the purpose of this study 12 of iridium complexes containing various alkyl chains have been synthesized. The first group of complexes (**3** to **8**) contains simple alkyl chains from four to twelve carbon atoms long, while the second group of complexes (**9** to **14**) contains those where the alkyl chain is terminated with a hydroxy group (**Table 5**).



Scheme 26 The synthesis procedure of aminol alkyl iridium(III) complexes.

Table 5 List of symbols **R**, **R'**

Complex	R	R'
3	C ₄ H ₉	H
4	C ₆ H ₁₃	H
5	C ₈ H ₁₇	H
6	C ₄ H ₉	C ₄ H ₉
7	C ₁₀ H ₂₁	H
8	C ₁₂ H ₂₅	H
9	CH ₂ CH ₂ OH	H
10	CH ₂ CH ₂ CH ₂ OH	H
11	CH ₂ CH ₂ CH ₂ CH ₂ OH	H
12	CH ₂ CH ₂ CH ₂ CH ₂ CH ₂ CH ₂ OH	H
13	CH ₂ CH ₂ OCH ₂ CH ₂ OH	H
14	CH ₂ CH ₂ OH	CH ₂ CH ₂ OH

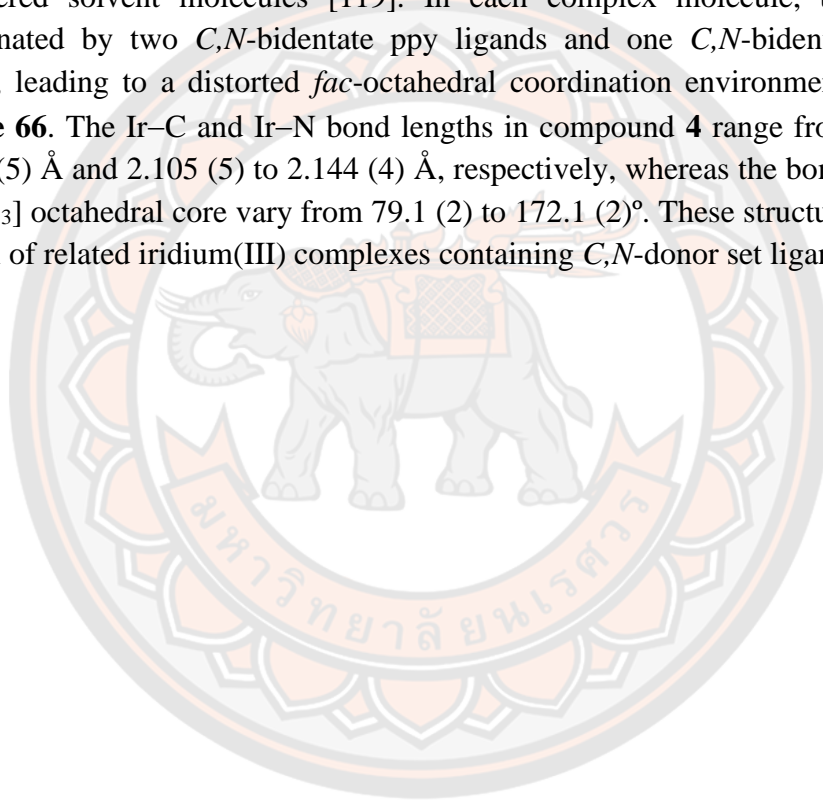
Iridium(III) complexes (**3-14**) have been synthesized in three steps. Firstly, iridium chloride bridged dimer was made in a reaction of iridium chloride and 2-phenylpyridine (**Scheme 26**). This was then converted into the key intermediate *fac*-[Ir(ppy)₂(fppy)] (**2**) (fppy:4-(pyridine-2-yl)benzaldehyde) in a reaction with 4-(pyridine-2-yl)benzaldehyde). Finally, all aminoalkyl complexes were made in a reductive amination step where *fac*-[Ir(ppy)₂fppy] was combined with an appropriate amine. All of the complexes were purified by column chromatography followed by their recrystallization from a mixture of dichloromethane and hexane. The complexes were characterized by ¹H-, ¹³C-NMR, and HRMS (ES)⁺. In some cases the complexes were isolated as the hydrochloride salts rather than the expected free amines. The isolation of the hydrochloride salts was not deliberate and is ascribed to the formation of HCl from impurities in the dichloromethane used in chromatographic purification.

5.3 Crystal structures

Structural description of *fac*-[Ir(ppy)₂(Hppy-NC₆)]Cl

Crystals suitable for the single crystal X-ray diffraction analysis were grown by slow diffusion of hexane into the solution of complex **4** (hexyl chain) in acetone for complex **4**. The X-ray structure analysis at 298 K reveals that complex **4** crystallizes in the monoclinic system with space group $P2_1/c$ (**Figure S53**). The asymmetric unit consists of two [Ir(ppy)₂(Hppy-NC₆)]⁺ cations and two Cl⁻ anions (**Figure 67**).

As shown in **Figure 66**, the crystallographically independent unit contains the asymmetric unit of two *fac*-[Ir(ppy)₂(Hppy-NC₆)]⁺ cations, two Cl⁻ anions and disordered solvent molecules [119]. In each complex molecule, the Ir³⁺ ion is coordinated by two *C,N*-bidentate ppy ligands and one *C,N*-bidentate Hppy-NC₆ ligand, leading to a distorted *fac*-octahedral coordination environment as shown in **Figure 66**. The Ir–C and Ir–N bond lengths in compound **4** range from 2.010 (6) to 2.036 (5) Å and 2.105 (5) to 2.144 (4) Å, respectively, whereas the bond angles in the [IrN₃C₃] octahedral core vary from 79.1 (2) to 172.1 (2)°. These structural features are typical of related iridium(III) complexes containing *C,N*-donor set ligands [122].



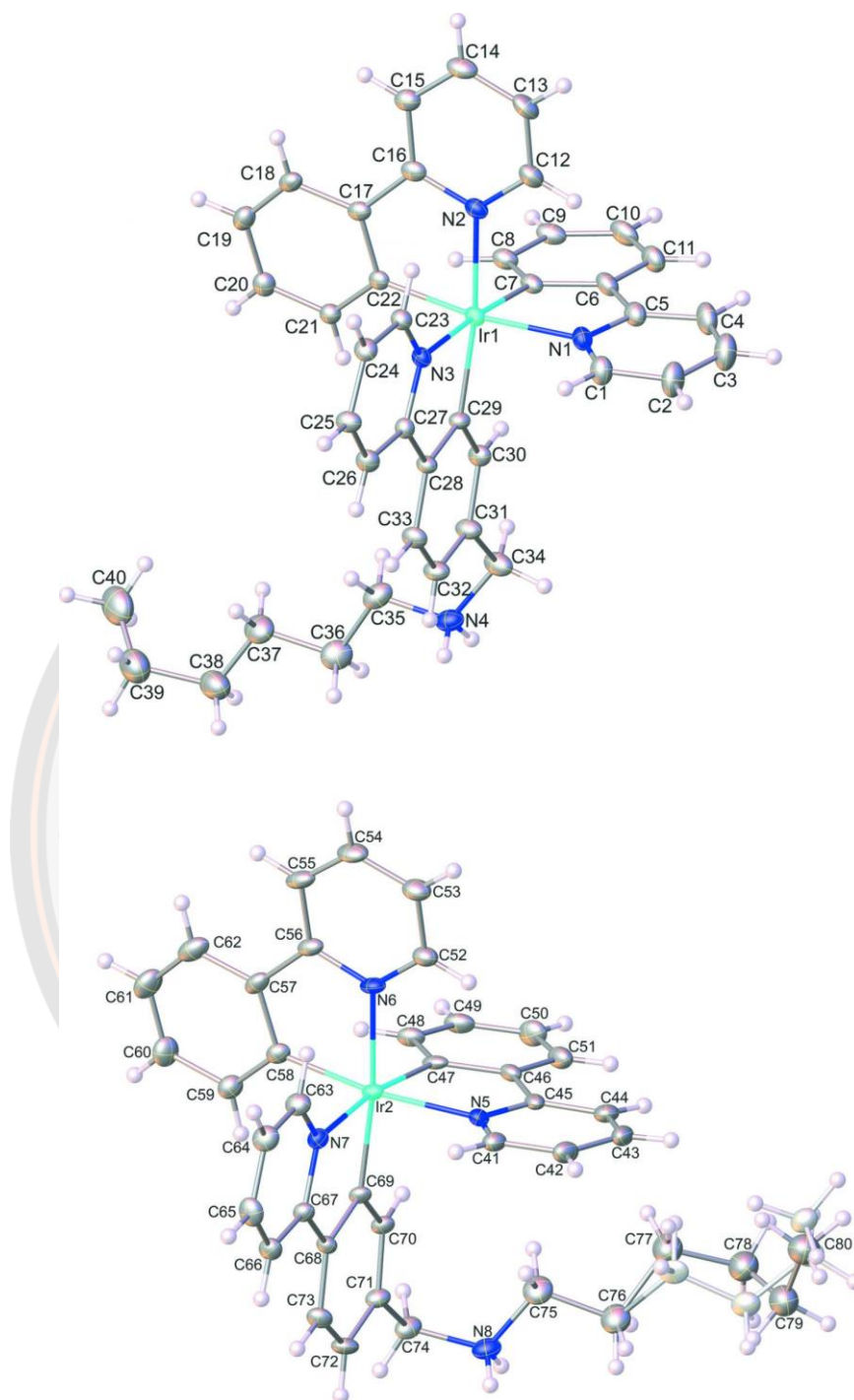


Figure 66 A view of the molecular structures of the two independent cationic molecules of the complex 4, with the atom labelling. Displacement ellipsoids are drawn at the 35% probability level. Symmetry codes: (i) $x + 1, -y + \frac{1}{2}, z + \frac{1}{2}$; (ii) $-x + 2, -y + 1, -z + 1$; (iii) $x, -y + \frac{1}{2}, z - \frac{3}{2}$.

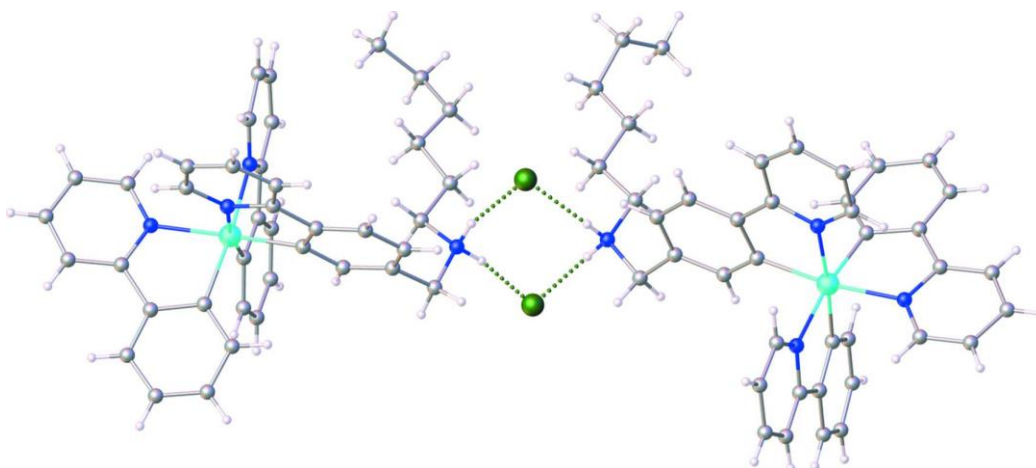


Figure 67 A perspective view of the complex 4, showing the intermolecular N–H...Cl hydrogen bonds (dotted lines) between the two independent molecules.

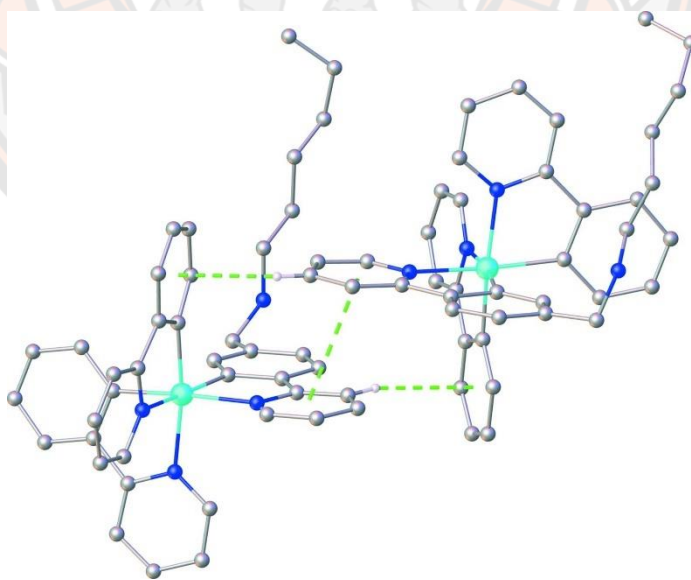
In the crystal, pairs of cationic $[\text{Ir}(\text{ppy})_2(\text{Hppy-NC}_6)]^+$ complex molecules are linked through N–H...Cl hydrogen bonds (**Table 6**) between the amino groups of the ppy-NC₆ ligands and chloride anions (**Figure 67**) with an Ir...Ir separation of 15.8207 (7) Å. Simultaneously, pairs of cationic complexes with an Ir...Ir separation of 8.5468 (4) Å (**Figure 68**) also interact with each other *via* a parallel fourfold phenyl embrace[123], which contains one π – π stacking [centroid-to-centroid distance between the N3/C23–27 and N7/C63–C67 rings = 3.682 (3) Å; dihedral angle = 6.5 (5) °] and two edge-to-face (phenyl)–C–H... π (phenyl) interactions (H26...Cg5 = 2.79 Å and H65...Cg3 = 2.85 Å; Cg5 and Cg3 are the centroids of the C57–C62 and C17–C22 rings, respectively). Numerous weak (phenyl)–C–H... π (phenyl) and (methylene)–C–H... π (phenyl) are observed with H...centroid distance ranging from 2.79 to 3.12 Å (**Table 6**).

Table 6 Hydrogen-bond geometry (Å, °).

*Cg*1–*Cg*6 are the centroids of the C6–C11, N2/C12–C16, C17–C22, C46–C51, C57–C62, C68–C73 rings, respectively.

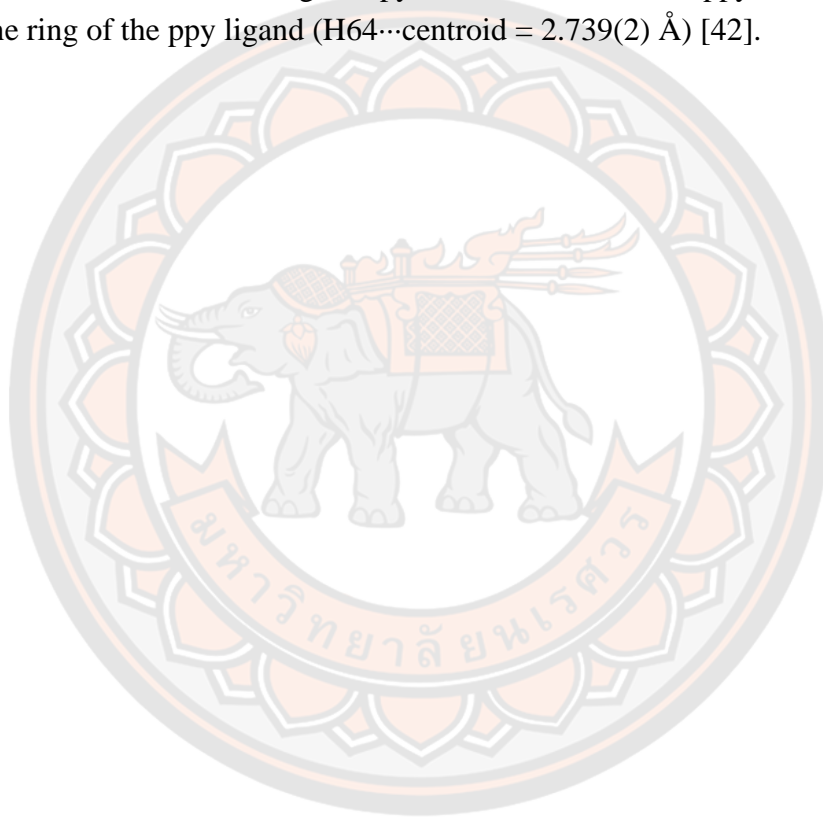
<i>D</i> – <i>H</i> ... <i>A</i>	<i>D</i> – <i>H</i>	<i>H</i> ... <i>A</i>	<i>D</i> ... <i>A</i>	<i>D</i> – <i>H</i> ... <i>A</i>
N4–H4 <i>A</i> ...C12 ⁱ	0.89	2.30	3.172 (6)	168
N4–H4 <i>B</i> ...C11 ⁱ	0.89	2.26	3.142 (6)	172
N8–H8 <i>A</i> ...C12	0.89	2.21	3.073 (6)	165
N8–H8 <i>A</i> ...C11	0.89	2.16	3.044 (6)	171
C20–H20... <i>Cg</i> 1 ⁱ	0.93	3.12	3.497 (7)	145
C24–H24... <i>Cg</i> 4 ⁱⁱⁱ	0.93	2.89	3.532 (7)	139
C26–H26... <i>Cg</i> 5	0.93	2.79	3.645 (7)	158
C34–H34 <i>B</i> ... <i>Cg</i> 3 ⁱⁱ	0.97	2.91	3.422 (7)	160
C37–H37... <i>Cg</i> 1 ⁱⁱ	0.97	3.01	3.818 (7)	141
C49–H49... <i>Cg</i> 2 ⁱⁱⁱ	0.93	3.07	3.705 (7)	145
C53–H53... <i>Cg</i> 6 ⁱⁱⁱ	0.93	3.10	3.692 (7)	135
C65–H65... <i>Cg</i> 3	0.93	2.86	3.530 (7)	135

Symmetry codes: (i) $x + 1, -y + \frac{1}{2}, z + \frac{1}{2}$; (ii) $-x + 2, -y + 1, -z + 1$; (iii) $x, -y + \frac{1}{2}, z - \frac{3}{2}$.

**Figure 68** A perspective view showing the parallel fourfold phenyl embrace in the complex 4.

In addition, a comparison of the effect of the alkyl chain length between the ppy-NC₆ in complex **4** and the related complex with ppy-NC₄ [42] on the packing arrangement suggests that the key intermolecular interactions (N–H...Cl, C–H... π and π – π) remain the same.

Complex **3** crystallized in the monoclinic space group $P2_1/c$ with two [Ir(ppy)₂ppy-NC₄] \cdot H⁺ cations, two Cl[–] anions and disordered solvent molecules in the symmetric unit (**Figure S54**). These pairs are further linked to the neighboring pairs of molecules *via* π – π stacking interactions between the pyridine rings of the ppy-NC₄ ligands (centroid to centroid distance = 3.644(3) Å; dihedral angle = 1.25(19) °) and C–H... π interactions involving the pyridine H atom of the ppy-NC₄ ligand and the benzene ring of the ppy ligand (H64...centroid = 2.739(2) Å) [42].



5.4 Photophysical properties in organic solvents

All measurements were performed at room temperature, in organic solution (concentration 10 μM).

5.4.1 UV-vis spectra of complexes 3-14

All of the aminoalkyl iridium(III) complexes (**3** to **14**) exhibit similar absorption spectra in dilute dichloromethane solution. The absorption spectrum of complex **4**, recorded in dichloromethane and shown in **Figure 69** as a representative of these compounds, exhibits features of cyclometalated iridium(III) complexes. The peaks between 250 nm and 320 nm are assigned to ligand centered $\pi\text{-}\pi^*$ transitions. The broad bands observed between 320 nm and 430 nm, on the other hand, can be assigned to spin-allowed metal to ligand charge transfer ($^1\text{MLCT}$) transitions. Finally, the tails of these bands extending beyond 500 nm are associated with spin forbidden metal to ligand charge transfer ($^3\text{MLCT}$) transitions. These features and the slight differences between the complexes are consistent with previous reports [44].

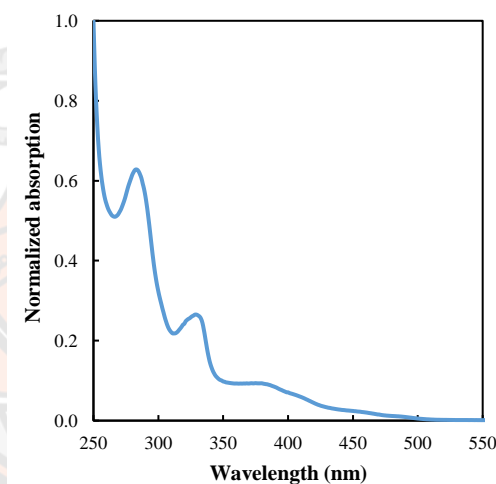


Figure 69 Normalized absorption spectrum of complex **4** (10 μM) recorded in dichloromethane.

5.4.2 Photoluminescence

The emission spectra for complexes **3** to **14** were also very similar as can be seen in **Figure 70** and **Figure 71**. **Figure 70** shows the emission spectrum of complex **4** (10 μ M) recorded in dichloromethane with excitation at 390 nm, as a representative example, while **Figure 71** shows the overlay of emission spectra of complexes **2** to **14** recorded under the same conditions. The photophysical data of these complexes from this experiment are summarized in **Table 7**. The spectrum of complex **4** exhibits a maximum at 517 nm. The emission maxima for the other complexes were in the range 514 to 522 nm, while complex **2** has its emission maximum at 602 nm. The closely matching maxima for complexes **3** to **14** indicate limited influence of the aminoalkyl side chain on the photophysical properties of these complexes. In fact, the position of the emission maximum of the unsubstituted parent complex *fac*-[Ir(ppy)₃] is also very similar to the position of the emission maxima for these complexes. The significantly shifted emission maximum for complex **2** has previously been rationalized by the involvement of the formyl group in its excited states [44]. **Table 7** also shows photoluminescence quantum yields for selected complexes (**2**, **3**, **8**, **9** and **14**). It can be seen that, with the exception of complexes **2**, the complexes have quantum yields values between 34 and 44%, which is in line with the value reported for the parent unsubstituted complex.

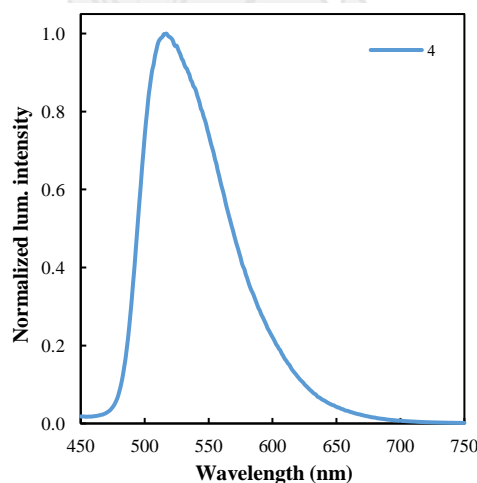


Figure 70 Normalized luminescence intensity of complex *fac*-[Ir(ppy)₂(ppy-NC₆)] (**4**) (10 μ M) measured in dichloromethane. Emission spectra were recorded with λ_{ex} = 390 nm at room temperature.

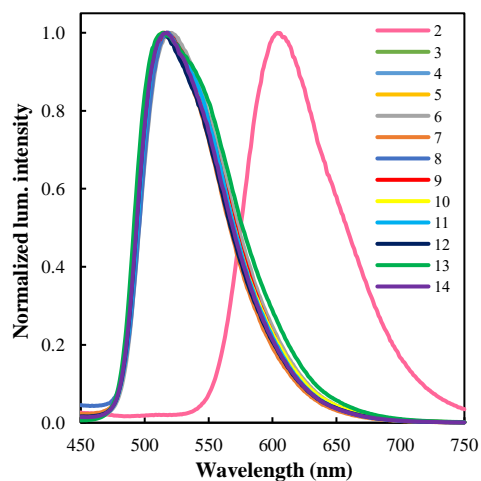


Figure 71 Normalized luminescence intensity of complex 2 to 14 (10 μ M) measured in dichloromethane. Emission spectra were recorded with $\lambda_{\text{ex}} = 390$ nm at room temperature.

Table 7 Selected photophysical data in dichloromethane for complexes 2 to 14.

Complex	λ_{em} (nm)	ϕ_{lum}
2	604	0.03
3	522	0.38
4	517	n/a
5	516	n/a
6	521	n/a
7	519	n/a
8	519	0.34
9	517	0.41
10	515	n/a
11	518	n/a
12	515	n/a
13	514	n/a
14	518	0.44

n/a is not applicable.

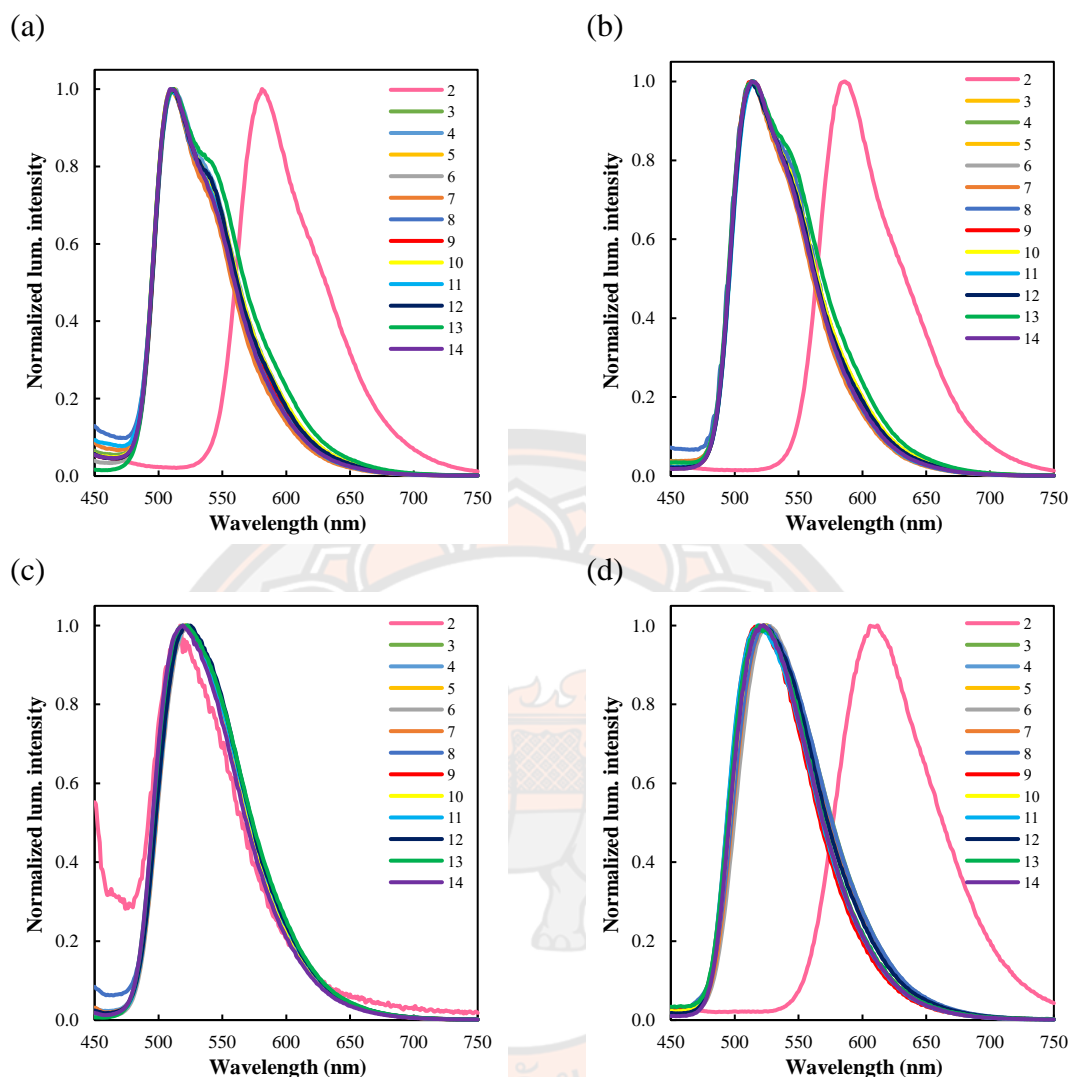


Figure 72 Normalized luminescence intensity of complex **2** to **14** (10 μ M) in toluene (a), tetrahydrofuran (b), methanol (c), and acetonitrile (d), respectively. Emission spectra were recorded with $\lambda_{\text{ex}} = 390$ nm at room temperature.

Solvatochromism is a potentially important probe in assessing charge distributions in both ground and excited states. Normally MLCT phosphorescence should exhibit a hypsochromic shift on moving from polar to non-polar solvents. Therefore, we have investigated the photoluminescence properties of the complexes in four other organic solvents (toluene, tetrahydrofuran (THF), methanol (MeOH), and acetonitrile (ACN)). The results of this investigation are shown in **Figure 72** and summarized in **Table 8**. The emission spectra of complexes **2** to **14** (10 μ M) recorded in toluene are shown in **Figure 72a**. The figure shows that the emission maximum of complex **2** has shifted to 581 nm, as previously observed, while the emission maxima

of the other complexes appear between 510 and 520 nm. The emission spectra of all of complexes **3** to **14** (10 μ M) in tetrahydrofuran are shown in **Figure 72b**. The figure shows that the emission maximum of all complexes **3** to **14** moved to higher emission wavelength, relative to toluene, and appearing between 513 and 515 nm while that of complex **2** has shifted to 586 nm. **Figure 72c** shows the normalized luminescence intensity in methanol of the complexes **2** to **14** (10 μ M). The figure shows that the emission maximum of complexes **3** to **14** moved to even higher emission wavelength, in comparison to tetrahydrofuran, appearing between 520 and 524 nm. Interestingly, the emission wavelength of complex **2** has shifted to 517 nm, potentially due to formation of the corresponding hemiacetal. The emission spectra of complexes **3** to **14** (10 μ M) recorded in acetonitrile are shown in **Figure 72d**. The figure shows that the emission maxima appear in the range 518-526 nm. The emission maxima of all complexes observed in the five solvents, arranged by their polarity, are summarized in **Table 8**. The values of emission maxima shown in **Table 8**, show that the band maxima for all complexes undergo hypsochromic shift (blue shift) on moving from polar to non-polar solvents which supports the assignment of the 3 MLCT state as a key component of the photophysical properties of these complexes. It can also be seen that the emission intensity for the complex in non-polar solvents (Toluene and DCM) is found to be almost higher than in polar solvents. This can be due to the fact that the ground and excited state dipoles originating in cyclometalated iridium complexes are stabilized in non-polar solvents, which results in a separation, that is, how much the charge distribution is different between ground and excited states.

Table 8 The emission maximum of all complexes in organic solvents (Toluene, DCM, THF, MeOH and ACN).

Complex	λ_{em}/nm (intensity/a.u.)				
	Toluene	DCM	THF	Methanol	ACN
2	581 (261169)	604 (259312)	586 (280164)	517 (8383)	612 (98354)
3	511 (380024)	522 (705847)	513 (372255)	522 (306149)	523 (6095810)
4	511 (362368)	517 (486766)	515 (310747)	523 (258833)	525 (293221)
5	510 (322322)	516 (528675)	514 (304857)	521 (286394)	526 (4087890)
6	510 (458398)	521 (671813)	513 (400668)	524 (362939)	524 (297403)
7	512 (233984)	519 (405712)	514 (214785)	522 (177581)	523 (337652)
8	511 (201063)	519 (339672)	515 (184763)	519 (134157)	525 (4318080)
9	512 (339376)	517 (738305)	514 (313949)	521 (274021)	520 (66783)
10	512 (419279)	515 (635513)	514 (342624)	521 (272957)	524 (886300)
11	511 (388253)	518 (641256)	515 (347754)	521 (335958)	518 (270645)
12	511 (337595)	515 (590030)	514 (324393)	525 (276313)	522 (251543)
13	511 (623677)	514 (992965)	513 (603454)	520 (542761)	519 (605350)
14	511 (423341)	518 (647181)	513 (362542)	519 (297392)	523 (132145)

5.4.3 Lifetime in organic solvent

Time resolved luminescence measurements were carried out with complexes **2-14** to gain further understanding into their photophysical properties. The measurements were carried out in dichloromethane and tetrahydrofuran. The decay curves in both organic solvents are monoexponential for all of the complexes. This is shown for air equilibrated solutions of complex **9** and **14** in dichloromethane in **Figure 73**. The fitted lifetime of complexes **2** to **14** are shown in **Table 9**. For complexes **3** to **14** the lifetime values in dichloromethane are between 40 and 70 ns while in tetrahydrofuran they fall between 10 and 20 ns. These values are consistent

with previously reported data [44]. The values of lifetimes for complex **2** in dichloromethane and tetrahydrofuran are 100 and 60 ns respectively.

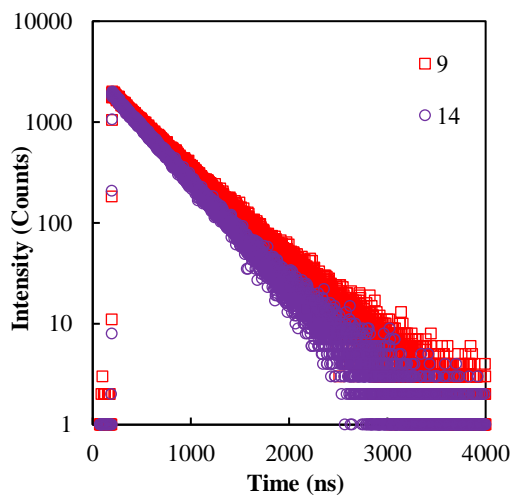


Figure 73 Plot emission intensity decay for complexes **9** and **14** in aerated dichloromethane solution.

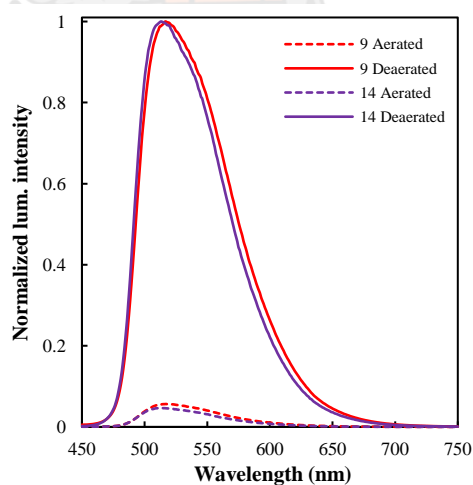


Figure 74 Luminescence intensity of complexes **9** and **14** in dichloromethane aerated and deaerated. Emission spectra were recorded with $\lambda_{\text{ex}} = 390$ nm. Slit 2-2 nm.

It is well known that the emission of cyclometalated iridium complexes is quenched by molecular oxygen given the triplet nature of their excited state. This is shown for complexes **9** and **14** in **Figure 74**. Therefore, the lifetimes for selected complexes were measured in deaerated solutions as well. As expected the lifetimes measured under these conditions are significantly longer with values falling between 1.30 and 1.60 μs (**Table 9**). These results are again in line with our previously published data and the values observed for the parent unsubstituted complex.

Table 9 Luminescence lifetime (μs) obtained for 10 μM solutions of complexes **3**, **8**, **9**, and **14** various organic solvents ($\lambda_{\text{ex}} = 372 \text{ nm}$) (values in brackets are for measurements in deaerated solutions).

Complex	Dichloromethane	Tetrahydrofuran
2	0.10 (0.24)	0.06 (0.36)
3	0.06 (1.56)	0.03 (1.59)
4	0.07 (1.44)	0.03 (0.01)
5	0.06 (0.26)	0.02 (0.14)
6	0.05 (0.19)	0.02 (0.01)
7	0.06 (0.16)	0.02 (0.09)
8	0.05 (1.55)	0.04 (1.59)
9	0.05 (1.42)	0.02 (0.10)
10	0.05 (0.12)	0.03 (0.08)
11	0.06 (0.12)	0.02 (0.08)
12	0.05 (0.12)	0.02 (0.08)
13	0.05 (0.11)	0.02 (0.07)
14	0.04 (1.30)	0.02 (0.07)

5.4.4 Density Functional Theory Calculations

Further insights into the photophysical properties of these complexes were obtained with the help of Density Functional Theory (DFT) calculations with the Gaussian09 software package. These calculations were carried out using the polarizable continuum model for a vacuum environment as well dichloromethane ($\epsilon = 8.93$) solution at the hybrid functional B3LYP and the double-zeta basis set LANL2DZ level of theory for complexes **9** and **14** as the model examples. The molecular orbitals were visualized using the Gabeit program package.

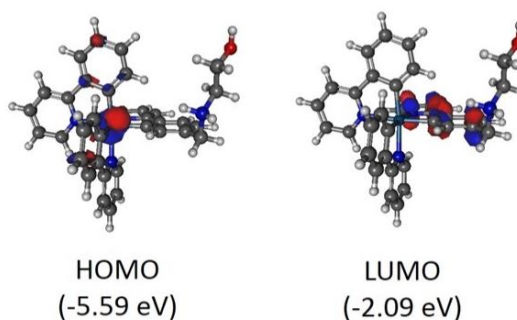


Figure 75 The HOMO and LUMO orbitals of complex **9** calculated in dichloromethane.

The results of this calculation are shown in **Figure 75**, which demonstrates that the HOMO orbital for complex **9** is mainly located on the iridium atom while the LUMO orbital is predominantly located on the cyclometalating ligand carrying the aminoalkyl substituent. Similar localizations of these orbitals are observed for complex **14** as shown in **Figure 76**. This is consistent with the expected MLCT nature of the electronic transitions in this type of cyclometalated iridium complexes. In addition, the calculated energy difference between these orbitals is 3.50 eV, which is consistent with the observed absorption spectrum of both complexes. In addition, the calculated complexes **9** and **14** are also in the same line with previous reported of *fac*-[Ir(ppy)₂(Hppy-NC₄)] and *fac*-[Ir(ppy)₂(Hppy-NC₁₂)] from our group [44], the HOMO-LUMO gap increases from less than 3.3 eV in a vacuum to more than 3.5 eV in the models involving the dichloromethane solvent.

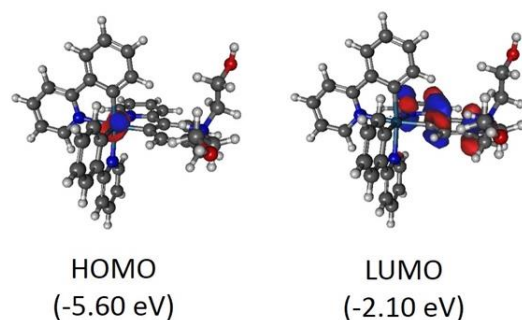


Figure 76 The HOMO and LUMO orbitals of complex **14** calculated in dichloromethane.

Furthermore, TD-DFT calculations have been carried out to model the UV-Vis spectra of complexes **9** and **14**. Comparison of the experimental and calculated spectra can be seen in **Figure 77**, which shows a good match between the observed and simulated data.

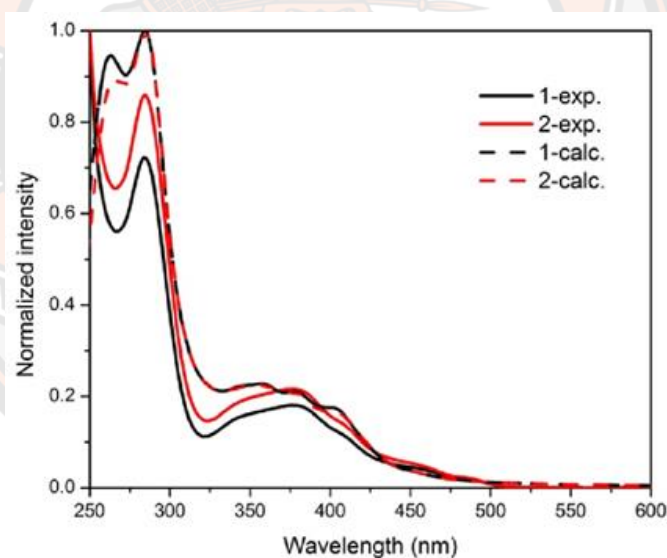


Figure 77 Comparison of experimental and calculated (TD-DFT) spectra of **1** (complex **9**) and **2** (complex **14**) in dichloromethane.

5.5 Photophysical properties in aqueous and mixed media

As mentioned above, the property of the initially synthesized complexes with butyl and dodecyl chains (**3** and **8**) that sparked our interest were their photophysical properties in aqueous solutions where they showed structure dependent responsive behavior related to the appearance of a second emission band at approximately 580 nm. Our early work has indicated that this behavior is related to aggregation of these

complexes and is affected by the nature of the alkyl chain. Therefore, herein we describe photophysical behavior of the synthesized complexes in aqueous media.

5.5.1 Photoluminescence

1) Photoluminescence in water and PBS

The emission spectra of complexes **3** to **14** recorded in water and PBS buffer (50 mM, pH 7.4) can be seen in **Figure 78**. It can be seen in **Figure 78a** that for complexes **3** to **8** in water the peak at 580 nm becomes more dominant while the peak at 520 nm diminishes with increasing the chain length of the alkyl group for complexes **3** to **8**. On the other hand, it can be seen that the addition of the hydroxy group onto the alkyl chain for complexes **9** to **14** leads to diminished emission intensity at 580 nm and restoration of the peak at 520 nm, for most complexes, as the emission maximum likely due to limited propensity to aggregate. In this case, the increase in the number of methylene units from 2 to 6 for complexes **9** to **12** does not results in any systematic change in the emission properties. The two complexes exhibiting somewhat different behavior are complex **11**, which shows a more broad emission peak than others with a maximum at 540 nm, and complex **14**, which, unlike the other complexes containing the hydroxy groups, shows a discernable shoulder at 580 nm, indicating more significant aggregation for this complex.

Interestingly, when the experiment is carried out in phosphate buffer (50 mM, pH 7.4), the observed spectra are significantly different in comparison to those recorded in water. This can be observed by comparing **Figures 78a** and **78b**. The latter of these two contains the emission spectra of a select group of complexes in phosphate buffer (50 mM, pH 7.4). In general, all of the complexes show significant increases in the emission intensities at 590 nm for their spectra recorded in phosphate buffer in comparison to spectra recorded in water. Thus, even for complex **14** containing two hydroxy groups the emission maximum for spectrum recorded in phosphate buffer is at 590 nm shoulder at 520 nm. Complexes **9** to **13** show their emission maximum intensity between 530 nm and 540 nm. However, their spectra are broader than they were in water with a more discernable shoulder at 590 nm.

Overall, the emission spectra of this class of complexes in aqueous media depends on the structure of the group attached to the nitrogen atom as has been reported in previous work where butyl and dodecyl chains have been used. The appearance of the emission peak at 590 nm was attributed to aggregation of the complex in solution and indeed the intensity at this wavelength systematically increases with the length of the attached alkyl chain. On the other hand, making the alkyl chain more hydrophilic by inclusion of hydroxy groups did lead to restoration of emission at 520 nm as the maximum in water, presumably due to limited propensity to aggregate. In addition, the emission spectra observed in PBS indicate that the aggregation state of these complexes can be modulated by the presence of various solutes.

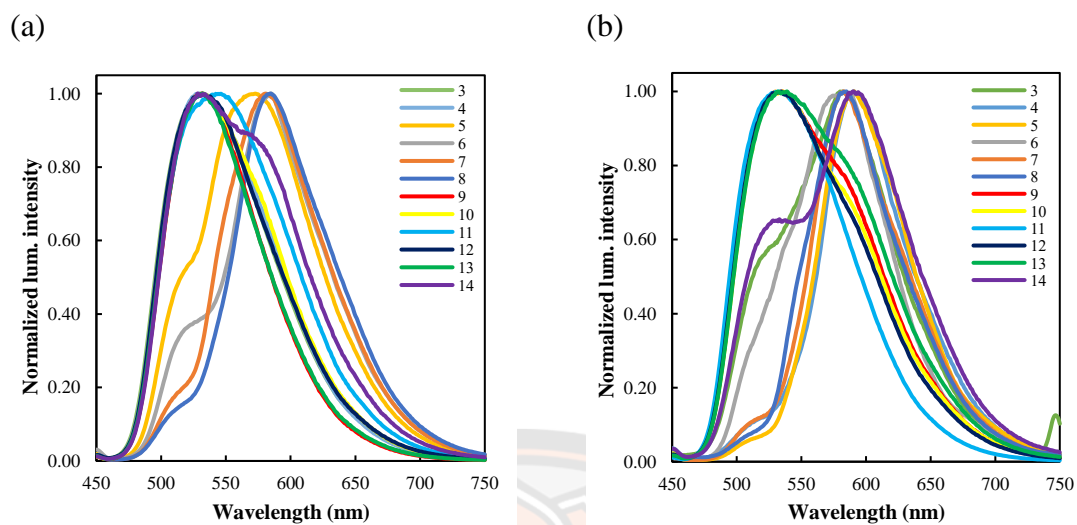


Figure 78 Normalized luminescence intensity of complexes 3 to 14 in water (a) and phosphate buffer (pH 7.4) (b). Excitation spectra were recorded with $\lambda_{\text{ex}} = 390$ nm for the emission.

Table 10 The emission maximum of complexes 3 to 14 in water and phosphate buffer (pH 7.4).

Complex	λ_{em} (nm)	
	water	PBS
3	531	580
4	527	590
5	573	591
6	584	582
7	581	583
8	582	585
9	532	535
10	533	536
11	546	532
12	532	534
13	532	539
14	528	590

2) Photoluminescence in water and acetonitrile mixtures

In order to obtain more detailed information on the effect of water on the emissive properties of complexes **3** to **14** we carried out measurements of their photoluminescence properties in mixtures of water and acetonitrile as this solvent mixture allows the continuous variation of the water content from 0 to 100 %. Emission spectra for selected complexes are shown in **Figure 79**, while the data for all complexes is summarized **Table 11**. The results indicate that the maximum emission intensity appears between 520 and 530 nm for most of the complexes up to the solvent mixture containing 80% of water. In this solvent mixture it is only complex **8** with the dodecyl chain that exhibits emission maximum at 580 nm as **Figure 79b**. For complexes **5** to **8** in water the peak at 573, 583, 581, and 585 nm, respectively, becomes the maximum. This peak also appears more dominant with increasing the chain length of the alkyl group for complexes **5** to **8**. The emission wavelength maxima for complexes **3** and **4** with the shortest alkyl chains remain around 530 nm even in pure water, likely due to limited propensity to aggregate.

On the other hand, it can be seen that the addition of the hydroxy group onto the alkyl chain for complexes **9** to **14** leads to diminished emission intensity at 580 nm and restoration of the peak at 530 nm, for most complexes, as the emission maximum likely due to limited propensity to aggregate. The only exception is complex **11**, which exhibits a very broad peak with maximum at 546 nm in pure water. It should also be noted that there are further finer differences in the emission spectra of these complexes. For example, **Figure 79c** shows that complex **9** containing single hydroxy group exhibits a single emission peak with maximum intensity at 532 nm. On the other hand, **Figure 79d** shows that complex **14** containing two hydroxy groups exhibits emission maximum at 528 nm and a shoulder at 576 nm.

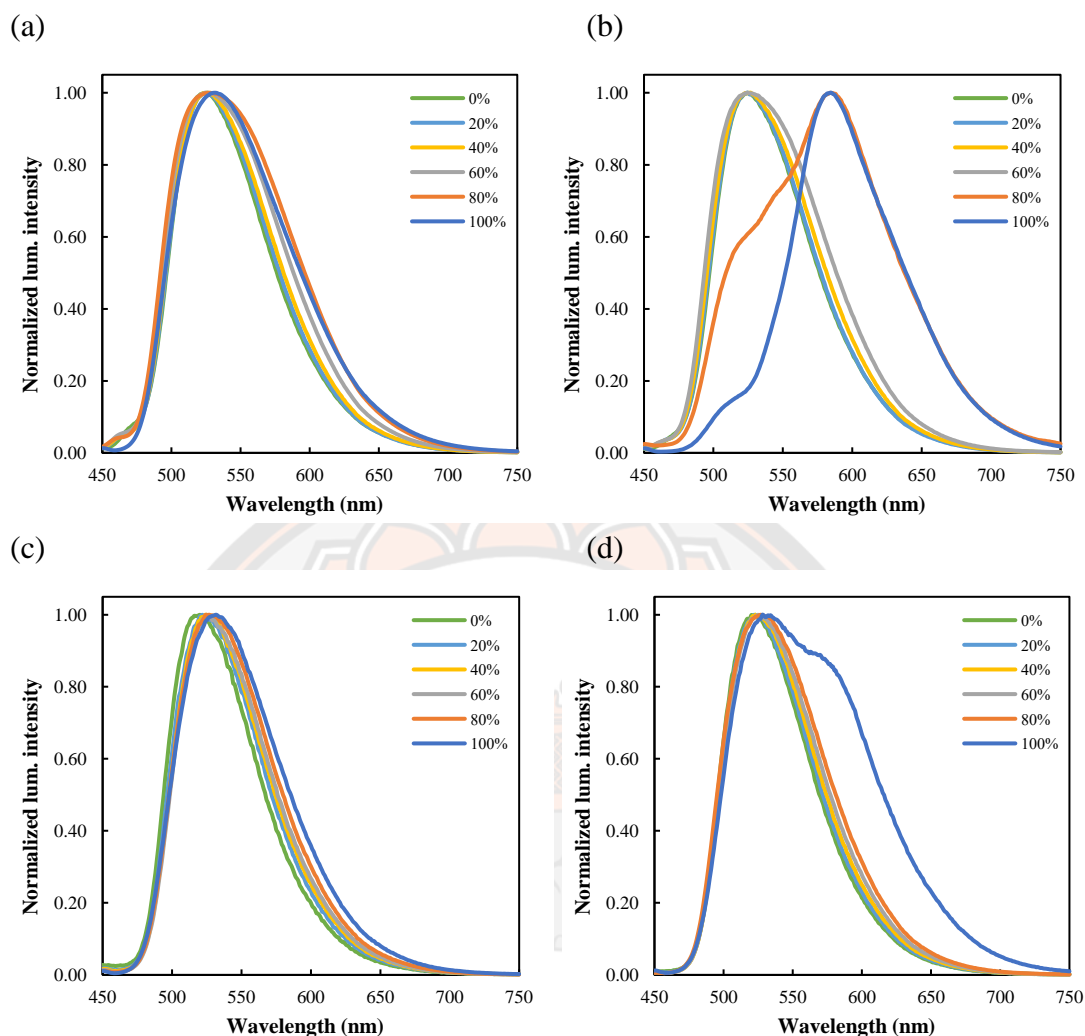


Figure 79 Normalized luminescence intensity of complexes 3 (a), 8 (b), 9 (c), and 14 (d) in water and acetonitrile mixtures. Excitation spectra were recorded with $\lambda_{\text{ex}} = 390$ nm for the emission.

The changes in the emission spectra can be observed by naked eye as can be seen in the image in **Figure 80**.

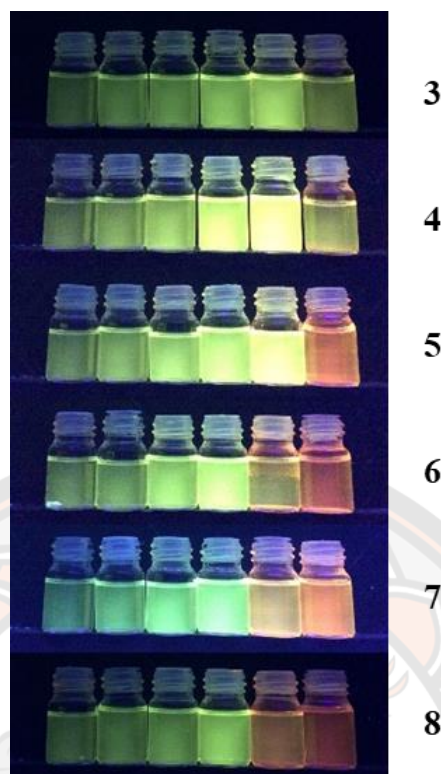


Figure 80 Photograph of complexes 3 to 8 solutions (10 μM) in 0-100% water/acetonitrile (left→right) was observed with the naked eye under 365 nm.

Table 11 The emission maximum of complexes 3 to 14 in water and acetonitrile mixtures.

Complex	λ_{em} (nm)					
	0%	20%	40%	60%	80%	100%
3	525	525	526	526	528	531
4	525	526	525	526	525	530
5	526	525	526	526	526	573
6	524	526	526	528	528	583
7	523	528	525	525	541	581
8	525	524	527	525	584	585
9	520	522	525	525	527	532
10	524	522	524	527	525	533
11	518	526	526	525	532	546
12	522	523	524	525	526	532
13	519	523	525	524	534	532
14	523	524	523	525	527	528

This data is further presented in **Figure 81**, which shows the plot of the ratio of emission intensity at 580 nm to emission intensity at 520 nm measured in various mixtures of water and acetonitrile. A higher value of this ratio indicates a higher propensity to aggregate. The data is summarized in **Table 12**.

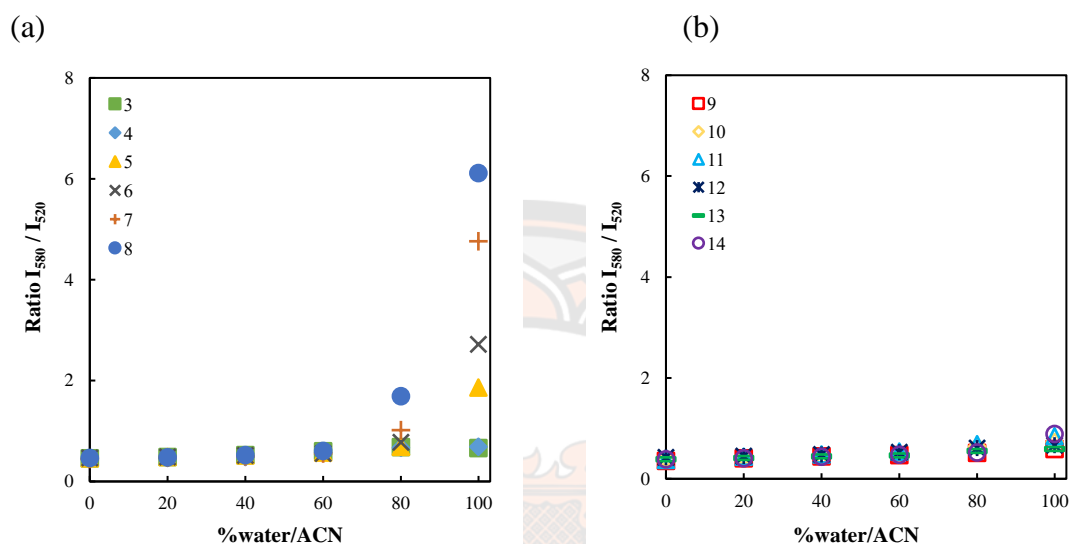


Figure 81 Ratio luminescence intensity at 580/520 nm of complex 3 to 8 (a) and 9 to 14 (b) in 0-100% water/acetonitrile solvent mixtures with varying amount of water (% v/v). Emission spectra were recorded with $\lambda_{\text{ex}} = 390$ nm.

It can be seen that the values of this ratio are very similar for all complexes in pure acetonitrile and mixtures of water and acetonitrile containing up to 60% of water. Indeed, the range of the emission intensity ratio values is 0.36 to 0.47 in pure acetonitrile and only increases to a range of 0.46 to 0.60 in the mixture with 60% of water. In line with the observation in the emission spectra, first clear divergence in the values of the ratio is observed in the solvent mixture containing 80% of water. Values of the ratio of most complexes in this solvent mixture are less than 0.80. However, the values for the most hydrophobic complexes **7** and **8** containing the decyl and dodecyl chains are 1.02 and 1.69 indicating their increased propensity to aggregate. This confirms, that the complex **8** is much more prone to aggregate in solvents with high content of aqueous media. The values for this ratio for complexes **9** to **14** containing 80% of water (**Figure 81b**).

Further divergence in the values of this ratio can be observed in pure water. In the case of simple alkyl complexes values of the ratio below 1 are observed for complex **3** (0.66) and complex **4** (0.69). The values of the ratio for complexes **5**, **6**, **7**, and **8** are 1.86, 2.71, 4.76, and 6.11, respectively, indicating that they have a strong tendency to aggregate.

Increasing value of the ratio in this series with increasing alkyl chain length can be seen in this series. It should be noted that complexes **5** and **6** are similar in that they both contain 8 carbon atoms attached to the amino group. However, complex **5** is a secondary amine with a single octyl chain while complex **6** is a tertiary amine containing two butyl chains. The fact that the emission intensity ratios for the solutions of these complexes differ indicates that this structural difference has an effect on their aggregation.

Table 12 Ratio luminescence intensity at 580/520 nm of complexes **3** to **14** in 0-100% water/acetonitrile solvent mixtures with varying amount of water (% v/v). Spectra were recorded with $\lambda_{\text{ex}} = 390$ nm.

Complex	Ratio I_{580}/I_{520} nm					
	0%	20%	40%	60%	80%	100%
3	0.46	0.49	0.52	0.60	0.68	0.66
4	0.45	0.47	0.49	0.56	0.67	0.69
5	0.46	0.48	0.51	0.58	0.69	1.86
6	0.47	0.49	0.52	0.55	0.78	2.71
7	0.45	0.47	0.50	0.55	1.02	4.76
8	0.46	0.48	0.52	0.60	1.69	6.11
9	0.36	0.41	0.44	0.47	0.51	0.59
10	0.39	0.42	0.43	0.47	0.64	0.73
11	0.38	0.44	0.48	0.54	0.68	0.84
12	0.42	0.45	0.48	0.53	0.61	0.67
13	0.39	0.41	0.44	0.46	0.55	0.59
14	0.38	0.41	0.44	0.47	0.52	0.89

5.5.2 Lifetime in water and acetonitrile mixtures

As mentioned above, luminescence lifetime is an important property of a luminophore, which can provide information about its environment. Therefore, the lifetimes of the series of aminoalkyl iridium complexes (**3-14**) 10 μM in water/acetonitrile solvent mixtures with varying amount of water (% v/v) were determined in addition to the steady state spectra described above. It can be seen that in pure acetonitrile all of the complexes exhibit the same lifetime on the order of 22 to 30 ns (**Figure 82**). This situation is similar also in the solvent mixtures containing 20 and 40% of water where the ranges of lifetime values are 35 to 52 ns and 62 to 91 ns, respectively. The values of the lifetimes increase even further upon increasing the content of water to 60%. The divergence in the values increases even further with the minimum being 114 ns and maximum being 157 ns. The emission lifetime values then increase to be in the range from 240 to 330 ns in 80% water. Finally, in pure water the lifetime values cover the range from 250 to 470 ns. These changes in the observed emission lifetimes can in part be explained by the fact that the solubility of molecular oxygen in water is significantly lower than in acetonitrile. However, this factor alone cannot explain the big range of lifetimes observed, especially in pure water. It should be noted that in pure water the complexes can be divided into two groups. Complexes **3**, **4**, and **9** to **14** have all lifetimes below 340 ns, while complexes **5** to **8** have lifetimes above 370 ns. This indicates that the complexes less prone to aggregation (i.e. with shorter alkyl chains or more hydrophilic chains) exhibit shorter lifetimes than those more prone to aggregation. This observation could be explained by more extensive protection of the emissive center from molecular oxygen in the case of the more substantially aggregated complexes.

The above discussion is based on lifetimes obtained with fitting the data using a mono exponential decay. However, it was noticed that for solutions containing 80% and 100% water, the fitting of the data with the mono exponential decay law did not result in satisfactory fit. Therefore, the observed data was also fitted with bi-exponential decay laws. The results are summarized in **Table 14** and **Table 15**, which show the values of the dominant lifetime and its percent contribution, respectively. In solution containing 80% water most of the complexes, with the exception of complexes **6** to **8**, exhibit more than 95% contribution from the dominant lifetime. This indicates that for the majority of the complexes in this solvent mixture describing their excited state decay by monoexponential decay law is sufficient. It is only in the cases of complexes **6** to **8** where biexponential decay needs to be invoked, which indicates more complex speciation of these compounds likely linked to aggregation. In pure water the group of complexes for which the contribution of the major lifetime is less than 95% includes also complexes **5** and **14**. These observations are in line with data from the emission spectra. The presence of multiple decay kinetics for the more lipophilic compounds further supports the presence of complex aggregation behavior. It is interesting to note the difference between the octyl (**5**) and di-butyl (**6**) analogues

in solvent mixture containing 80% (v/v) water. The luminescence lifetimes of the complex **6** longer luminescence lifetime than for the complex **5** contain octyl group on side chain.

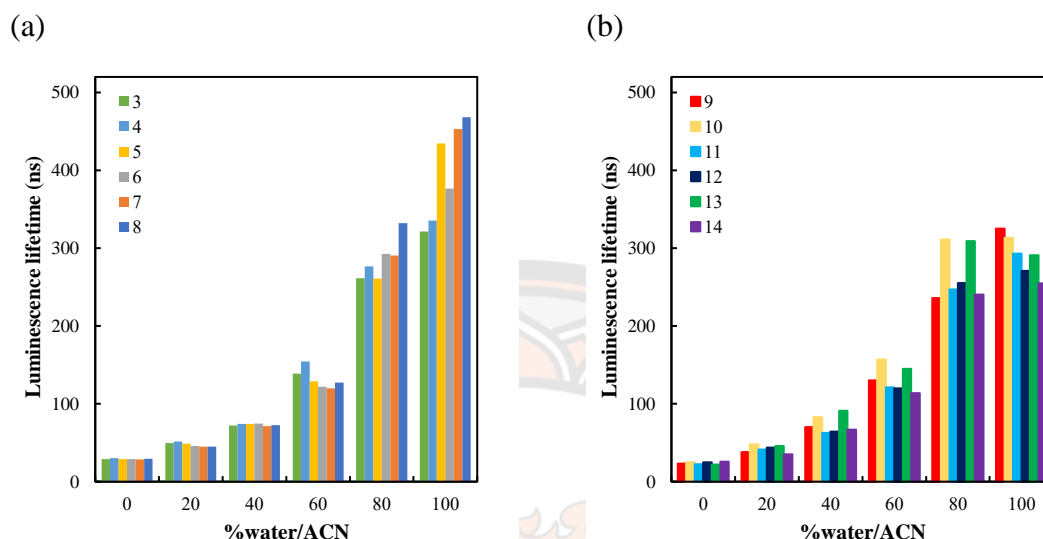


Figure 82 Lifetime of series of aminoalkyl iridium complexes **3** to **8** (a) and **9** to **14** (b) 10 μ M in water/acetonitrile solvent mixtures with varying amount of water (% v/v) for the monoexponential.

Table 13 Lifetime of complexes **3** to **14** in 0-100% water/acetonitrile for the monoexponential.

Complex	τ_{lum} (ns)					
	0%	20%	40%	60%	80%	100%
3	28.9	49.6	72.1	138.8	261.4	321.3
4	30.1	51.7	74.2	154.3	276.5	335.5
5	28.9	48.8	74.1	128.8	260.8	434.7
6	29.0	45.8	74.5	121.8	292.8	376.7
7	28.4	45.0	71.4	119.7	290.7	453.2
8	29.5	45.1	72.4	127.3	332.2	468.3
9	23.0	38.0	70.0	130.0	236.0	325.0
10	25.0	48.0	83.0	157.0	311.0	313.0
11	22.2	41.2	62.5	121.0	247.0	293.0
12	24.8	43.7	64.3	120.0	255.0	271.0
13	22.0	46.0	91.0	145.0	309.0	291.0
14	25.5	35.0	66.9	113.6	240.3	254.8

Table 14 Lifetime of complexes 3 to 14 in 80-100% water/acetonitrile for the dominant lifetime for the biexponential.

Complex	τ_{lum} (ns)	
	80%	100%
3	264.7	333.2
4	277.1	348.9
5	267.3	561.7
6	351.1	453.4
7	401.7	555.4
8	418.0	557.3
9	237.0	330.0
10	317.0	319.0
11	249.0	302.0
12	258.0	287.0
13	314.0	294.0
14	251.3	300.4

Table 15 %Value contribution of this dominant lifetime of complexes 3 to 14 in 80-100% water/acetonitrile for the biexponential.

Complex	%Value contribution	
	80%	100%
3	98.75	96.76
4	99.63	96.24
5	95.08	82.13
6	74.50	84.85
7	59.40	84.83
8	78.96	87.06
9	99.54	99.09
10	98.80	99.01
11	98.62	97.77
12	99.22	96.22
13	98.91	99.28
14	97.23	89.75

Table 16 Lifetime of complexes 3 to 14 in 80-100% water/acetonitrile for the secondary lifetime for the biexponential.

Complex	τ_{lum} (ns)	
	80%	100%
3	28.0	20.3
4	139.7	48.1
5	147.5	60.4
6	158.9	41.8
7	167.9	81.8
8	109.5	86.4
9	44.0	24.0
10	13.0	10.0
11	119.0	27.2
12	11.5	29.6
13	22.0	18.0
14	39.7	16.3

Table 17 %Value contribution of this secondary lifetime of complexes 3 to 14 in 80-100% water/acetonitrile for the biexponential.

Complex	%Value contribution	
	80%	100%
3	1.25	3.24
4	0.37	3.76
5	4.92	17.87
6	25.50	15.15
7	40.60	15.17
8	21.04	12.94
9	0.46	0.91
10	1.20	0.99
11	1.38	2.23
12	0.78	3.78
13	1.09	0.72
14	2.77	10.25

5.5.3 Dynamic light scattering

Dynamic light scattering experiments with solutions of the aminoalkyl iridium complexes described above were carried out, given the fact that the photophysical behavior of complexes **3** to **14** in aqueous and mixed organic aqueous media is presumed to depend on aggregation (**Figure 83**). Well behaved aggregates, for some of the complexes, were observed in solvent mixtures containing 60% (v/v), 80% (v/v), and 100% (v/v) water. Data from these measurements is summarized in **Figure 83**, which shows the z-average values, and **Table 19** where the polydispersity index is reported as well. Aggregates with size 207.5 nm (PDI: 0.341) and 152.0 nm (PDI: 0.441) were detected for complex **7** and **8**, respectively, in the solvent mixture containing 60% v/v of water. No aggregates were detected for complexes **2** to **6** and **9** to **13** in this solvent mixture. Aggregates were observed for complexes **3** to **10** and **13** in the solvent mixture containing 80% v/v of water. The sizes were 370.9 nm (PDI: 0.343), 590.2 nm (PDI: 0.292), 137.6 nm (PDI: 0.364), 234.1 nm (PDI: 0.232), 163.6 nm (PDI: 0.109), 130.8 nm (PDI: 0.118), 134.0 nm (PDI: 0.268), 416.7 nm (PDI: 0.578), and 569.6 nm (PDI: 0.501), respectively. Finally, in pure water aggregates were detected for complexes **3** to **5**, **7**, and **9** to **13**. The sizes were 573.7 nm (PDI: 0.471), 65.31 nm (PDI: 0.312), 57.58 nm (PDI: 0.466), 65.38 nm (PDI: 0.231), 296.1 nm (PDI: 0.418), 64.2 nm (PDI: 0.492), and 72.5 nm (PDI: 0.357), respectively. The dynamic light scattering experiment was not successful for complexes **6** and **8** in pure water most likely due to the presence of very large aggregates. These results support the presumption of this work that these complexes aggregate in solutions containing large amounts of water. Furthermore, they also support the notion that this behavior can be modulated by structural change. This is for example demonstrated by the fact that in the solvent mixture containing 60% (v/v) of water only complexes **7** and **8** with the longest alkyl chains show the presence of detectable aggregates. Finally, these results also suggest that the changes in the photophysical behavior of these complexes such as appearance of bands in the region 580 to 590 nm reflects a change in the aggregation behavior rather than simple change from non-aggregated to aggregated status, as aggregates are observed by DLS even in the instances where emission maxima are observed at 520 to 530 nm. While lower concentration at 5 μ M, aggregation with size 648.7 nm (PDI: 0.402) was detected for complex **14** in the pure water.

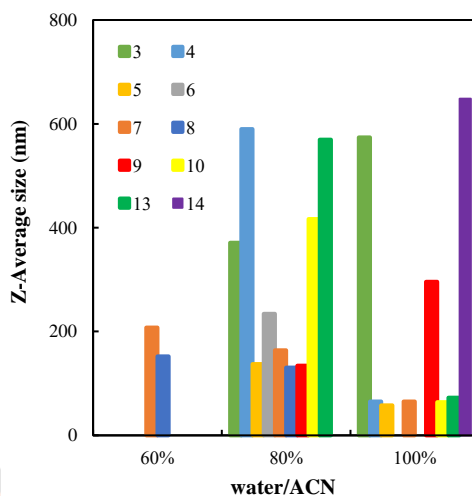


Figure 83 Z-Average size(nm) distribution by intensity of a series of aminoalkyl iridium complexes 3-10 and 13-14 in water/acetonitrile solvent mixtures with varying amount of water (%v/v).

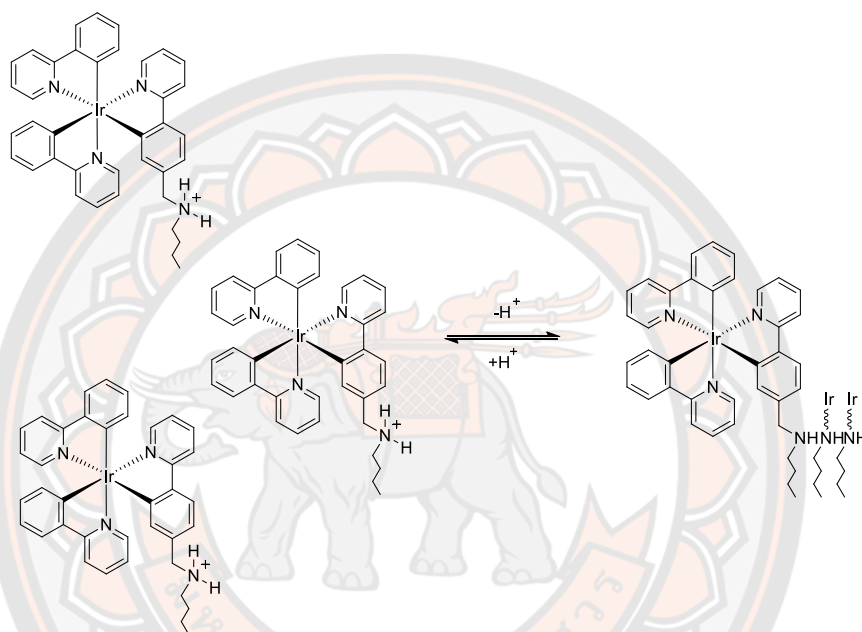
Table 18 Dynamic Light Scattering Data of complexes 3-10 and 13-14 (10 μ M) in water/acetonitrile solvent mixtures with varying amount of water (60-100 %v/v), showing size-average by intensity distributions and Polydispersity Index (PDI).

Complex	Z-Average size/d.nm (PDI)		
	60%	80%	100%
3	n/a	370.9 (0.343)	573.7 (0.471)
4	n/a	590.2 (0.292)	65.31 (0.312)
5	n/a	137.6 (0.364)	57.58 (0.466)
6	n/a	234.1 (0.232)	n/a
7	207.5 (0.341)	163.6 (0.109)	65.38 (0.231)
8	152.0 (0.441)	130.8 (0.118)	n/a
9	n/a	134.0 (0.268)	296.1 (0.418)
10	n/a	416.7 (0.578)	64.2 (0.492)
13	n/a	569.6 (0.501)	72.5 (0.357)
14	n/a	n/a	648.7 (0.402) ^a

^aconcentration 5 μ M and n/a is not applicable.

5.5.4 Effect of pH

Given the fact that the photophysical properties of complexes **3** to **14** in aqueous media are affected by aggregation, it was expected that these should also be affected by the pH value of these solutions as the pH of the solution will affect the protonation of the amino group changing its charge from +1 for the protonated ammonium salt to 0 for the free amine, ongoing from acidic to basic solutions. This change of charge on the complex is expected to affect the aggregation due to changes in electrostatic repulsion as shown in **Scheme 27**.



Scheme 27 Aggregation form of iridium complex from protonation and deprotonation in various pH.

Furthermore, as described above, the propensity of the complexes to aggregate is dependent on their structure, such as the length of the chain attached to the amino group. Therefore, we investigated, the emission properties of complexes **3** to **9** and **14** as a function pH to understand how this interplay of structural factors and protonation equilibria overlay. The results are shown in **Figure 82**. Furthermore, normalized emission spectra of complexes **4**, **9**, and **14** are shown in **Figure 82** and the values of the emission intensity ratios are summarized in **Table 20**. Indeed, a change in the ratio of emission intensity at 580 and 520 nm was observed for complex **3** to **9** and **14**.

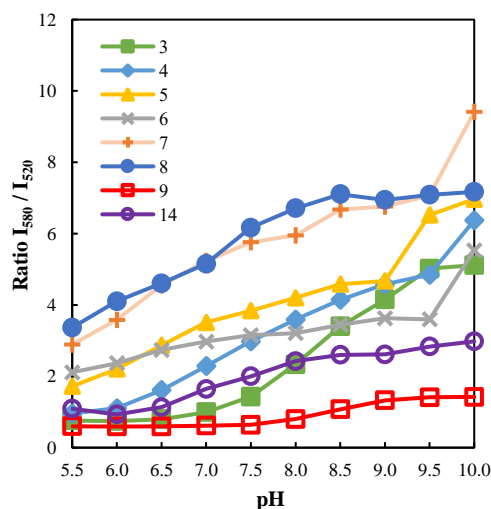


Figure 84 Ratio luminescence intensity at 580/520 nm of complexes 3 to 9 and 14 in various pH 5.5-10.0 from phosphate buffer. Emission spectra were recorded with $\lambda_{\text{ex}} = 390$ nm.

Change in the ratio of emission intensity at 580 nm to emission intensity at 520 nm measured in phosphate buffer for the pH range 5.5 to 10.0 was observed for complexes 3 to 9 and 14 and the results are shown in **Figure 82**. **Figure 82** shows that the originally described butyl (3) and dodecyl (8) complexes exhibit markedly different behaviors. The initial ratio values at pH 5.5, are 0.76 and 3.37 for complex 3 and complex 8, respectively. This shows that while protonation of the amino group in the butyl chain containing complex 3 can significantly inhibit its aggregation due to coulombic repulsion, the hydrophobicity of complex 8 containing the dodecyl chain is so large that its propensity to aggregate is not affected significantly by protonation. On increasing the pH to 7.5 the ratio values for complex 3 and 8 are 1.43 and 6.17, respectively. Finally, at pH 10.0 the ratio values for complexes 3 and 8 are 5.12 and 7.17, respectively. These results show that the tendency to aggregate increases for both complexes with increasing pH and remains higher for the more lipophilic one over the whole range.

Furthermore, the graph shows that complexes 4 to 7 with intermediate chain lengths exhibit behavior that lies between these two cases as expected. In fact, the emission ratios for the alkyl complexes at pH 5.5 are increasing in the order of their increasing alkyl chain length. For example, complex 4 with hexyl chain exhibits properties similar to the parent butyl analogue (complex 3), which stem from their decreased propensity to aggregate in comparison to the other simple alkyl complexes, due to their shorter chain lengths, which was described above. The emission intensity ratio for complex 4 changes from a value 0.96, which is nearly identical to the value observed for complex 3, at pH 5.5 to 6.37 at pH 10.0. However, it can be seen that the curves for complex 3 and 4 show differences at intermediate pH values. For example,

the ratio remains relatively unchanged up to pH 7.0 for complex **3** but it starts to gradually increase from pH 6.0 for complex **4**. The changes in the ratio are then more dramatic for complex **3** between pH values of 7.5 and 9.5, with the ratios becoming nearly equivalent at pH 9.5.

In the case of complex **5**, the ratio changes from a value of 1.72 at pH 5.5 to a value of 6.97 at pH 10.0. The trend for complex **5** is close to linear from pH 5.5 to 9.0 followed by a plateau and a significant jump at pH 10.

For complex **6**, the ratio changes from a value of 2.11 at pH 5.5 to a value of 5.53 at pH 10.0. The shape of the curve is similar to complex **5**. The trend for complex **6** is linear from pH 5.5 to 9.5 followed by a plateau and a significant jump at pH 10. However, the ratio shows small change from 2.11 to 3.60 at between pH 5.5 and 9.5. Complexes **7** and **8** then show similar behavior to complex **5**, albeit at higher values of the ratio. In summary the behavior is in line with previous observations, which have shown that complexes **3** and **4** form one group in their behavior while complexes **5** to **8** form another, with complex **6** deviating somewhat on account of it being a tertiary amine.

The behavior of complexes **9** and **14** is similar to the parent butyl analogue (complex **3**) at lower pH values, while showing decreased propensity to aggregates, as exhibited by lower values of the ratio, at higher pH values. For complex **9** this ratio at pH 5.5 has the value of 0.61 while for complex **14** the ratio value is 1.10. At the pH 10.0, the emission intensity ratio values are 1.42 and 2.98 for complexes **9** and **14**, respectively. The somewhat unexpected behavior of complex **14** could be explained by the fact that it is less basic, i.e. less likely to be found in the aggregation inhibiting protonated form at a given pH.

Table 19 Ratio luminescence intensity at 580/520 nm of complexes **3** to **9** and **14** in various pH 5.5-10.0 from phosphate buffer.

Complex	pH									
	5.5	6.0	6.5	7.0	7.5	8.0	8.5	9.0	9.5	10.0
3	0.76	0.75	0.80	0.99	1.43	2.34	3.40	4.15	5.02	5.12
4	0.96	1.11	1.62	2.29	2.98	3.59	4.15	4.58	4.85	6.37
5	1.72	2.21	2.87	3.51	3.84	4.20	4.58	4.67	6.52	6.97
6	2.11	2.37	2.74	2.97	3.15	3.21	3.45	3.63	3.60	5.53
7	2.89	3.58	4.56	5.23	5.76	5.95	6.68	6.76	7.07	9.42
8	3.37	4.10	4.61	5.15	6.17	6.71	7.11	6.95	7.09	7.17
9	0.60	0.59	0.59	0.62	0.64	0.80	1.07	1.33	1.41	1.42
14	1.09	0.93	1.13	1.65	2.00	2.43	2.60	2.62	2.84	2.98

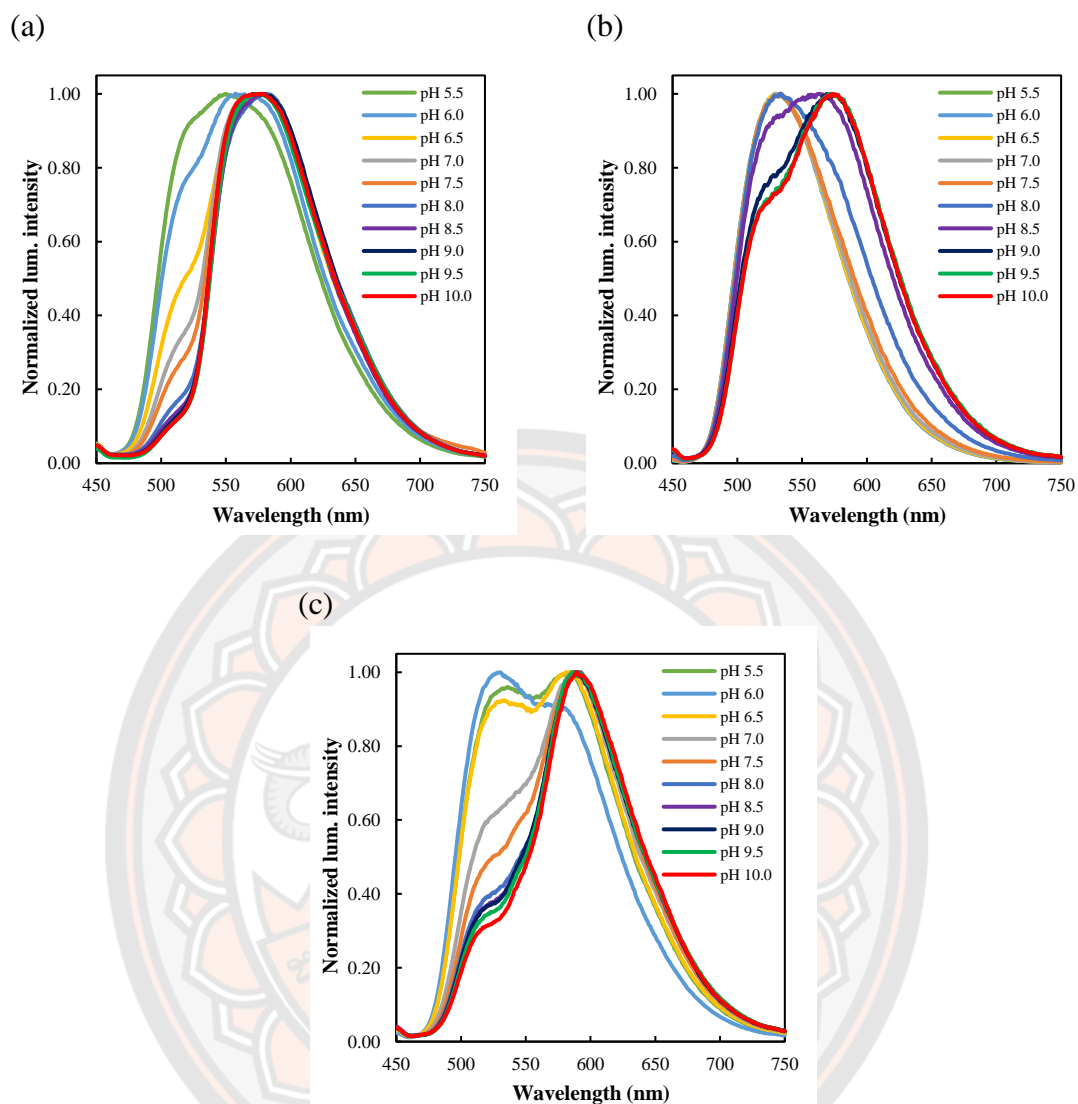


Figure 85 Normalized luminescence intensity at 580/520 nm of complex 4 (a), 9 (b) and 14 (c) in various pH 5.5-10.0 from phosphate buffer. Emission spectra were recorded with $\lambda_{\text{ex}} = 390$ nm.

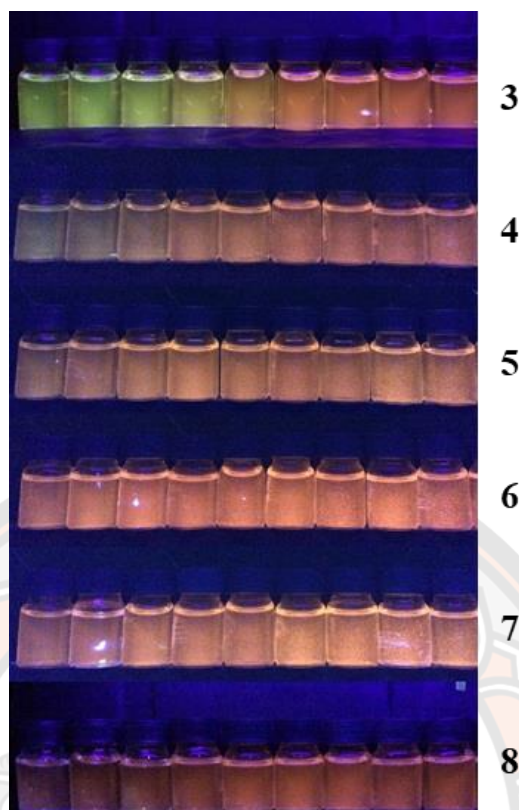


Figure 86 Photograph of complexes **3** to **8** solutions ($10\ \mu\text{M}$) with different phosphate buffer from pH 5.5 to 9.5 (left→right) was observed with the naked eye under 365 nm.

Finally, as shown in **Figure 86**, the changes in the emission ratio in response to pH can be detected by naked eye for complexes **3** and **4** as the emission color changes from green to red.

5.6 Cellular experiments

As mentioned above the fact that the previously synthesized complexes **3** and **8** have shown the ability to stain live cells in fluorescence microscopy experiments, has been a further motivation to carry out this study of these further analogues. Therefore, a selected group of these complexes has been used in further imaging studies.

Specifically, the suitability of four novel cyclometalated iridium(III) complexes bearing amino alkyl groups on one of the phenylpyridine rings as cellular stains in live cell imaging studies was investigated. These compounds, shown in **Figure 87**, are complexes **5**, **6**, **9**, and **14**. The aim of this work was to evaluate the cellular uptake and sub-cellular localization profile of these compounds using laser scanning confocal microscopy (LSCM) as a tool for determining their properties *in cellulo*. Furthermore, the toxicity and intracellular concentration of the complexes were determined by ChemoMetec A/S NucleoCounter3000-Flexicyte instrument with the overarching purpose of finding a complex suitable to use as a cellular stain in live cell imaging studies. Complexes **5** and **6** were chosen for this study as they contain an intermediate number of carbons in comparison to the previously studied complexes **3** and **8**. In addition they present two alternative ways of arranging the alkyl sidechains as complex **5** has a single octyl chain while complex **6** has two butyl chains present on the amine nitrogen. Similarly, complexes **9** and **14** were chosen as presentative examples of the hydrophilic chain substituted complexes, again with one and two chains attached to the nitrogen, respectively.

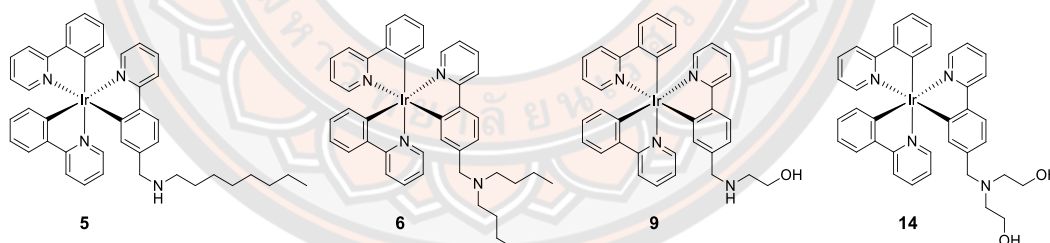


Figure 87 Cyclometalated Ir(III) complexes to be investigated.

5.6.1 Cytotoxicity

To find a suitable range of loading concentrations of complexes **5**, **6**, **9**, and **14** to be used in LSCM experiments with live cells such that they didn't die as a result of incubation with the compounds, a cytotoxicity assay was performed on the compounds to find their IC_{50} values. This value indicates the inhibitor (compound) concentration at which the viability of the cells has been reduced by a half of its maximum value. **Figure 88** shows the dose response curves generated from the assay for complex **5**, **6**, **9** and **14**. The summarized the IC_{50} values extrapolated from these curves in **Table 22**.

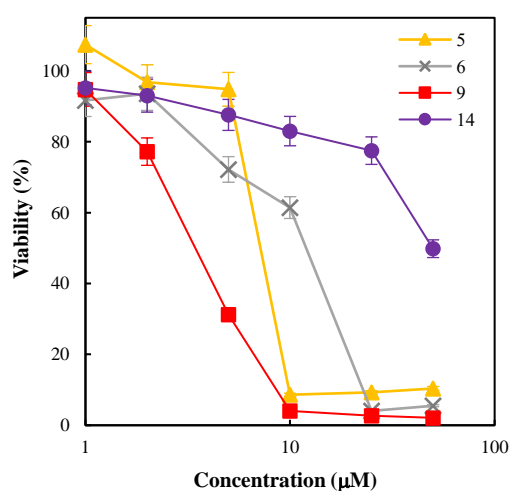


Figure 88 Viability of NIH-3T3 cells after 24 h exposure complexes **5**, **6**, **9**, and **14**.

The cytotoxicity of the complexes **5**, **6**, **9**, and **14** were evaluated using imaging cytometry. This has shown that the IC_{50} for 24 h exposure was on the order of 7.0 μ M with complex **5** being more toxic than complex **6** for which the IC_{50} was order of 11.9 (**Figure 89**). It can be seen, that complex **9** shows IC_{50} below 3.6 μ M, which is similar to what was observed for the alkyl complexes. On the other hand, complex **14** shows significantly lower cytotoxicity with IC_{50} value on the order of 50 μ M. Lower cytotoxicity, especially for complex **14**, was observed after 24 h incubation. These results indicated the existence of a safe imaging concentration window for the four complexes as images could be acquired after shorter loading times at lower concentrations. This idea was further investigated with complex **9** in an imaging experiment involving propidium iodide, which stains the nuclei of dying and dead cells red. The experiment has been carried out using loading concentrations of complex **9** of 5 μ M and 2 μ M. The results of these experiments are shown in **Table 20** and **Table 21**, respectively. The images in these tables clearly show the green luminescence assigned to complex **9** present in the cytoplasm. The nuclear staining by

propidium iodide becomes evident after 4 and 6 h with experiments conducted with 5 μM and 2 μM concentration of complex **9**, respectively. This result indicates the safe operating windows in terms of time for imaging experiments with complex **9** carried out at the specified concentrations.

Table 20 Cytotoxicity and cell staining in NIH-3T3 cells of complex **9** at concentration 5 μM .

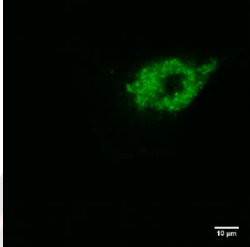
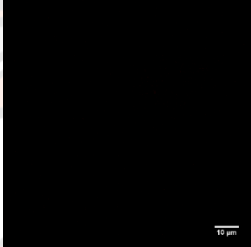
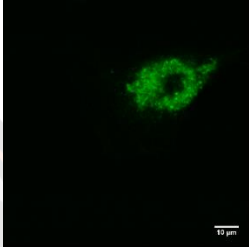
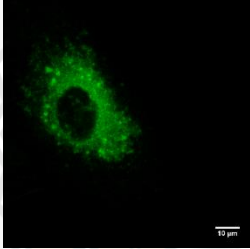
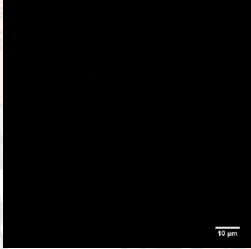
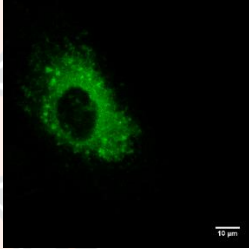
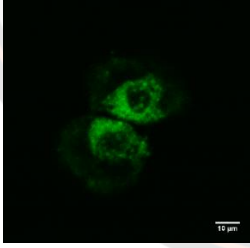
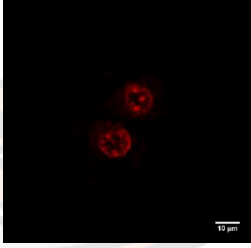
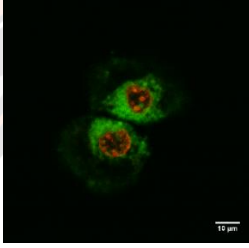
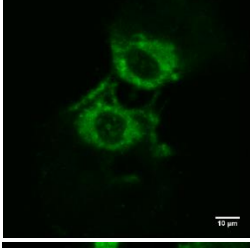
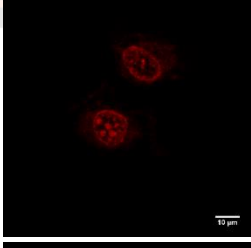
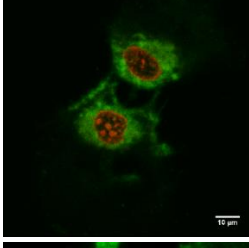
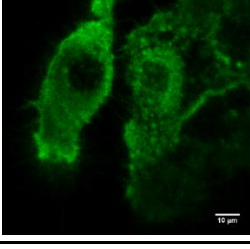
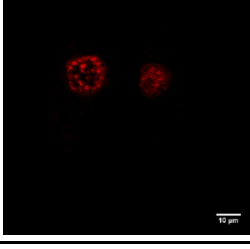
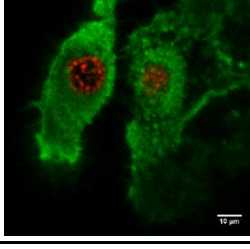
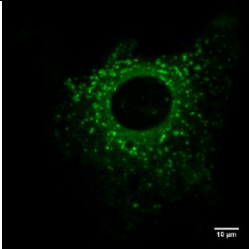
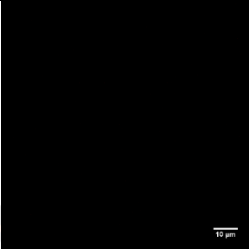
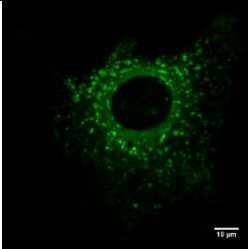
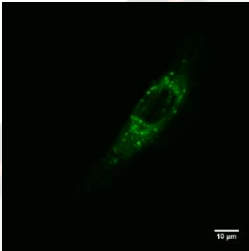
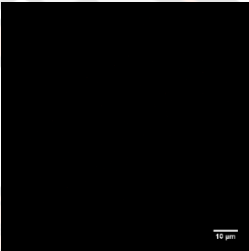
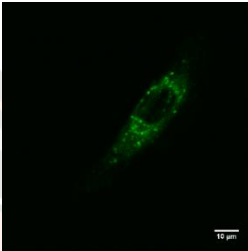
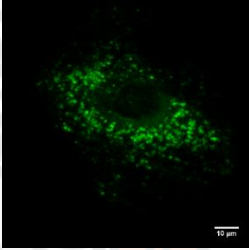
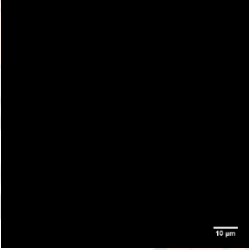
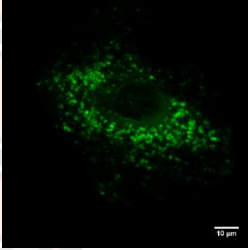
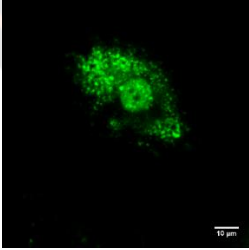
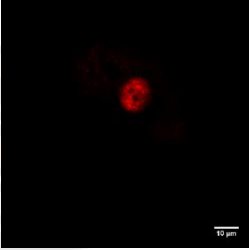
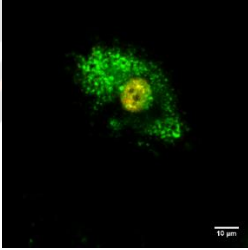
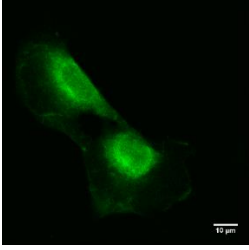
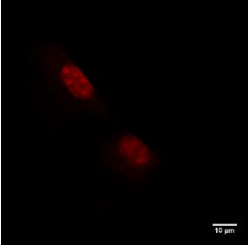
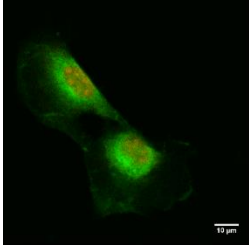
Loading time/h	Complex 9 (5 μM)	Propidium Iodide	RGB Merge
1			
2			
4			
6			
24			

Table 21 Cytotoxicity and cell staining in NIH-3T3 cells of complex 9 at concentration 2 μ M.

Loading time/h	Complex 9 (2 μ M)	Propidium Iodide	RGB Merge
1			
2			
4			
6			
24			

Results reported for complexes **9** at concentrations 5 μM and 2 μM , and those shown above in **Table 20** and **Table 21** indicate that these complexes are entering the cells. To verify these observations, and to investigate whether the amount of iridium complex present in the cell correlates with the cytotoxicity ICP-MS analyses for iridium were carried out for cell lysates after loading cells with complexes **5**, **6**, **9**, and **14**. The results of this experiment are shown in **Table 22**. These results indicate a presence of micromolar concentrations of iridium inside cells, thus giving further proof of the internalization of the complexes. However, the values of iridium present in the cell does not seem to correlate well with the observed cytotoxicity.

Table 22 IC_{50} values of complexes **5**, **6**, **9**, and **14**.

Complex	$\text{IC}_{50}/\mu\text{M}$
5	7.0
6	11.9
9	3.6
14	50.0

5.6.2 Brightness analysis

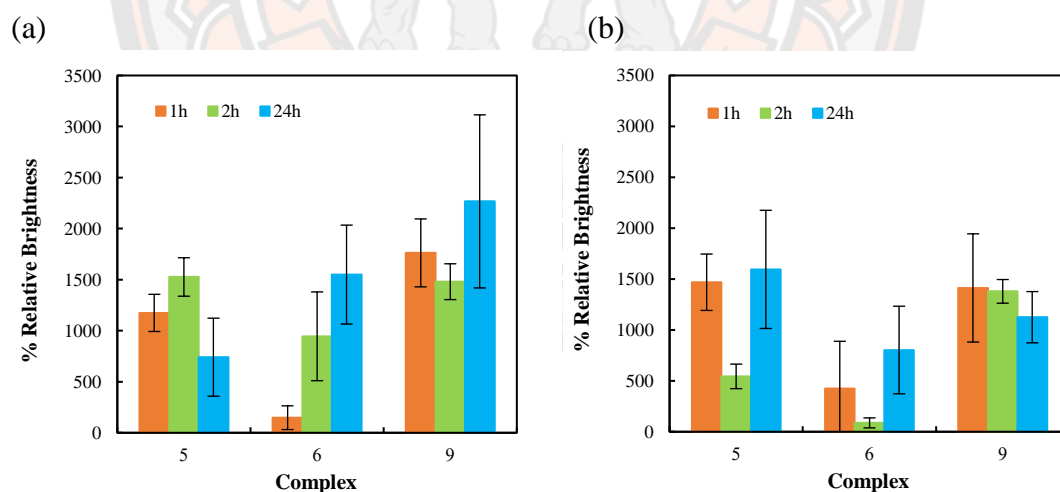


Figure 89 Brightness analysis of microscopy image of cells incubated with complexes **5**, **6**, and **9** relative to control image of cell at a) 5 μM , b) 2 μM .

Brightness analysis of complexes **5**, **6**, and **9** relative to control image of cell at 5 μM (**Figure 89a**) and 2 μM (**Figure 89b**) was investigated. In general, large increases in observed brightness are observed. For example, the % relative brightness increases after incubation for 24 h with complex **9** are 2266.34% and 1125.00% for loading with a concentration 5 μM and 2 μM respectively.

5.6.3 Microscopy studies

Having established the presence of safe window for imaging experiments the study of subcellular localization for the studied complexes was undertaken. The localization of emission from the studied complexes was compared to that of lysotracker red as the previously studied complexes **3** and **8** have shown lysosomal localization. **Figure 90** and **Figure 91** show the results of fluorescence (LSCM) imaging experiments with complexes **5** and **6**, respectively, in NIH-3T3 cells. Images for both complexes were acquired after 1 h incubation with 2 μM solution of the complex. It can be seen, that both complexes exhibit luminescence in the cytosol, which is more diffuse than that for lysotracker red. Complexes **6** (**Figure 91**) does exhibit more distinct lysosomal localization than complex **5** (**Figure 90**).

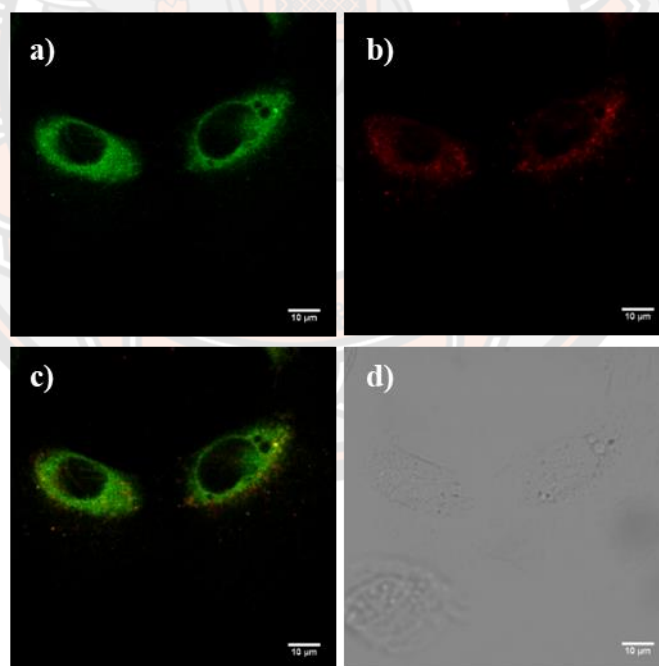


Figure 90 LSCM microscopy images of NIH-3T3 cells obtained with complex **5** (λ_{ex} 355 nm, λ_{em} 450-650 nm) (a), lysotracker red (λ_{ex} 543 nm HeNe laser, λ_{em} 600-650 nm) (b). Panel c shows the RGB overlay of panels a and b, while panel d is the brightfield image. (Scale bar: 10 μm).

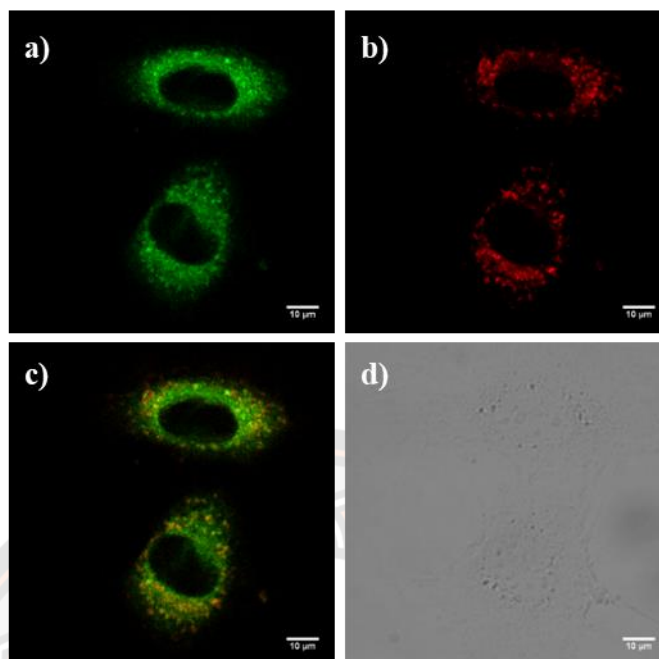


Figure 91 LSCM microscopy images of NIH-3T3 cells obtained with complex 6 (λ_{ex} 355 nm, λ_{em} 450-650 nm) (a), lysotracker red (λ_{ex} 543 nm HeNe laser, λ_{em} 600-650 nm) (b). Panel c shows the RGB overlay of panels a and b, while panel d is the brightfield image. (Scale bar: 10 μm).

Figure 92 and **Figure 93** show the results of fluorescence (LSCM) imaging experiments with complexes **9** and **14**, respectively, in NIH-3T3 cells. The cellular localization of the two complexes is compared to that of lysotracker red. Images for complex **9** were acquired after 1 h incubation with 2 μM solution of the complex. The lower cytotoxicity of complex **14** allowed incubation with a 5 μM solution of the complex for 2 h, which resulted in better quality images. It can be seen, that complex **14** (**Figure 93**) exhibits lysosomal localization, analogous to that observed for our previously reported complexes. On the other hand, while there is some degree of overlap between the images obtained with complex **9** (**Figure 92**) and lysotracker red, complex **9** does show a more diffuse emission throughout the cytosol.

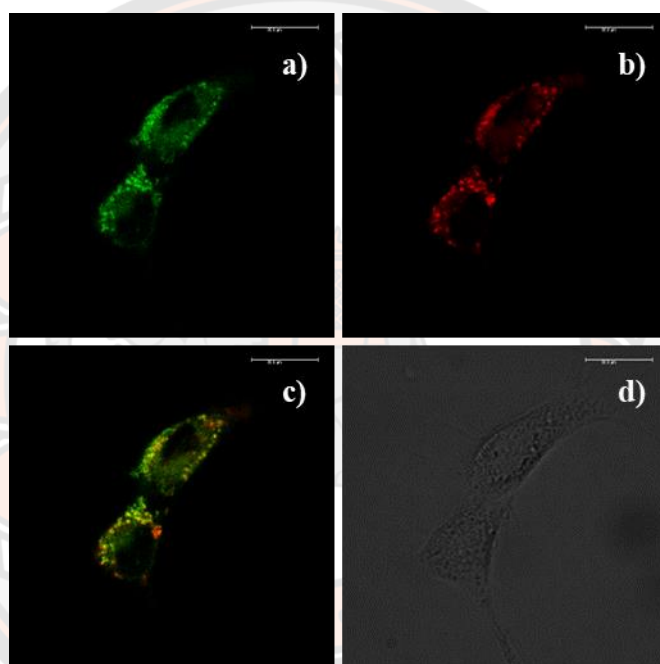


Figure 92 LSCM microscopy images of NIH-3T3 cells obtained with complex **9** (λ_{ex} 355 nm, λ_{em} 450-650 nm) (a), lysotracker red (λ_{ex} 543 nm HeNe laser, λ_{em} 600-650 nm) (b). Panel c shows the RGB overlay of panels a and b; $P = 0.68$, while panel d is the brightfield image. (Scale bar: 20 μm).

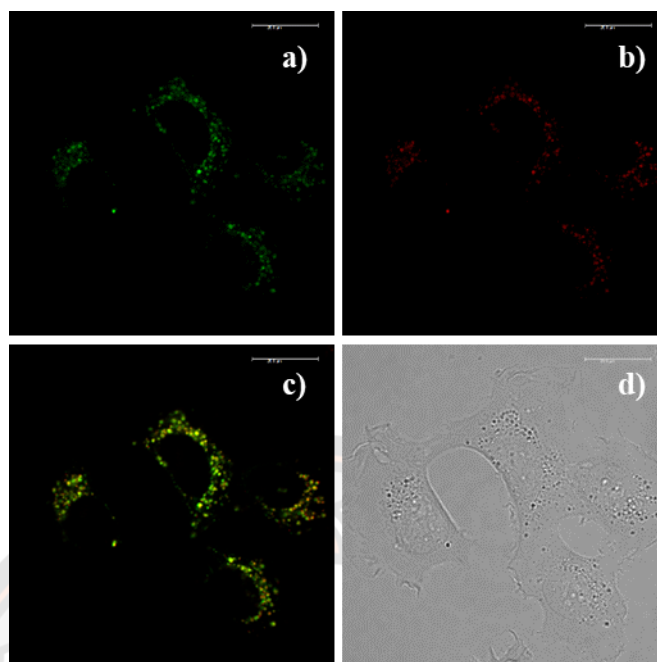


Figure 93 LSCM microscopy images of NIH-3T3 cells obtained with complex 14 (λ_{ex} 355 nm, λ_{em} 450-650 nm) (a), lysotracker red (λ_{ex} 543 nm HeNe laser, λ_{em} 600-650 nm) (b). Panel c shows the RGB overlay of panels a and b; $P = 0.74$, while panel d is the brightfield image. (Scale bar: 20 μm)

5.7 Conclusion

In conclusion, novel tris-cyclometalated iridium(III) complexes have been synthesized and investigated. These complexes are analogues of our previously reported aminoalkyl complexes containing alkyl groups and hydroxy groups on the nitrogen atoms. The photophysical properties of these complexes in organic solvent are similar to the parent complex *fac*-[Ir(ppy)₃] and our previously reported aminoalkyl complexes. These exhibit bright luminescence with long lifetimes even in aerated aqueous solutions. In aqueous media the photophysical properties clearly depend on the structure of the chain attached to the amino group. Increasing this chain length in the series of complexes **3** to **8** from butyl to dodecyl leads to increasingly pronounced appearance of second emission peak at 580 nm. The work reported herein demonstrated that this is due to structural effects on the ability of these complexes to aggregate in solutions with high content of water. Complexes containing hydrophilic hydroxy groups in these alkyl chains (**9** to **14**) exhibit decreased propensity to aggregate and in turn maintain position of the original emission peak observed between 520 and 530 nm. The possibility to affect this aggregation behavior as a source of ratiometric signal was demonstrated with the response of the emission spectra of these complexes to pH. Cellular experiments carried out with complexes **5**, **6**, **9**, and **14** indicate their ability to stain live cells with varying degree of lysosomal localization. Complex **14** stands out among these due to its significantly lower toxicity.

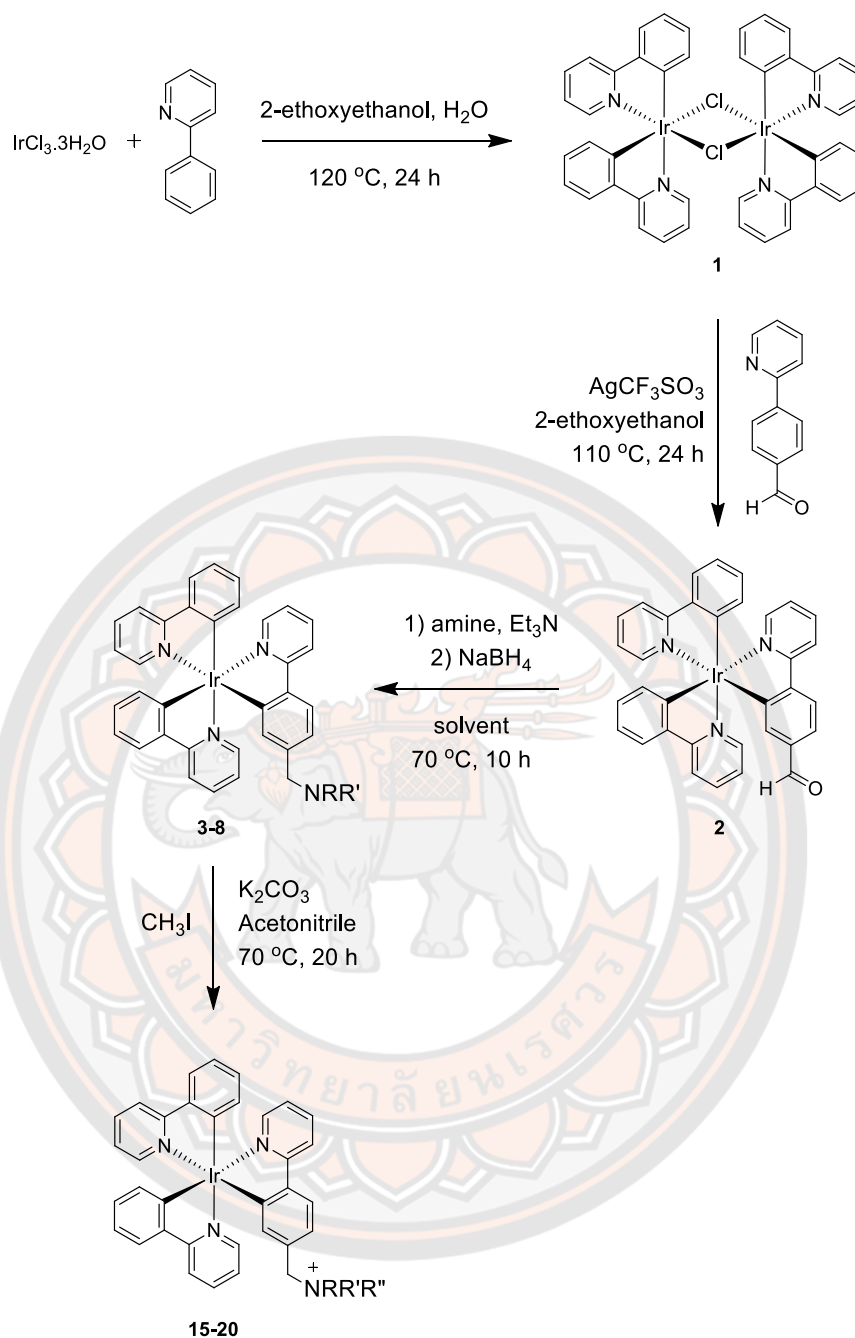
CHAPTER VI

QUATERNARY AMMONIUM TRIS-CYCLOMETALATED IRIDIUM COMPLEXES

6.1 Introduction

The previous chapter has discussed our work utilizing aminoalkyl substituted tris-cyclometalated iridium complexes. As was shown above, the aminoalkyl group undergoes protonation/deprotonation in aqueous media depending on the pH. Specifically, in the context of cellular imaging at physiological pH these complexes will be present in their protonated ammonium form, which likely aids their ability to enter cells and act as fluorescent stains. Therefore, we decided to synthesize and explore the quarternary ammonium salts of these complexes, which would be expected to be permanently charged.

The complexes were synthesized from the aminoalkyl complexes described above using methyl iodide as an alkylating reagent (**Scheme 28**). Initially, an attempt was made to synthesize these methylated quarternary salts for all of the simple aminoalkyl complexes **3** to **9**. However, while the formation of these products was observed using MS analyses of crude reaction mixtures (**Figure 94**), attempts to purify and isolate the products by column chromatography were not successful. Eventually, the quarternized product of the butyl complex **3** was isolated using direct precipitation of the crude product under dark and it was characterized by ^1H -, ^{13}C -NMR, and HRMS (ES) $^+$. The photophysical properties, photoreactivity, and cell imaging of this complex were studied and are reported below.



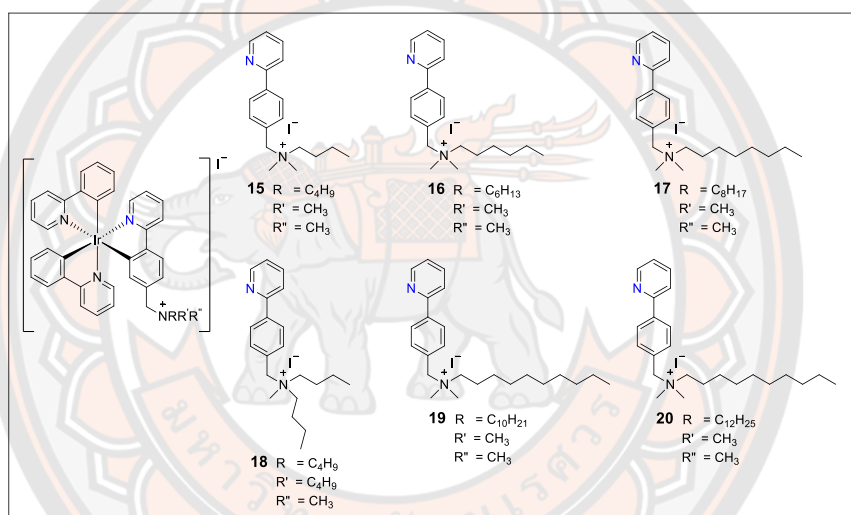
Scheme 28 The synthesis procedure of quarternary ammonium salts iridium(III) complexes.

Table 23 List of symbols R, R', R'' of the complexes discussed in this chapter.

Complex	R	R'	R''
15	C ₄ H ₉	CH ₃	CH ₃
16	C ₆ H ₁₃	CH ₃	CH ₃
17	C ₈ H ₁₇	CH ₃	CH ₃
18	C ₄ H ₉	C ₄ H ₉	CH ₃
19	C ₁₀ H ₂₁	CH ₃	CH ₃
20	C ₁₂ H ₂₅	CH ₃	CH ₃

6.2 Result and discussion

6.2.1 Synthesis

**Figure 94** Structural of quarternary ammonium salts iridium (III) complexes **15** to **20**.

The synthesis of iridium complexes (**15-20**) has been attempted using the four steps as shown in **Scheme 23** and as described in section 4.3. Four different reaction steps were used. The first three steps were adopted from the literature and involve the synthesis of the chloride bridged dimer using the Nonoyama reaction, conversion of this dimer into *fac*-[Ir(ppy)₂(fppy)] using 4-(2-pyridyl)benzaldehyde, and the reductive amination of the formyl group to yield complexes **3** to **8**. Complexes (**15-20**) were then made in the final step by transforming aminoalkyl complexes into quarternary ammonium salts by using methyl iodide as the alkylating agent. The formation of the quarternary ammonium complexes was confirmed by MS spectroscopy of the crude reaction mixture. For example, **Figure 95** shows mass spectrum of the reaction mixture making complex **15**. However, attempts to purify the complexes (**15-20**) by column chromatography were not successful. Elution of

complex **15** from the column was difficult requiring a mobile phase with high content of methanol in dichloromethane. Furthermore, mass spectrometry analysis of materials obtained after purification by column chromatography indicated that the product decomposed to methyl ether (**Figure 96**).

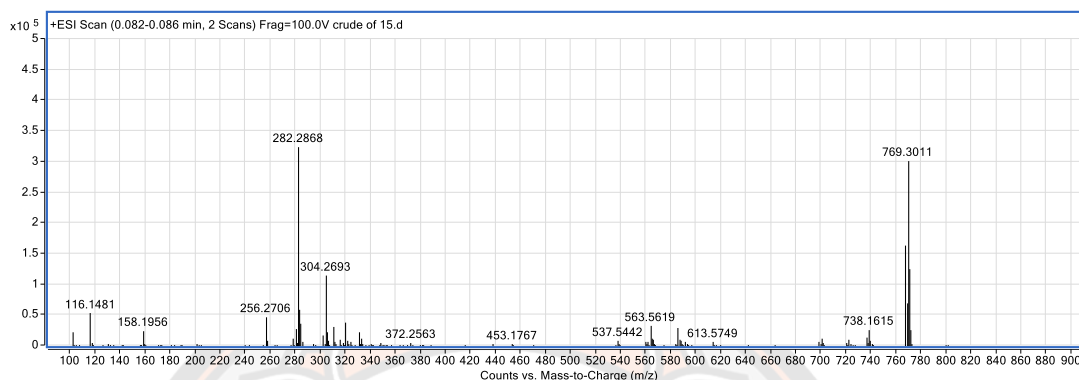


Figure 95 HRMS spectrum of the crude reaction mixture of complex **15**.

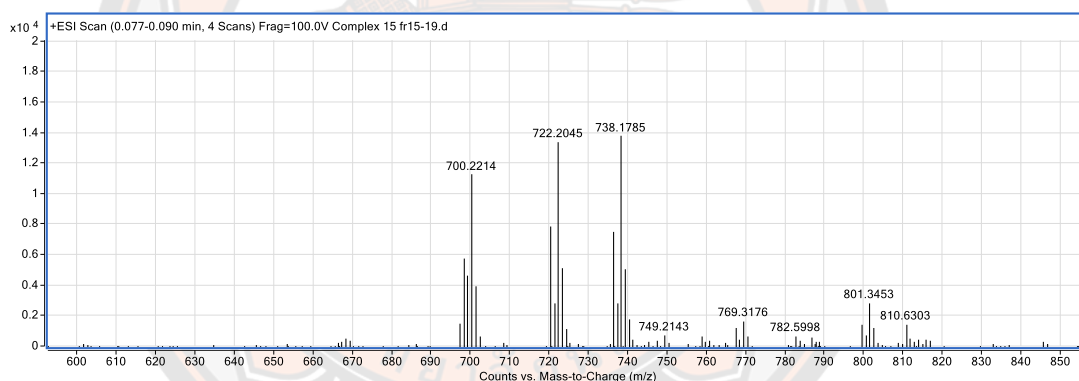


Figure 96 HRMS spectrum of complex **15** after purification by column chromatography.

Therefore, we decided to switch the method of purification to be crystallization or precipitation of crude product with dichloromethane and hexane. The results from mass spectrum found the complex as the crystallization occurs rapidly at room temperature (**Figure 97**). Thus, it was possible to isolate pure complex **15** by using precipitation with dichloromethane and hexane.

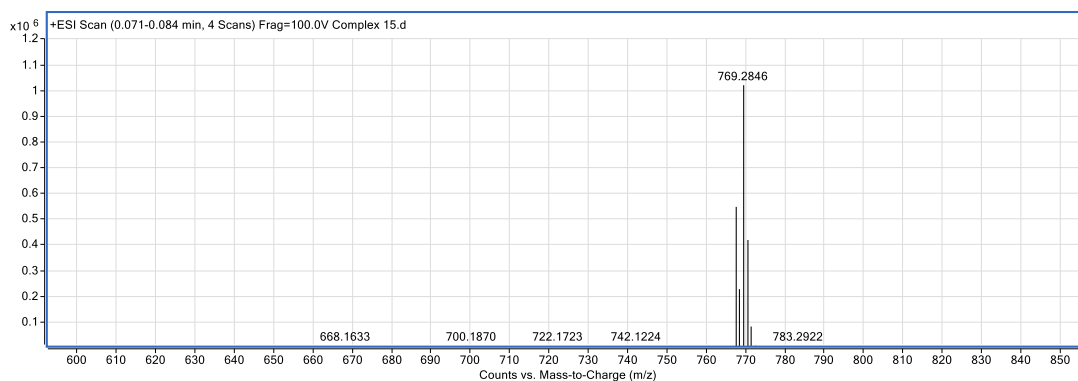


Figure 97 HRMS spectrum of complex **15** after purification by recrystallization.

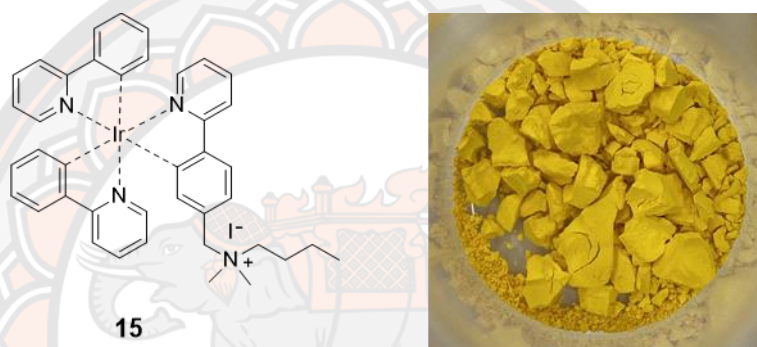


Figure 98 Structure and precipitates image of complexes **15** to be investigated in this chapter.

A serendipitous observation has shown that complex **15** can undergo decomposition in an NMR sample tube. This further indicated the potential stability issues with this compound. This issue, which confirmed our suspicions formed during the purification of the complex, was noticed for a sample, which has been left in solution in the NMR cuvette for several days. ¹H-NMR analysis of the decomposed sample indicated that the product formed in this process is the precursor complex *fac*-[Ir(ppy)₂(fppy)] as shown in **Figure 99**.

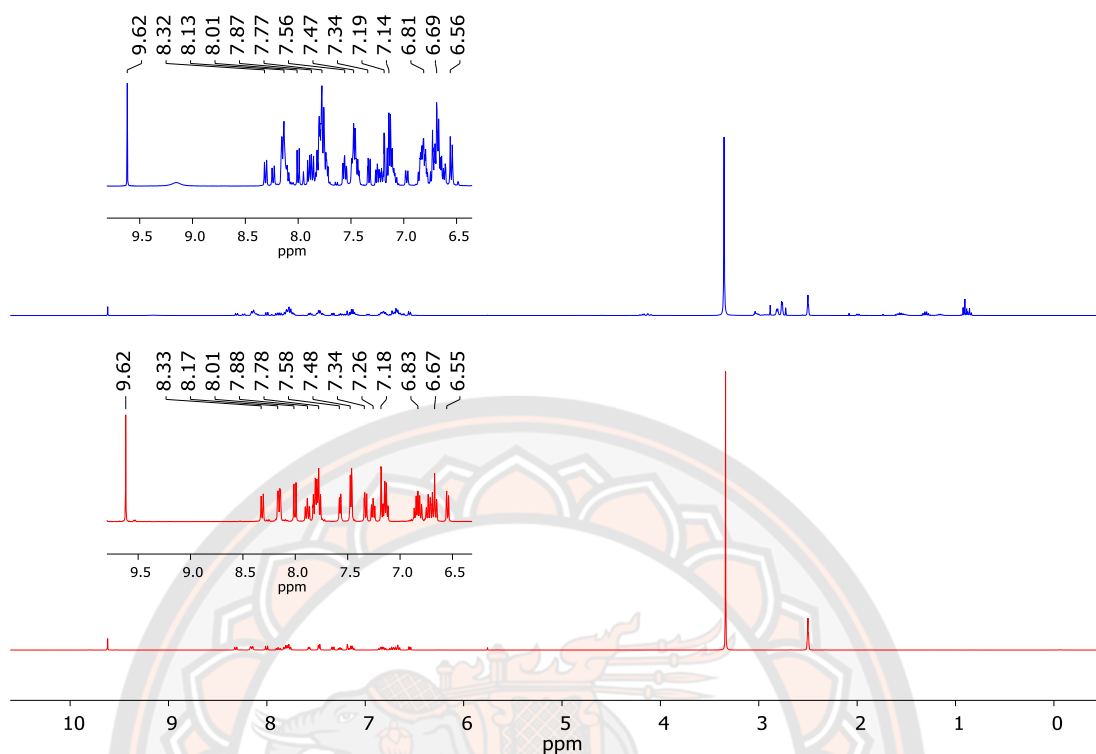


Figure 99 ^1H -NMR spectrum of complex **15** kept in light at ambient conditions (top) and *fac*-[Ir(ppy)₂(fppy)] (bottom) in DMSO-*d*₆.

The formation of this precursor complex was confirmed ^1H -NMR of the reaction mixture (**Figure 99**) with the appearance of the aldehyde peak of *fac*-[Ir(ppy)₂(fppy)] at 9.62 ppm (top). While complex **15** was observed aldehyde peak at 9.62 ppm (bottom).

6.2.2 Photophysical properties in organic solvents

The photophysical properties of quaternary ammonium iridium(III) complex **15** were investigated via UV-vis, steady state luminescence, photoluminescence quantum yield, and luminescence lifetime. All measurements were performed at room temperature, in organic solution at concentration 10 μM . The absorption properties of the complex **15** in dichloromethane is shown in **Figure 100**. The photophysical properties are summarized in **Table 24**.

1) UV-Vis spectrum

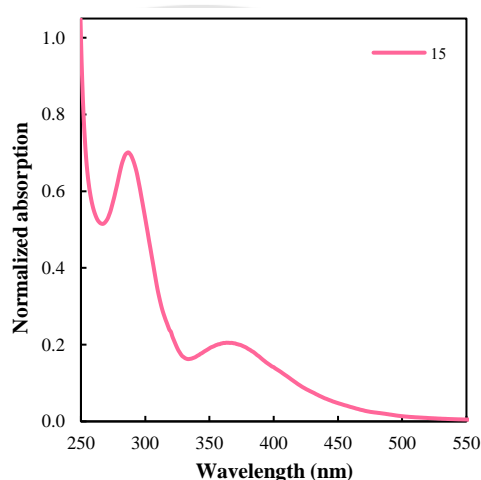


Figure 100 Absorption spectrum of complex **15** (10 μM) recorded in dichloromethane.

Absorption spectrum of complex **15** was measured in dichloromethane and is shown in **Figure 100**. The UV-Vis absorption spectrum is typical for cyclometalated iridium(III) complexes. There are three main features in this spectrum. The first is a peak with a maximum at 286 nm, which can be attributed to ligand centered $\pi-\pi^*$ transitions. The second feature is a peak with maximum at 365 nm, which can be attributed to spin-allowed metal to ligand charge transfer ($^1\text{MLCT}$) transitions. The final feature is a tail extending beyond 500 nm corresponding to forbidden metal to ligand charge transfer ($^3\text{MLCT}$) transitions.

2) Photoluminescence

The steady state photoluminescence spectrum for complex **15** can be seen in **Figure 101**. The emission spectrum of complex **15** in dichloromethane, recorded after excitation at 390 nm, is also similar to analogous tris-cyclometalated iridium complexes showing a maximum at 514 nm. These spectral properties are analogous to both the parent compound *fac*-[Ir(ppy)₃] [5] as well as the precursor complex *fac*-[Ir(ppy)₂(ppy-NC₄)] previously reported by our group [42]. Photoluminescence properties are summarized in **Table 24**. The emission spectrum of complex **15** was recorded at 77K and it shows maxima at 513, 549, 590, and 649 nm. The spectrum can be seen in the **Figure S63**. The quantum yields observed for complex **15** is on the order of 9% and is different to the parent complex and our previously reported structures.

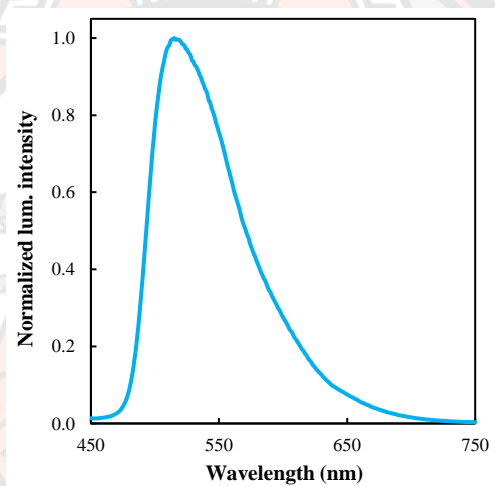


Figure 101 Normalized luminescence intensity spectrum of complex **15** (10 μM) recorded in dichloromethane.

Table 24 Photophysical properties of complex **15**.

	15
Absorption (λ_{max} /nm) ^a	286, 365
Emission (λ_{max} /nm) ^a	515
Quantum Yield (ϕ_{lum}) ^a	0.09
Emission 77 K (λ_{max} /nm) ^b	513, 549, 590, 649

^a Dichloromethane and ^b Dimethylsulfoxide.

3) Lifetime

Excited-state lifetimes of the complexes can provide evidence as to the nature of excited states of transition metal complexes. The instrumental procedures and conditions that were used to carry out the excited state lifetime measurements were time-correlated-single-photon-counting (TCSPC) using a laser diode (372nm) as the excitation source. It should be noted that all excited state lifetimes reported here have an error of $\pm 10\%$. These measurements were first carried out in organic solvents (dichloromethane, tetrahydrofuran and acetonitrile) where the emission intensity decays were monoexponential (**Table 25**).

Table 25 Lifetime data for the complex **15** were obtained in aerated and deaerated organic solvents at room temperature (298 K) using TCSPC.

Complex		Lifetime (ns)		
		DCM	THF	ACN
15	aerated	64	35	26
	deaerated	739	1035	916

These measurements have revealed that in aerated dichloromethane, tetrahydrofuran, and acetonitrile the lifetimes are 64 (± 6.4), 35 (± 3.5), and 26 (± 2.6) ns, respectively. These values are comparable to those observed for the precursor amine complex. On the other hand, the lifetime values of 739 (± 74) ns, 1.03 (± 0.10) μ s and 916 (± 92) ns in degassed dichloromethane, tetrahydrofuran, and acetonitrile respectively, are significantly shorter than those observed for the precursor complex [42]. In addition, the photoluminescence quantum yield for complex **15** is only 9%, which is significantly less than observed for either *fac*-[Ir(ppy)₃] or the precursor complex *fac*-[Ir(ppy)₂(ppy-NC₄)]. This, together with the shorter lifetimes indicates additional non-radiative decay pathways for the excited state of complex **15**.

6.2.3 Photophysical properties in water and PBS

1) UV-vis and Photoluminescence spectra

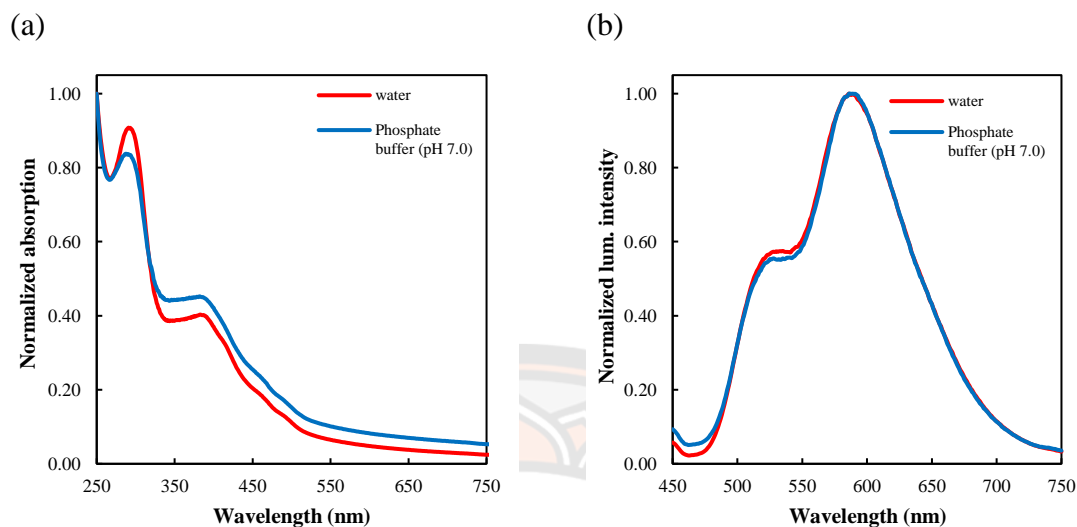


Figure 102 Normalized absorption (a) and luminescence intensity (b) of complex **15** (10 μ M) in water and phosphate buffer (pH 7.0).

Absorption spectra of complex **15** were measured in water and phosphate buffer (pH 7.0) and are shown in **Figure 102a**. The UV–Vis absorption spectrum is typical for cyclometalated iridium complexes also similar to that observed for the precursor complex and for the complex itself in organic solvent. There are three main features in this spectrum. The first is a peak with a maximum at 297 nm, which can be attributed to ligand centered $\pi-\pi^*$ transitions. The second feature is a peak with maximum at 401 nm, which can be attributed to spin-allowed metal to ligand charge transfer ($^1\text{MLCT}$) transitions. The final feature is a tail extending beyond 500 nm corresponding to forbidden metal to ligand charge transfer ($^3\text{MLCT}$) transitions. The emission spectrum of complex **15** in aqueous solution is also similar to that observed for the precursor complex with features observed at 533 and 586 nm in water and in phosphate buffer solution observed for the precursor complex with features at 532 and 587 nm as shown **Figure 102b**.

2) Effect of pH

As mentioned above, the quaternary ammonium derivative complex has been synthesized with the aim of endowing the structure with a permanent positive charge and thus removing its acid base protonation equilibria. Therefore, it was expected that the complex will not show any significant pH dependence as shown in **Figure 103**.

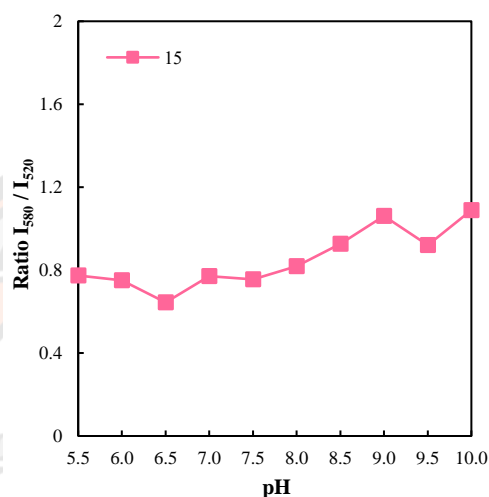


Figure 103 Ratio luminescence intensity at 580/520 nm of complex **15** in various pH 5.5-10.0 from phosphate buffer. Emission spectra were recorded with $\lambda_{\text{ex}} = 390$ nm.

A small change in the ratio of emission intensity at 580 and 520 nm was observed for complex **15** as a function of pH. The ratio value change from 0.8 at pH 5.5 to a value of 1.1 at pH 10.0. This change is much smaller than that observed for the parent butyl complex **3**, for which this ratio changes from 0.8 to 5.1 in the pH range from 5.5 to 10.0. This behavior can be rationalized by the expected limited sensitivity of complex **15** to pH changes due to the absence of an amino group that can undergo protonation/deprotonation equilibria.

6.3 Density functional theory calculations

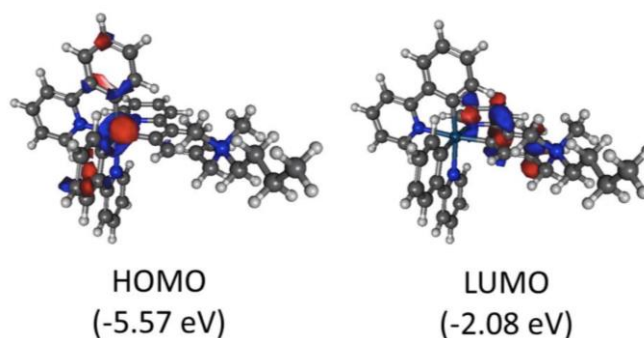


Figure 104 The HOMO and LUMO orbitals of complex **15** calculated in dichloromethane.

Density Functional Theory (DFT) calculations for complex **15** were carried out using the polarizable continuum model as an approximation for solution in a vacuum environment as well dichloromethane ($\epsilon = 8.93$). The calculations were carried out at the B3LYP/LANL2DZ level of theory. The molecular orbitals were visualized using the Gabeit program package. The results shown in **Figure 104** indicate that the HOMO orbital is predominantly located on the iridium atom while the LUMO orbital localizes mainly on the substituted phenylpyridine ligand. This is in line with the expected MLCT nature of the transitions observed absorption spectrum. The geometry and orbitals localization for the HOMO orbital of the T_1 state can be seen in **Figure 105**. The electrons in this state are also located on the substituted phenylpyridine ligand indicating MLCT character of the emission. The calculated energy difference between this state and the singlet HOMO state (2.16 eV) is also in line with the observed emission.

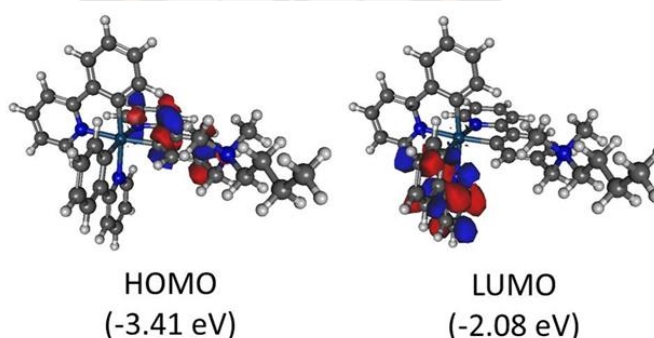
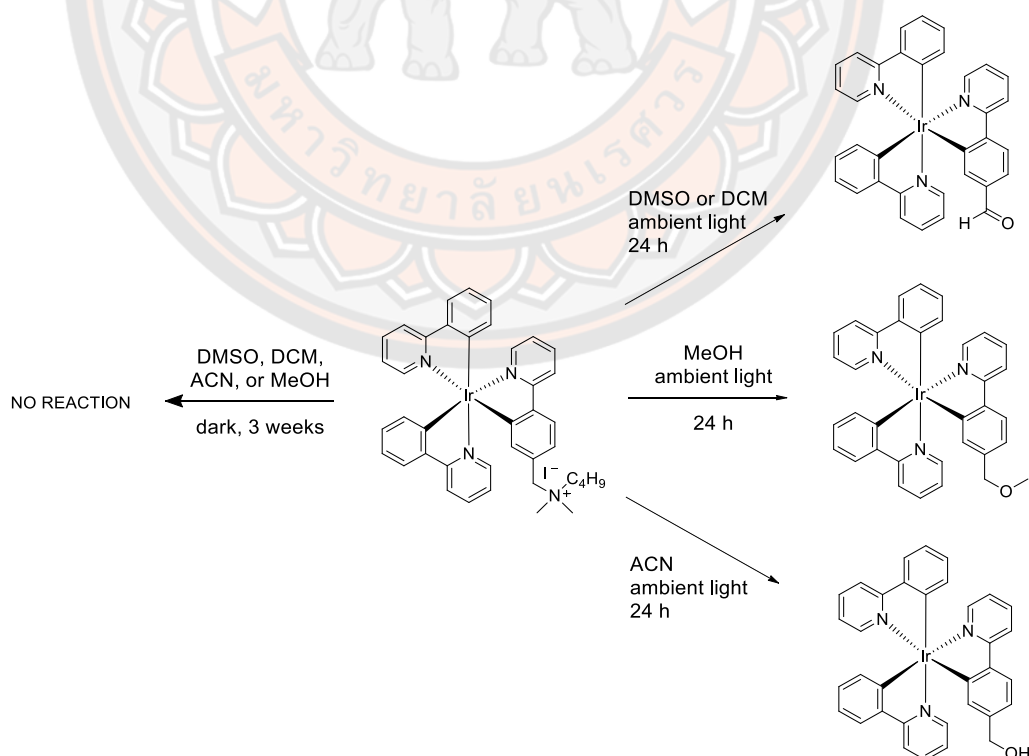


Figure 105 The HOMO and LUMO orbitals of the triplet state of complex **15** calculated in dichloromethane.

6.4 Photoreactivity

As noted above, a serendipitous observation from ^1H -NMR provided support for the decomposition of complex **15**. This ^1H -NMR analysis of the decomposed sample indicated that the product formed in this process is the precursor complex *fac*- $[\text{Ir}(\text{ppy})_2(\text{fppy})]$. Subsequent experiments, where different solutions of complex **15** in DMSO were simultaneously kept in dark and irradiated by ambient light in the laboratory, provided evidence suggesting that the observed reactivity was indeed promoted by light (**Scheme 29**). It was observed, using mass spectroscopy, that complex **15** kept in solution in dark remained intact for more than 3 weeks (**Figure 106**). On the other hand, decomposition was observed in the solution kept in light within 24 hours (**Figure 107**). To gain further understanding, the reaction was then carried out in dichloromethane, methanol, and acetonitrile to evaluate the effect of the solvents. In all cases, the solution kept in dark did not undergo decomposition of complex **15**, providing further support for the light induced nature of the transformation. Different products have been observed in these reactions. In the reaction carried out in dimethyl sulfoxide and dichloromethane, formation of *fac*- $[\text{Ir}(\text{ppy})_2(\text{fppy})]$ was observed as shown in **Figure 107** and **Figure 108**, respectively. The reaction in methanol lead to the formation of the corresponding methyl ether (**Figure 109**). Finally, the reaction in acetonitrile lead to formation of several unidentified products as well as of the corresponding alcohol (**Figure 110**).



Scheme 29 Photo transformation of complex **15** in different solutions.

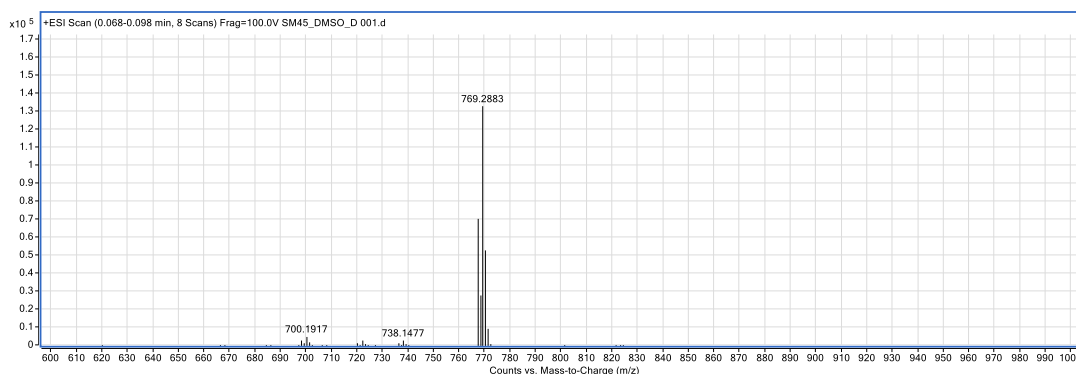


Figure 106 ES⁺ HRMS spectrum of complex 15 kept in dark at ambient conditions in DMSO solution for 3 weeks.

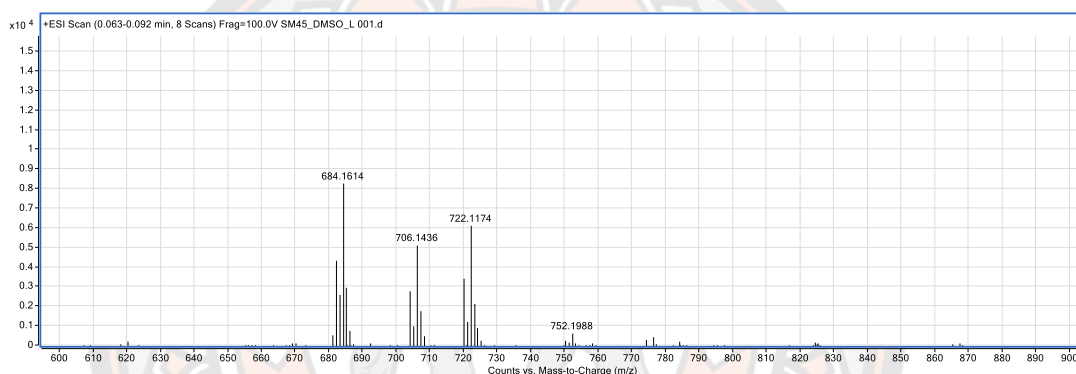


Figure 107 ES⁺ HRMS spectrum of complex 15 kept in light at ambient conditions in DMSO solution for 24 hours.

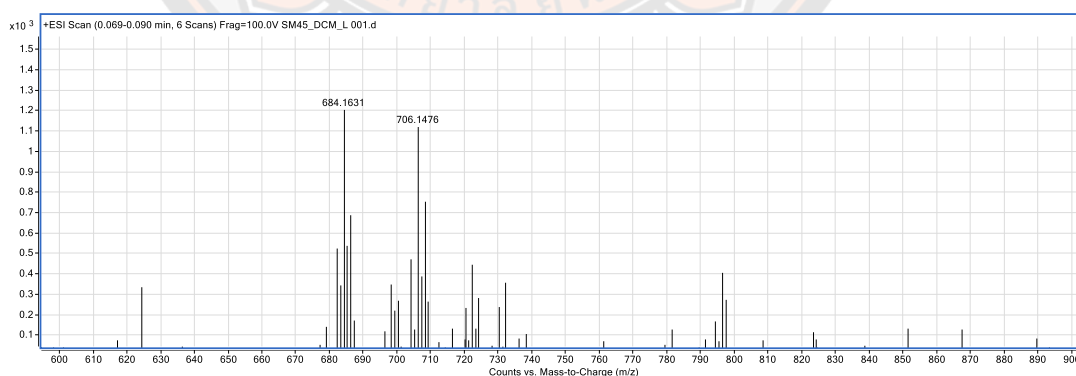


Figure 108 ES⁺ HRMS spectrum of complex 15 kept in light at ambient conditions in DCM solution for 24 hours.

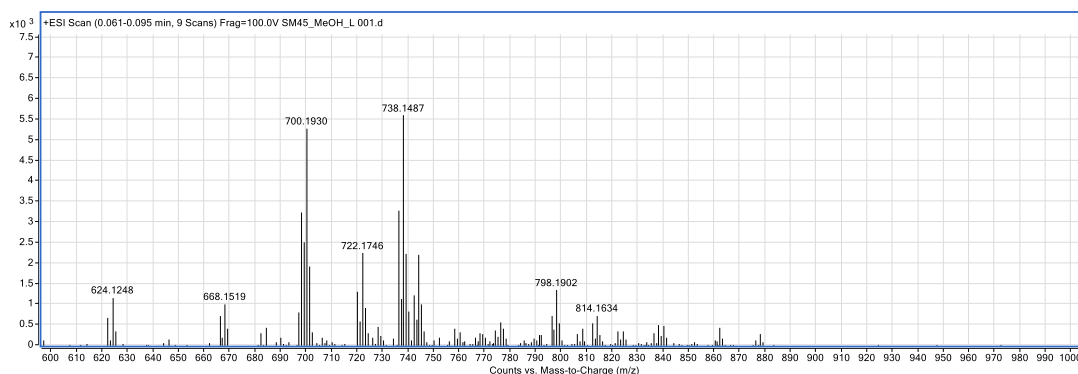


Figure 109 ES⁺ HRMS spectrum of complex **15** kept in light at ambient conditions in MeOH solution for 24 hours.

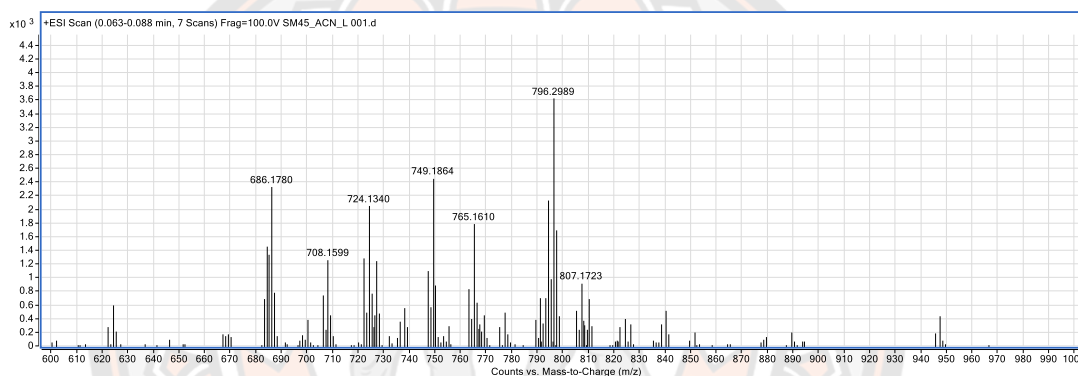
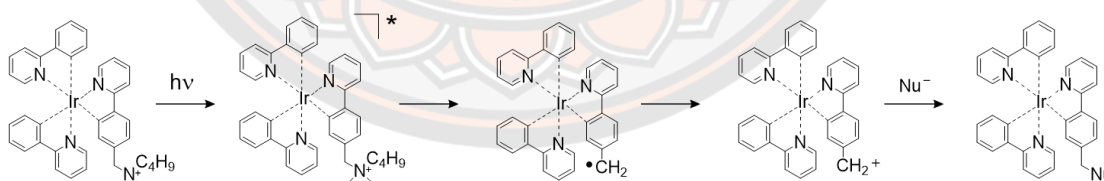


Figure 110 ES⁺ HRMS spectrum of complex **15** kept in light at ambient conditions in ACN solution for 24 hours.



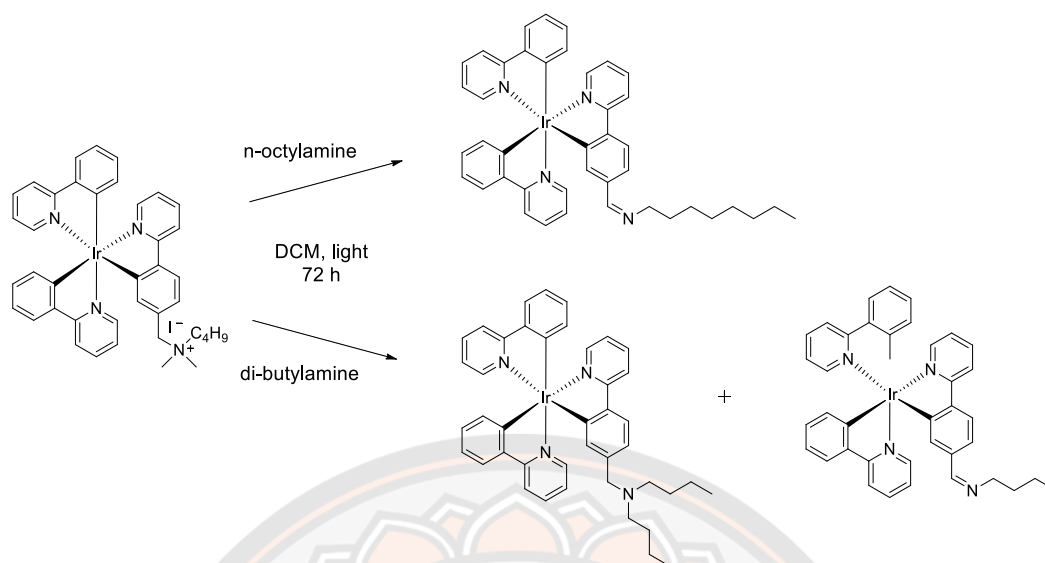
Scheme 30 Proposed mechanism for the photoconversion of complex **15**.

Scheme 30 shows the proposed mechanism for the reactivity of complex **15** promoted by light. It is presumed that the photoexcitation of complex **15** leads to oxidative quench of the excited state of the complex by the quaternary ammonium moiety [124, 125]. This step would lead to the cleavage of the C–N bond and produce a benzylic radical on the benzylic position of the iridium complex and oxidize the iridium center to oxidation state +4. Similar reductive decomposition of quaternary ammonium salts has been observed in electrochemical studies [126, 127]. Subsequent

one electron transfer from the benzylic radical to the iridium center would lead to restoring of oxidation state +3 on the iridium center and formation of an electrophilic benzylic cation that could be involved in a reaction with various nucleophilic species, which could be water present in the DMSO solvent in this case. It should also be noted that the reactions were performed in the presence of oxygen, which is the likely reason for the observation of oxidation of the initial product from containing a hydroxy methyl group to the formyl group in *fac*-[Ir(ppy)₂(fppy)] (**Figure 106**). As mentioned above, the formation of this precursor complex was confirmed ¹H-NMR of the reaction mixture (**Figure 99**) with the appearance of the aldehyde peak at 9.62 ppm.

The involvement of electrophilic species in the photodegradation reactions described above suggested the possibility that such species could undergo reactions with other nucleophiles (**Scheme 30**). Therefore, reactions with benzylamine, benzyl alcohol, and benzyl hydrosulfide were carried out as models for reactions with N, O, and S nucleophiles (**Scheme 31**). These experiments have been carried out using a household lamp with an LED bulb to ensure more controlled irradiation. Reactivity was observed in all cases. However, only the reactions with benzylamine and benzyl alcohol resulted in formation of discernable products. The product formed when the reaction was carried out in the presence of benzylamine was the corresponding benzyldiene imine (**Figure 111**). This observation is in line with the presumed mechanism involving the formation of an electrophilic species, its capture by a nucleophile, and subsequent oxidation. The reaction with benzyl alcohol resulted in the formation of the corresponding ether (**Figure 112**). The reaction was then performed with several other amines leading to similar observations. **Table 26** shown predicted masses for products formed during photochemical transformations of complex **15**.

Interestingly, while the reaction with octylamine resulted in the formation of the corresponding imine as in the previous reactions. HRMS (ES)⁺ mass spectrum **Figure 113** of imine reveals the molecular ion of interest at 795.3 m/z along with some of the starting material complex **15** at 769.4 m/z. While HRMS (ES)⁺ mass spectrum **Figure 114** of reaction complex **15** with di-butylamine resulted in the formation of both the tertiary amine at 797.3 m/z and an imine where one of the butyl groups has been removed from the nitrogen atom to imine at 739.2 m/z.



Scheme 31 Photo transformation of complex 15 in the presence of secondary and tertiary amine.

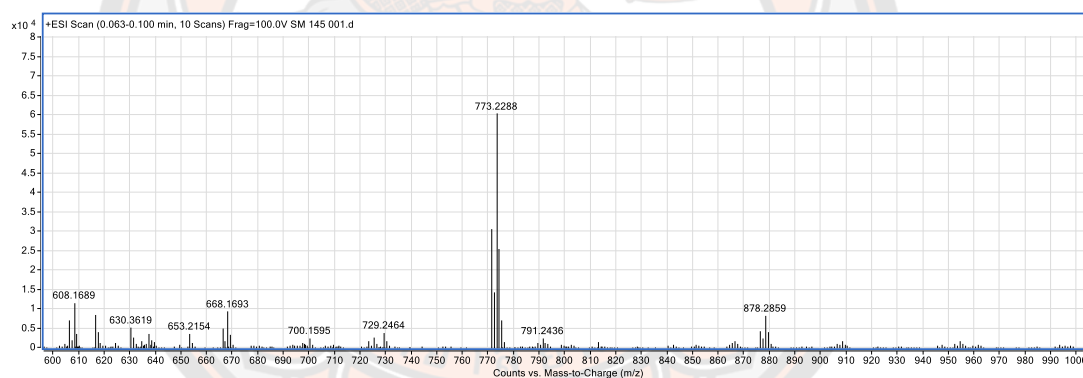


Figure 111 ES⁺ HRMS spectrum of reaction mixture containing complex 15 and benzylamine irradiated by LED lamp for 72 hours.

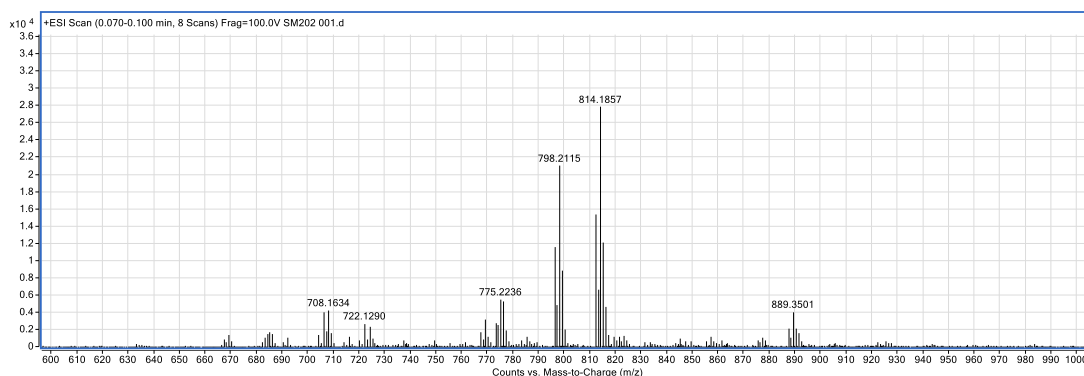


Figure 112 ES⁺ HRMS spectrum of reaction mixture containing complex 15 and benzylalcohol irradiated by LED lamp for 72 hours.

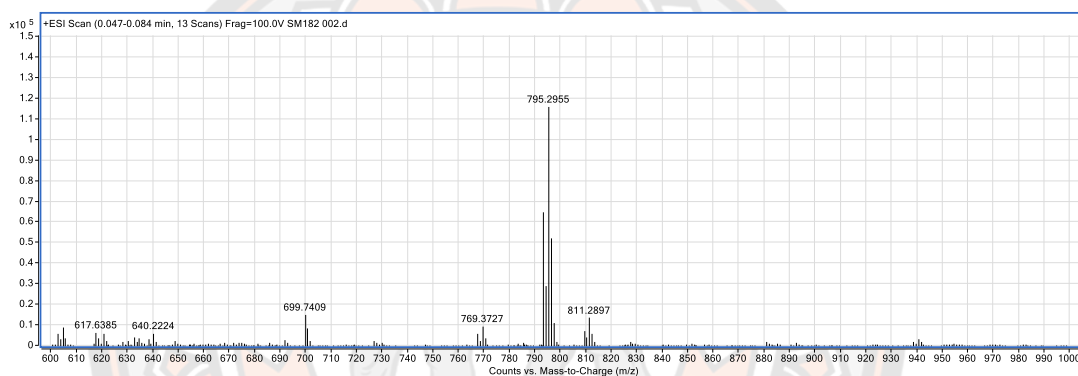


Figure 113 ES⁺ HRMS spectrum of reaction mixture containing complex 15 and octylamine irradiated by LED lamp for 72 hours.

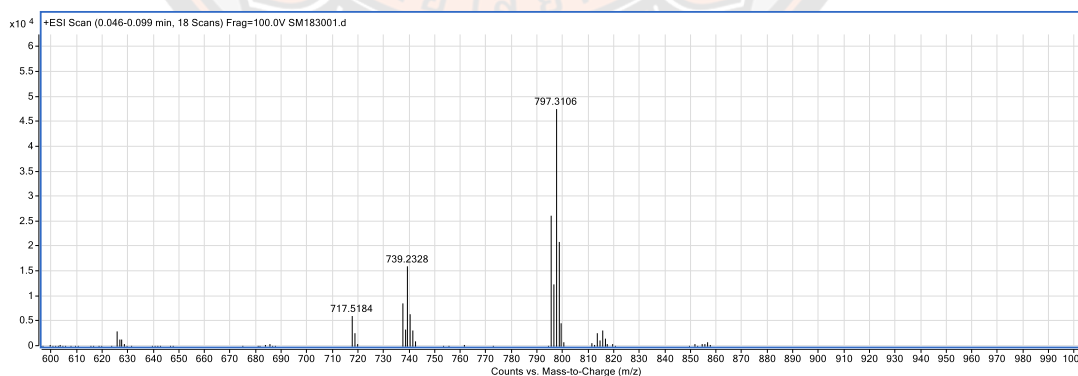


Figure 114 ES⁺ HRMS spectrum of reaction mixture containing complex 15 and di-butylamine irradiated by LED lamp for 72 hours.

Table 26 Structures and predicted masses for products formed during photochemical transformations of complex 15.

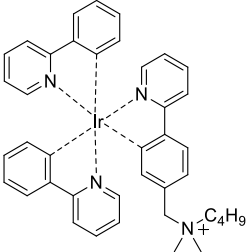
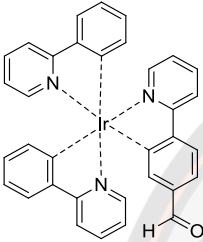
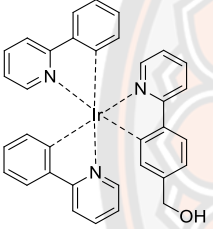
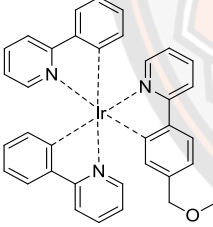
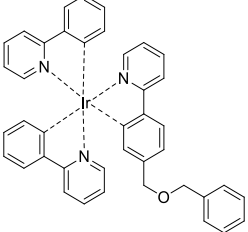
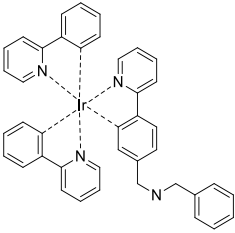
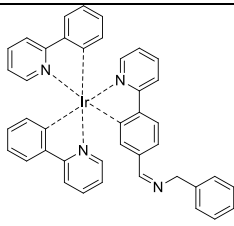
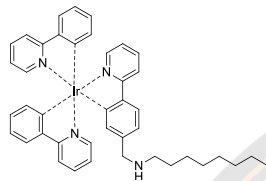
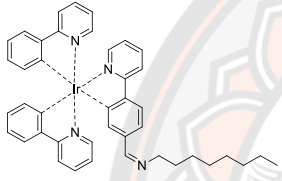
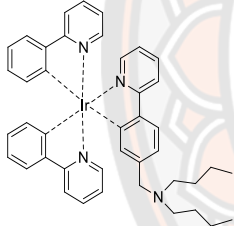
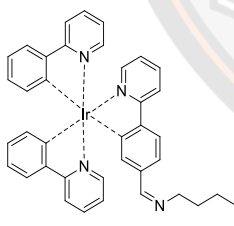
Structure	M	[M+H] ⁺	[M+Na] ⁺	[M+K] ⁺
	769.3	-	-	-
	683.2	684.2	706.1	722.1
	685.2	686.2	708.2	724.1
	699.2	700.2	722.2	738.2
	775.2	776.2	798.2	814.2
	774.2	775.2	797.2	813.2

Table 26 (cont.)

Structure	M	[M+H] ⁺	[M+Na] ⁺	[M+K] ⁺
	772.2	773.2	795.2	811.2
	796.3	797.3	819.3	835.3
	794.3	795.3	817.3	833.3
	796.3	797.3	819.3	835.3
	738.2	739.2	761.2	777.2

6.5 Cellular experiments

As for the aminoalkyl complexes discussed above, the ultimate purpose for the quarternary complex **15** is its potential application as cellular stain in live cell imaging studies. These experiments will be described above.

6.5.1 Cytotoxicity

The investigation of the behavior of complex **15** in cells was performed in NIH-3T3 cells. Initially, the cytotoxicity of complex **15** was investigated. The plot of cell viability of the NIH-3T3 as a function of concentration of complex **15** for 1h and 24h exposure can be seen in **Figure 115**. The IC_{50} values for 1h and 24 h exposure are more than 50 μ M and 20 μ M, respectively. These results show that complex **15** is significantly less toxic than the precursor amine complex **3**, which showed IC_{50} values below 10 μ M.

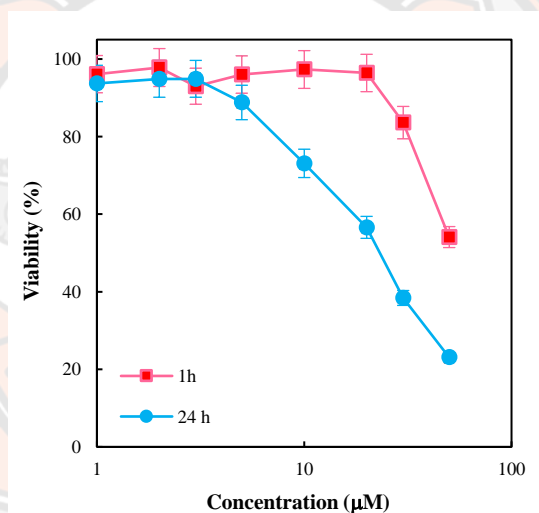


Figure 115 Plot viability of NIH-3T3 cells versus concentration of complex **15**.

6.5.2 Microscopy studies

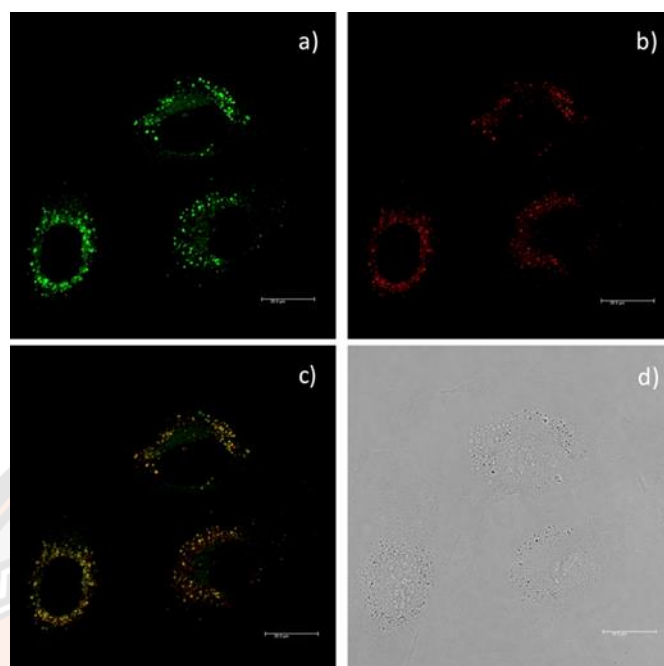


Figure 116 Fluorescence microscopy images of NIH-3T3 cells obtained with complex **15** (λ_{ex} 355 nm, λ_{em} 450-650 nm) (a), lysotracker red (λ_{ex} 543 nm HeNe laser, λ_{em} 600-650 nm) (b). Panel c shows the RGB overlay of panels a and b; $P = 0.80$, while panel d is the brightfield image. (Scale bar: 20 μm).

The potential of complex **15** to act as a cellular stain was then investigated using laser scanning confocal microscopy to evaluate its ability to enter cells and its subcellular localization properties. The imaging experiment was carried out after loading the cells with 5 μM solution of the complex for 1h. The ability of complex **15** to cross cellular membranes can be seen from **Figure 116a**) The cellular localization of complex **15** was compared to that of lysotracker red (**Figure 116b**). Good overlap ($P > 0.80$) of both channels was observed (**Figure 116c**) supporting lysosomal localization of complex **15**.

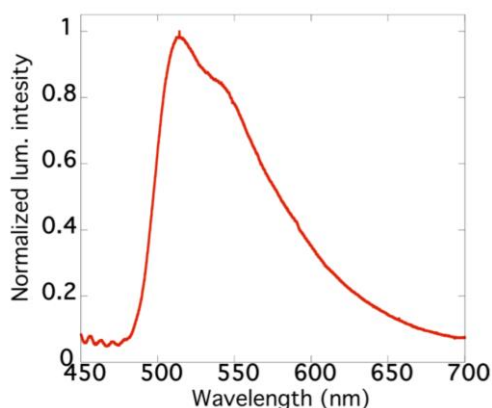


Figure 117 Emission spectrum obtained from lysed cells loaded with complex **15**.

Emission spectra were recorded for cell lysate and are shown in **Figure 117**. These are similar to those observed in solution indicating the integrity of the iridium coordination sphere after internalization in the cells. In addition, the brightness of cell images for cells loaded with complex **15** (5 μM for 24h), was 680% higher than that of blank cells, which supports the presence of emissive cyclometalated iridium complex in the cells. Uptake of complex **15** was evaluated using ICP-MS analysis of cell lysates for the presence of iridium after their exposure to 5 μM solution of complex **1** for 24 h. The observed intracellular iridium concentration was 3.4 μM , which is significantly higher than that for blank sample, further supporting the ability of complex **15** to translocate across the cell membrane.

Finally, the possibility to perform imaging with complex **15** using two photon excitation was evaluated. The imaging was performed using excitation at 720 nm and the image is shown in **Figure 118**.

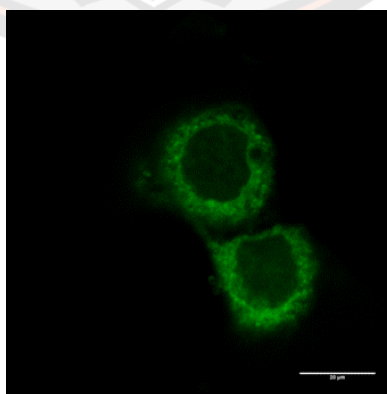
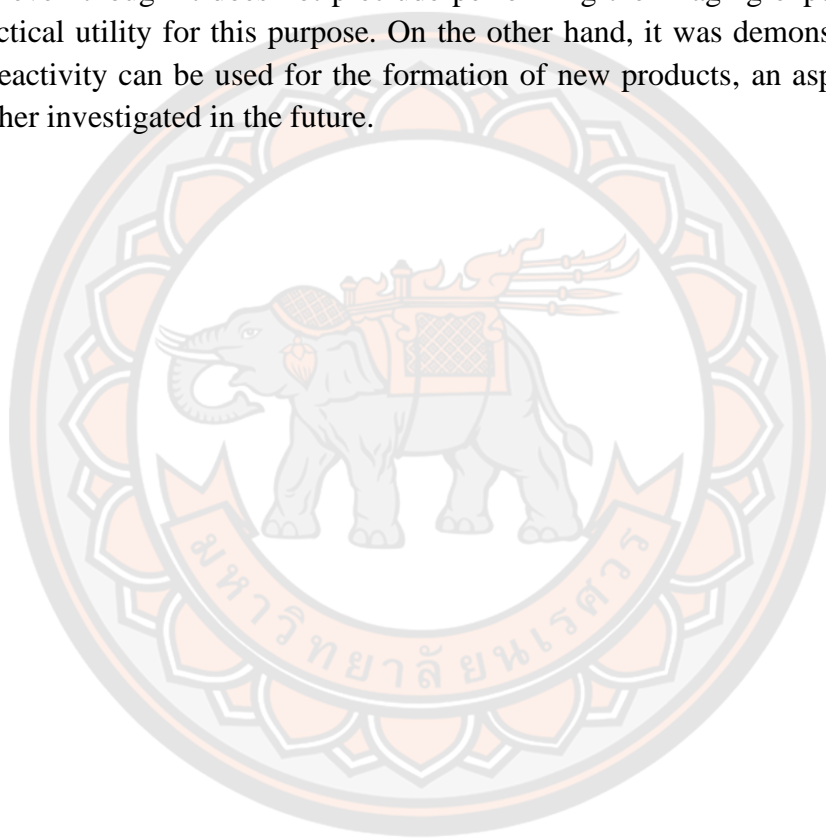


Figure 118 Two photon microscopy image of NIH-3T3 cells incubated with complex **15** and acquired at 720 nm excitation, with emission collected using a 510 nm longpass filter.

6.6 Conclusion

In conclusion, a novel tris-cyclometalated iridium(III) complex (**15**) containing a quaternary ammonium group has been synthesized and investigated. The complex shows good photophysical properties enabling its use as a cellular stain in fluorescence microscopy. Cellular imaging experiments have demonstrated that the complex is less toxic than its secondary amine precursor, which was previously reported by our group, but shows lysosomal localization as this previously reported complex. The ability possibility to perform two-photon imaging with complex **15** has been demonstrated as well. However, complex **15** exhibits rapid photoreactivity, which, even though it does not preclude performing the imaging experiments, limits its practical utility for this purpose. On the other hand, it was demonstrated that this photoreactivity can be used for the formation of new products, an aspect which will be further investigated in the future.



CHAPTER VII

PHOTOREDOX CATALYSIS WITH TRIS-CYCLOMETALATED IRIIDIUM COMPLEXES

7.1 Introduction

Photoactive cyclometalated iridium complexes are being used for other applications apart from luminescence and imaging. One of these applications, which has seen significant increase of interest in recent years lies in the field of photoredox catalysis. Photoactive cyclometalated, iridium complexes, both bis-cyclometalated and tris-cyclometalated, have been used in this context depending on the requirements placed on the redox properties of the photocatalyst. The prototypical tris-cyclometalated iridium complex *fac*-[Ir(ppy)₃] has been used most commonly in case where tris-cyclometalated iridium complexes are being used as the photocatalyst.

The ultimate goal of this part of the project is to immobilize the iridium complexes on solid support so that the catalyst could be recovered from reaction mixtures and reused. However, the initial goal of this work was to investigate whether the functional groups present in the derivatives synthesized in our laboratory will have and detrimental effect on their ability to catalyze these reactions.

7.2 Results and discussion

7.2.1 Reactions with soluble complexes

As mentioned above, while our ultimate goal is to carry out immobilization of the iridium catalyst on a suitable support in order to obtain a catalyst that could be recycled we have first attempted these reactions with the soluble iridium complexes described in the previous chapters, to be able to evaluate whether the presence of the functional groups might have a detrimental effect. Complexes **2**, **3**, and **15** containing the formyl, amino butyl, amino octyl, and quaternary ammonium groups, respectively, were used for these exploratory photoredox reactions. This investigation of the suitability of our complexes as photoredox catalysts was carried out using three reactions reported in the literature, namely: 1) α -Amino C–H arylation reaction of amine, 2) β -arylation of ketones, 3) direct arylation of allylic sp^3 C–H bonds reaction, and 4) difluoromethylation. The reaction set up used in these experiments can be seen in **Figure 119**.

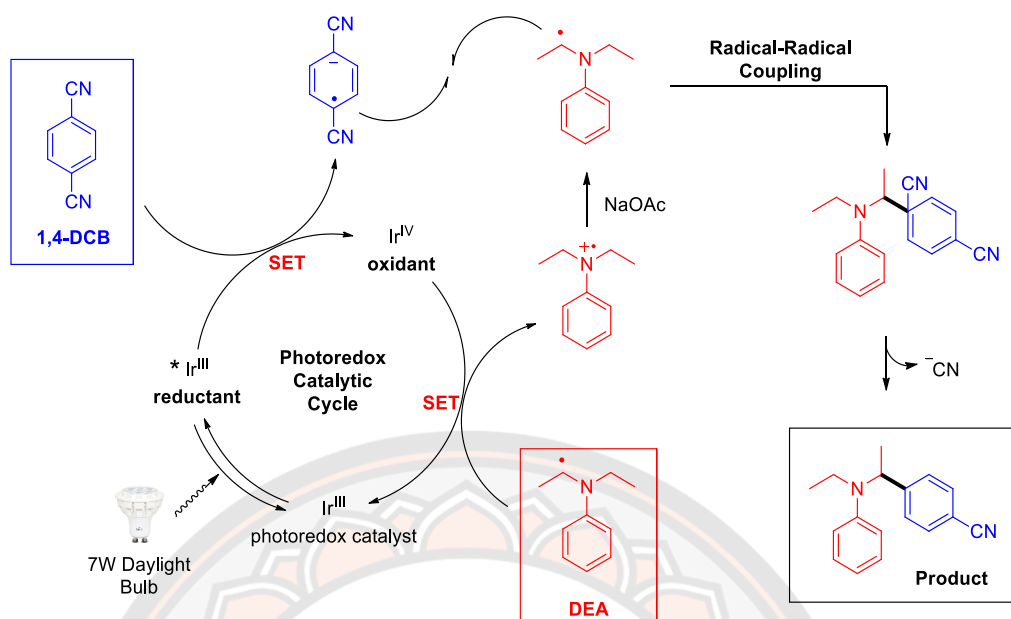


Figure 119 Set up reaction of photoredox catalysis.

1) α -Arylation of amines

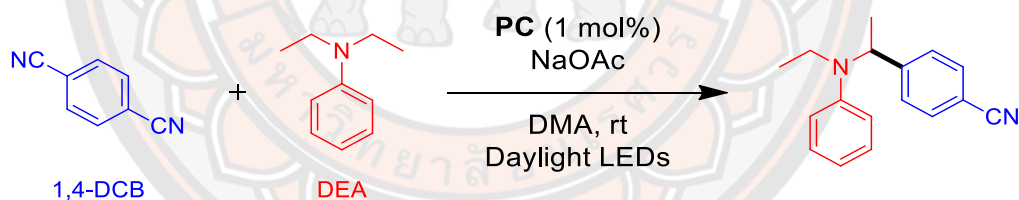
The first reaction that we investigated in this work was the α -amino C–H arylation reaction reported by MacMillan and co-workers in 2011. Possible mechanism for this reaction can be seen in **Scheme 32** the visible-light photoredox α -amino C–H arylation reaction. Our analysis method to detect potential coupling products was based on mass spectroscopy where peaks of correct molecular weight were an indication of possible coupling between the two reactants, and $^1\text{H-NMR}$ spectroscopy.

Proposed mechanistic explanation for the C–H arylation process is described in **Scheme 32**. Tris-cyclometalated iridium(III) complexes, as Ir^{III} , are reversibly promoted to their excited state form $^*\text{Ir}^{\text{III}}$ upon absorption of a photon. $^*\text{Ir}^{\text{III}}$ is a powerful reductant and, upon encountering 1,4-Dicyanobenzene (1,4-DCB), could donate an electron to form the corresponding arene radical anion (DEA). The resultant Ir^{IV} is a strong oxidant and capable of undergoing a single-electron transfer event with amine, generating amine radical cation, as well as re-forming Ir^{III} and thereby completing the photoredox cycle. The C–H bonds adjacent to the nitrogen atom are weakened by about 40 kcal/mol and can undergo deprotonation by NaOAc (where OAc is an acetoxy group) to give α -aminoradical. A radical-radical coupling reaction could then unite intermediates, the key bond-forming step. Elimination of CN^- would then form the aromatized benzylic amine of 4-(1-(ethyl(phenyl)amino)ethyl)benzonitrile.



Scheme 32 Photoredox C-H arylation: proposed mechanistic pathway. SET, single-electron transfer.

Table 27 Conditions of photoredox catalyzed reaction of α -amino C-H arylation carried out with complexes 2, 3, and 15.



Entry	Catalyst (1 mol%)	1,4-DCB (equiv.)	DEA (equiv.)	Reaction condition	Time/ h
1a	2	1	3	DMA, LEDs, N ₂	24
2a	3	1	3	DMA, LEDs, N ₂	24
3a	15	1	3	DMA, LEDs, N ₂	24

The reaction conditions for the photoredox catalyzed α -amino C–H arylation reactions carried out with complexes **2**, **3**, and **15** are summarized in **Table 27**. The results of these reactions are then displayed in **Figure 120**, **Figure 121**, and **Figure 122**. Which show the mass and ^1H -NMR spectra of the crude reaction mixtures carried out with complexes **2**, **3**, and **15**, respectively. The evidence for the formation of the expected product in reaction **1a-3a** can be seen in both mass and ^1H -NMR spectra. The expected product has a molecular weight of 250.2 g/mol and the MS spectra from all of the reactions contain peaks with m/z ratio of 251.2 corresponding to the $[\text{M}+\text{H}]^+$ peak of the expected product. In addition, the ^1H -NMR spectra of the crude products contained the expected peaks. The most prominent of these indicating the formation of the product are the two doublets, at 7.6 and 7.5 ppm, from the para substituted cyano containing aromatic ring, and the multiplet at 5.1 ppm, from the α -substituted position. It is noteworthy that the ^1H -NMR spectrum for reaction **2a** carried out with complex **3** contains only minor impurities.

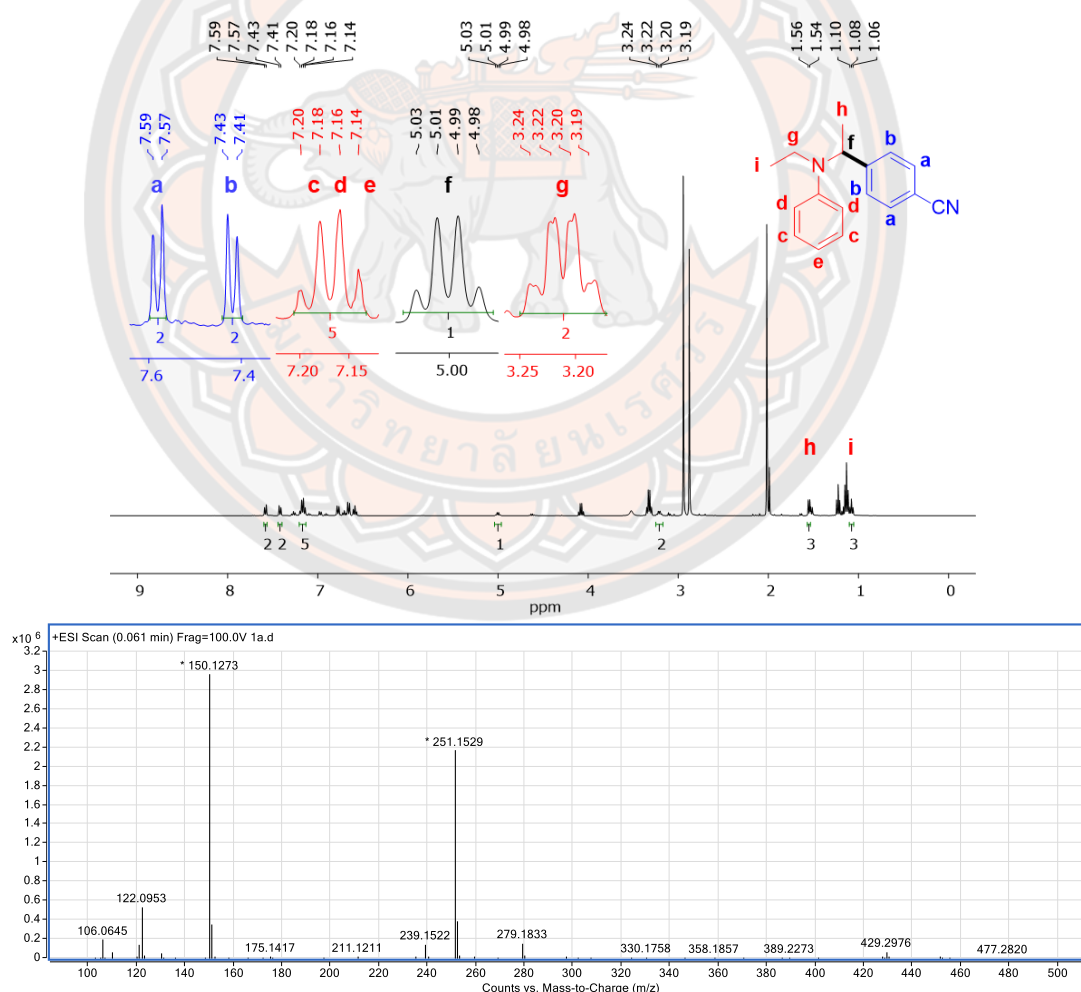


Figure 120 ^1H -NMR (top) and Mass spectrum (bottom) of **1a**.

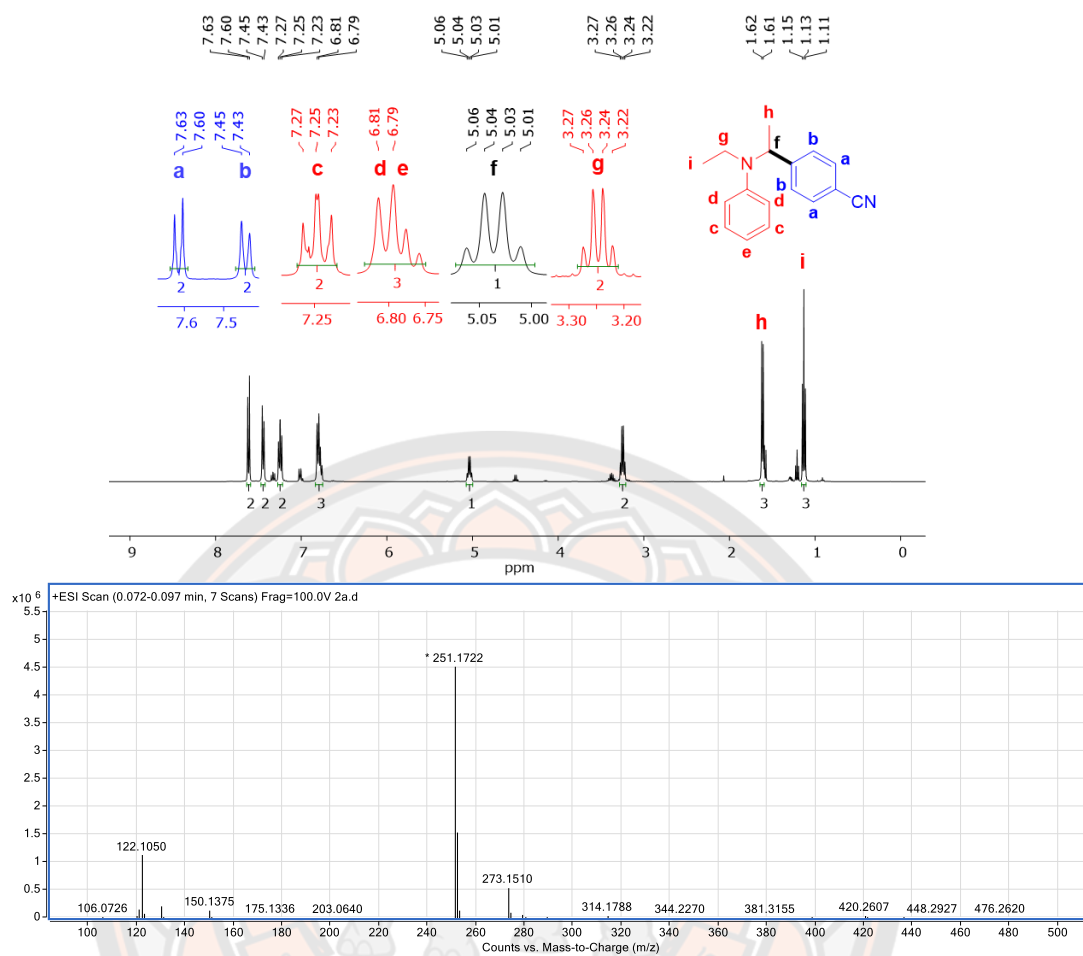


Figure 121 ¹H-NMR (top) and Mass spectrum (bottom) of 2a.

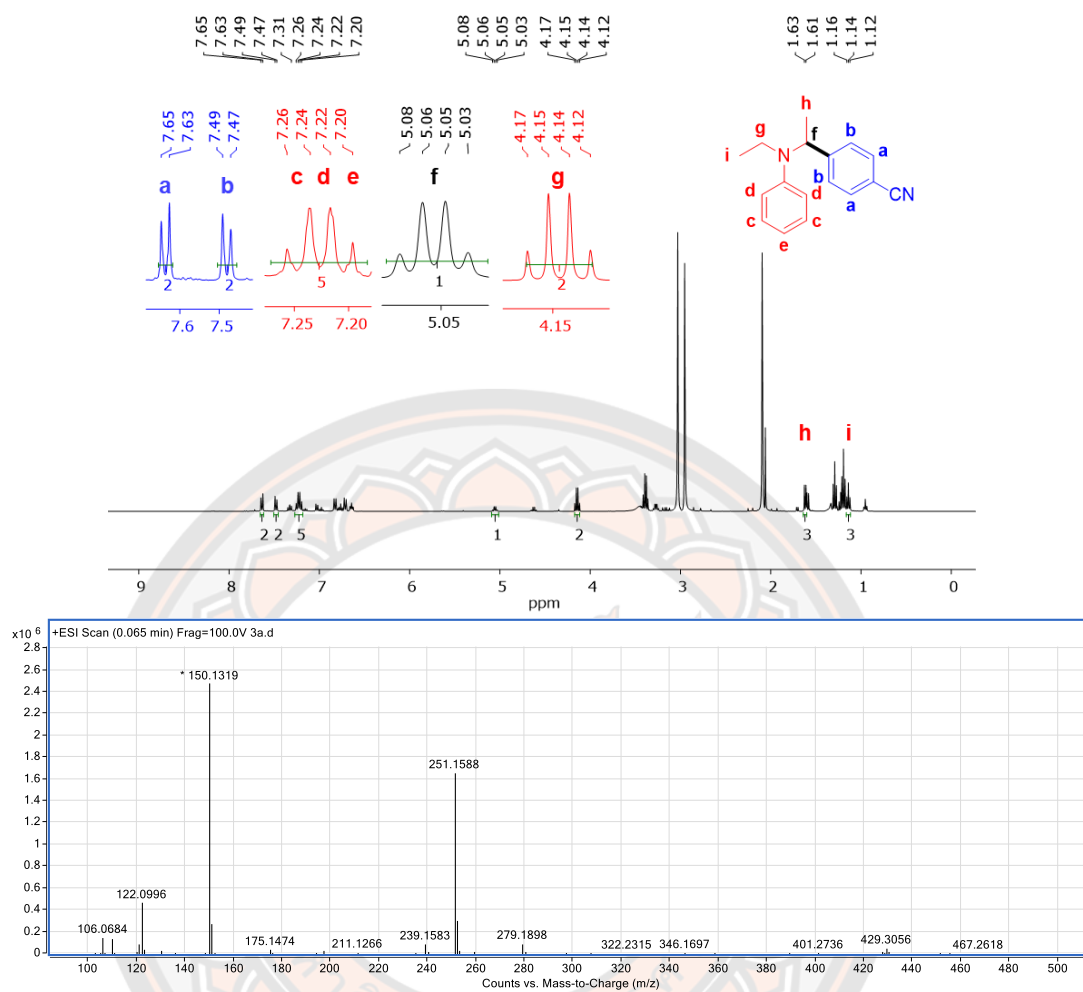
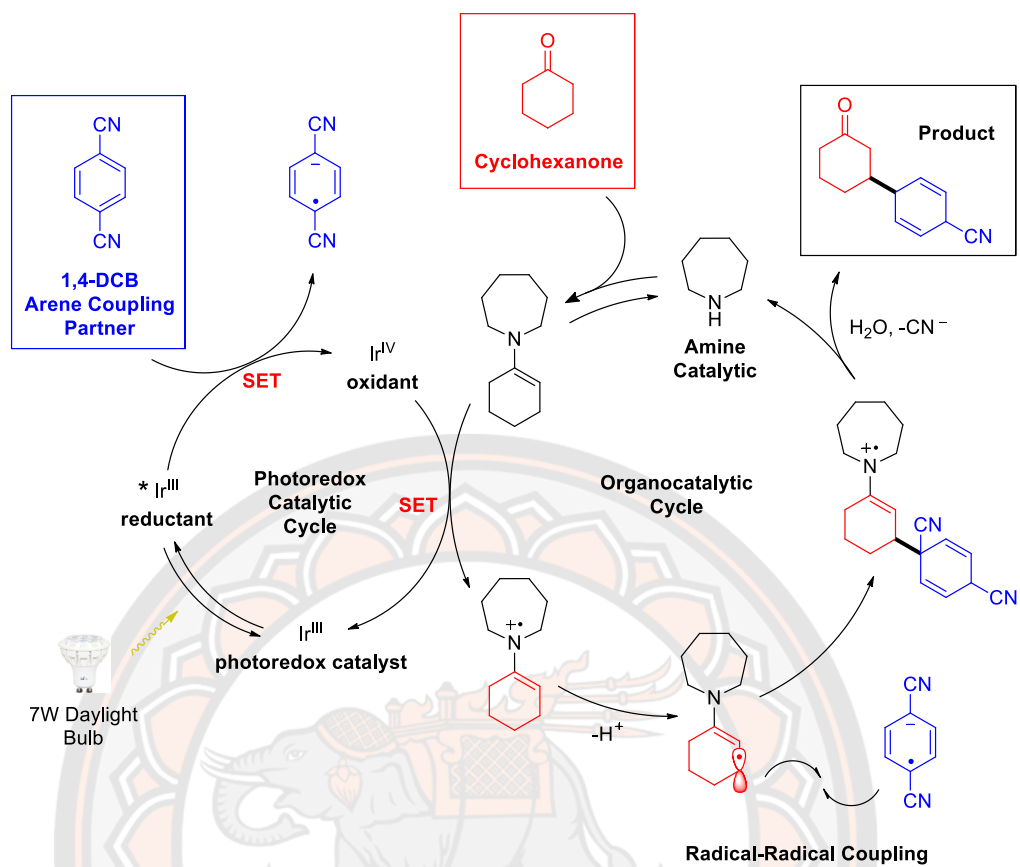


Figure 122 ^1H -NMR (top) and Mass spectrum (bottom) of 3a.

2) β -Arylation of ketones

The second reaction that we investigated in this work was the direct β -arylation of ketones reported by MacMillan and co-workers in 2013. Possible mechanism for this reaction can be seen in **Scheme 33** the visible-light photoredox direct β -functionalization of carbonyls. Our analysis method to detect potential coupling products was based on $^1\text{H-NMR}$ at appropriate chemical shifts and exhibiting expected splitting patterns were an indication of possible proton coupling of product in the crude reaction mixture. The reaction conditions for reactions carried out using complex **5** are summarized in **Table 28**.

The proposed mechanistic explanation for the β -arylation process is described in **Scheme 33**. Tris-cyclometalated iridium(III) complexes, as Ir^{III} , are reversibly promoted to their excited state form $^*\text{Ir}^{\text{III}}$ upon absorption of a photon. $^*\text{Ir}^{\text{III}}$ is a powerful reductant and, upon encountering 1,4-Dicyanobenzene (1,4-DCB), could donate an electron to form the corresponding arene radical anion (DEA). The resultant Ir^{IV} is a strong oxidant and capable of undergoing a single-electron transfer event with amine, in this case the enamine formed in the reaction. This step re-forming Ir^{III} and thereby completes the photoredox cycle. The reaction also forms a radical cation from the enamine, which is subsequently deprotonated by acetate present in the reaction mixture on the β -carbon. The resulting radical and the radical anion originally formed from 1,4-dicyanobenzene undergo a radical-radical recombination to form an anion, which finally aromatizes by eliminating a cyanide and forms the desired product of 4-(3-Oxocyclohexyl)benzonitrile.



Scheme 33 Proposed mechanistic pathway of β -arylation of ketones via photoredox and organic catalysis. SET, single-electron transfer.

Table 28 Conditions of photoredox reaction of β -arylation carried out with complex **5**.

1,4-DCB + cyclohexanone $\xrightarrow[\text{DMPU, H}_2\text{O, AcOH, rt, Daylight LEDs}]{\text{PC (1 mol\%), DABCO, azepane}}$ Product

Entry	Catalyst (1 mol%)	1,4-DCB (equiv.)	Cyclohexanone (equiv.)	Reaction condition	Time/ h
1b	5	1	5	DMPU, LEDs, N ₂	24

The reaction conditions for the photoredox catalyzed β -arylation of ketones reactions carried out with complex **5** is summarized in **Table 28**. The results of these reactions are then displayed in **Figure 123**. Which show the ¹H-NMR spectra of the crude reaction mixture for the reactions carried out with complex **5**. The evidence for the formation of the expected product in reaction **1b** can be seen in ¹H-NMR spectra of the crude products, which contain the expected peaks. The most prominent of these indicating the formation of the product are the two doublets, at 7.6 and 7.3 ppm, from the para substituted cyano containing aromatic ring, and the multiplet at 3.5 ppm, from the β -substituted position.

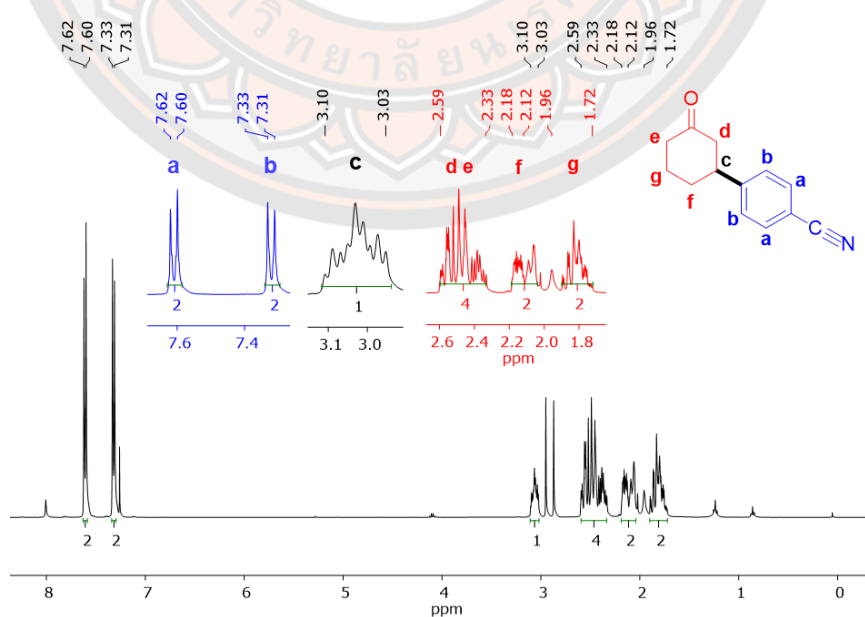
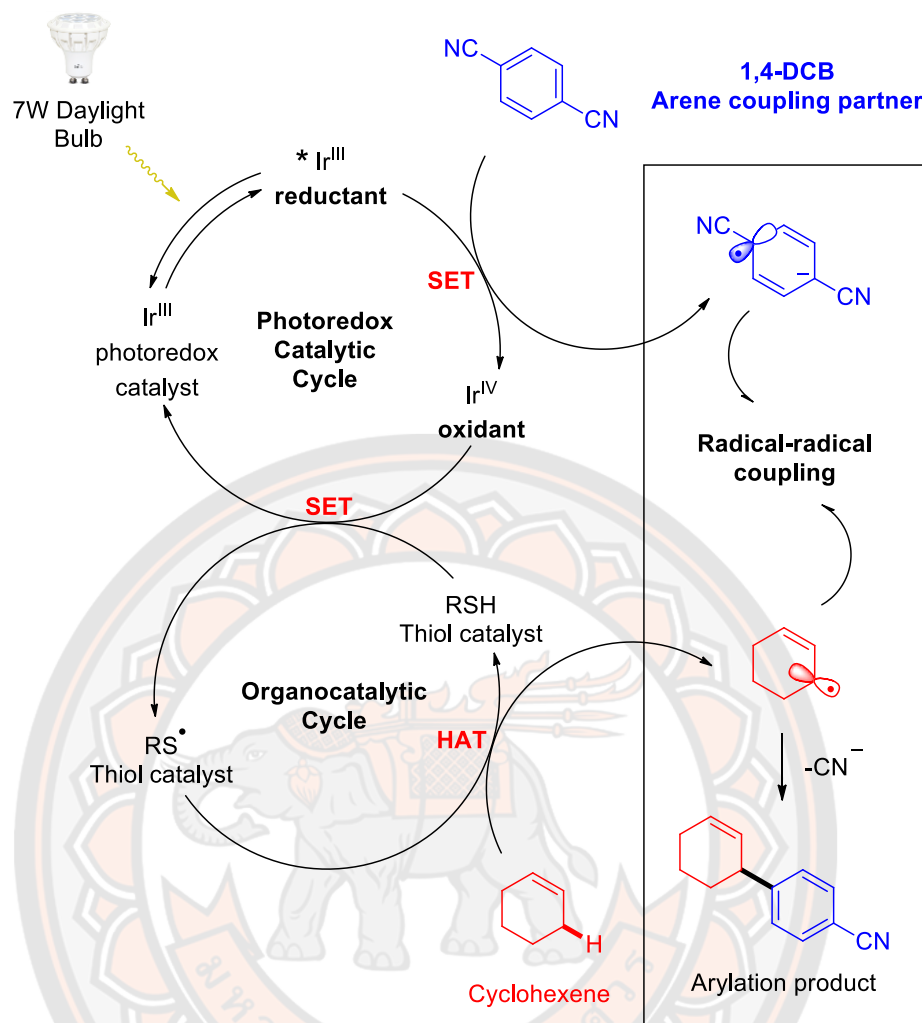


Figure 123 ¹H-NMR spectrum of **1b**.

3) Direct allylic C-H arylation

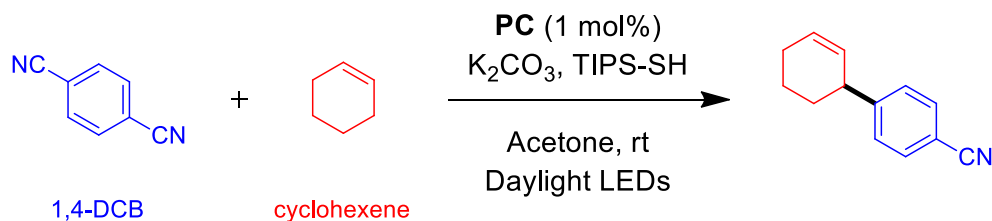
The third reaction that we investigated in this work was the direct arylation of allylic sp^3 C-H bonds reported by MacMillan and co-workers in 2015. Possible mechanism for this reaction can be seen in **Scheme 34**. Our analysis method to detect potential coupling products was based on ^1H NMR investigation of the crude product.

The proposed mechanistic explanation for the direct arylation of allylic sp^3 C-H bonds process shown **Scheme 34** can be described as follows. Tris-cyclometalated Ir(III) complexes (Ir^{III}) are reversibly promoted to their excited state form $^*\text{Ir}^{\text{III}}$ upon absorption of a photon. $^*\text{Ir}^{\text{III}}$ is a strong reductant, which acts as one electron reducing agent for the 1,4-dicyanobenzene to generate an arene radical anion. This single electron transfer results in the formation of the radical ion of 1,4-dicyanobenzene and oxidation of the iridium complex from oxidation state +III to oxidation state +IV. The oxidized iridium complex Ir^{IV} undergoes a second single electron transfer reaction with the thiol. The weakly acidic thiol is deprotonated to thiolate anion is readily oxidized by the photocatalyst. The thiyl radical is then expected to abstract an allylic hydrogen atom from the alkene substrate to provide allylic radical and the regenerated catalyst. An intermolecular radical-radical coupling and subsequent elimination of cyanide serve to construct the new C-C bond and form the arylation product of 1',2',3',4'-Tetrahydro-[1,1'-biphenyl]-4-carbonitrile. The reaction conditions for reactions carried out using complexes **2**, **3**, and **15** are summarized in **Table 29**.



Scheme 34 Proposed mechanism for the direct arylation of allylic C-H bonds via photoredox and organic catalysis. SET, single-electron transfer.

Table 29 Conditions of photoredox reactions of allylic arylations carried out with complexes **2**, **3**, and **15**.



Entry	Catalyst (1 mol%)	1,4-DCB (equiv.)	Cyclohexene (equiv.)	Reaction condition	Time/ h
1c	2	1	5	Acetone, LEDs, N ₂	24
2c	3	1	5	Acetone, LEDs, N ₂	24
3c	15	1	5	Acetone, LEDs, N ₂	24

The results of the attempted allylic arylations carried out with complexes **2**, **3**, and **15** can be seen in the crude product ¹H-NMR spectra shown in **Figure 124**, **Figure 125**, and **Figure 126**. The ¹H-NMR spectra of the crude products contained the expected peaks. These inspection of these spectra indicates the presence of evidence for the formation of the desired product can be found in the case of reaction **2b** and **3c** catalyzed by complexes **3** and **15**, respectively. The most prominent of these indicating the formation of the product are the two doublets, at 7.5 and 7.3 ppm, from the para substituted cyano containing aromatic ring, the multiplets at 5.9 and 5.6 ppm corresponding to the double proton positions d and e, and the multiplet at 3.4 ppm, from the allylic C-H bond position. It is noteworthy that the ¹H-NMR spectrum for reaction **2c** carried out with complex **3** contains only minor impurities.

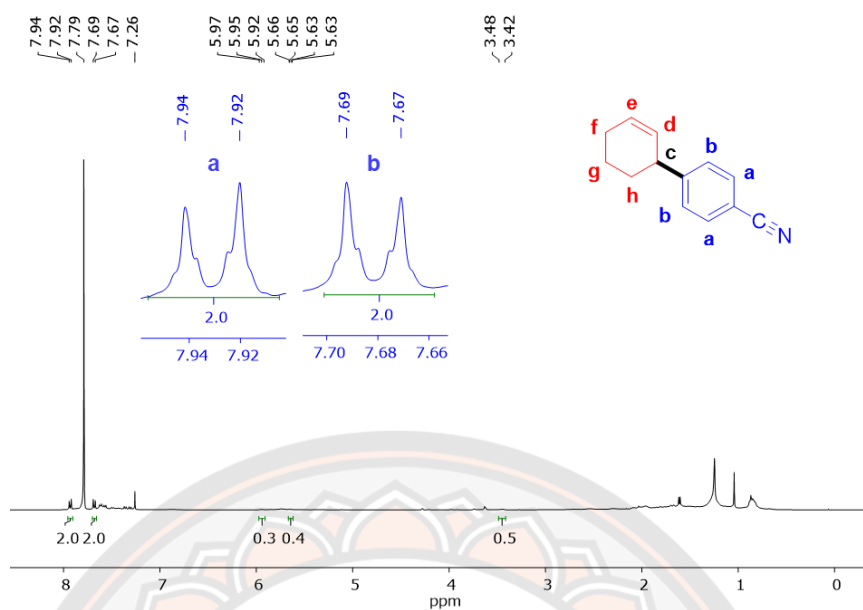


Figure 124 ^1H -NMR spectrum of compound 1c.

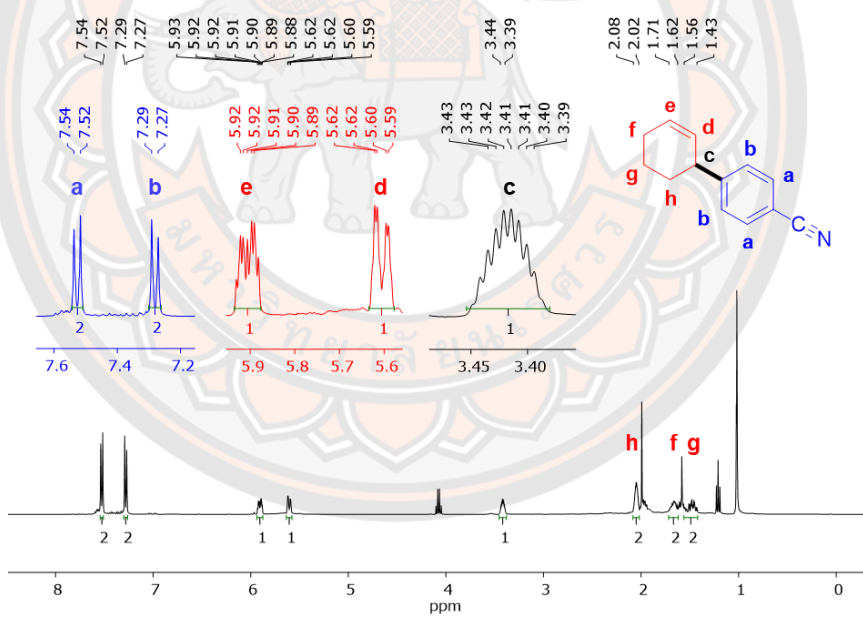


Figure 125 ^1H -NMR spectrum of compound 2c.

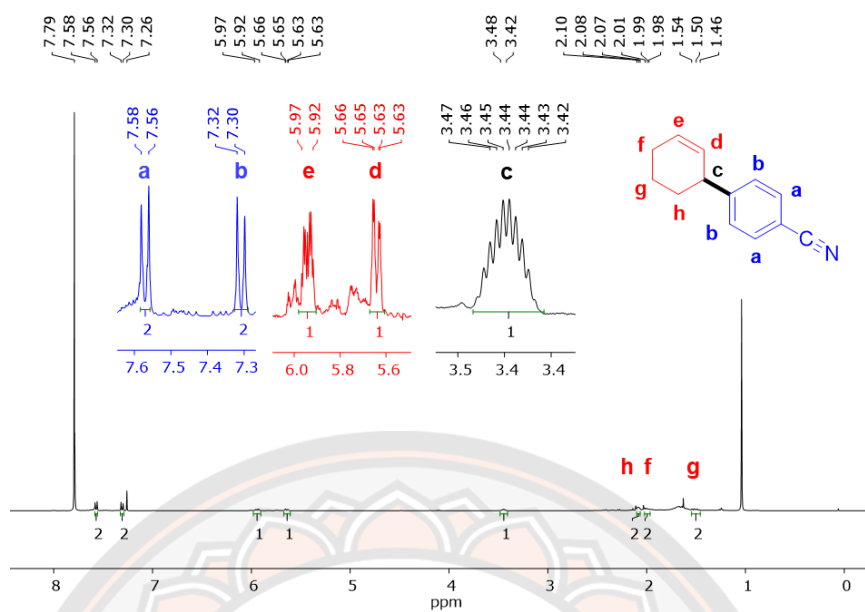
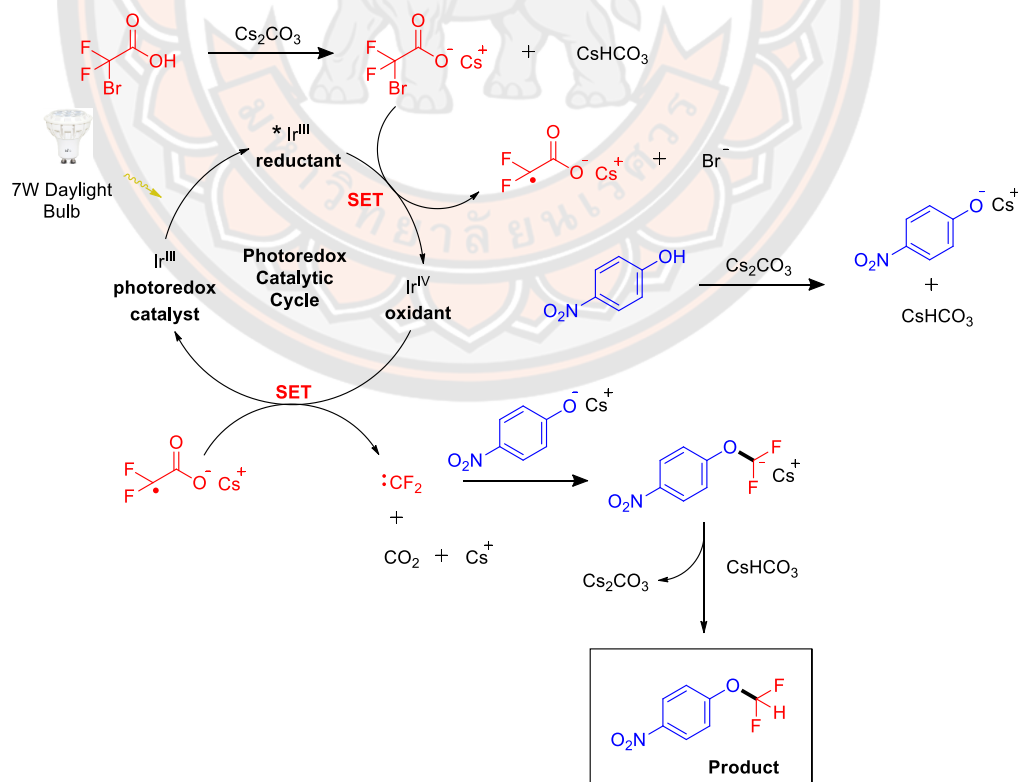


Figure 126 ¹H-NMR spectrum of compound 3c.

4) Difluoromethylation

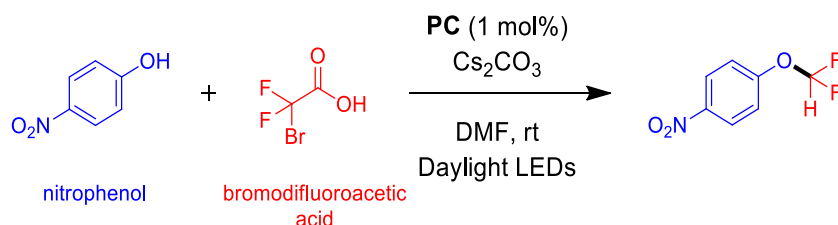
The final reaction that we investigated in this work was the difluoromethylation reported by Jinyan Yang and co-workers in 2017. Possible mechanism for this reaction can be seen in **Scheme 35** the visible-light photoredox difluoromethylation of phenols. Our analysis method to detect potential coupling products had its basis in ^1H -NMR in some cases ^{19}F -NMR as well.

The proposed mechanistic explanation for difluoromethylation process is shown in **Scheme 35** can be described as follows. Treatment of difluorobromoacetic acid with Cs_2CO_3 gives carboxylate and CsHCO_3 . Irradiation of photocatalyst Ir^{III} with visible light gives the excited-state $^*\text{Ir}^{\text{III}}$, and a single electron transfer (SET) from $^*\text{Ir}^{\text{III}}$ to $\text{BrCF}_2\text{COOCs}$ leads to Ir^{IV} and carbon-centered radical of $\text{BrCF}_2\text{COOCs}$ leaving Br^- . Treatment of nitrophenol with Cs_2CO_3 gives nitrophenol-Cs and CsHCO_3 . A SET of carboxylate anion to Ir^{IV} regenerates the photocatalyst Ir^{III} , freeing difluorocarbene, CO_2 , and Cs^+ . Reaction of difluorocarbene with nitrophenol-Cs donates 1-(cesiumdifluoromethoxy)-4-nitrobenzene, and subsequent treatment of 1-(cesiumdifluoromethoxy)-4-nitrobenzene with CsHCO_3 affords the desired difluoromethylation product of 1-(difluoromethoxy)-4-nitrobenzene. The reaction conditions for the difluoromethylation reaction carried out using complexes **2**, **3**, and **15** are summarized in **Table 30**.



Scheme 35 Proposed mechanistic pathway of difluoromethylation via photoredox and organic catalysis. SET, single-electron transfer.

Table 30 Reaction conditions for photoredox catalyzed difluoromethylation using complexes **2**, **3**, and **15**.



Entry	Catalyst (1 mol%)	Nitrophenol (equiv.)	Bromodifluoro acetic acid (equiv.)	Reaction condition	Time/ h
1d	2	1	1	DMF, LEDs, N ₂	24
2d	3	1	1	DMF, LEDs, N ₂	24
3d	15	1	1	DMF, LEDs, N ₂	24

The results from the photoredox difluoromethylation reactions carried out with complexes **2**, **3**, and **15** are shown in **Figure 127**, **Figure 128**, and **Figure 129** showing the ¹H-NMR and ¹⁹F-NMR spectra of the crude reaction mixtures. The reaction conditions reactions carried out with complexes **2**, **3**, and **15** are summarized in **Table 30**. The results of these reactions are then displayed in **Figure 127**, **Figure 128**, and **Figure 129**. The ¹⁹F-NMR spectra of the crude reaction mixtures were acquired for reactions carried out with complexes **2**, and **3**. The evidence for the formation of the expected product in reaction **1d-3d** can be seen in ¹H-NMR spectra. The ¹H-NMR spectra of the crude products contained the expected peaks. The most prominent of these indicating the formation of the product are the two doublets, at 8.1 and 7.2 ppm, from the para substituted aromatic ring, and the triplet at 6.6 ppm, from proton the position c. In addition, this investigation was carried out to evaluate ¹⁹F-NMR as the expected product Fluorine coupling at –81.7 ppm and the ¹⁹F-NMR from **1f** and **2f** of the reactions contain chemical shift at –82.8 and –82.8 ppm respectively, of the expected product.

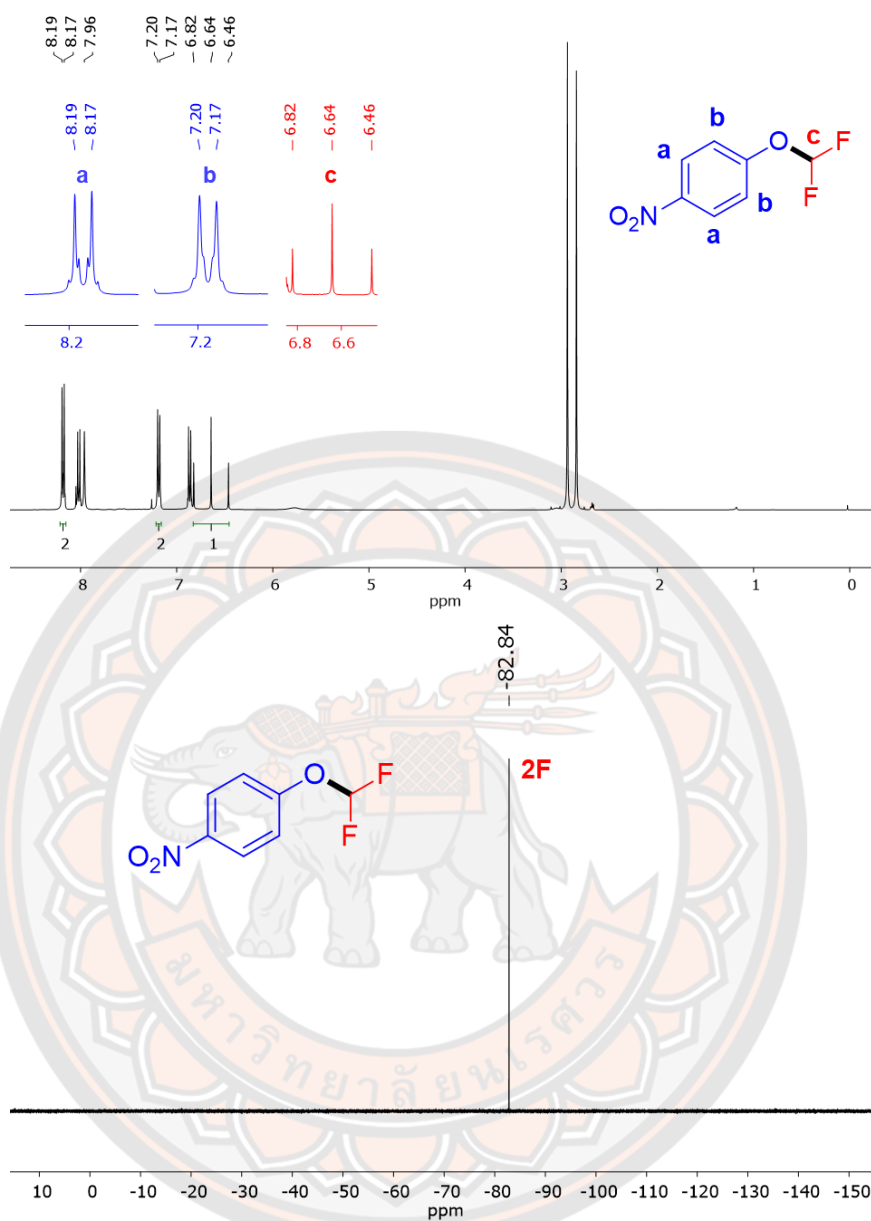


Figure 127 ^1H -NMR (top) and ^{19}F -NMR (bottom) spectrum of **1d** in CDCl_3 .

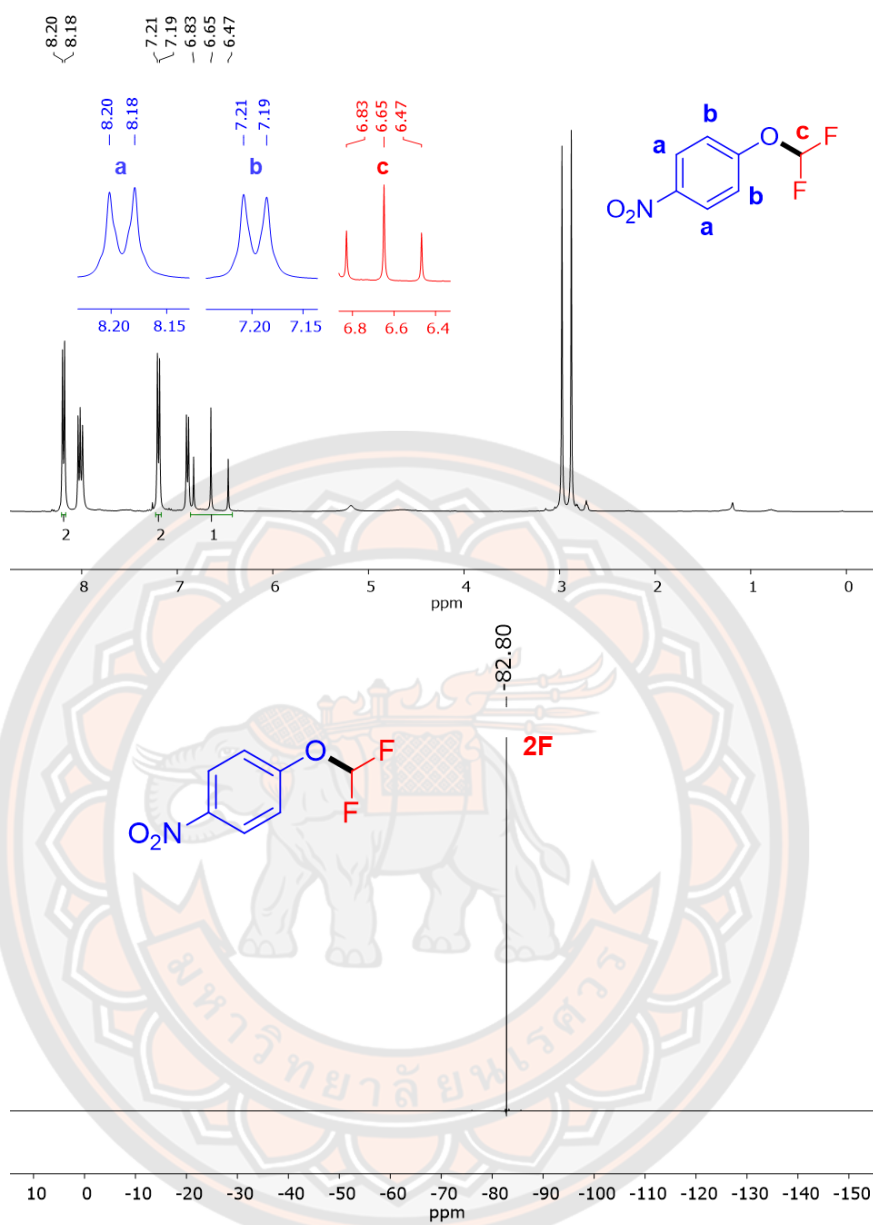


Figure 128 ^1H -NMR (top) and ^{19}F -NMR (bottom) spectrum of **2d** in CDCl_3 .

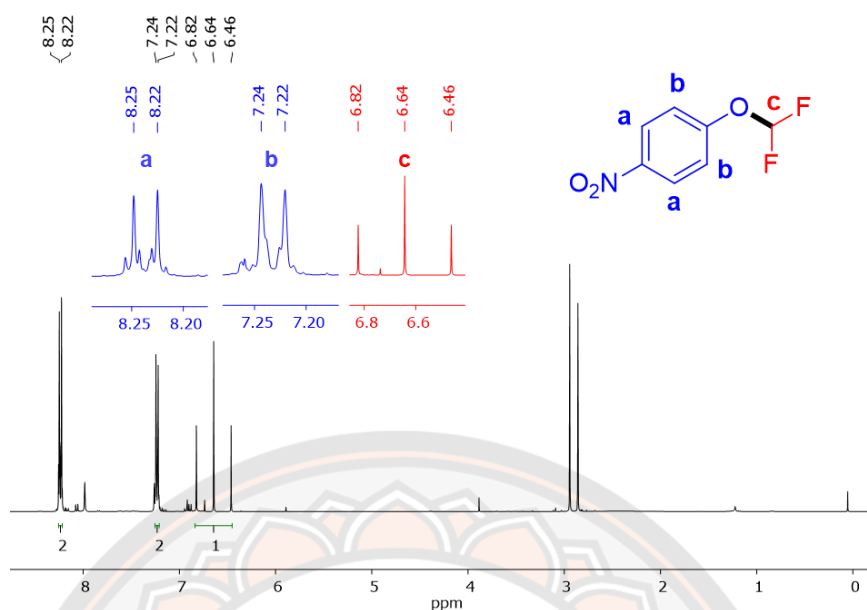


Figure 129 ^1H -NMR spectrum of **3d** in CDCl_3 .

In summary, carrying out the test photoredox reactions described above with complexes **2**, **3**, **5**, and **15** indicated that these complexes are capable of acting as photocatalysts in these transformations. Thus, the presence of the functional groups in these complexes did not result in abolishing of their catalytic ability. Interestingly, even complex **2** containing the formyl group, which significantly affects its photophysical and redox properties [42] exhibits catalytic properties. It is also evident that whatever degradation product forms from complex **15** in the photoreactions it does remain catalytically active as well. While there are a number of aspects of these reactions that do require further attention (e.g. isolated yields, catalyst loading, comparison of performance with $[\text{Ir}(\text{ppy})_3]$) these have not been investigated as the results obtained in this part of work were sufficient to justify proceeding to the next stage, attempts of catalyst immobilization.

7.2.2 Attempts at immobilization

The previous section describes initial photoredox catalysis experiments carried out homogeneous solution with a selection of soluble complexes as catalysts. However, the real goal of this work was to develop heterogeneous catalytic systems derived from these complexes as such heterogeneous catalysts offer the advantages of simplified product separation and catalyst recycling. We have therefore attempted to synthesize such immobilized catalysts by immobilizing of our homogeneous complexes on solid supports such as silica (SiO_2), polystyrene, and poly-L-lysine glass).

1) Synthesis

The synthesis of iridium complexes (**21-25**) has been attempted using the three steps, the final step is shown in **Scheme 36** and as described in section 4.3. Three different reaction steps were used. The steps were adopted from the literature and involve the synthesis of the chloride bridged dimer using the Nonoyama reaction, conversion of this dimer into *fac*-[Ir(ppy)₂(fppy)] using 4-(2-pyridyl)benzaldehyde, and the final step by the reductive amination of the formyl group to yield immobilized complexes **23** to **25**. The immobilization reaction using reductive amination involves the formation of an initial Schiff base between the aldehyde and amine groups (such as poly-L-lysine glass slide, and 2-aminomethyl(polystyrene)), which is then reduced to a secondary amine by the addition of sodium borohydride (NaBH_4). In the case of immobilized complexes **21** and **22** they were made in two steps from *fac*-[Ir(ppy)₂(fppy)] of an intermediate complex with the triethoxy silyl group made by the reductive amination step describe above. This intermediate was then reacted with either silica gel of TEOS to yield complexes **21** and **22** respectively.

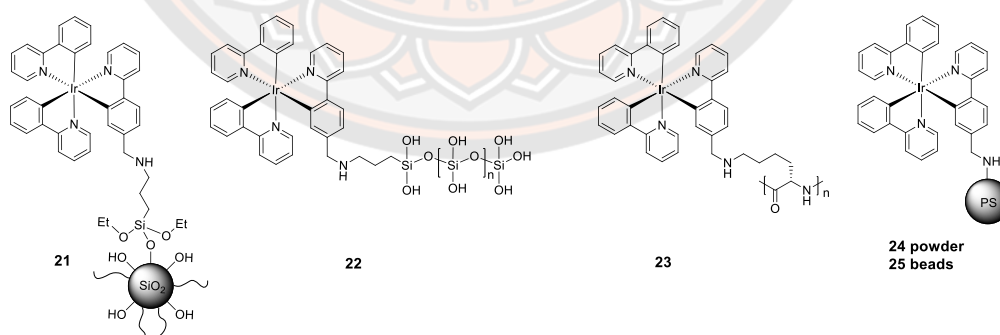
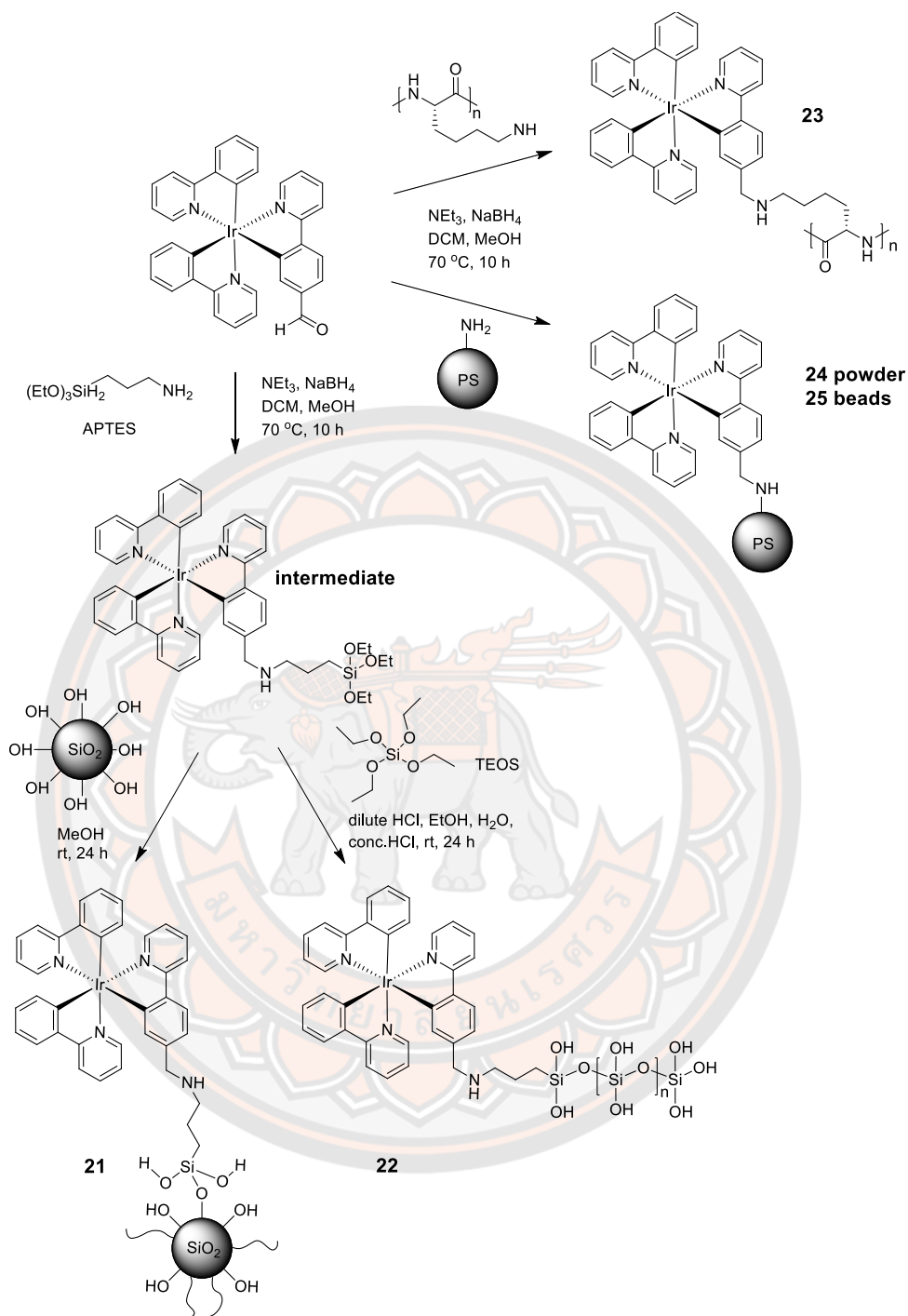


Figure 130 Structure of photoredox catalysts **21-25** immobilized on solid particles.



Scheme 36 The synthesis of iridium complexes (21-25) has been attempted using the three steps.

Table 31 **Structure of iridium immobilized on solid-support.**

Complex	Structure	Observed
21		
22		
23		
24		
25		

2) Photophysical properties

Figure 131 shows the normalized solid-state luminescence emission spectra of the immobilized iridium(III) complexes **21** to **25**. The emission spectra were obtained with excitation at 390 nm. The immobilized complexes **21** to **25** present emission maxima located at 531, 526, 541, 555, and 548 nm, respectively. In solid, these complexes are fluorescent in the green-yellow regions. The original support materials did not contain these emission peaks, thus their presence in the products provides supporting evidence for the immobilization of the iridium complexes. The relevant emission data are summarized in **Table 32**. It can be noticed that the emission of immobilized complex **23** is much weaker than for the other complexes, indicating low loading of the iridium units.

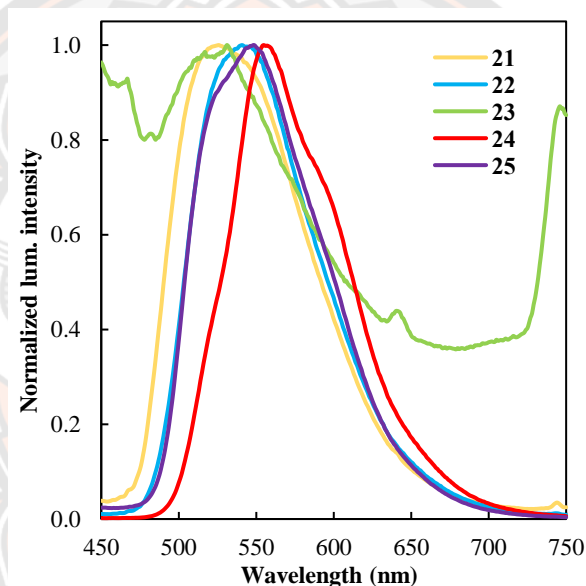


Figure 131 Normalized luminescence intensity in the solid state recorded for immobilized complexes **21** to **25** upon excitation the samples at 390 nm at room temperature.

Table 32 Relevant solid-state luminescence emission data of the immobilized iridium(III) complex.

Complex	λ_{em} (nm)
21	526
22	541
23	531
24	555
25	548

3) Stability

Stability of the immobilized catalysts is of crucial importance given the desire for their long term and repeated use. A serendipitous observation from mass provided support for the potential decomposition of immobilized complexes **21** to **24**. Subsequent experiments, where different solutions of complexes **21** to **25** in DMF were simultaneously kept in dark and irradiated by ambient light in the laboratory, provided evidence suggesting that the observed reactivity was indeed promoted by light. It was observed, using mass spectroscopy, that the complexes kept in solution in dark remained intact for more than 24 hours (**Figure 132, 134, 136, 138, and 140**). On the other hand, decomposition was observed in the solution kept in light within 24 hours (**Figure 133, 135, 137, 139, and 141**). This mass analysis of the decomposed sample indicated that the product formed in this process is the fragment $[\text{Ir}(\text{ppy})_2(\text{ppy-CH}_2\text{NHCH}_2)]^+$ given the corresponding isotopic pattern and molecular weight of 697.19 g/mol which were observed in the MS spectra shown in **Figure 133, 135, and 139**. There is no decomposition of immobilized complexes **23** and **25** in DMF solution after 24 hours when stored in light (**Figure 137 and 139**) and relatively very small intensity of this peak was observed for catalyst **24** (**Figure 138**). This is an important issue for the catalysts and will be investigated further in the future.

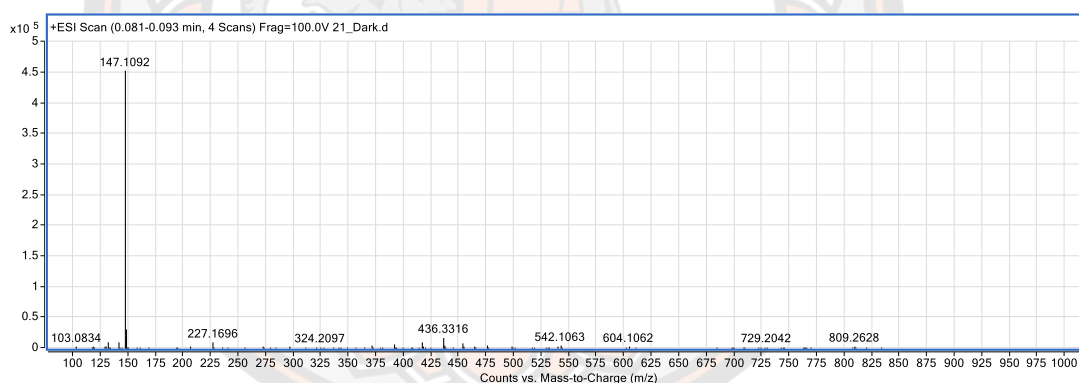


Figure 132 Mass spectrum of complex 21_Dark 24 h.

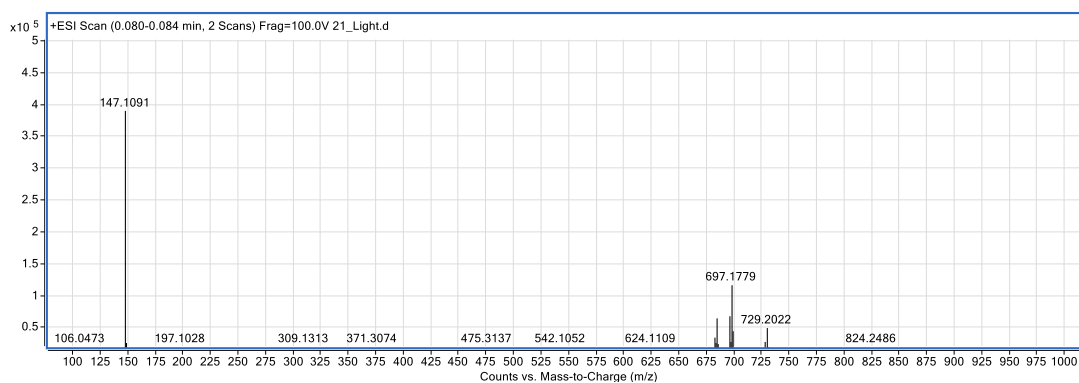


Figure 133 Mass spectrum of complex 21_Light 24 h.

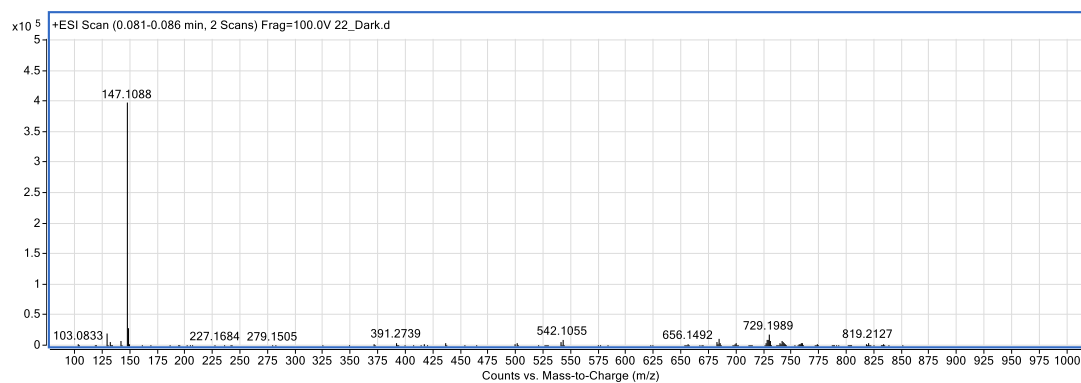


Figure 134 Mass spectrum of complex 22_Dark 24 h.

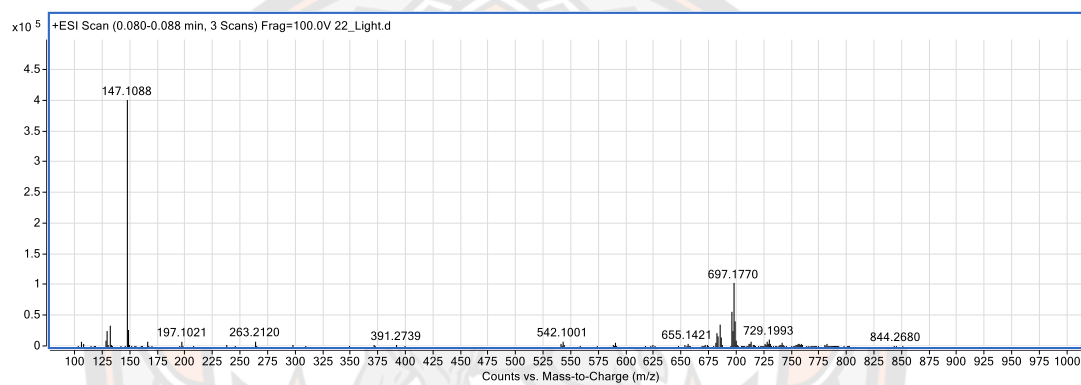


Figure 135 Mass spectrum of complex 22_Light 24 h.

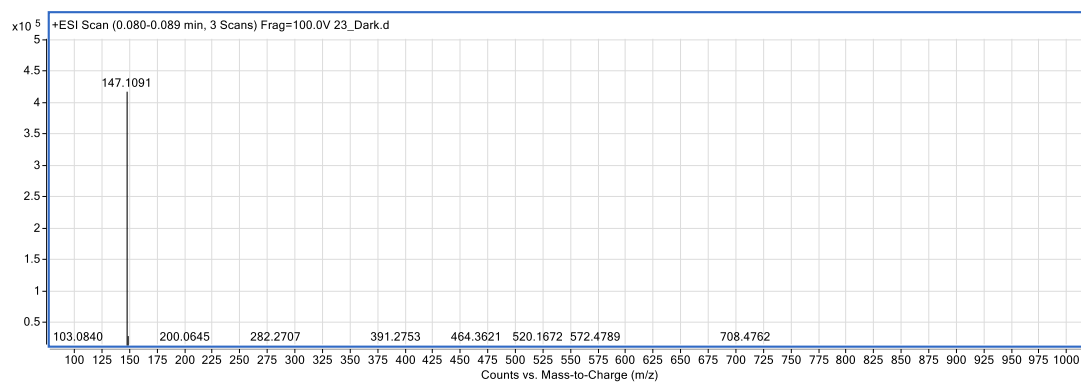


Figure 136 Mass spectrum of complex 23_Dark 24 h.

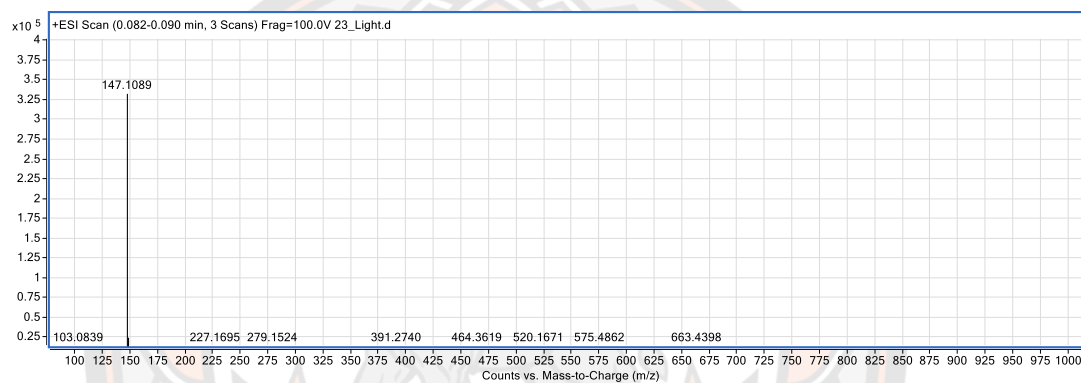


Figure 137 Mass spectrum of complex 23_Light 24 h.

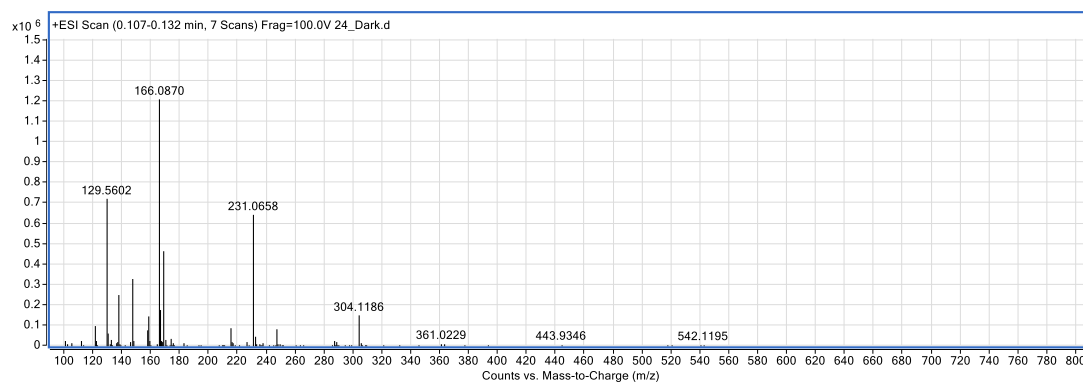


Figure 138 Mass spectrum of complex 24_Dark 24 h.

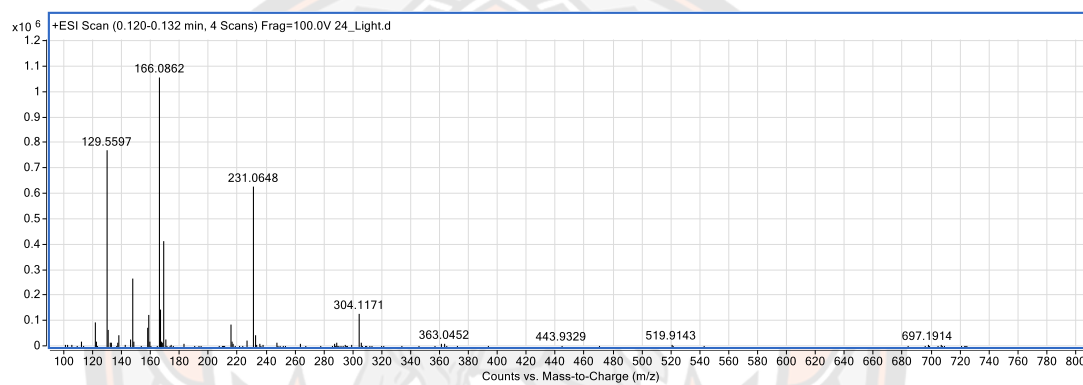


Figure 139 Mass spectrum of complex 24_Light 24 h.

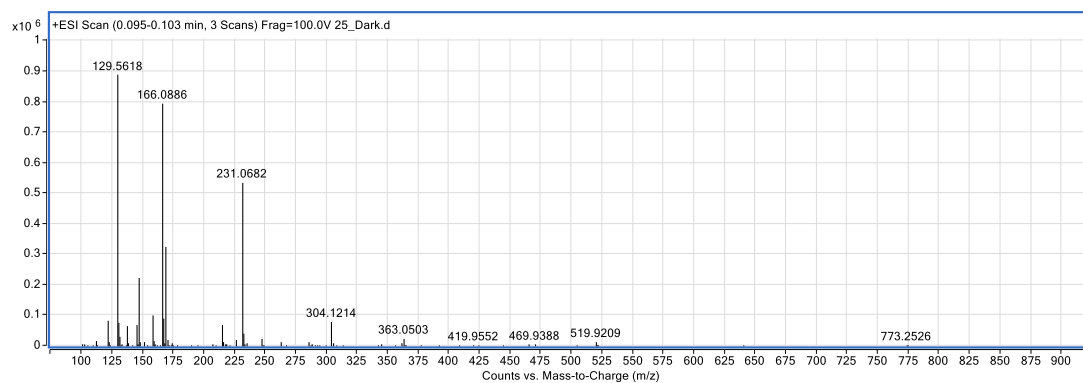


Figure 140 Mass spectrum of complex 25_Dark 24 h.

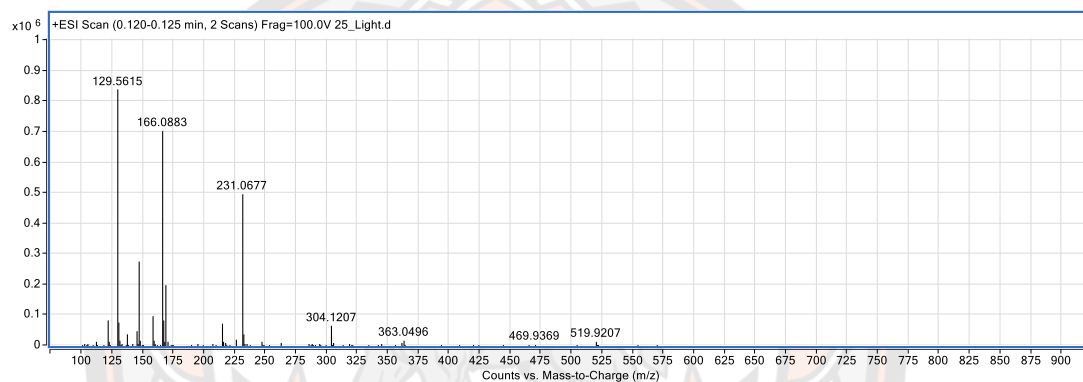


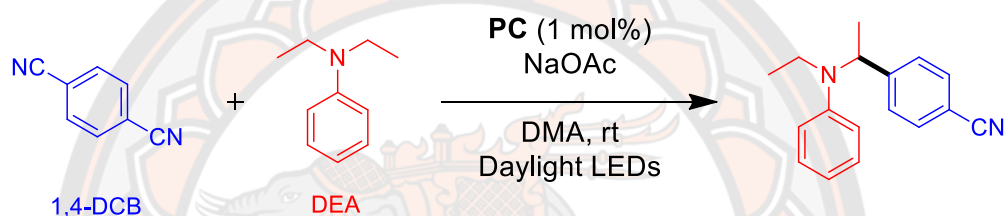
Figure 141 Mass spectrum of complex 25_Light 24 h.

7.2.3 Photoredox catalyzed reactions with immobilized catalysts

Having prepared the immobilized catalysts **21** to **25** and carried out an initial investigation of their stability, we have turned to carrying out initial attempts of photoredox reactions with these materials. The key points of interest in this work were to establish whether these materials are indeed capable of catalyzing these reactions and whether it is possible to recycle and reuse them. These attempts have been carried out with the α -arylation of amines and difluoromethylation reaction.

1) α -Arylation of amines with immobilized catalysts

Table 33 Conditions of photoredox reactions of allylic arylations carried out with immobilized complex **21**.



Entry	Catalyst (1 mol%)	1,4-DCB (equiv.)	DEA (equiv.)	Reaction condition	Time/ h
1e	21	1	3	DMA, LEDs, N ₂	24
1e_recycle	21	1	3	DMA, LEDs, N ₂	24
2e	21	1	3	DMA, LEDs, N ₂	48
2e_recycle	21	1	3	DMA, LEDs, N ₂	48

The reaction conditions for the photoredox catalyzed α -amino C–H arylation reactions carried out with immobilized complex **21** are summarized in **Table 33**. The results of these reactions are then displayed in **Figure 142-146**. Which show the mass and ^1H -NMR spectra of the crude reaction mixtures carried out with complex **21**. The evidence for the formation of the expected product in reaction **1e**, **1e_recycle**, **2e**, and **2e_recycle**, can be seen in mass spectroscopy. The expected product has a molecular weight of 250.2 g/mol and the MS spectra from all of the reactions contain peaks with m/z ratio of 251.2 corresponding to the $[\text{M}+\text{H}]^+$ peak of the expected product. In addition, the ^1H -NMR spectra of the crude products contained the expected peaks for reaction **2e** carried out with complex **21**. It should be noted that the desired product formation in the case of utilizing the recycled catalyst has been seen only in the case of reaction **1e_recycle**. The possibility to reuse the catalysts will need to be investigated in the future.

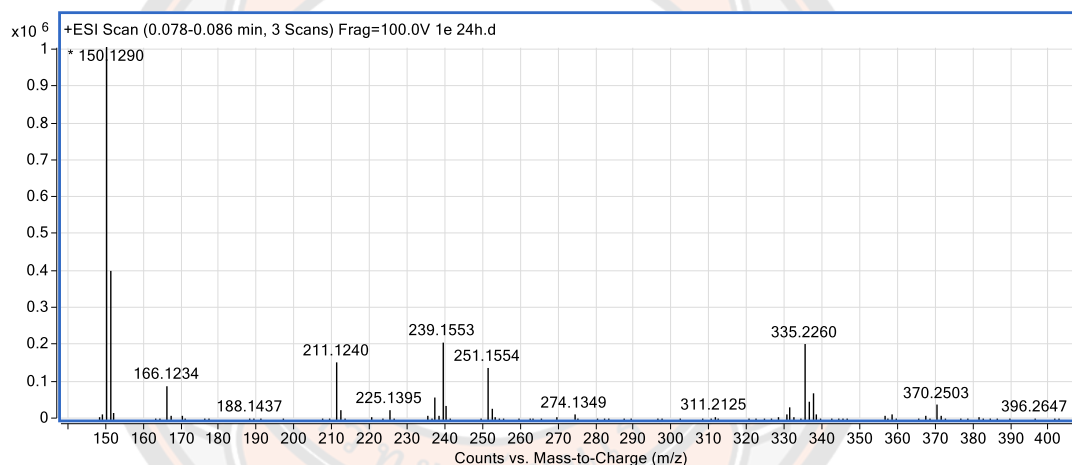


Figure 142 Mass spectrum of **1e**.

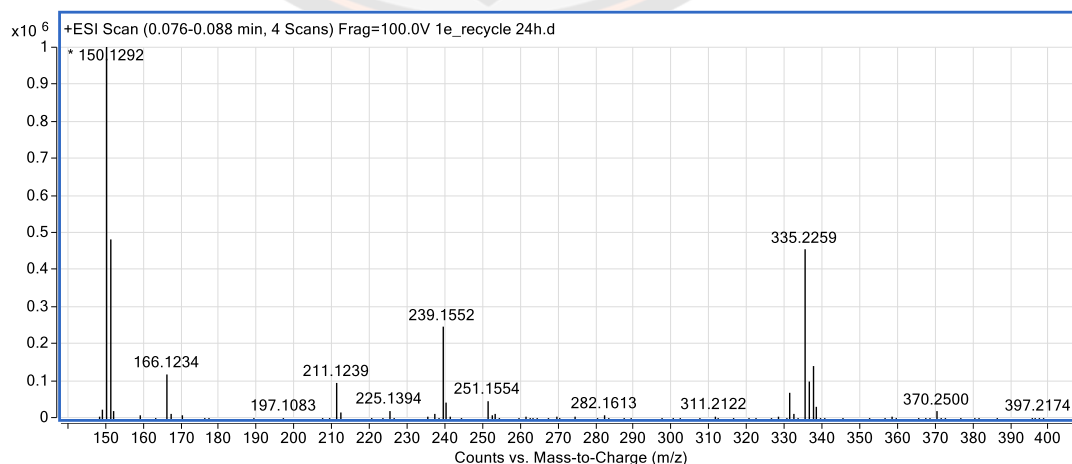


Figure 143 Mass spectrum of **1e_recycle**.

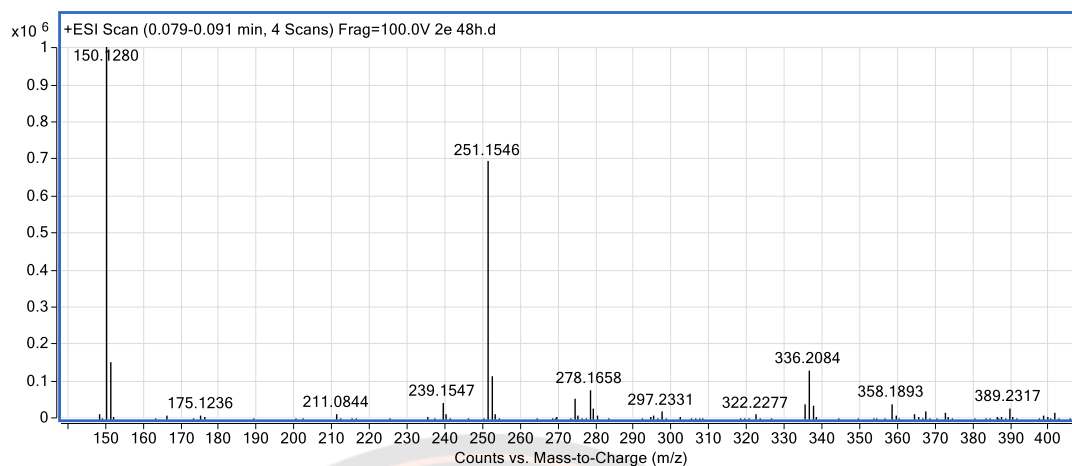


Figure 144 Mass spectrum of 2e.

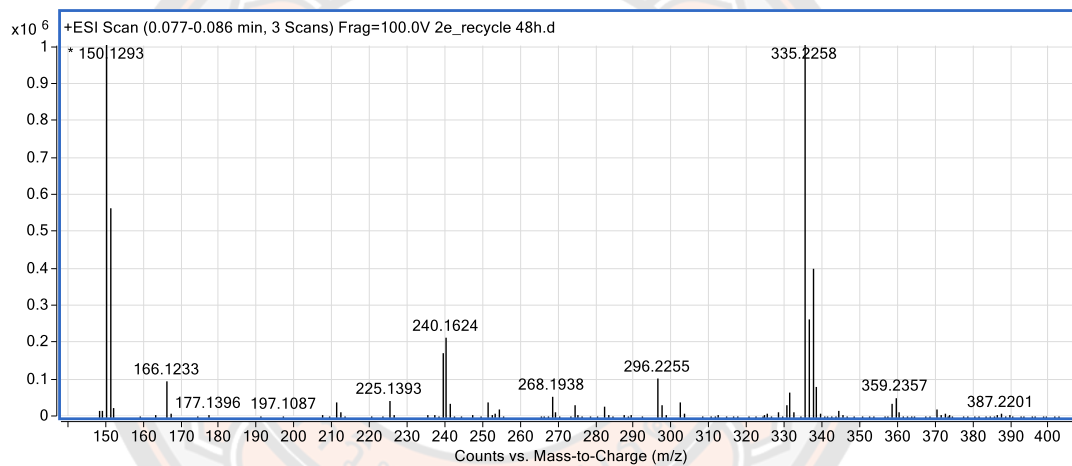


Figure 145 Mass spectrum of 2e_recycle.

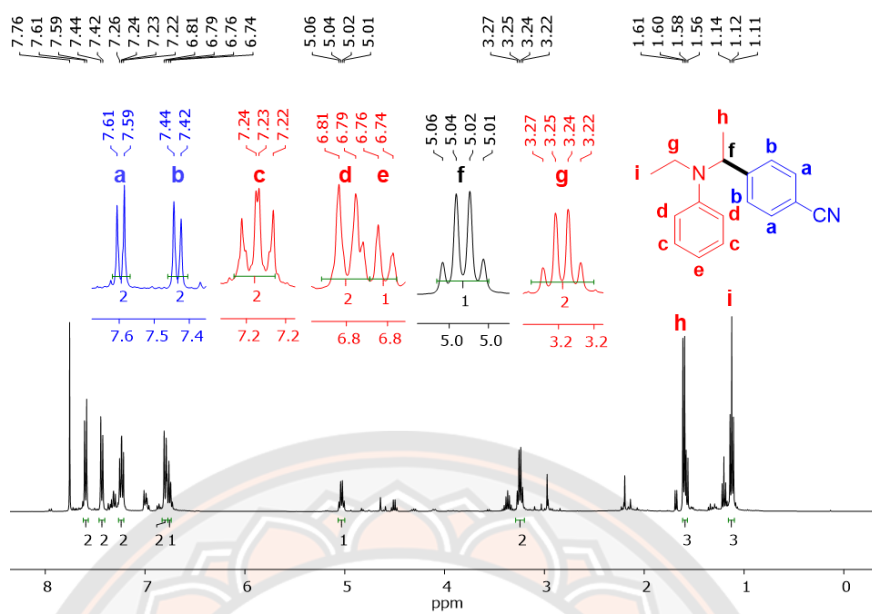
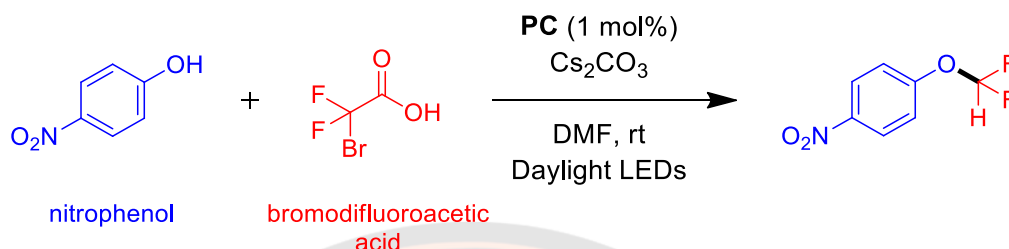


Figure 146 ^1H -NMR spectrum of 2e in CDCl_3 .

2) Difluoromethylation with immobilized catalysts

Table 34 Reaction conditions for photoredox catalyzed difluoromethylation using immobilized complexes 21, 22, 23, 24, and 25.

Entry	Catalyst (1 mol%)	Nitrophenol (equiv.)	Bromodifluoro acetic acid (equiv.)	Reaction condition	Time h
1f	21	1	1	DMF, LEDs, N ₂	24
1f_recycle	21	1	1	DMF, LEDs, N ₂	24
2f	22	1	1	DMF, LEDs, N ₂	24
2f_recycle	22	1	1	DMF, LEDs, N ₂	24
3f	23	1	1	DMF, LEDs, N ₂	24
4f	24	1	1	DMF, LEDs, N ₂	24
4f_recycle	24	1	1	DMF, LEDs, N ₂	24
5f	25	1	1	DMF, LEDs, N ₂	24
5f_recycle #1	25	1	1	DMF, LEDs, N ₂	24
5f_recycle #2	25	1	1	DMF, LEDs, N ₂	24

The results from the photoredox difluoromethylation reactions carried out with immobilized complexes **21** to **25**. The results of these reactions are then displayed in **Figure 147-156**. Which show the ^1H -NMR spectra of the crude reaction mixtures. The evidence for the formation of the expected product of 1-(Difluoromethoxy)-4-nitrobenzene in all reactions can be seen in ^1H -NMR spectra. The ^1H -NMR spectra of the crude products contained the expected peaks. The most prominent of these indicating the formation of the product from **1f**, **2f**, **2f_recycle**, **3f**, **4f**, **5f**, **5f_recycle#1** and **5f_recycle#2** are the two doublets, at range 8.3–7.85 and 7.3–6.9 ppm, from the para substituted aromatic ring, and the triplet at range 6.8–6.5 ppm, from proton the position c. The ^1H -NMR spectra of the crude products contained the expected peaks. The possibility to recycle and reuse the catalysts needs to be investigated further in the future.

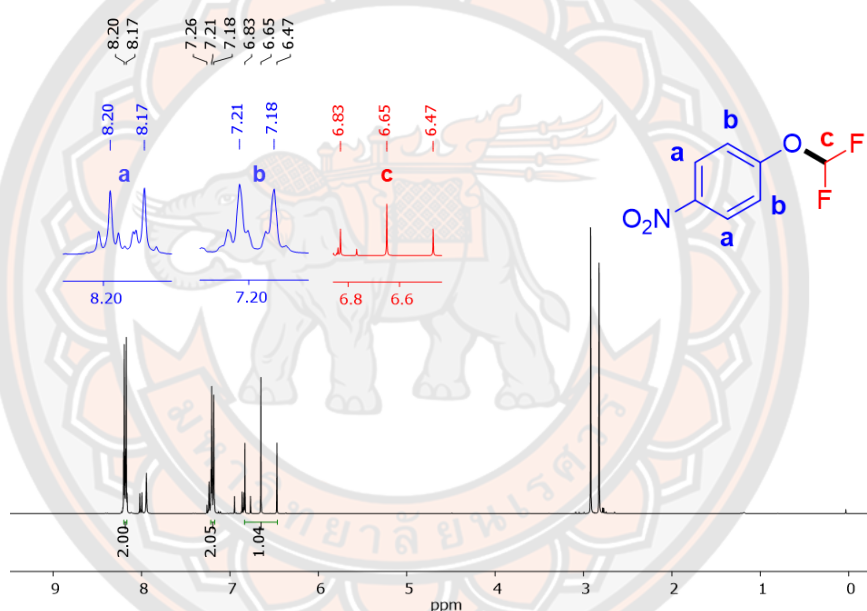


Figure 147 ^1H -NMR spectrum of **1f** in CDCl_3 .

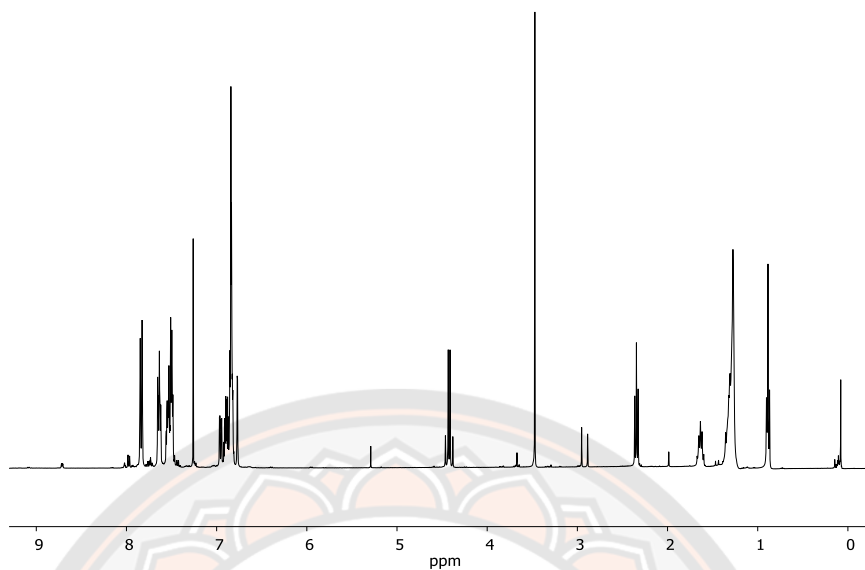


Figure 148 ^1H -NMR spectrum of 1f_recycle in CDCl_3 .

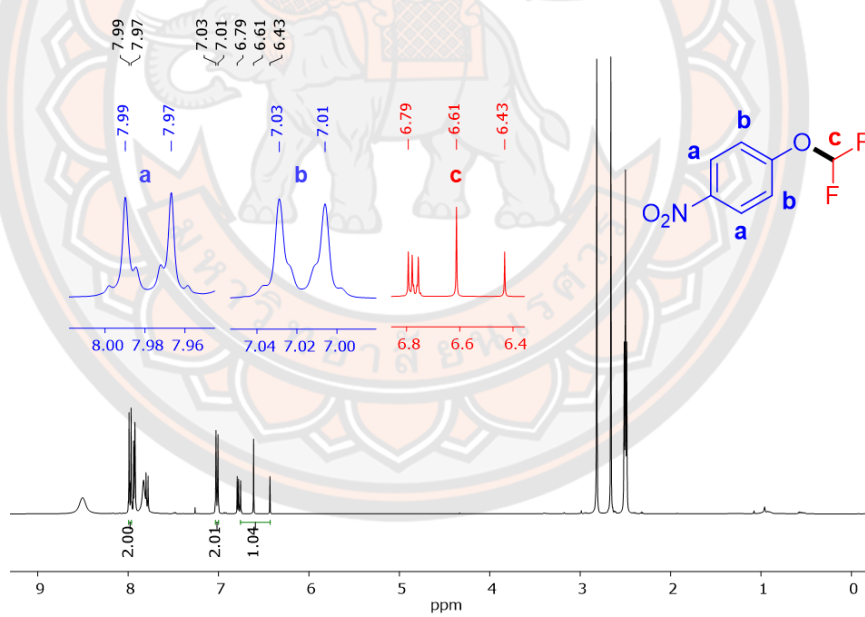


Figure 149 ^1H -NMR spectrum of 2f in CDCl_3 .

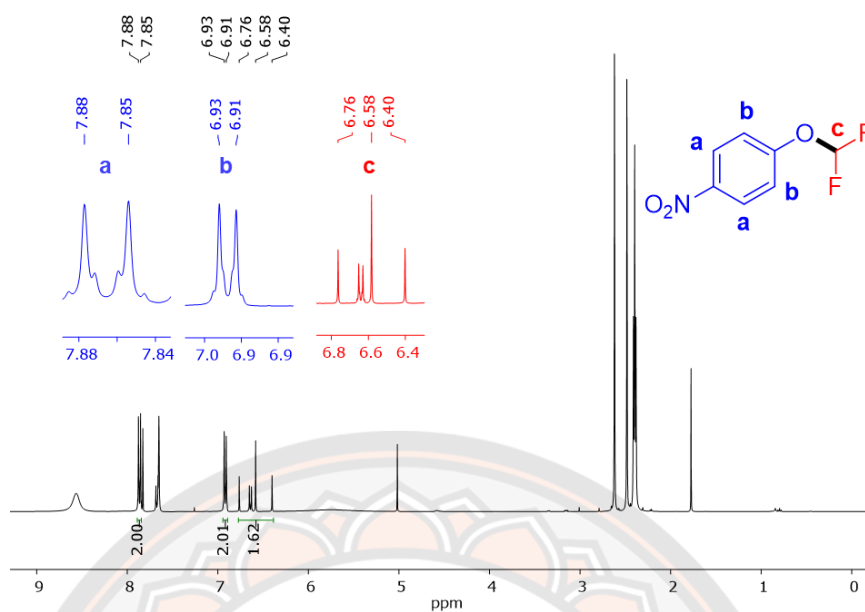


Figure 150 ¹H-NMR spectrum of 2f_recycle in CDCl₃.

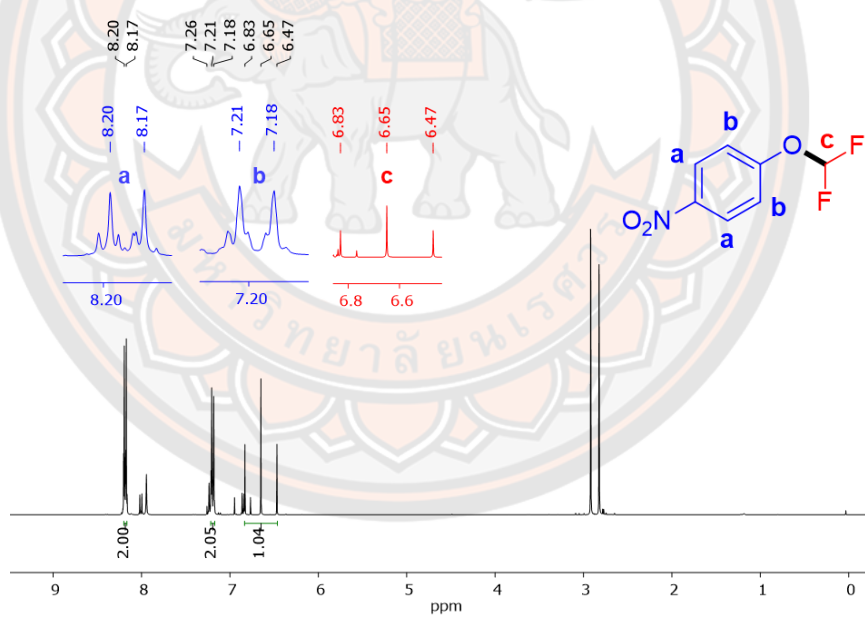


Figure 151 ¹H-NMR spectrum of 3f in CDCl₃.

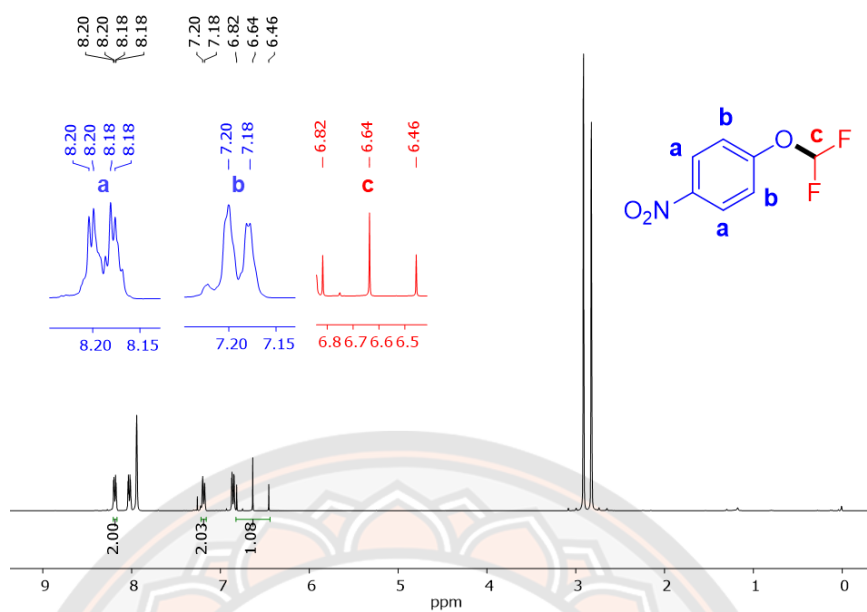


Figure 152 ¹H-NMR spectrum of 4f in CDCl₃.

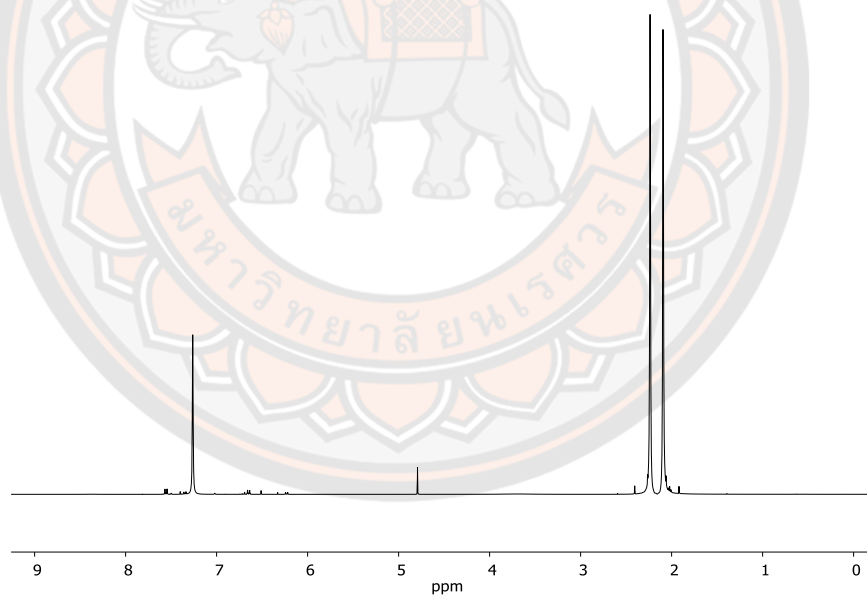


Figure 153 ¹H-NMR spectrum of 4f_recycle in CDCl₃.

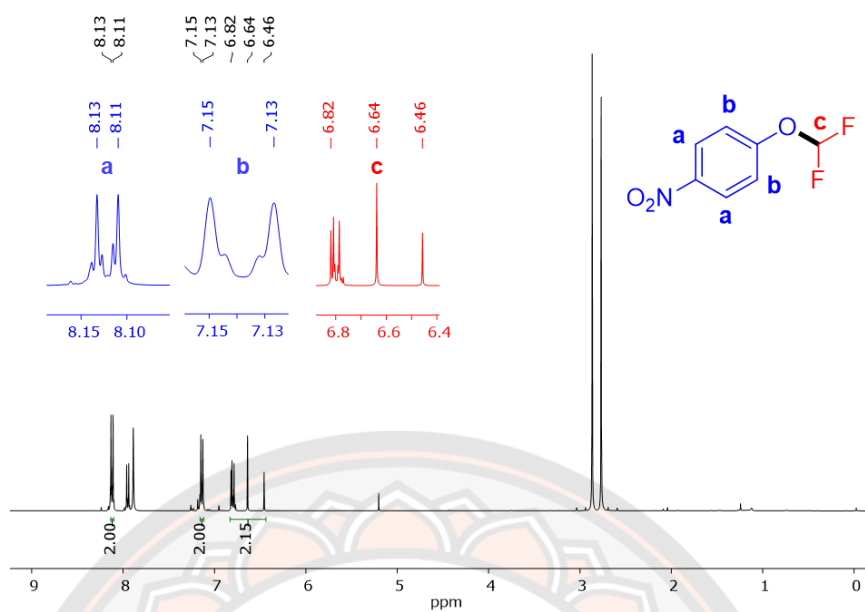


Figure 154 ¹H-NMR spectrum of 5f in CDCl₃.

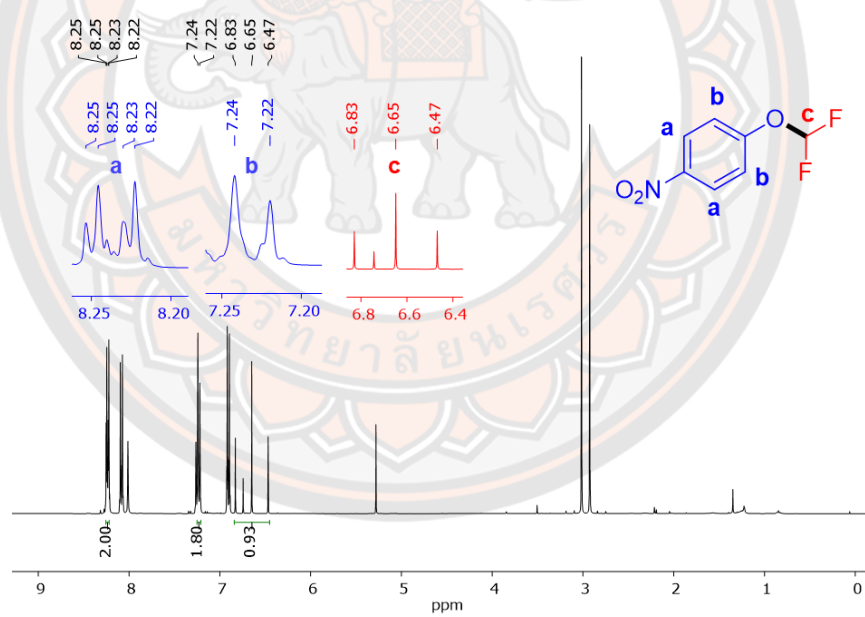


Figure 155 ¹H-NMR spectrum of 5f_recycle #1 in CDCl₃.

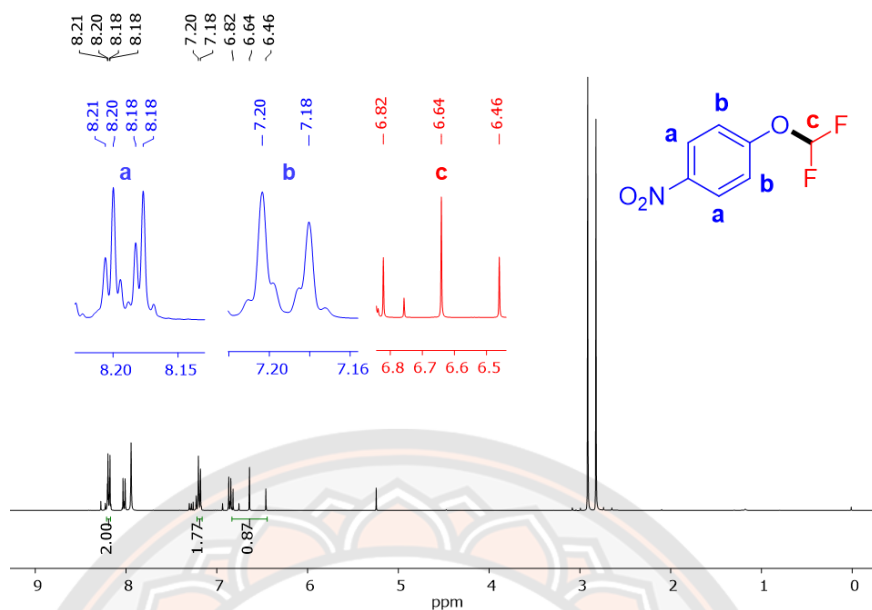


Figure 156 ^1H -NMR spectrum of **5f_recycle #2** in CDCl_3 .

7.3 Conclusion

Both homogeneous and heterogeneous catalysts were synthesized and investigated. Photoredox reactions carrying out complexes **2**, **3**, **5**, **15**, **21**, **22**, **23**, **24**, and **25** indicated that these complexes are capable of acting as photocatalysts in the selected transformations indicating that the functional groups and immobilization do not destroy the ability of these complexes to engage in photoredox catalysis. Stability experiments have suggested that some of the immobilized complexes might undergo light promoted decomposition. However, the polystyrene immobilized complex **25** appears to be stable. This issue, however, requires further detailed investigation. Furthermore, initial experiments have indicated that some of the immobilized complexes, for example polystyrene immobilized complex **25**, remain active after recycling. This issue will also require further investigation in the future.

CHAPTER VIII

CONCLUSION

The work carried out in this project and described in the preceding chapters of this thesis can be divided into three parts.

The first part of this thesis describes novel tris-cyclometalated iridium(III) complexes, which are derivatives of the prototypical structure $[\text{Ir}(\text{ppy})_3]$ bearing aminoalkyl groups. Twelve complexes (**3-14**) have been investigated in this part of the work and they can be divided into two groups. The members of the first group, complexes **3-8**, contain simple alkyl groups of different chain lengths, while the members of the second group, complexes **9-14**, contain hydrophilic chains terminated in hydroxy groups and in some cases containing ethylene oxy units. These complexes were investigated in order to gain understanding of the relationship between the structure of the luminescent iridium(III) complexes and their photophysical properties in aqueous solutions, which was hypothesized to depend on their propensity to aggregate. The results of this work have confirmed our previous results indicating the change of the maximum emission wavelength from the region of 520-530 nm to 580 nm in response to change in aggregation status. It was observed that this behavior change systematically in the expected manner for the simple alkyl complexes, in line with increasing chain length, and that inclusion of hydrophilic side chains did lead to the expected decrease of the propensity to exhibit this change. Live cell microscopy experiments carried out with complexes **5**, **6**, **9**, and **14** revealed that the complexes can localize in NIH-3T3 cells. Finally, it has been observed that the complex containing two 2-hydroxy ethyl groups (**14**) is less cytotoxic than the its mono-substituted counterpart.

The second part of thesis describes novel tris-cyclometalated iridium(III) complexes bearing quarternary ammonium groups on one of the phenylpyridine rings. These complexes were developed as the next generation of the aminoalkyl iridium(III) complexes studied in the first part of this thesis with the aim of providing them with permanent positive charge. Only complex **15** was isolated and studied in detail. It is stable in organic solution in dark but exhibits rapid photocatalyzed transformations. Investigations of this behavior have shown that these transformations involve the formation of an electrophilic species, which can be captured by a suitable nucleophile, leading to the formation of new product. The complex has also been investigated as a potential cellular stain and shown good photophysical properties enabling its use as cellular stain in fluorescence microscopy. Live-cell imaging have demonstrated that the complex is less cytotoxic than its secondary amine precursor and shows lysosomal localization as this previously reported by our group.

Finally, photoredox catalysis with the tris-cyclometalated iridium(III) complexes described above in a mild and environmentally friendly protocol for the

α -amino C–H arylation reaction of amine, β -arylation of ketones reaction, direct arylation of allylic sp^3 C–H bonds reaction, and difluoromethylation reaction were investigated. This work indicated that the presence of the functional groups in these complexes did not preclude their ability to act as photoredox catalysts. The recycling and reuse of homogeneous catalyst is a challenge in organic synthesis. Therefore, the immobilization of iridium(III) complexes on various supports was investigated. A number of heterogeneous catalysts was successfully synthesized and applied to reactions described above. The separation of catalyst from organic compounds by filtration and recycling of the catalyst for use in the next reaction was demonstrated as well. This shows that these catalysts exhibit stability, recoverability, and recyclability, however, this aspect requires further detailed investigation of photophysical properties and characterization.



APPENDIX

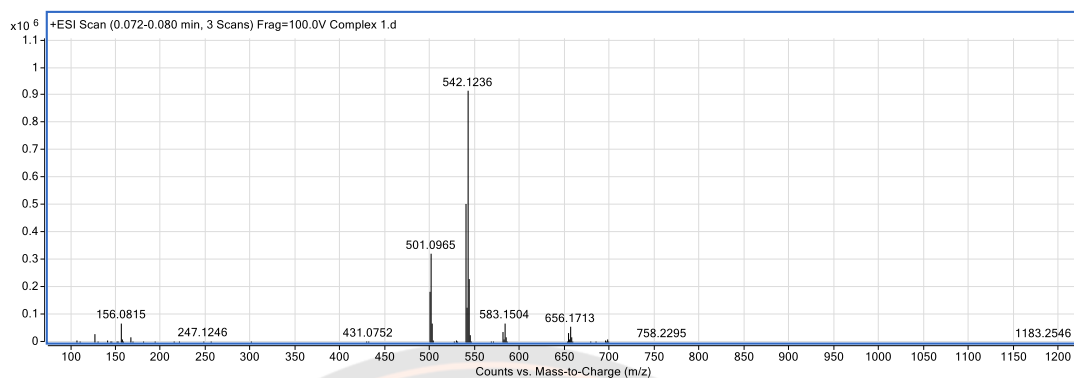
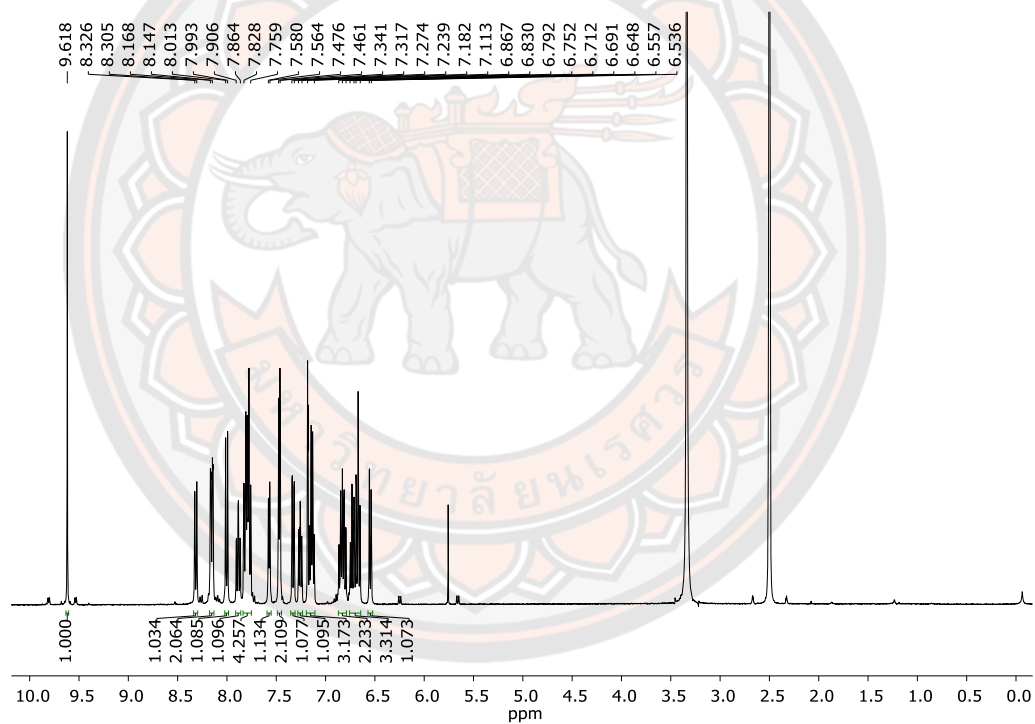


Figure S1 Mass spectrum of complex 1.

Figure S2 ^1H -NMR spectrum of complex 2 in $\text{DMSO}-d_6$.

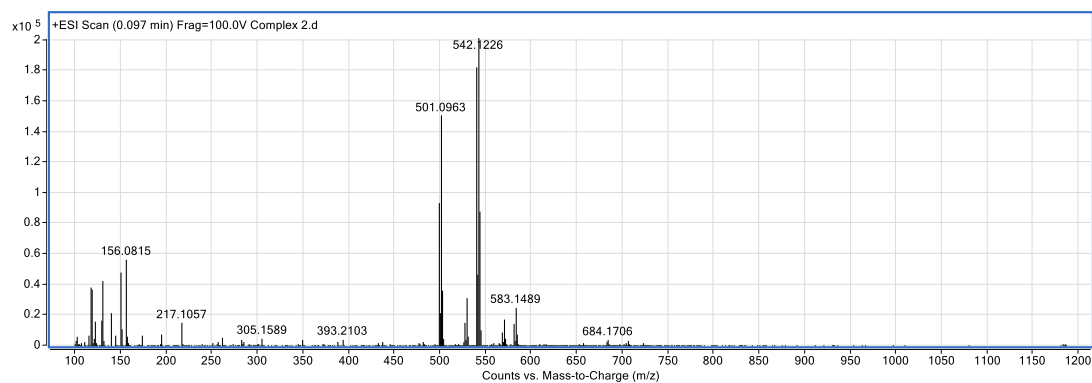


Figure S3 Mass spectrum of complex 2.

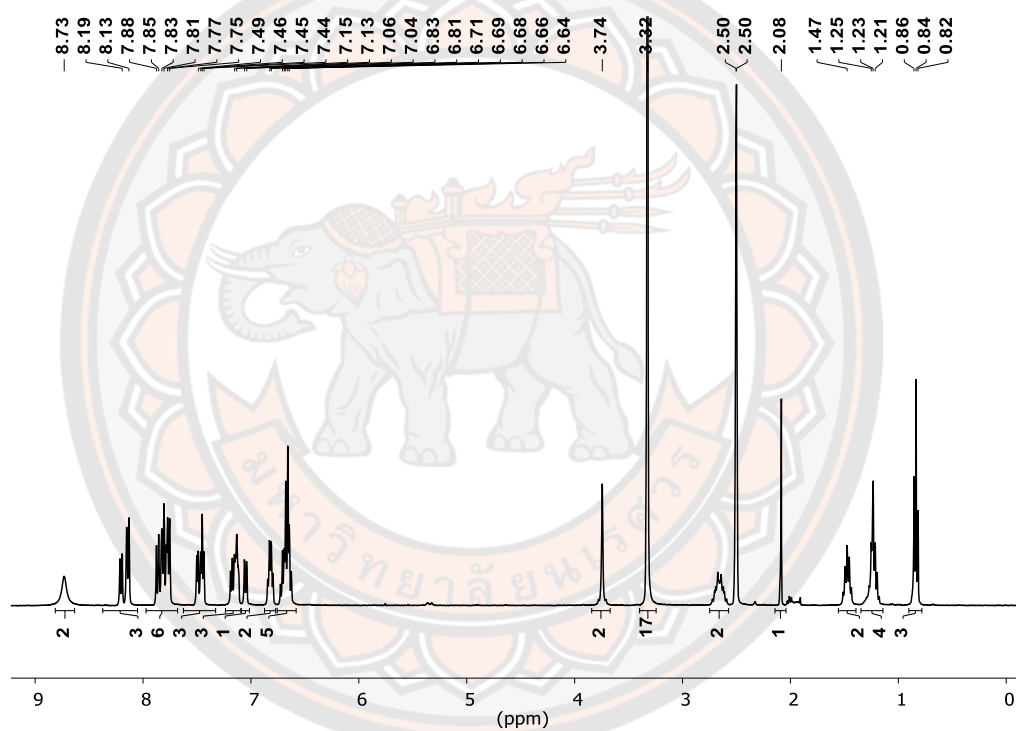


Figure S4 ¹H-NMR spectrum of complex 3 in DMSO-*d*₆.

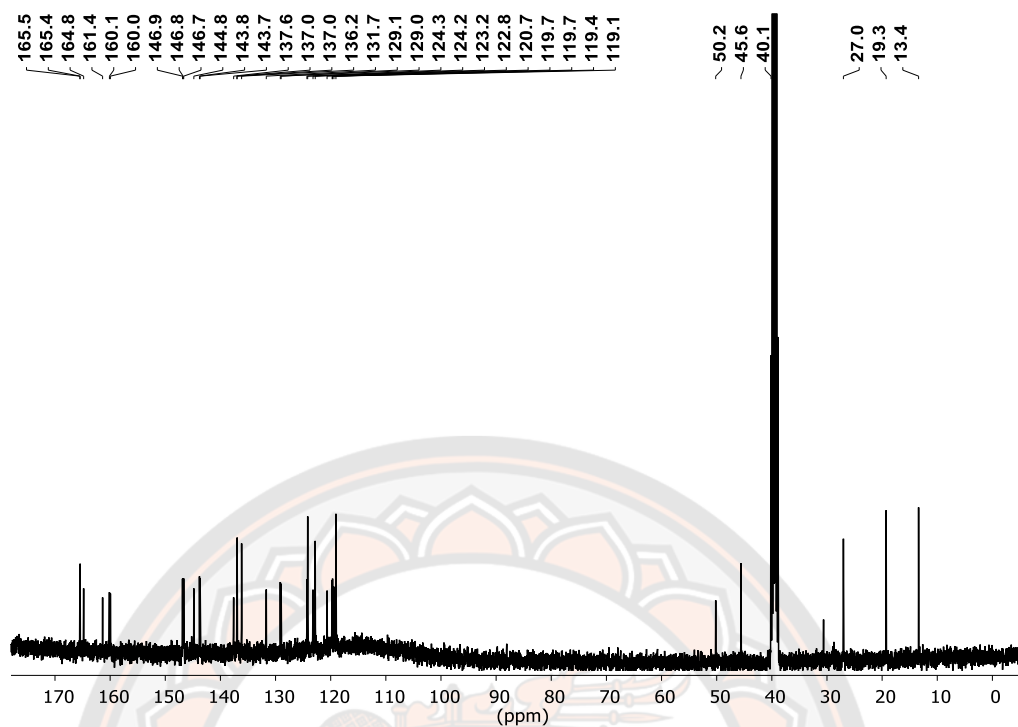


Figure S5 ^{13}C -NMR spectrum of complex 3 in $\text{DMSO-}d_6$.

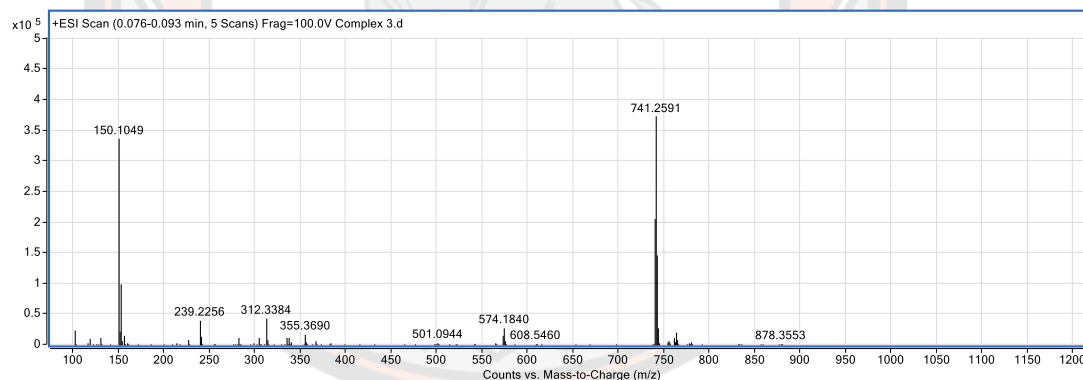


Figure S6 Mass spectrum of complex 3.

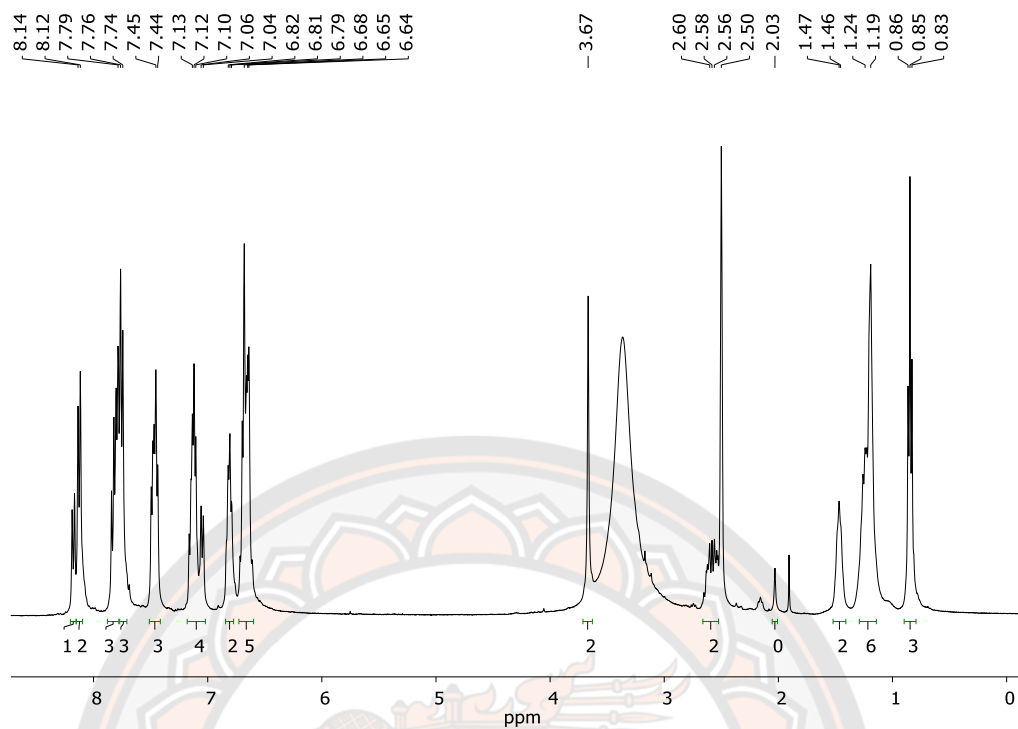


Figure S7 ¹H-NMR spectrum of complex 4 in DMSO-*d*₆.

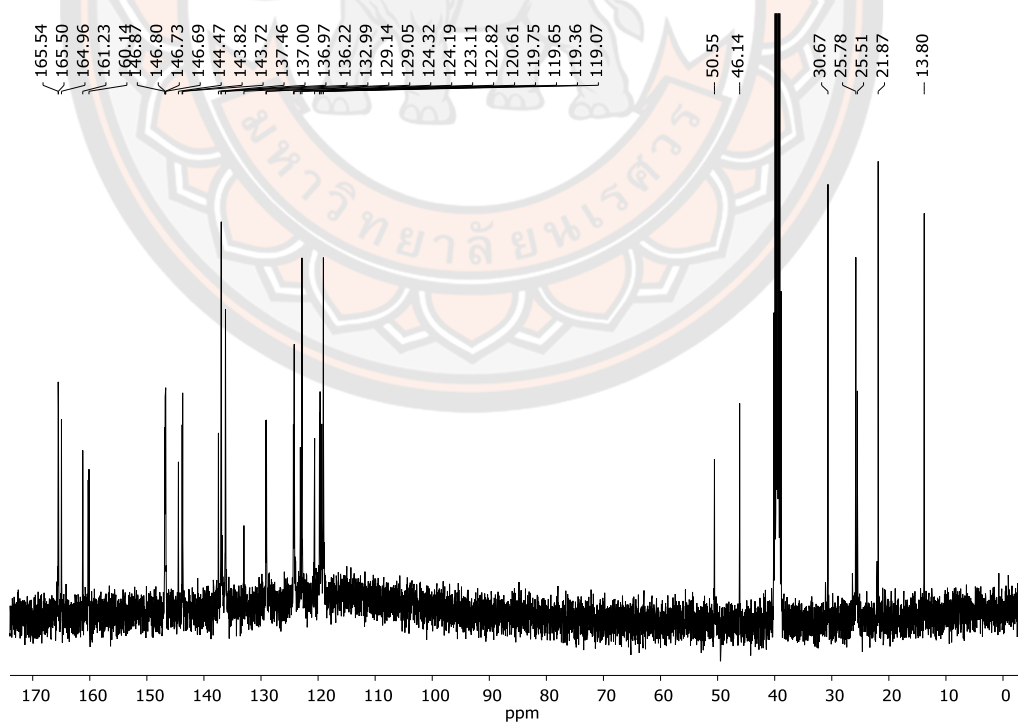


Figure S8 ¹³C-NMR spectrum of complex 4 in DMSO-*d*₆.

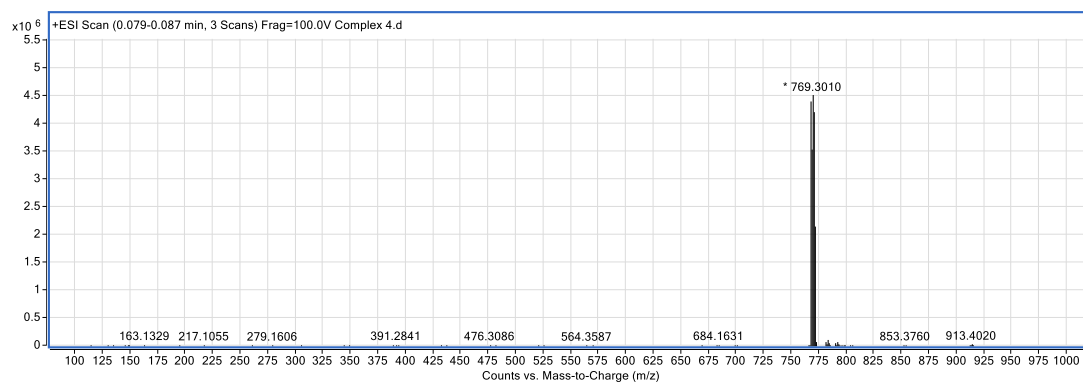


Figure S9 Mass spectrum of complex 4.

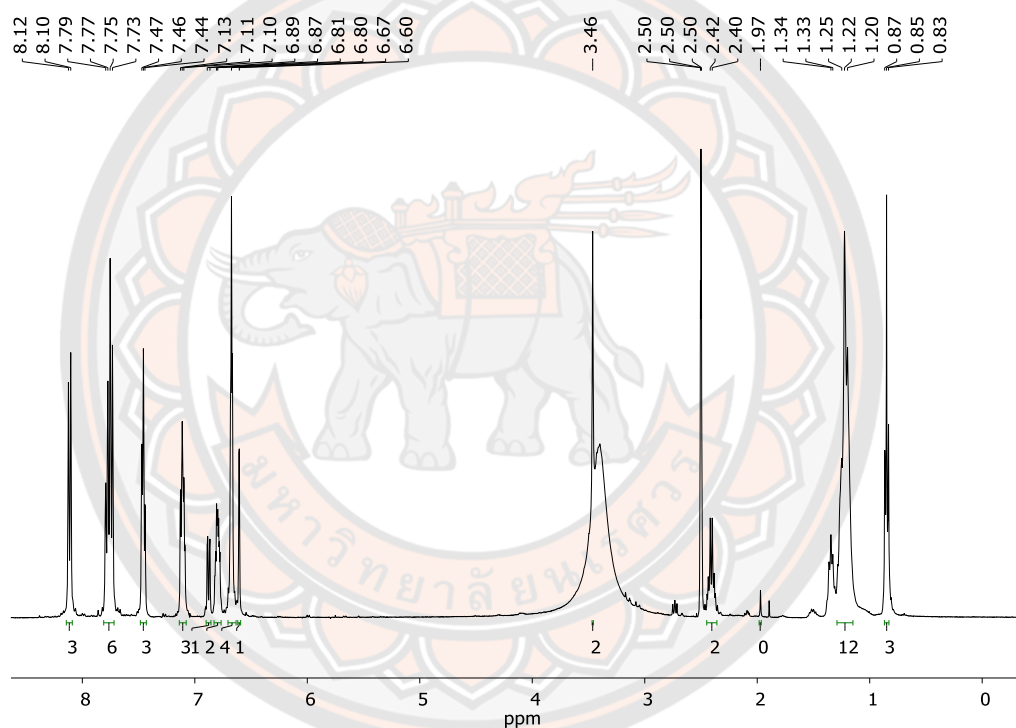


Figure S10 ¹H-NMR spectrum of complex 5 in DMSO-*d*₆.

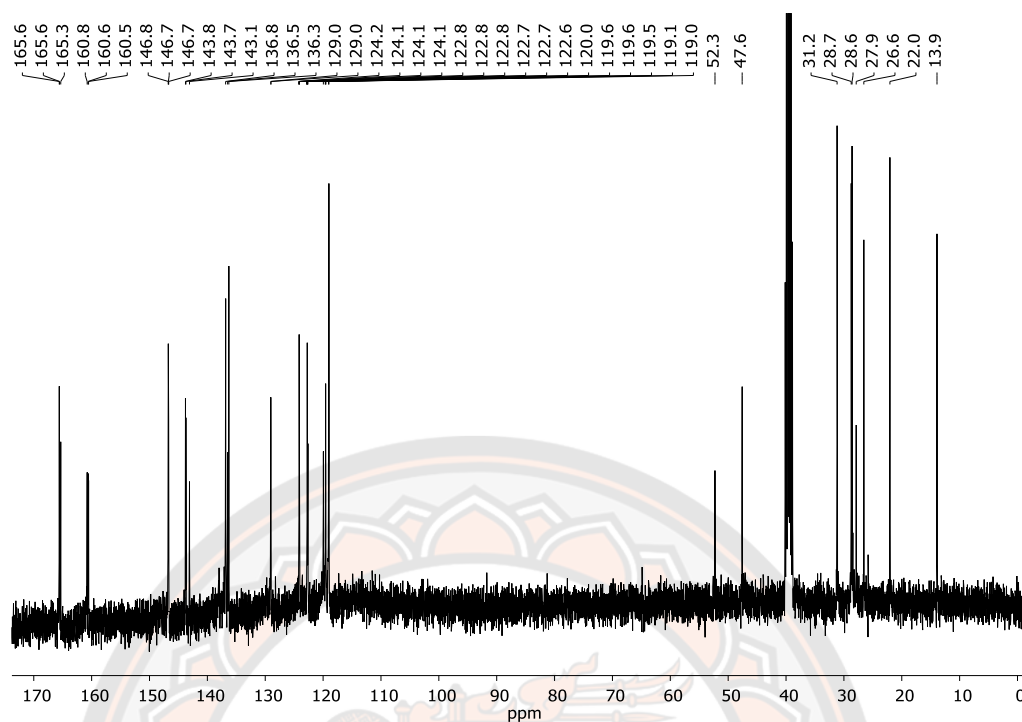


Figure S11 ¹³C-NMR spectrum of complex 5 in DMSO-*d*₆.

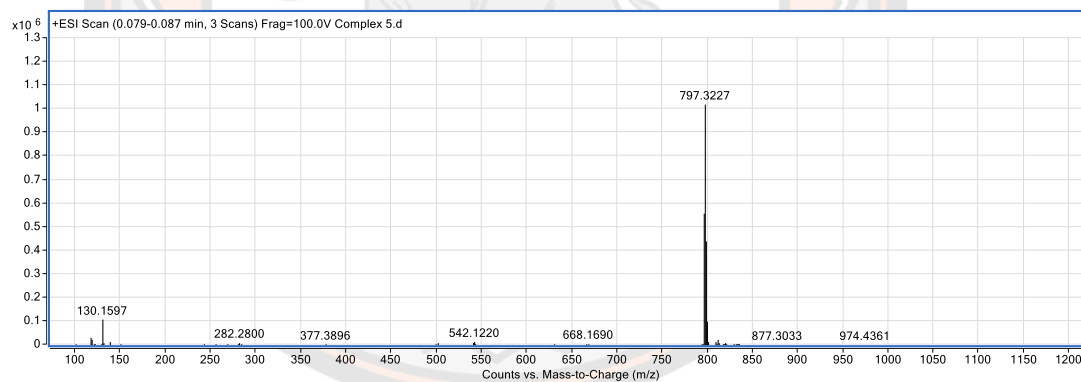


Figure S12 Mass spectrum of complex 5.

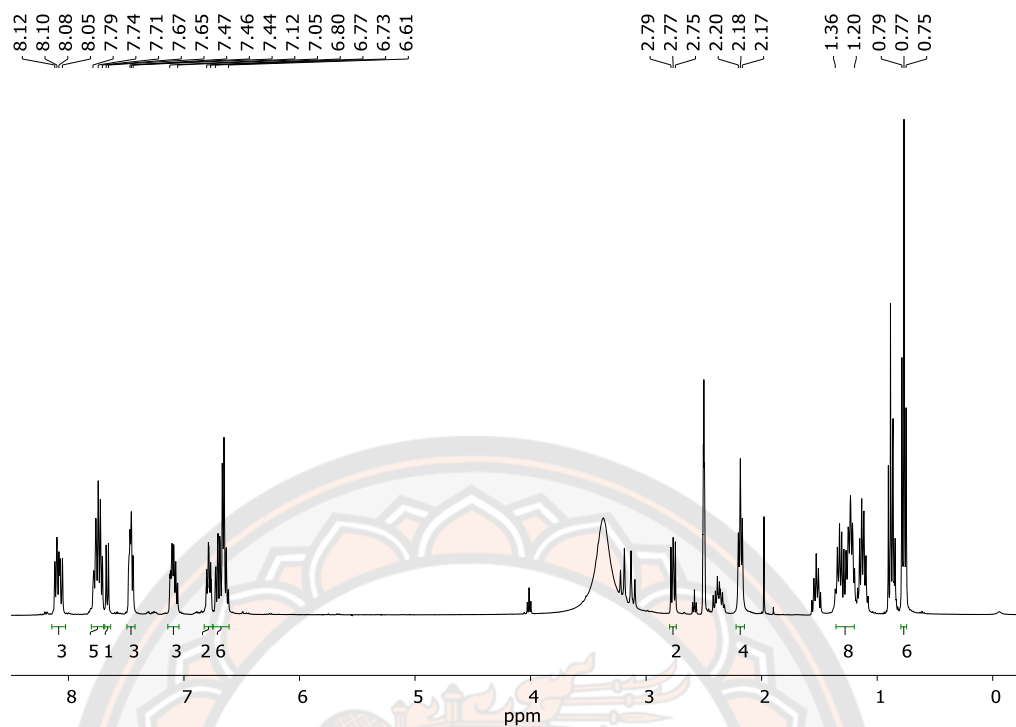


Figure S13 ¹H-NMR spectrum of complex 6 in DMSO-*d*₆.

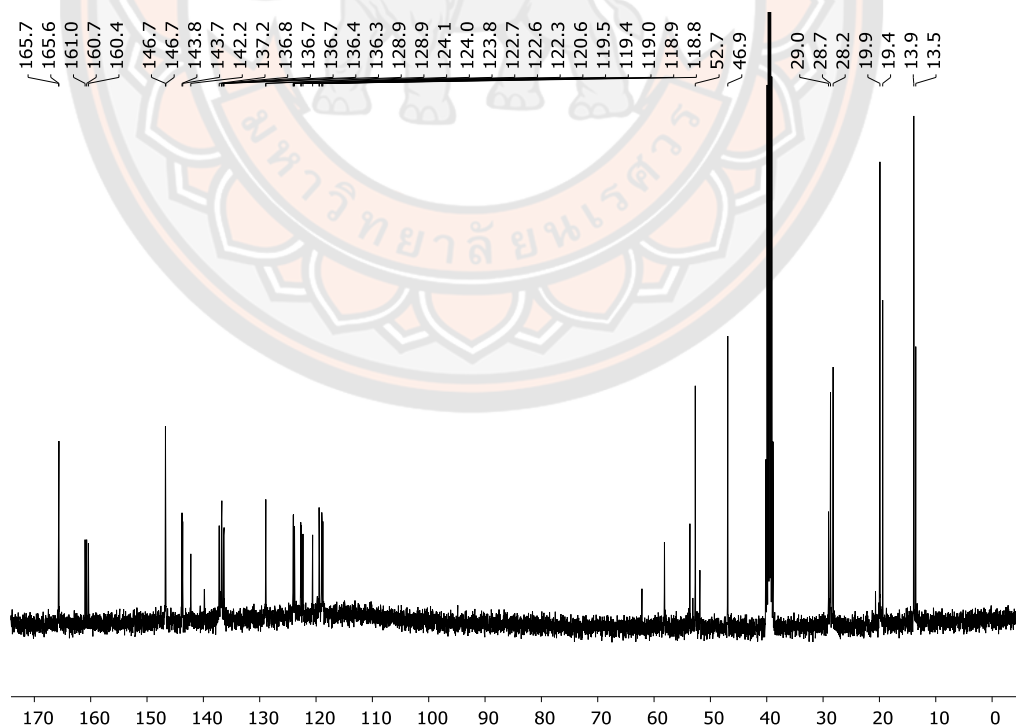


Figure S14 ¹³C-NMR spectrum of complex 6 in DMSO-*d*₆.

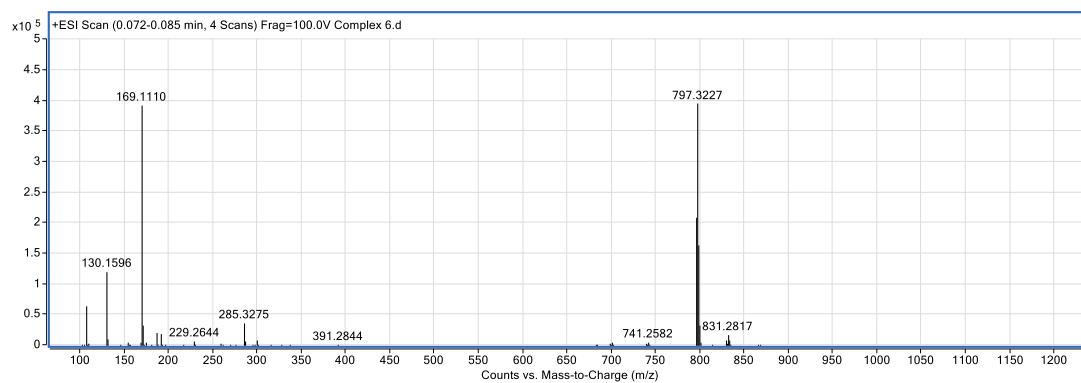


Figure S15 Mass spectrum of complex 6.

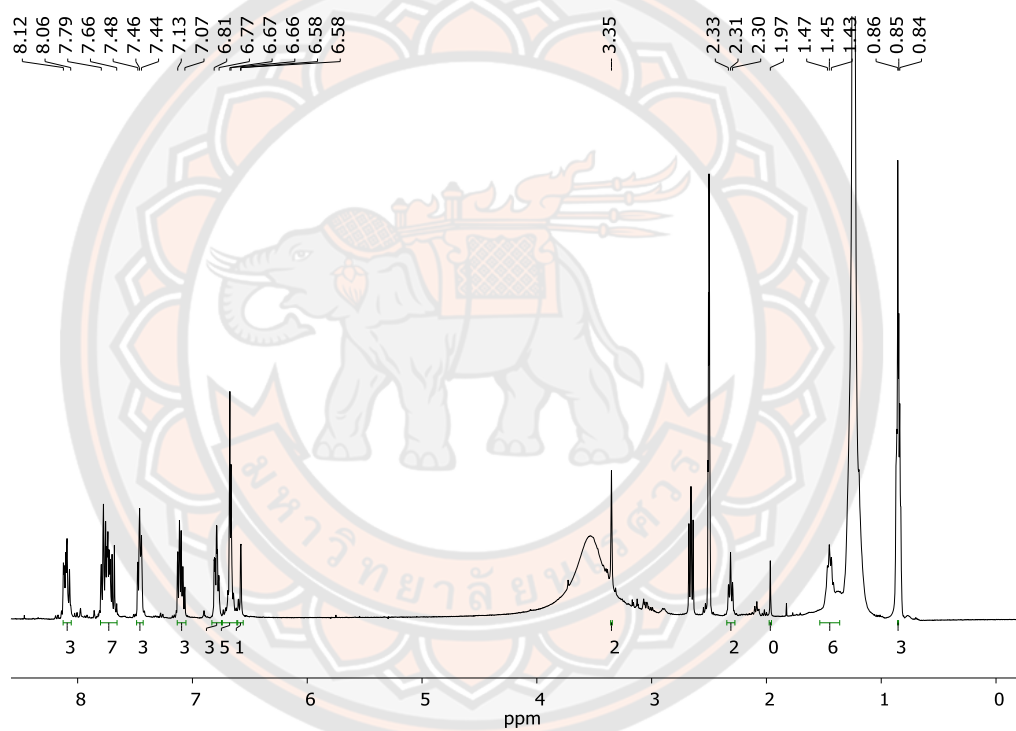


Figure S16 ¹H-NMR spectrum of complex 7 in DMSO-*d*₆.

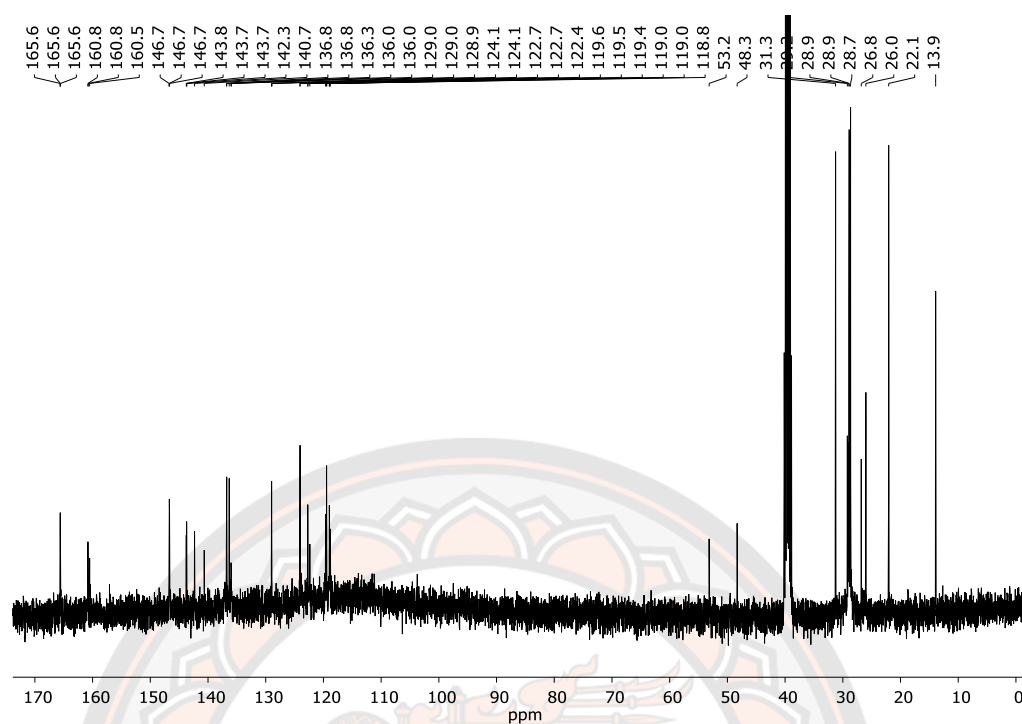


Figure S17 ¹³C-NMR spectrum of complex 7 in DMSO-*d*₆.

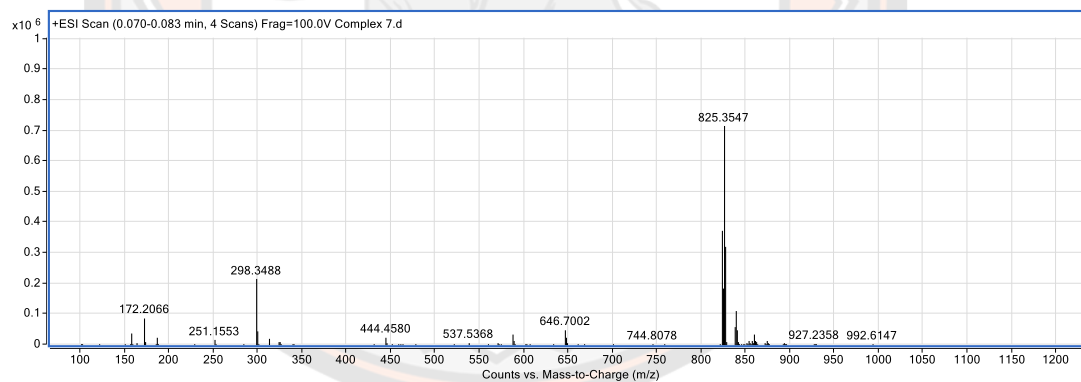


Figure S18 Mass spectrum of complex 7.

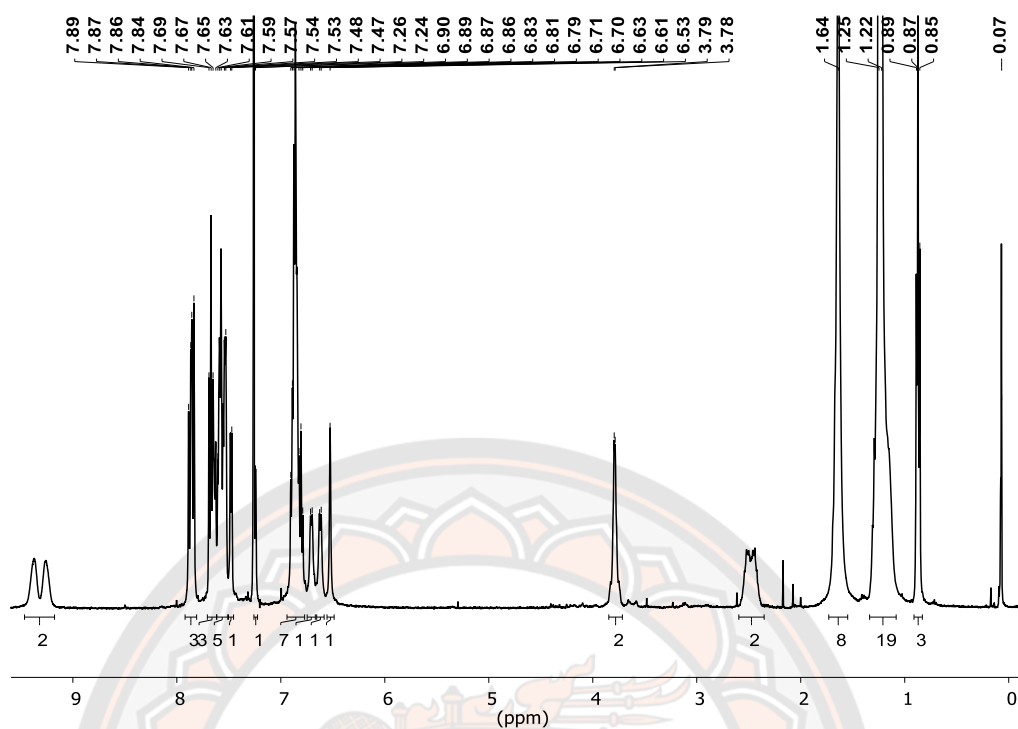


Figure S19 ^1H -NMR spectrum of complex 8 in $\text{DMSO-}d_6$.

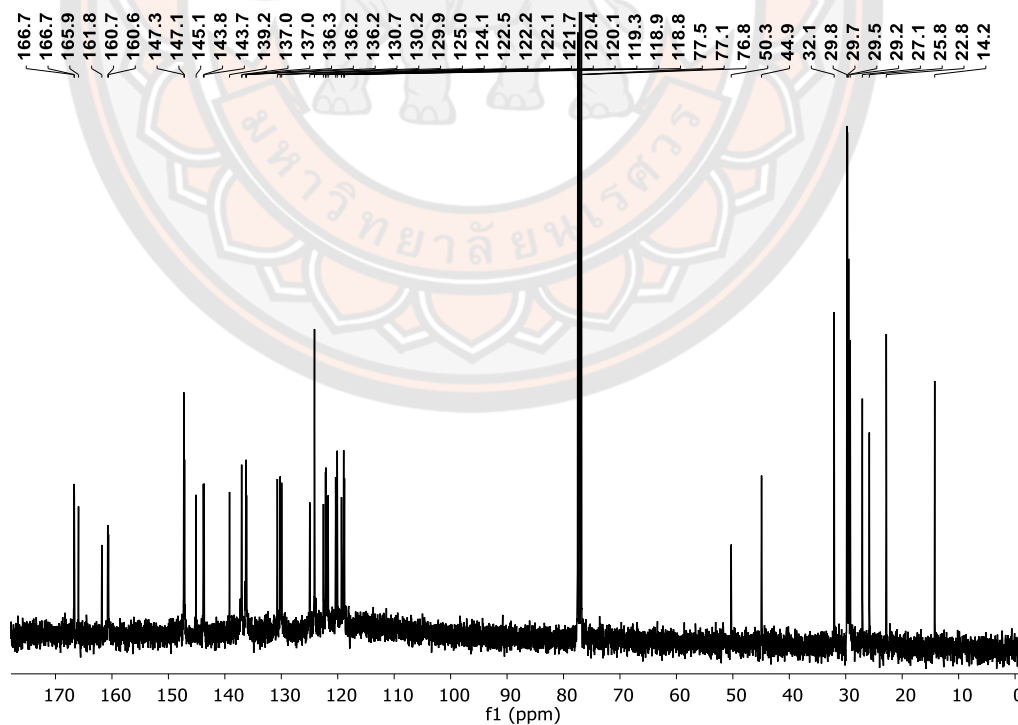


Figure S20 ^{13}C -NMR spectrum of complex 8 in $\text{DMSO-}d_6$.

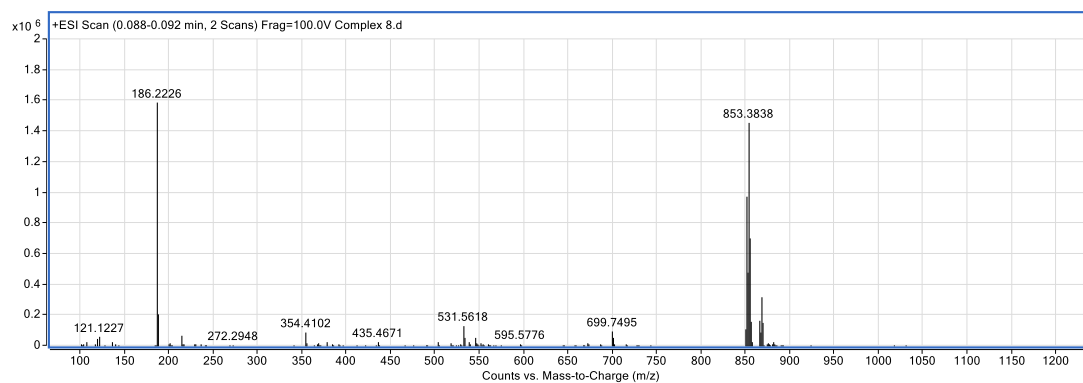


Figure S21 Mass spectrum of complex 8.

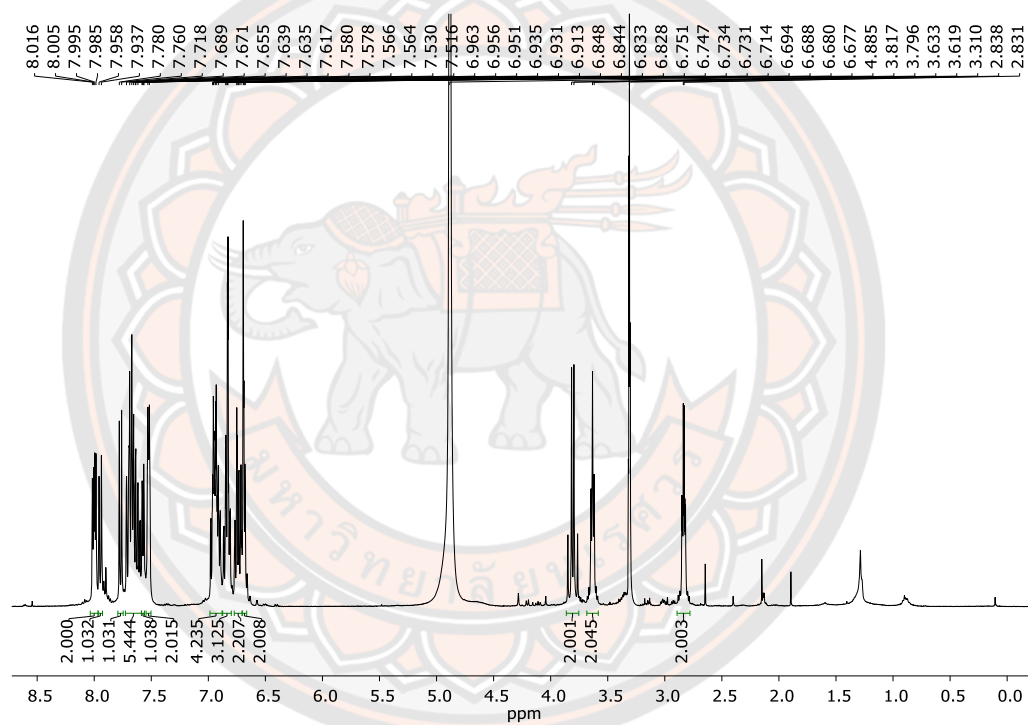


Figure S22 ¹H-NMR spectrum of complex 9 in methanol-*d*₄.

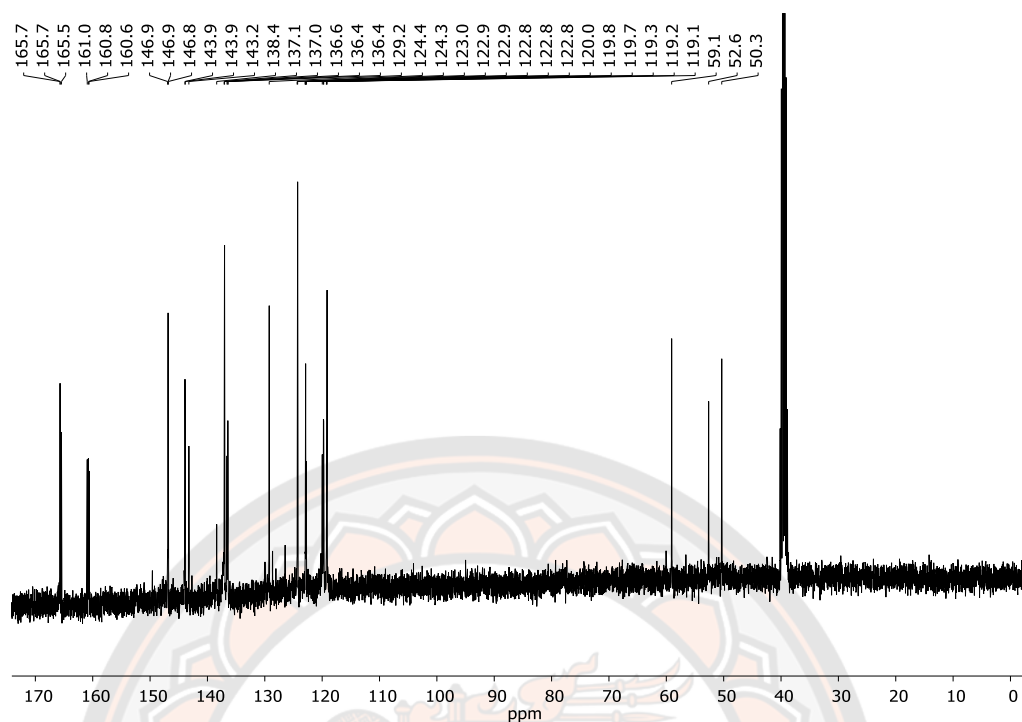


Figure S23 ^{13}C -NMR spectrum of complex 9 in methanol- d_4 .

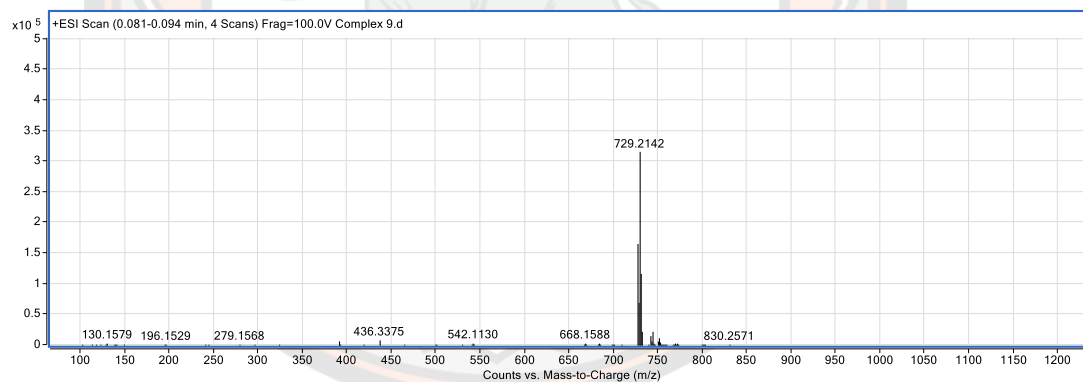


Figure S24 Mass spectrum of complex 9.

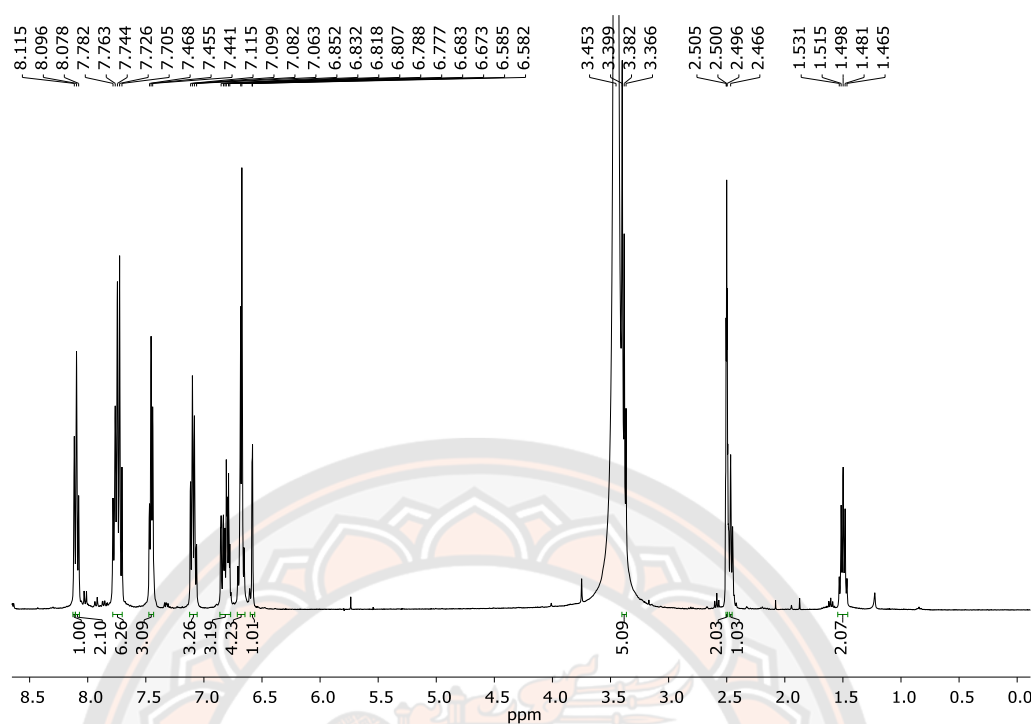


Figure S25 ¹H-NMR spectrum of complex 10 in methanol-*d*₄.

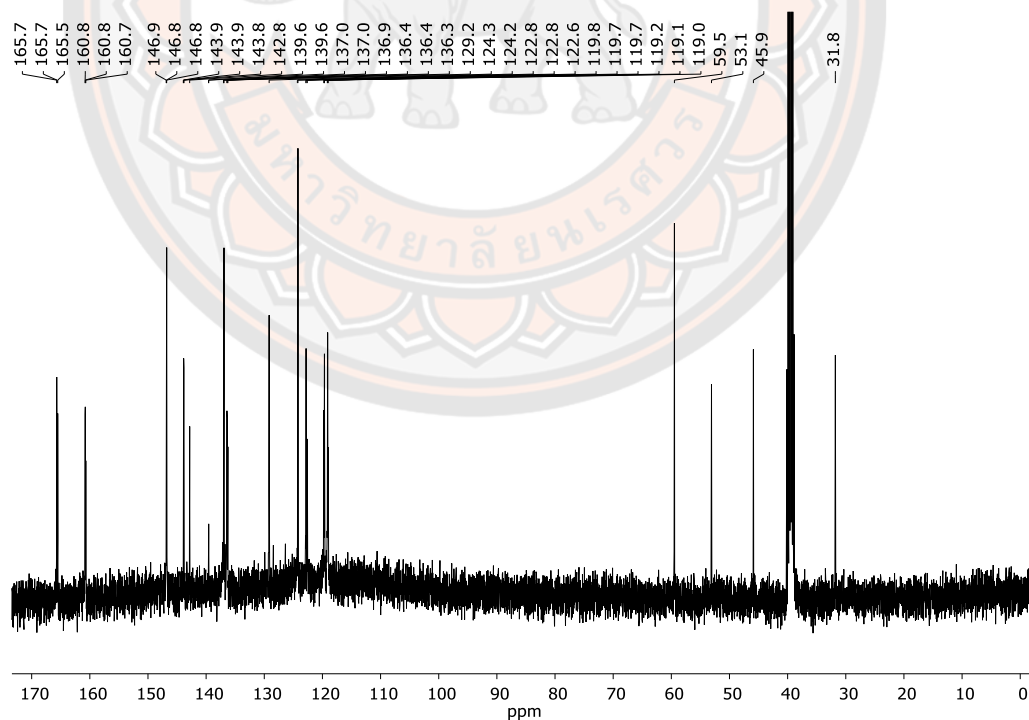


Figure S26 ¹³C-NMR spectrum of complex 10 in methanol-*d*₄.

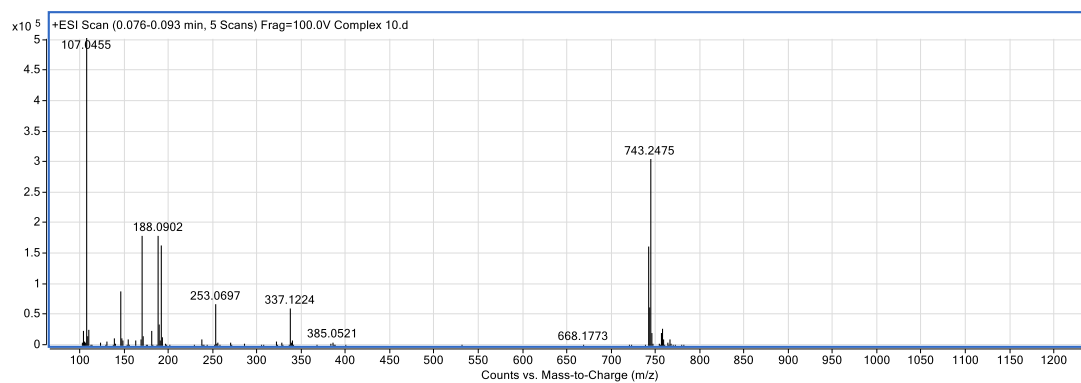


Figure S27 Mass spectrum of complex 10.

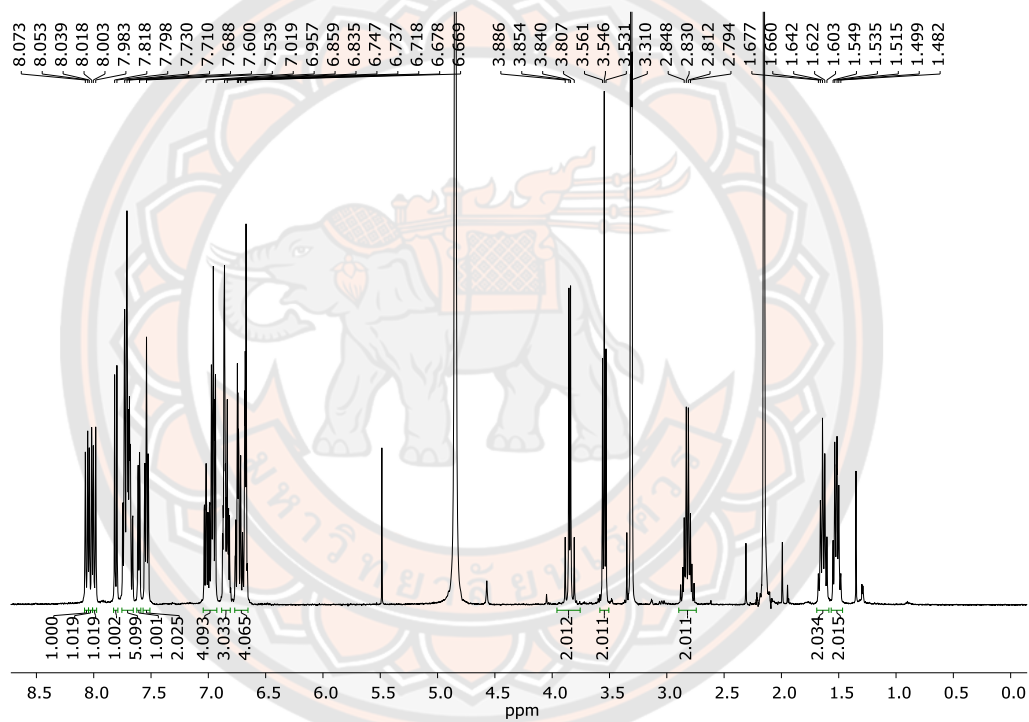


Figure S28 ¹H-NMR spectrum of complex 11 in methanol-d₄.

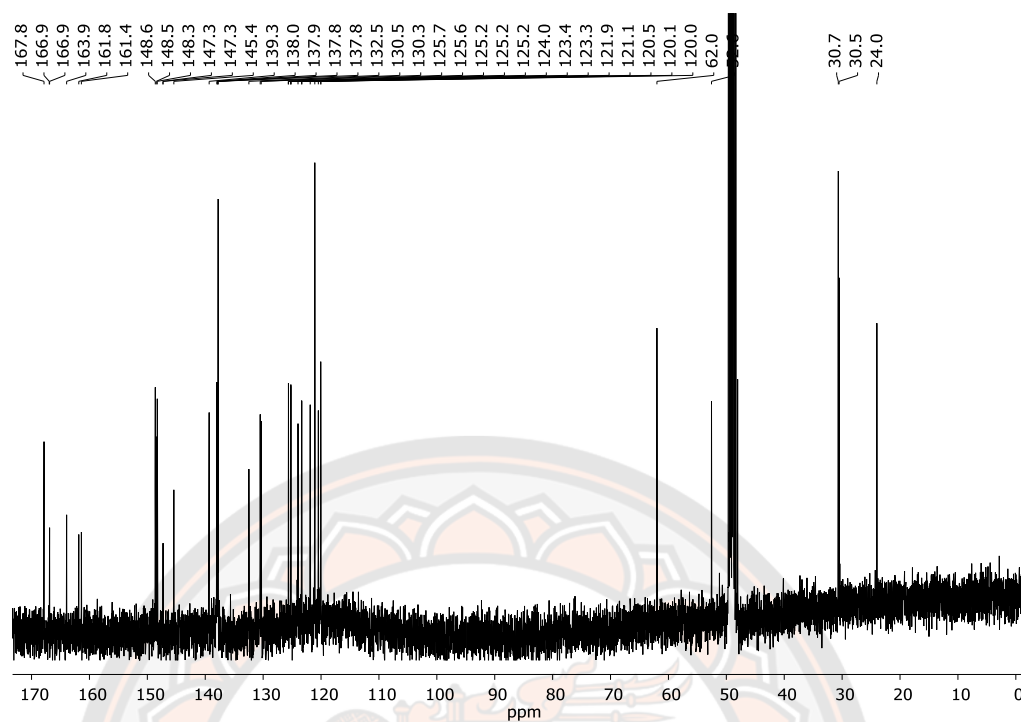


Figure S29 ¹³C-NMR spectrum of complex 11 in methanol-*d*₄.

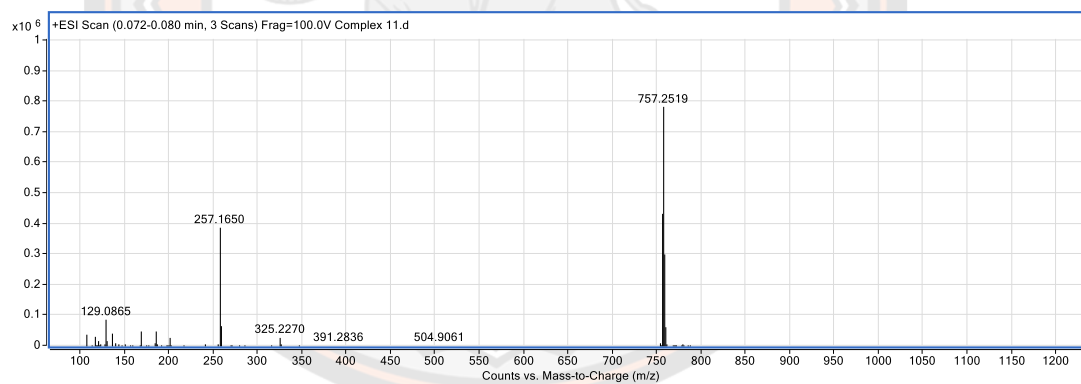


Figure S30 Mass spectrum of complex 11.

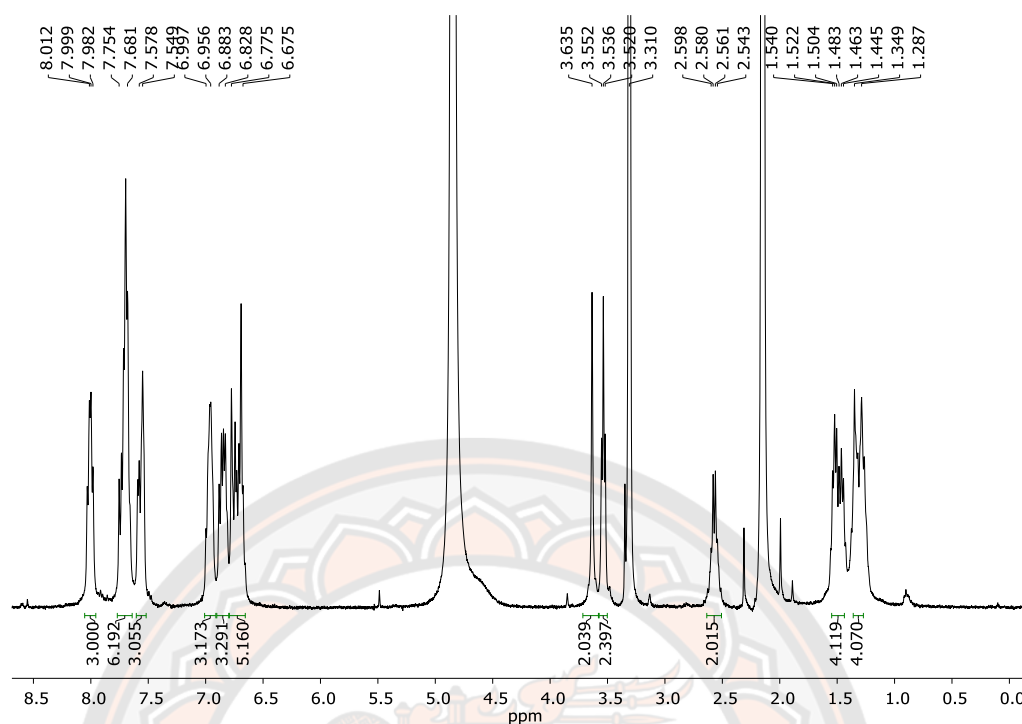


Figure S31 ¹H-NMR spectrum of complex 12 in methanol-*d*₄.

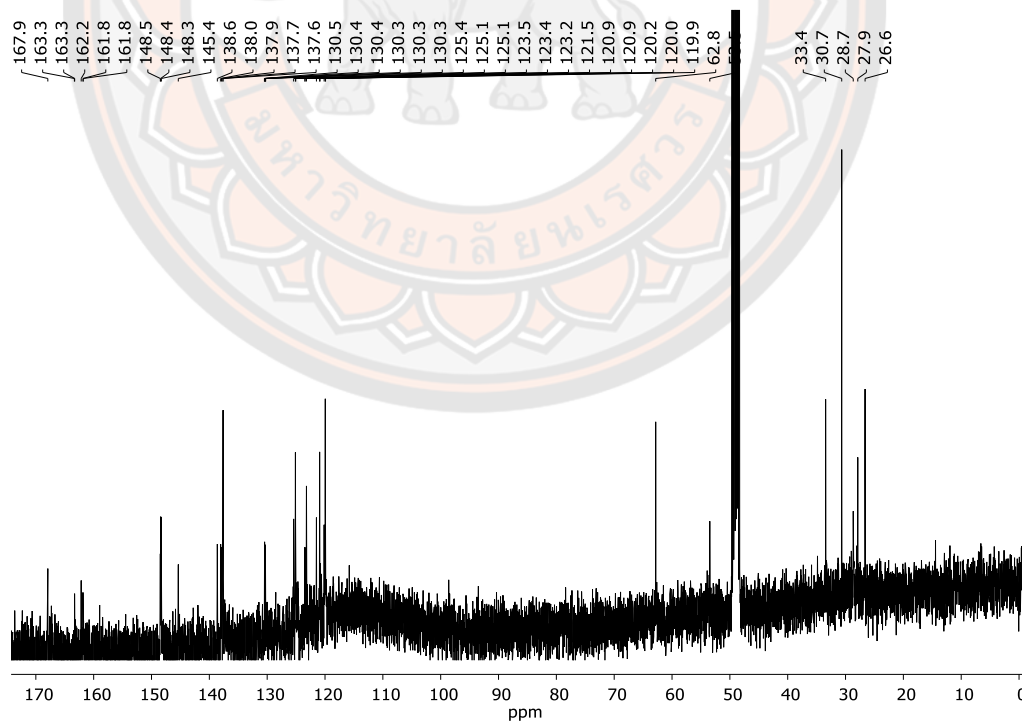


Figure S32 ¹³C-NMR spectrum of complex 12 in methanol-*d*₄.

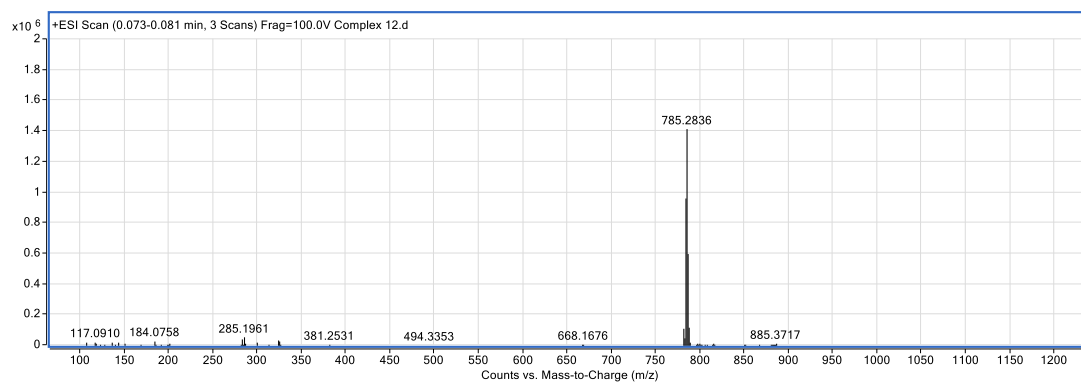


Figure S33 Mass spectrum of complex 12.

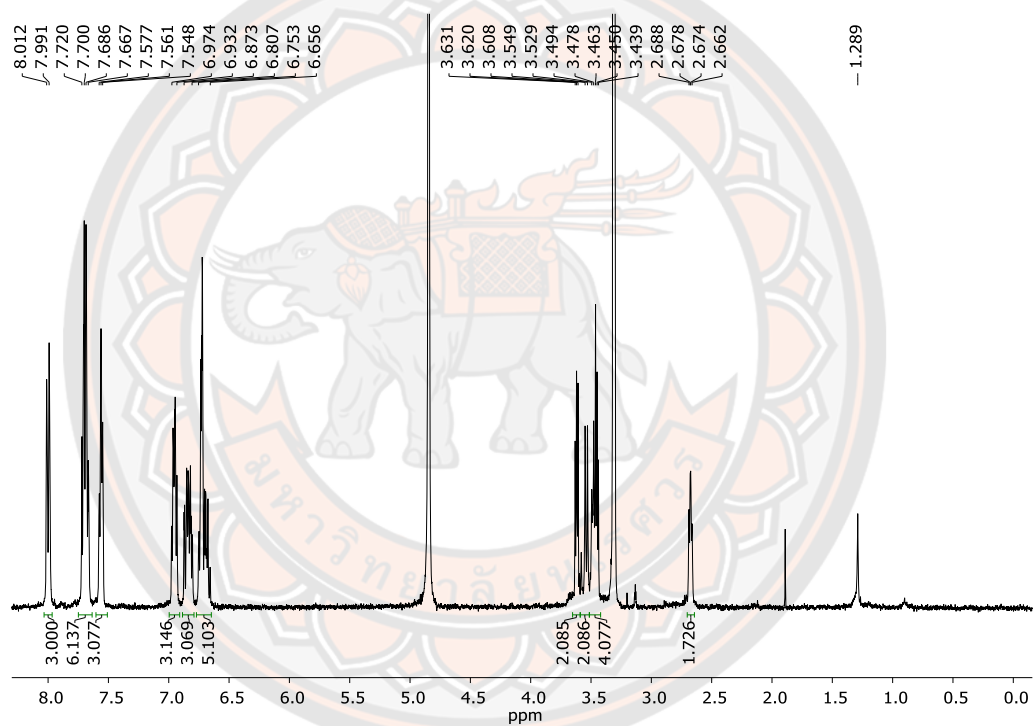


Figure S34 ^1H -NMR spectrum of complex 13 in methanol- d_4 .

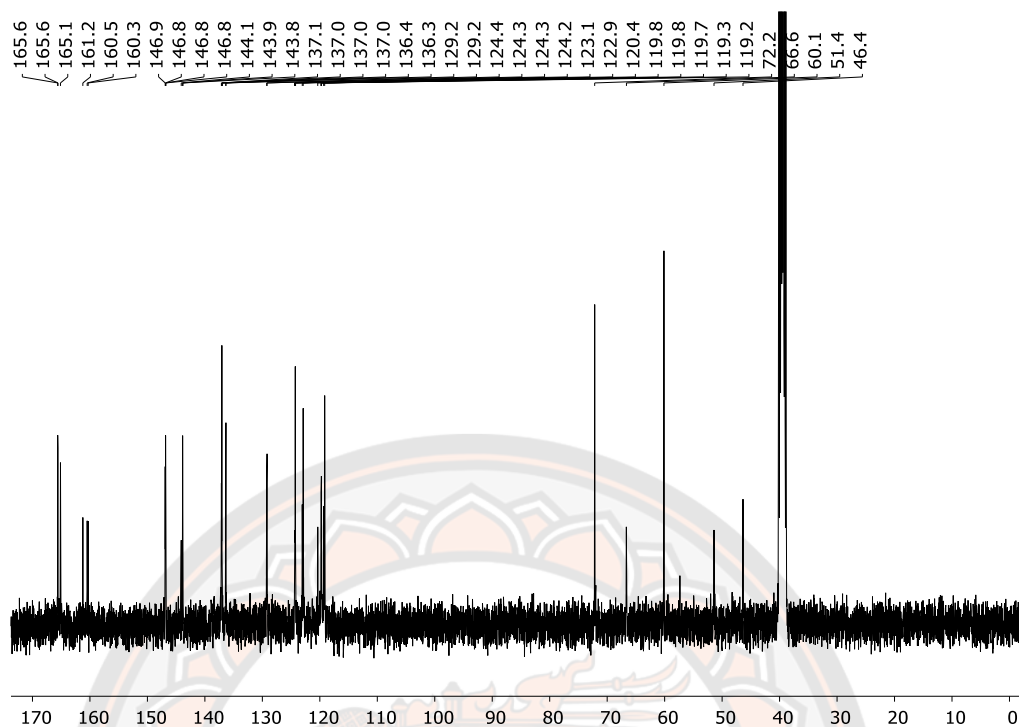


Figure S35 ^{13}C -NMR spectrum of complex 13 in methanol- d_4 .

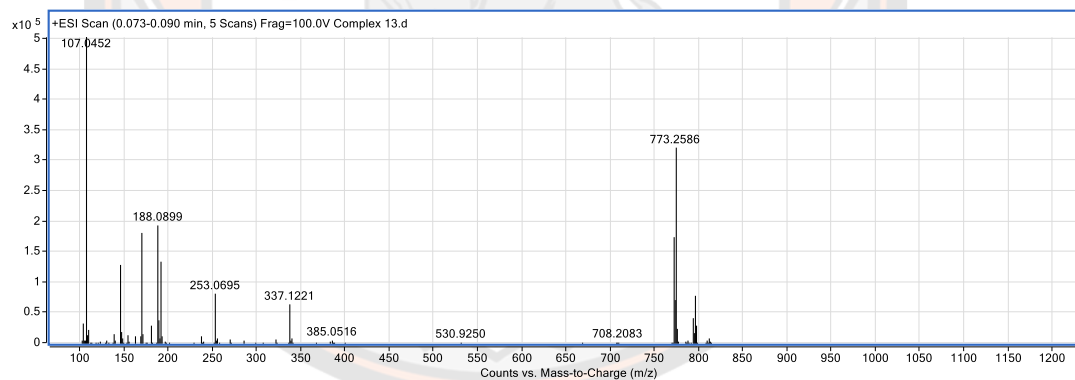


Figure S36 Mass spectrum of complex 13.

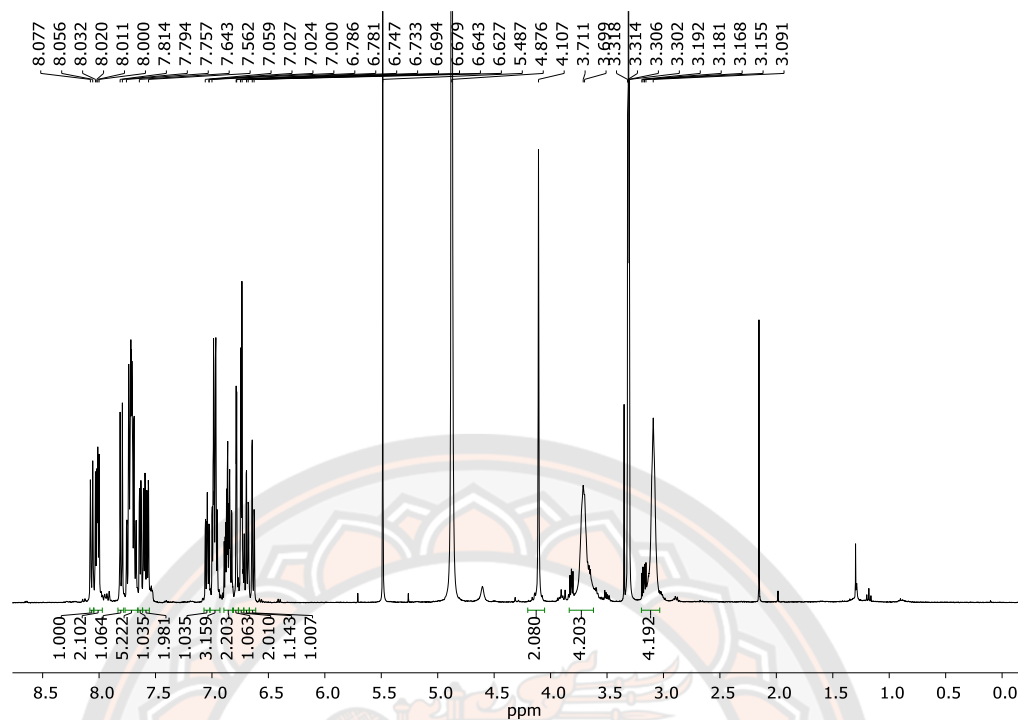


Figure S37 ¹H-NMR spectrum of complex 14 in methanol-*d*₄.

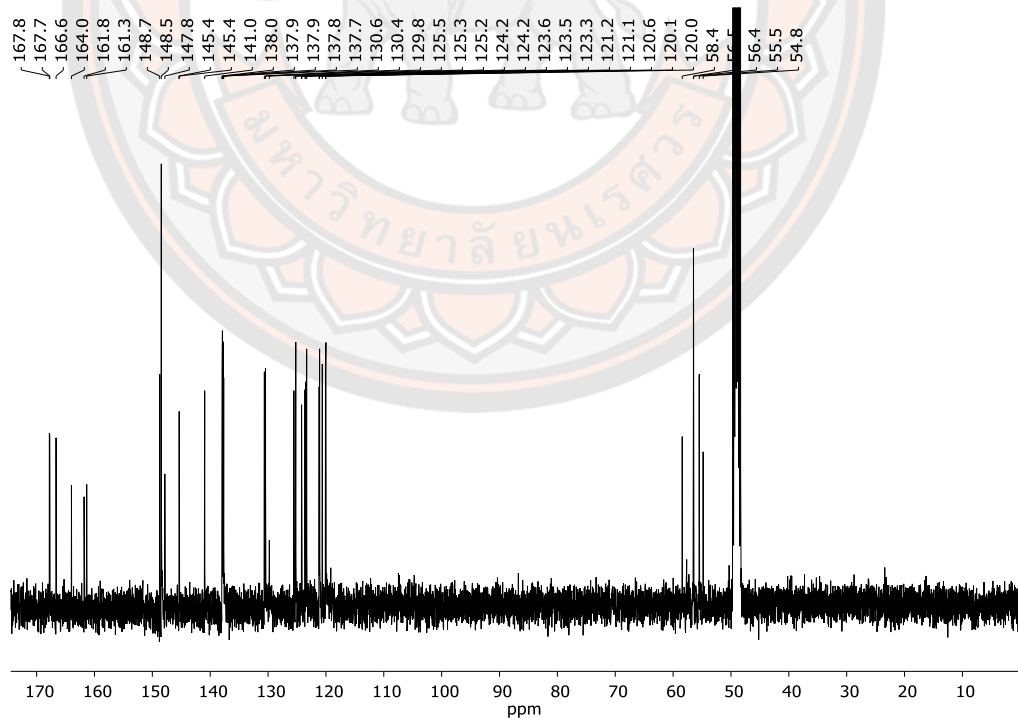


Figure S38 ¹³C-NMR spectrum of complex 14 in methanol-*d*₄.

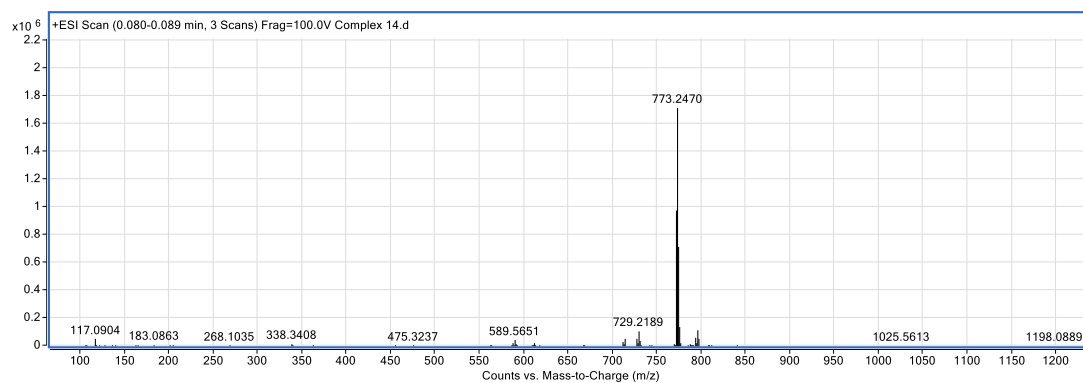


Figure S39 Mass spectrum of complex 14.

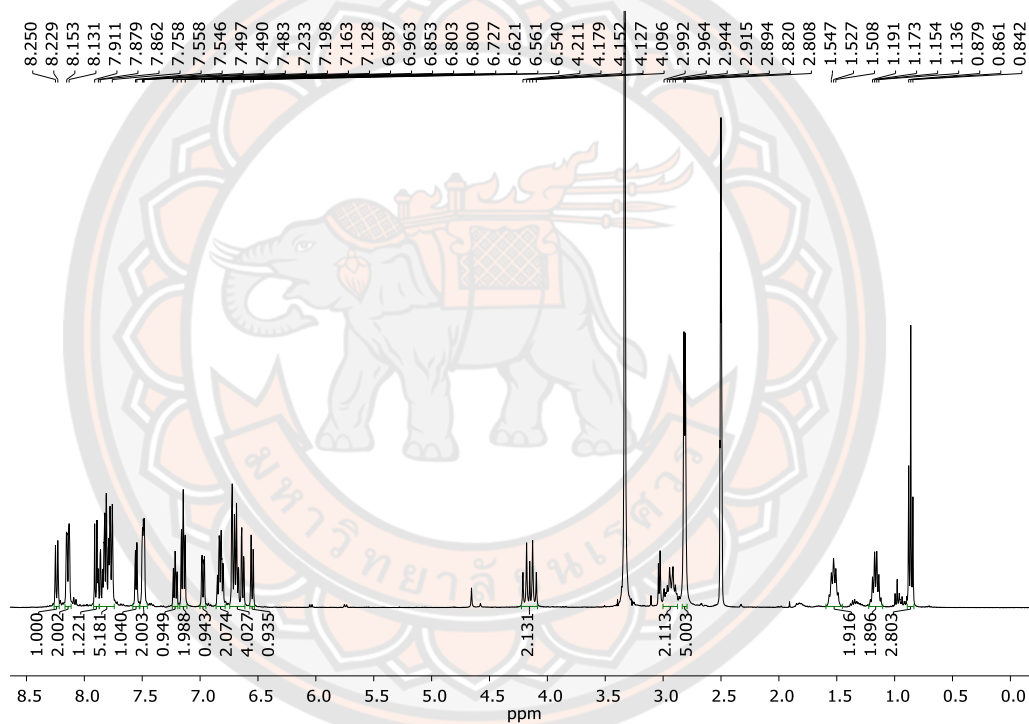


Figure S40 ^1H -NMR spectrum of complex 15 in $\text{DMSO}-d_6$.

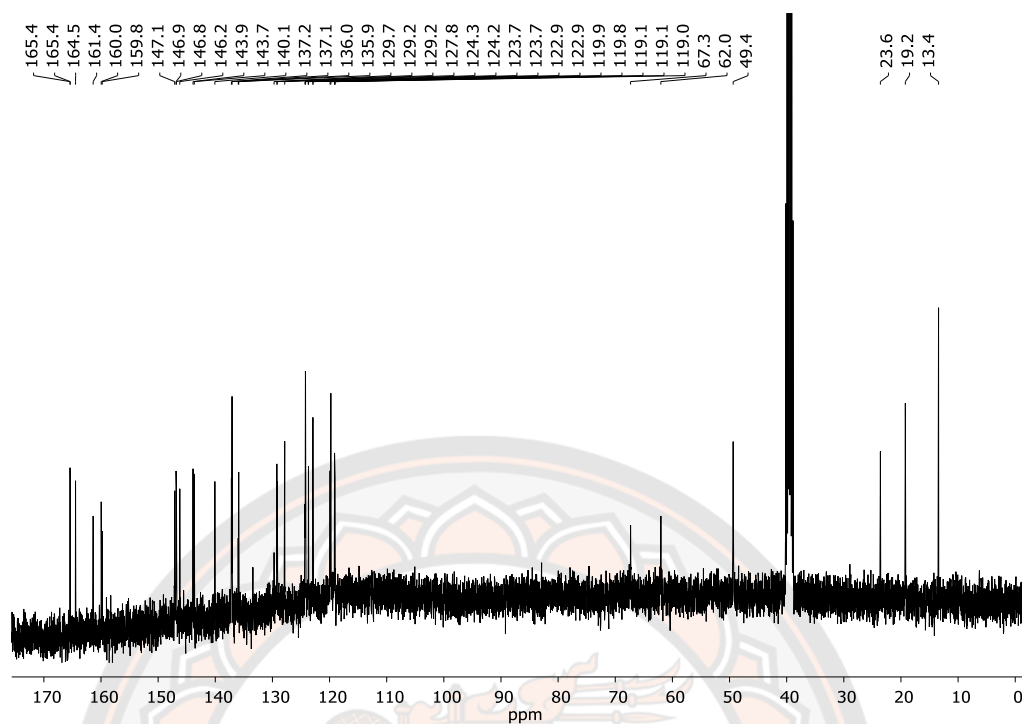


Figure S41 ¹³C-NMR spectrum of complex 15 in DMSO-*d*₆.

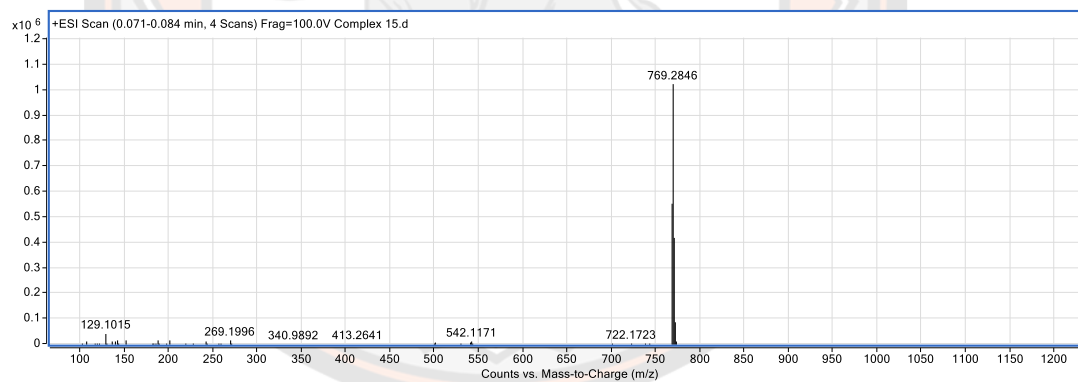


Figure S42 Mass spectrum of complex 15.

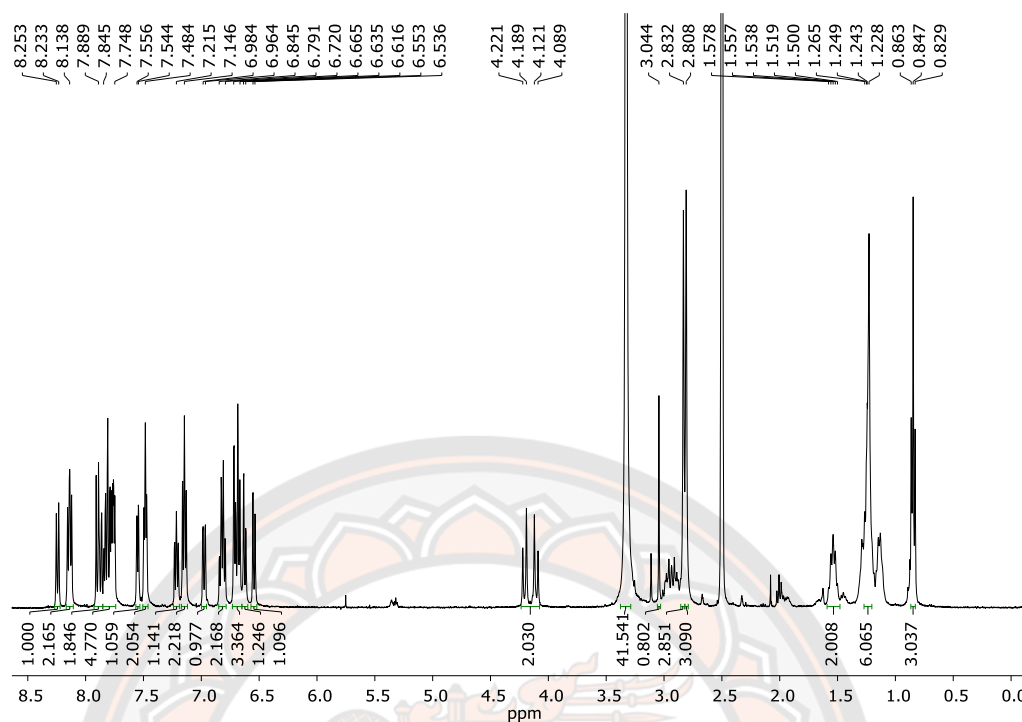


Figure S43 ¹H-NMR spectrum of complex 16 in DMSO-*d*₆.

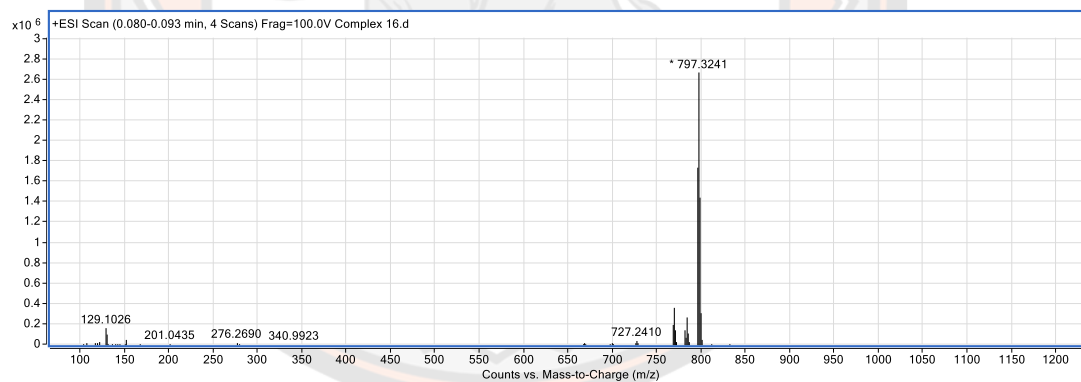


Figure S45 Mass spectrum of complex 16.

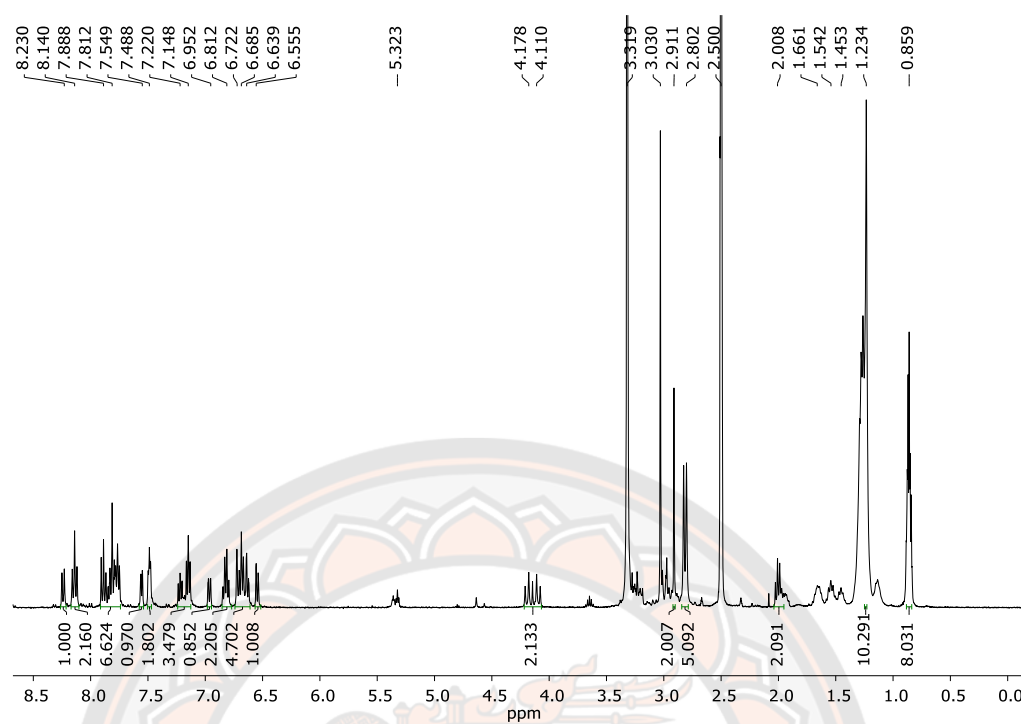


Figure S45 ¹H-NMR spectrum of complex 17 in DMSO-*d*₆.

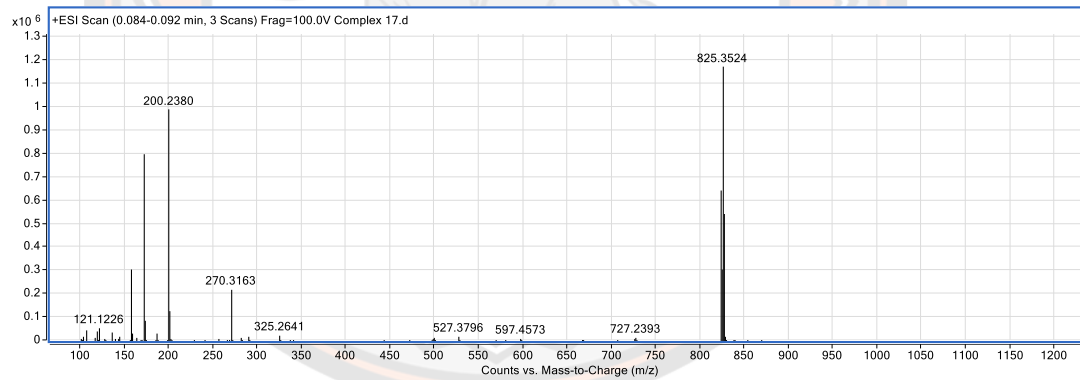


Figure S46 Mass spectrum of complex 17.

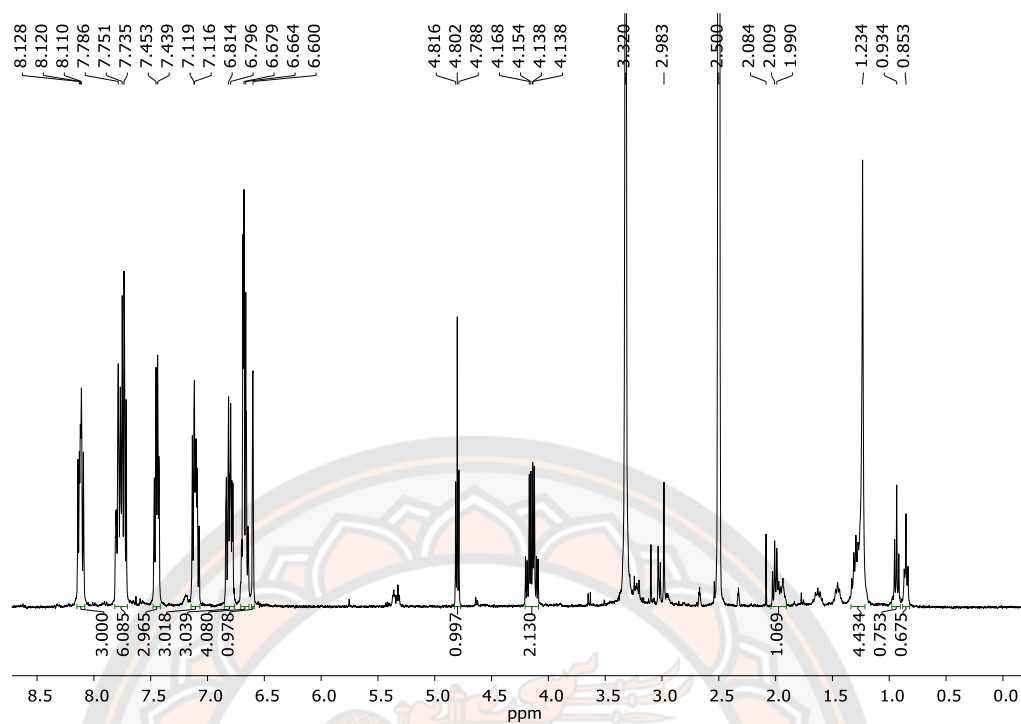


Figure S47 ¹H-NMR spectrum of complex 18 in DMSO-*d*₆.

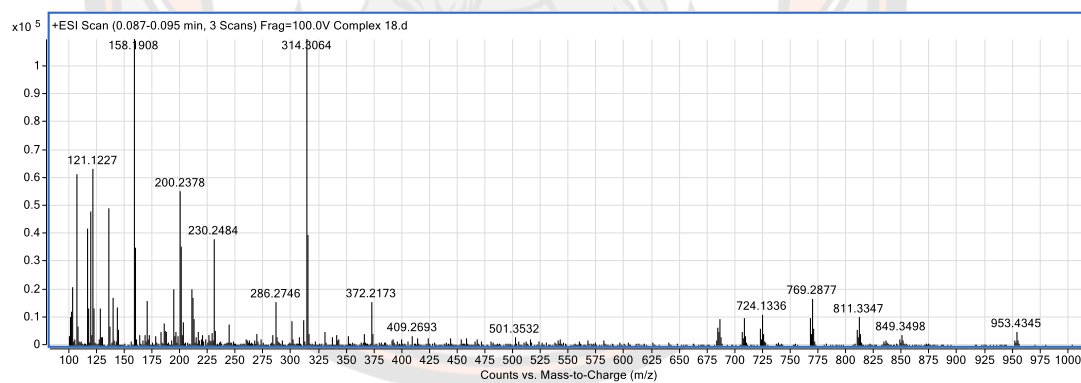


Figure S48 Mass spectrum of complex 18.

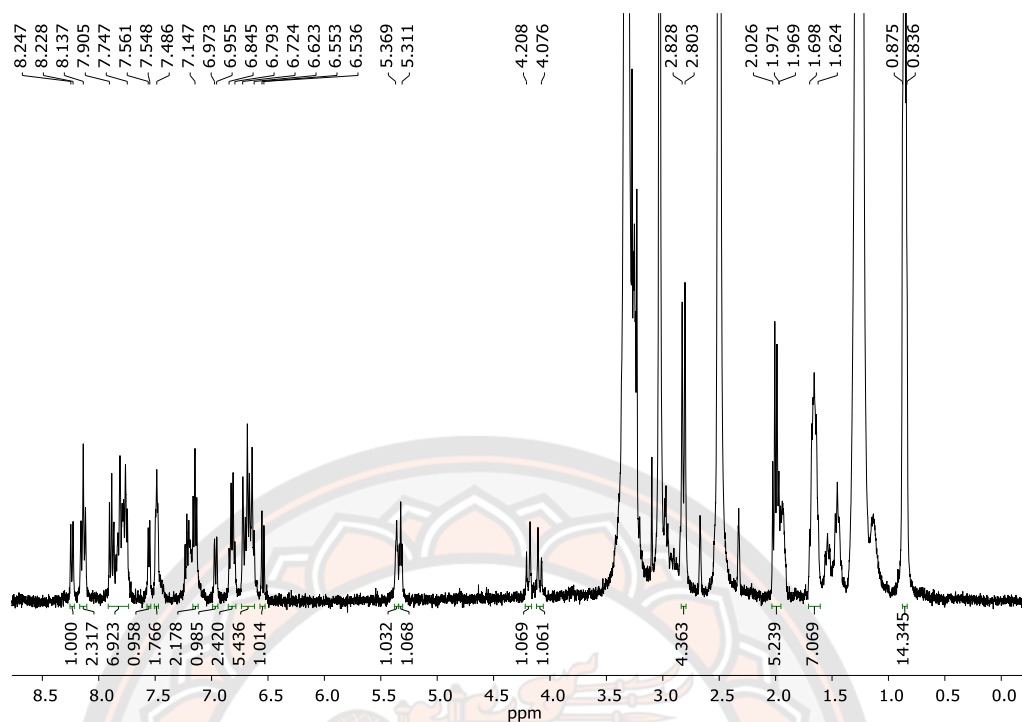


Figure S49 ¹H-NMR spectrum of complex 19 in DMSO-*d*₆.

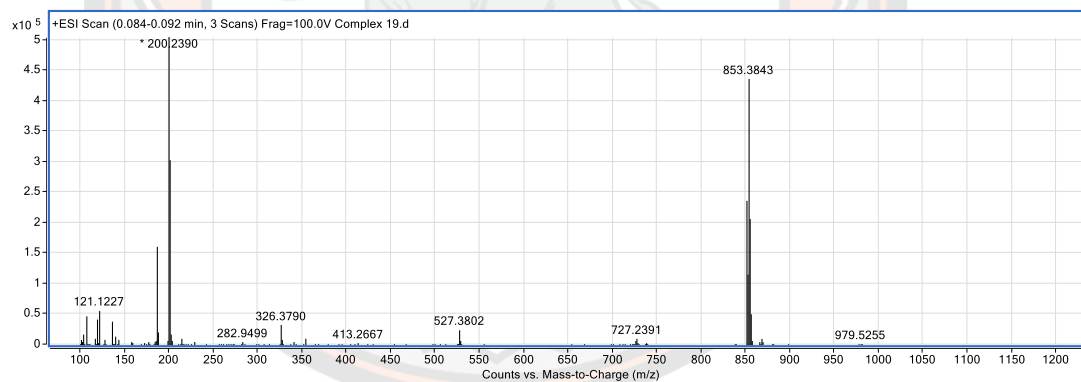


Figure S50 Mass spectrum of complex 19.

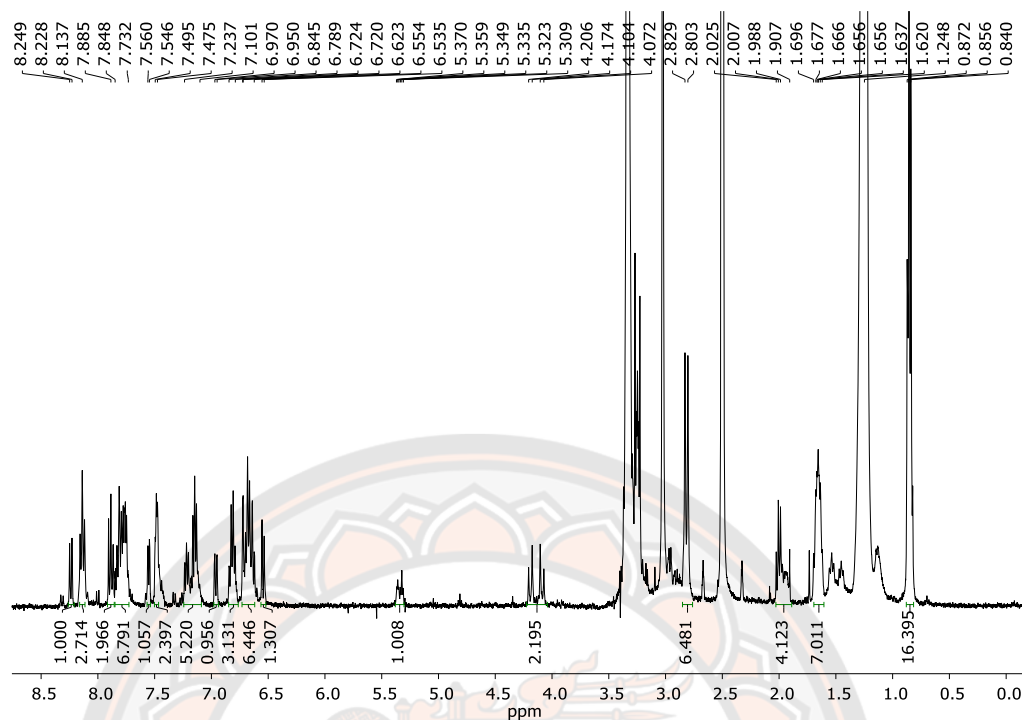


Figure S51 ¹H-NMR spectrum of complex 20 in DMSO-*d*₆.

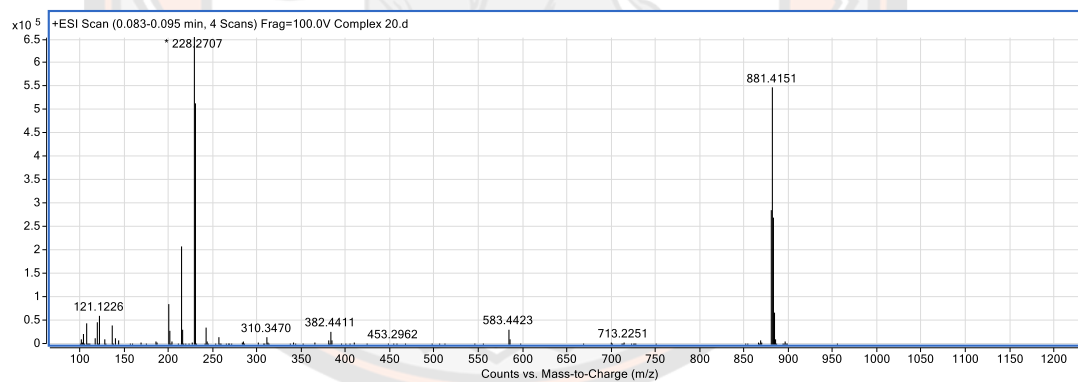


Figure S52 Mass spectrum of complex 20.

Figure S53 Crystallography details of complex 4.**Crystal data**

Chemical formula	[Ir(C ₁₁ H ₈ N) ₂ (C ₁₈ H ₂₄ N ₂)]Cl
<i>M</i> _r	804.41
Crystal system, space group	Monoclinic, <i>P</i> 2 ₁ / <i>c</i>
Temperature (K)	298
<i>a</i> , <i>b</i> , <i>c</i> (Å)	12.1012 (7), 34.267 (2), 18.4681 (11)
β (°)	94.471 (2)
<i>V</i> (Å ³)	7634.9 (8)
<i>Z</i>	8
Radiation type	Mo <i>K</i> α
μ (mm ⁻¹)	7.64
Crystal size (mm)	0.18 × 0.1 × 0.1

Data collection

Diffractometer	Bruker D8 VENTURE
Absorption correction	Multi-scan (<i>SADABS</i> ; Bruker, 2016)
<i>T</i> _{min} , <i>T</i> _{max}	0.635, 0.734
No. of measured, independent and observed [<i>I</i> > 2σ(<i>I</i>)] reflections	110242, 15577, 14944
<i>R</i> _{int}	0.056
(sin θ/λ) _{max} (Å ⁻¹)	0.626

Refinement

$R[F^2 > 2\sigma(F^2)]$, $wR(F^2)$, <i>S</i>	0.052, 0.135, 1.07
No. of reflections	15577
No. of parameters	869
No. of restraints	142
H-atom treatment	H-atom parameters constrained
ρ_{\max} , ρ_{\min} (e Å ⁻³)	3.11, -1.29

Computer programs: *APEX3* and *SAINT* [128], *SHELXT* [129], *SHELXL2014* [129] and *OLEX2*.

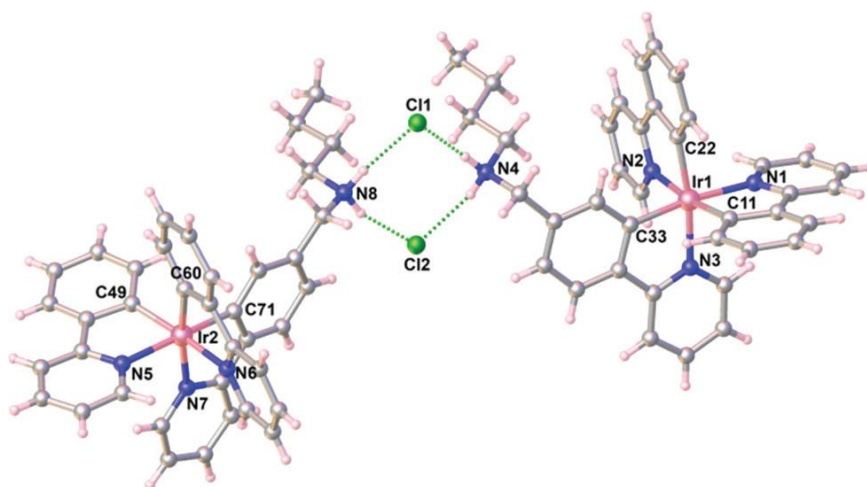
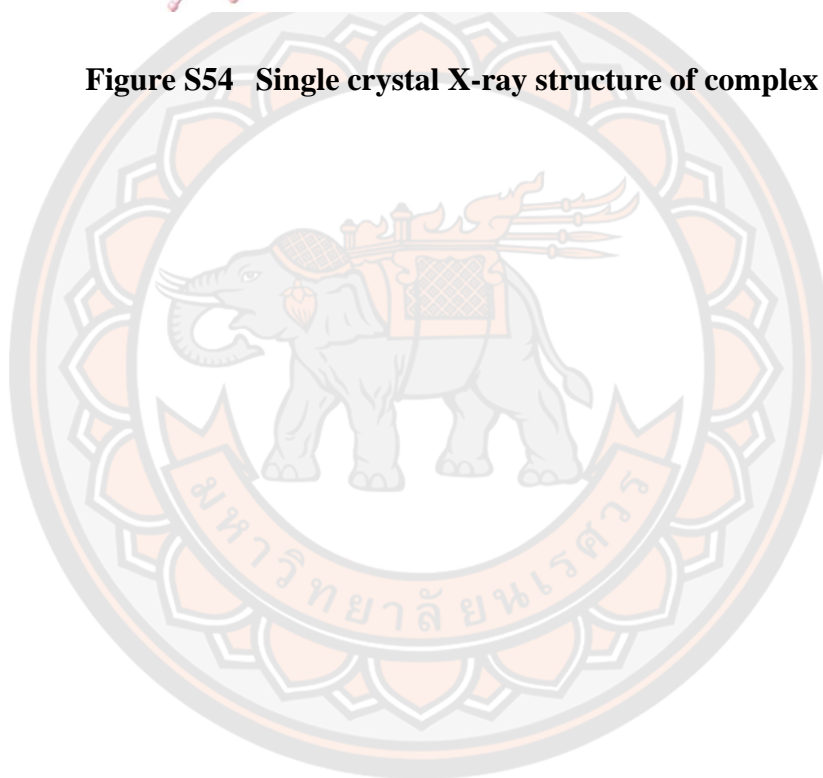


Figure S54 Single crystal X-ray structure of complex 3.



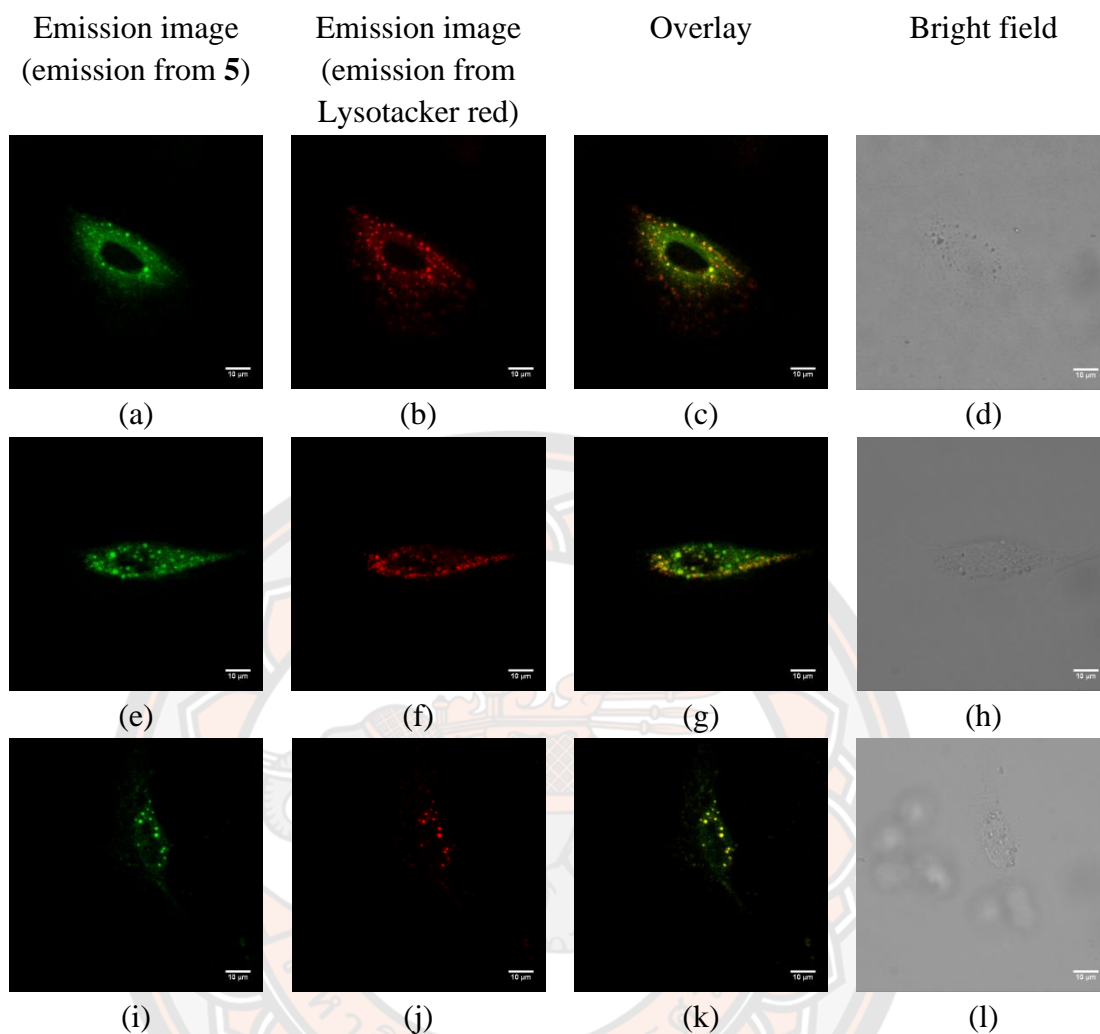


Figure S55 LSCM microscopy images of NIH-3T3 cells stained with complex **5**. (a-c) NIH-3T3 cells after incubation with complex **5** (5 μ M) at 37 $^{\circ}$ C for 1h; (d-f) NIH-3T3 cells after incubation with complex **5** (5 μ M) at 37 $^{\circ}$ C for 2h; (i-l) NIH-3T3 cells after incubation with complex **5** (5 μ M) at 37 $^{\circ}$ C for 24h. Scale bar (white) = 10 μ m.

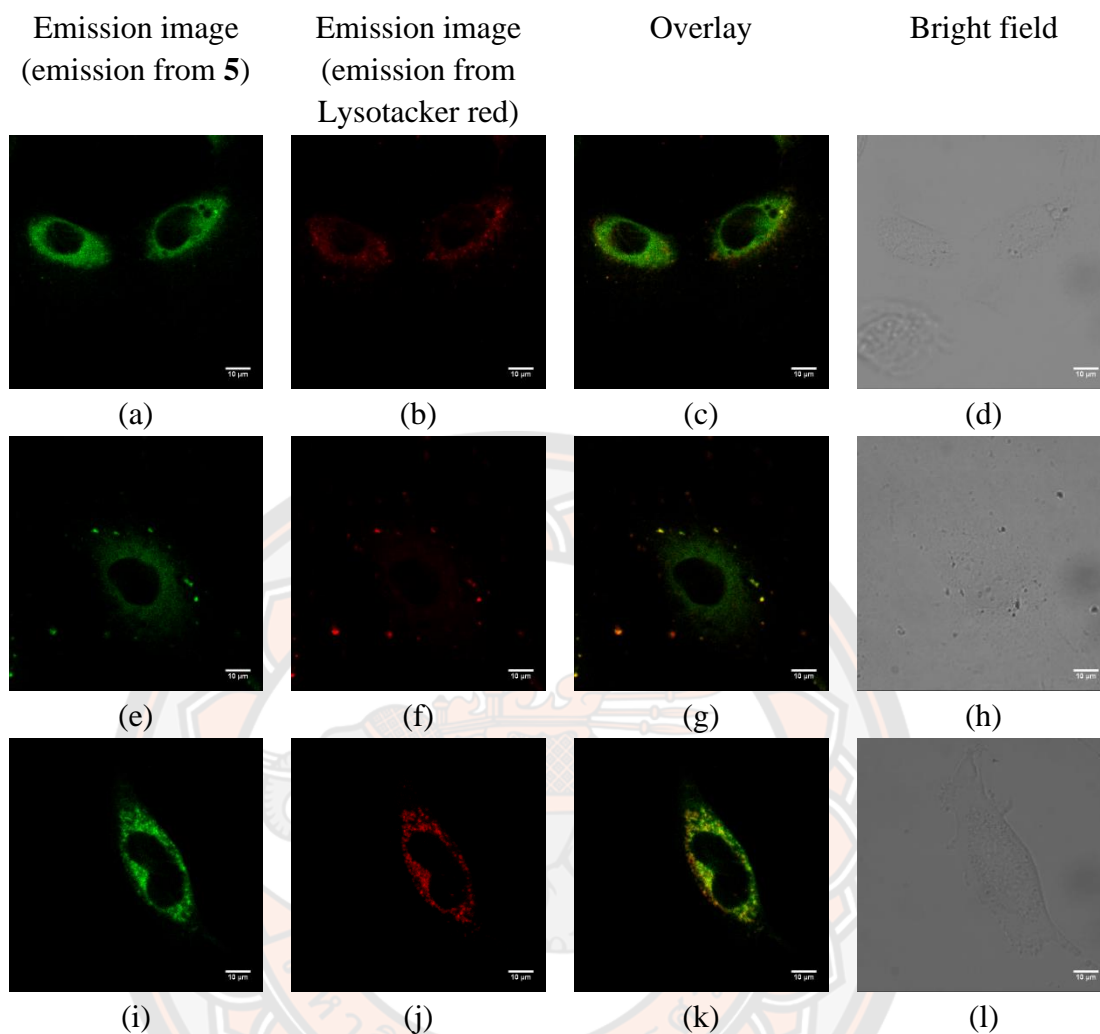


Figure S56 LSCM microscopy images of NIH-3T3 cells stained with complex **5**. (a-c) NIH-3T3 cells after incubation with complex **5** (2 μ M) at 37 $^{\circ}$ C for 1h; (d-f) NIH-3T3 cells after incubation with complex **5** (2 μ M) at 37 $^{\circ}$ C for 2h; (i-l) NIH-3T3 cells after incubation with complex **5** (2 μ M) at 37 $^{\circ}$ C for 24h. Scale bar (white) = 10 μ m.

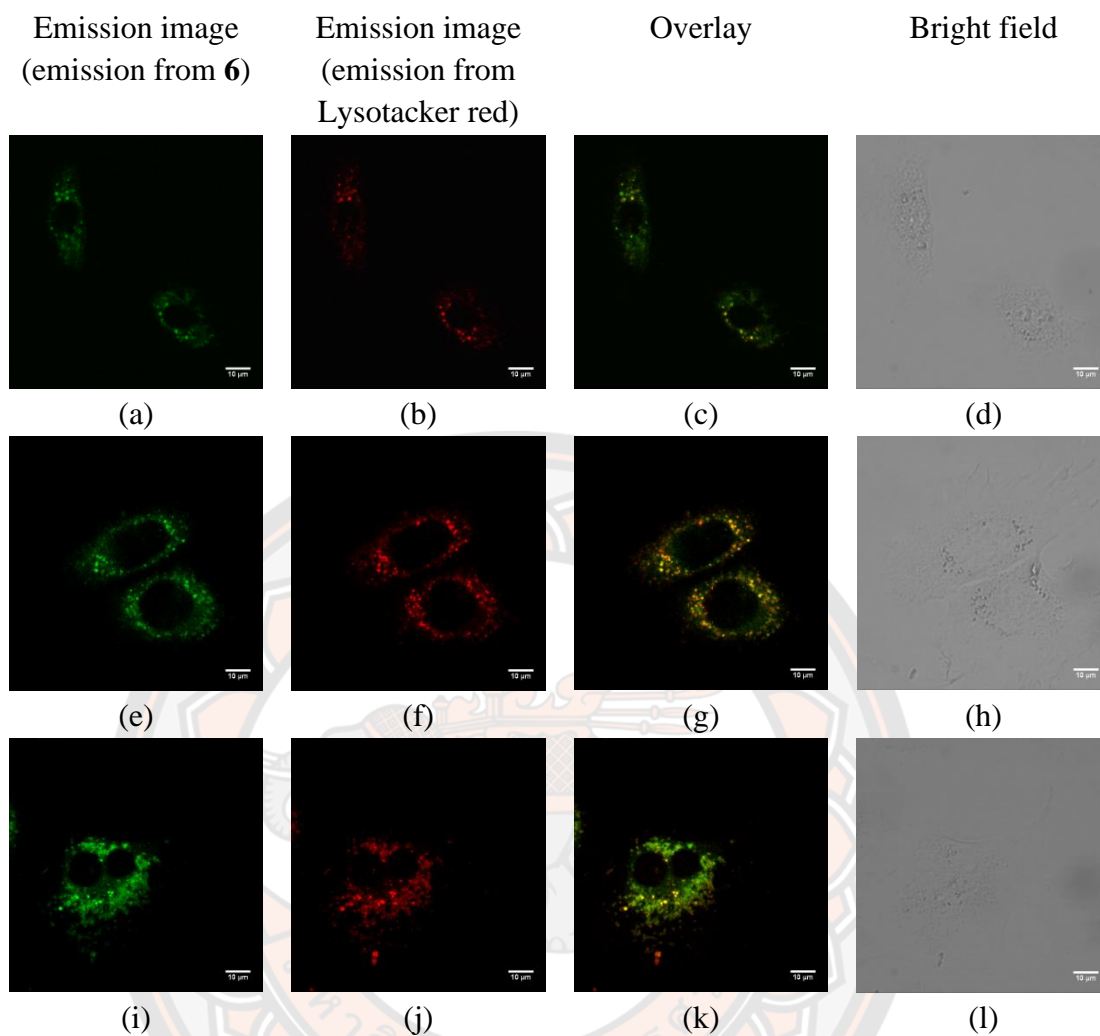


Figure S57 LSCM microscopy images of NIH-3T3 cells stained with complex **6**. (a-c) NIH-3T3 cells after incubation with complex **6** (5 μ M) at 37 $^{\circ}$ C for 1h; (d-f) NIH-3T3 cells after incubation with complex **6** (5 μ M) at 37 $^{\circ}$ C for 2h; (i-l) NIH-3T3 cells after incubation with complex **6** (5 μ M) at 37 $^{\circ}$ C for 24h. Scale bar (white) = 10 μ m.

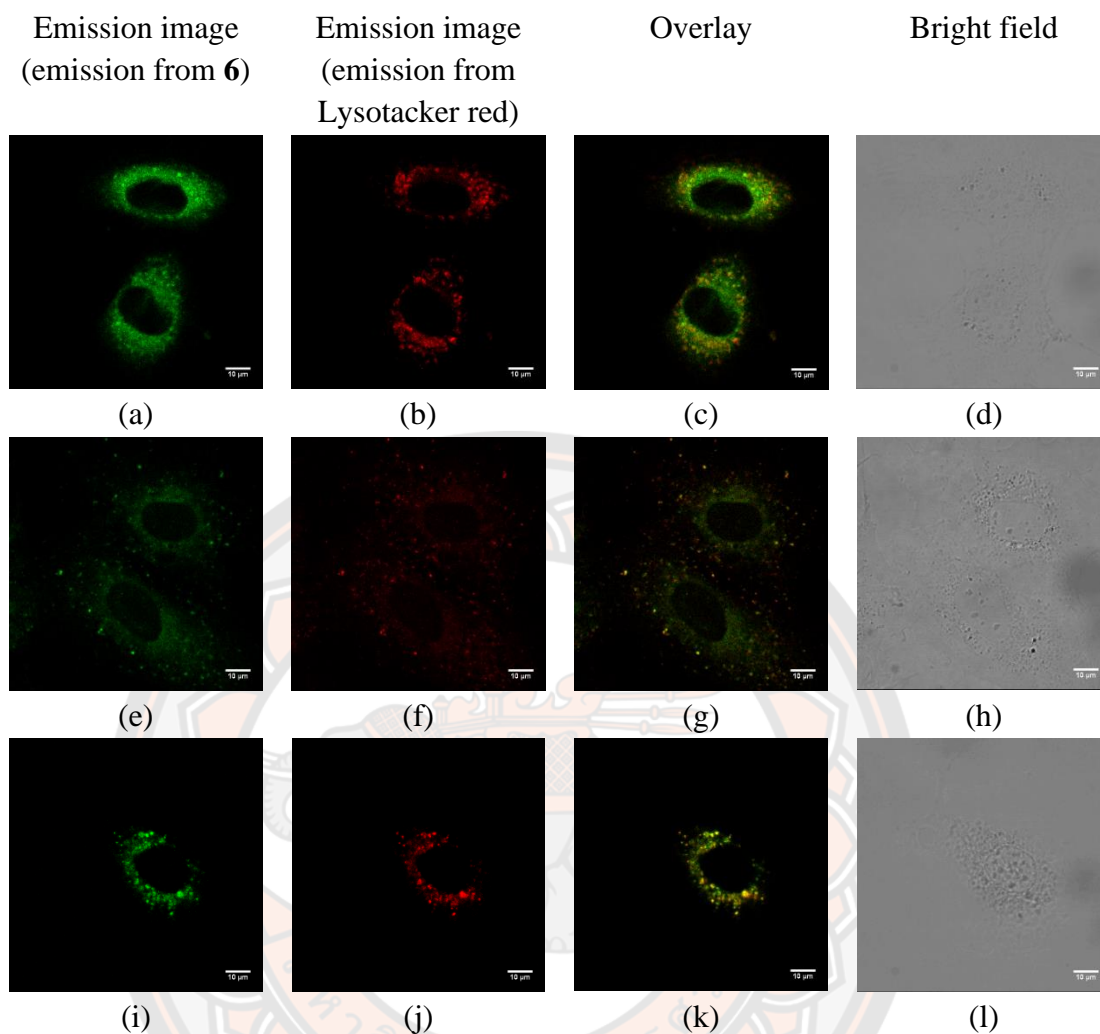


Figure S58 LSCM microscopy images of NIH-3T3 cells stained with complex **6**. (a-c) NIH-3T3 cells after incubation with complex **6** (2 μ M) at 37 $^{\circ}$ C for 1h; (d-f) NIH-3T3 cells after incubation with complex **6** (2 μ M) at 37 $^{\circ}$ C for 2h; (i-l) NIH-3T3 cells after incubation with complex **6** (2 μ M) at 37 $^{\circ}$ C for 24h. Scale bar (white) = 10 μ m.

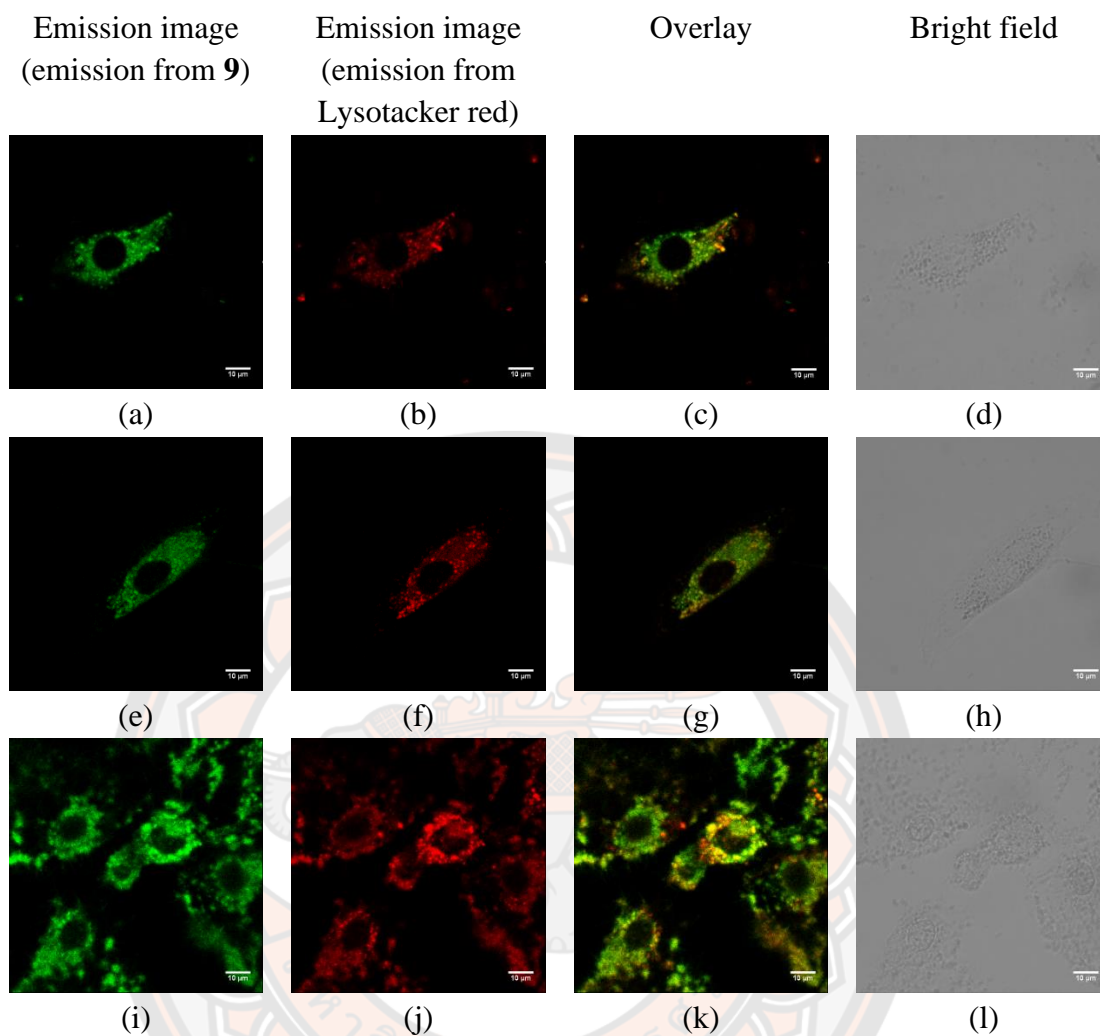


Figure S59 LSCM microscopy images of NIH-3T3 cells stained with complex **9**. (a-c) NIH-3T3 cells after incubation with complex **9** (5 μ M) at 37 $^{\circ}$ C for 1h; (d-f) NIH-3T3 cells after incubation with complex **9** (5 μ M) at 37 $^{\circ}$ C for 2h; (i-l) NIH-3T3 cells after incubation with complex **9** (5 μ M) at 37 $^{\circ}$ C for 24h. Scale bar (white) = 10 μ m.

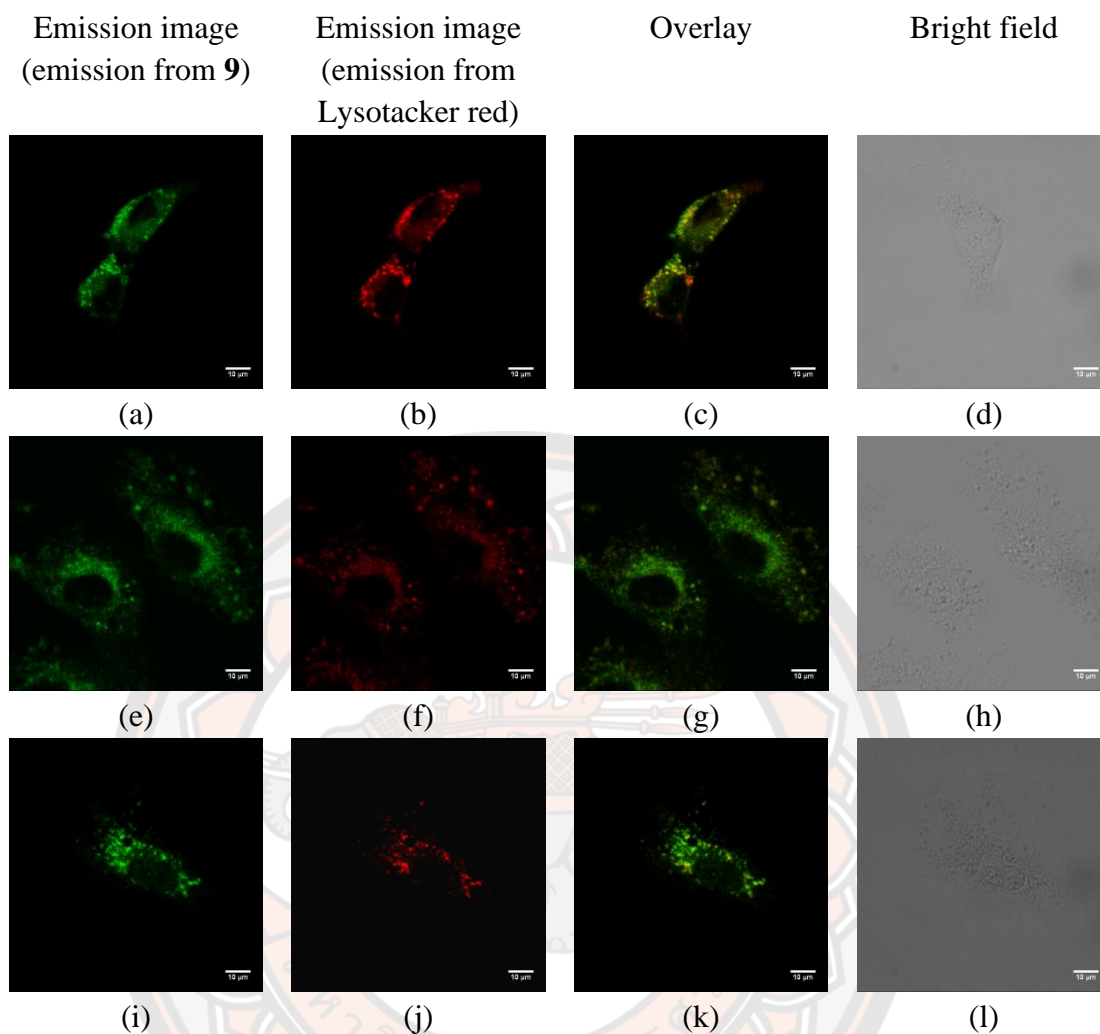


Figure S60 LSCM microscopy images of NIH-3T3 cells stained with complex 9. (a-c) NIH-3T3 cells after incubation with complex 9 (2 μ M) at 37 $^{\circ}$ C for 1h; (d-f) NIH-3T3 cells after incubation with complex 9 (2 μ M) at 37 $^{\circ}$ C for 2h; (i-l) NIH-3T3 cells after incubation with complex 9 (2 μ M) at 37 $^{\circ}$ C for 24h. Scale bar (white) = 10 μ m.

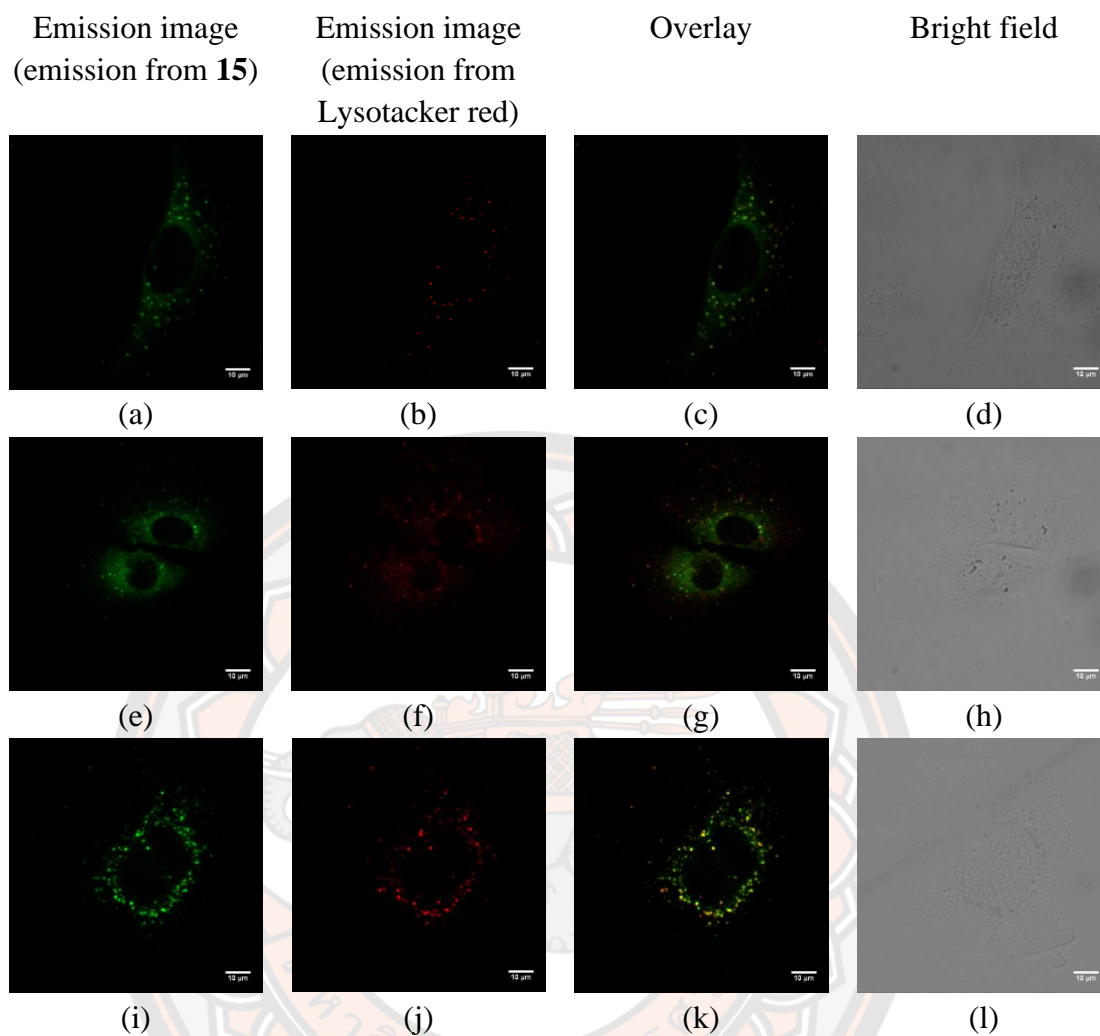


Figure S61 LSCM microscopy images of NIH-3T3 cells stained with complex **15**. (a-c) NIH-3T3 cells after incubation with complex **15** (5 μ M) at 37 $^{\circ}$ C for 1h; (d-f) NIH-3T3 cells after incubation with complex **15** (5 μ M) at 37 $^{\circ}$ C for 2h; (i-l) NIH-3T3 cells after incubation with complex **15** (5 μ M) at 37 $^{\circ}$ C for 24h. Scale bar (white) = 10 μ m.

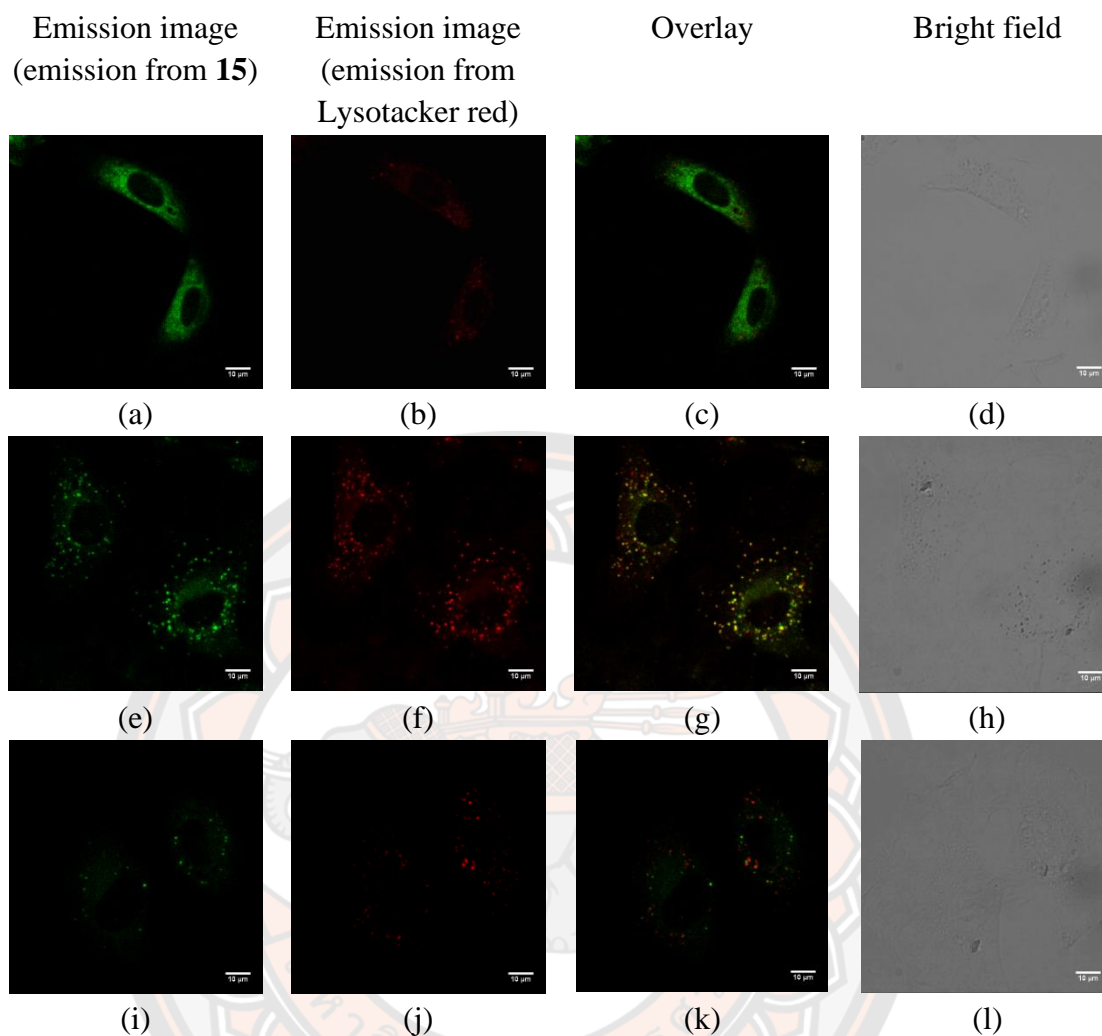


Figure S62 LSCM microscopy images of NIH-3T3 cells stained with complex **15**. (a-c) NIH-3T3 cells after incubation with complex **15** (2 μ M) at 37 °C for 1h; (d-f) NIH-3T3 cells after incubation with complex **15** (2 μ M) at 37 °C for 2h; (i-l) NIH-3T3 cells after incubation with complex **15** (2 μ M) at 37 °C for 24h. Scale bar (white) = 10 μ m.

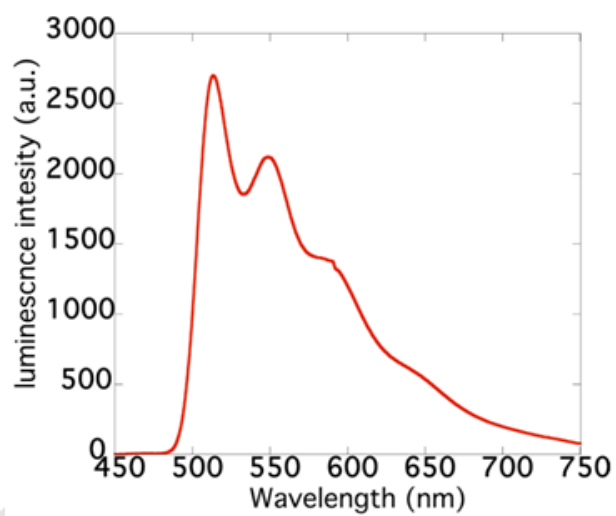
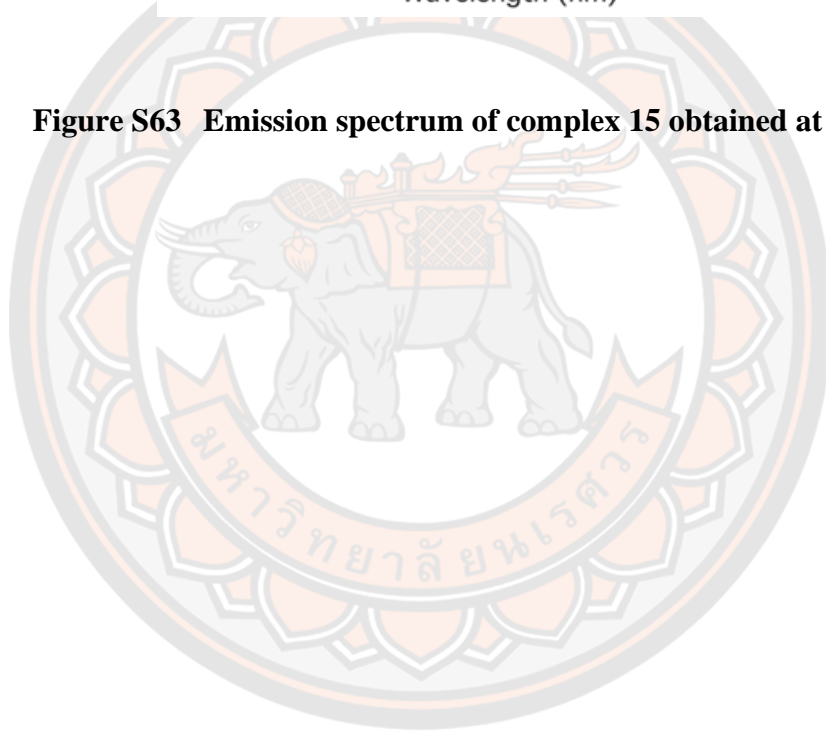


Figure S63 Emission spectrum of complex 15 obtained at 77 K.



REFERENCES

- [1] W. C. Wolsey, "Chemistry of the Elements (Greenwood, N. N.; Earshaw, A.)," *Journal of Chemical Education*, vol. 62, p. A133, 1985/04/01 1985.
- [2] A. F. Holleman, E. und Nils Wiberg, and G. Fischer, *Lehrbuch der Anorganischen Chemie*, 2009.
- [3] C. Housecroft and A. G. Sharpe, *Inorganic Chemistry*, 3rd Editio ed., 2007.
- [4] G. Schneider, "New inorganic iridium(III) complexes for photonic applications," 2009.
- [5] K. A. King, P. J. Spellane, and R. J. Watts, "Excited-state properties of a triply ortho-metalated iridium(III) complex," *Journal of the American Chemical Society*, vol. 107, pp. 1431-1432, 1985/03/01 1985.
- [6] M. A. Baldo, S. Lamansky, P. E. Burrows, M. E. Thompson, and S. R. Forrest, "Very high-efficiency green organic light-emitting devices based on electrophosphorescence," *Applied Physics Letters*, vol. 75, pp. 4-6, 1999.
- [7] A. B. Tamayo, B. D. Alleyne, P. I. Djurovich, S. Lamansky, I. Tsyba, N. N. Ho, *et al.*, "Synthesis and Characterization of Facial and Meridional Tris-cyclometalated Iridium(III) Complexes," *Journal of the American Chemical Society*, vol. 125, pp. 7377-7387, 2003/06/01 2003.
- [8] F. N. C. Joseph C. Deaton, "Archetypal Iridium(III) Compounds for Optoelectronic and Photonic Applications," in *Iridium(III) in Optoelectronic and Photonics Applications*, ed, 2017, pp. 1-69.
- [9] L. Flamigni, A. Barbieri, C. Sabatini, B. Ventura, and F. Barigelletti, "Photochemistry and photophysics of coordination compounds: Iridium," *Topics in Current Chemistry*, 2007.
- [10] M. Montalti, A. Credi, L. Prodi, and M. Teresa Gandolfi, *Handbook of Photochemistry, Third Edition*, 2006.
- [11] Y. You and W. Nam, "Photofunctional triplet excited states of cyclometalated Ir(III) complexes: Beyond electroluminescence," ed, 2012.
- [12] T. Hu, L. He, L. Duan, and Y. Qiu, "Solid-state light-emitting electrochemical cells based on ionic iridium(iii) complexes," *Journal of Materials Chemistry*, 2012.
- [13] J. D. Slinker, J. Rivnay, J. S. Moskowitz, J. B. Parker, S. Bernhard, H. D. Abruña, *et al.*, "Electroluminescent devices from ionic transition metal complexes," *Journal of Materials Chemistry*, 2007.
- [14] M. K. Nazeeruddin, R. T. Wegh, Z. Zhou, C. Klein, Q. Wang, F. De Angelis, *et al.*, "Efficient green-blue-light-emitting cationic iridium complex for light-emitting electrochemical cells," *Inorganic Chemistry*, 2006.
- [15] !!! INVALID CITATION !!! [14-16].
- [16] R. D. Costa, F. J. Céspedes-Guirao, E. Ortí, H. J. Bolink, J. Gierschner, F. Fernández-Lázaro, *et al.*, "Efficient deep-red light-emitting electrochemical cells based on a perylenediimide-iridium-complex dyad," *Chemical Communications*, 2009.
- [17] H. C. Su, H. F. Chen, F. C. Fang, C. C. Liu, C. C. Wu, K. T. Wong, *et al.*, "Solid-state white light-emitting electrochemical cells using iridium-based cationic transition metal complexes," *Journal of the American Chemical Society*, 2008.

- [18] M. S. Lowry and S. Bernhard, "Synthetically Tailored Excited States: Phosphorescent, Cyclometalated Iridium(III) Complexes and Their Applications," *Chemistry - A European Journal*, vol. 12, 2006.
- [19] G. A. Wagnières, W. M. Star, and B. C. Wilson, "In Vivo Fluorescence Spectroscopy and Imaging for Oncological Applications," vol. 68, ed, 1998.
- [20] V. Fernández-Moreira, F. L. Thorp-Greenwood, and M. P. Coogan, "Application of d6 transition metal complexes in fluorescence cell imaging," ed, 2010.
- [21] F. L. Thorp-Greenwood, R. G. Balasingham, and M. P. Coogan, "Organometallic complexes of transition metals in luminescent cell imaging applications," vol. 714, ed, 2012.
- [22] R. A. Benson, I. B. McInnes, J. M. Brewer, and P. Garside, "Cellular imaging in rheumatic diseases," vol. 11, ed, 2015.
- [23] P. Lang, K. Yeow, A. Nichols, and A. Scheer, "Cellular imaging in drug discovery," *Nature Reviews Drug Discovery*, vol. 5, 2006.
- [24] H. Zhu, J. Fan, J. Du, and X. Peng, "Fluorescent Probes for Sensing and Imaging within Specific Cellular Organelles," *Accounts of Chemical Research*, vol. 49, 2016.
- [25] T. Ueno and T. Nagano, "Fluorescent probes for sensing and imaging," vol. 8, ed, 2011.
- [26] Z. Yang, J. Cao, Y. He, J. H. Yang, T. Kim, X. Peng, *et al.*, "Macro-/micro-environment-sensitive chemosensing and biological imaging," vol. 43, ed, 2014.
- [27] G. Y. Wiederschain, "The Molecular Probes handbook. A guide to fluorescent probes and labeling technologies," *Biochemistry (Moscow)*, vol. 76, 2011.
- [28] M. A. Baldo, M. E. Thompson, and S. R. Forrest, "High-efficiency fluorescent organic light-emitting devices using a phosphorescent sensitizer," *Nature*, 2000.
- [29] M. Yu, Q. Zhao, L. Shi, F. Li, Z. Zhou, H. Yang, *et al.*, "Cationic iridium(III) complexes for phosphorescence staining in the cytoplasm of living cells," *Chemical Communications*, 2008.
- [30] K. Y. Zhang, S. P. Y. Li, N. Zhu, L. W. S. Or, M. S. H. Cheung, Y. W. Lam, *et al.*, "Structure, photophysical and electrochemical properties, biomolecular interactions, and intracellular uptake of luminescent cyclometalated iridium(III) dipyrrodoquinoxaline complexes," *Inorganic Chemistry*, 2010.
- [31] Y. Wu, H. Jing, Z. Dong, Q. Zhao, H. Wu, and F. Li, "Ratiometric phosphorescence imaging of Hg(II) in living cells based on a neutral iridium(III) complex," *Inorganic Chemistry*, vol. 50, 2011.
- [32] Y. Zhou, J. Jia, W. Li, H. Fei, and M. Zhou, "Luminescent biscarbene iridium(III) complexes as living cell imaging reagents," *Chemical Communications*, 2013.
- [33] R. Lüllmann-Rauch, "History and Morphology of the Lysosome," ed, 2007.
- [34] K. Qiu, H. Huang, B. Liu, Y. Liu, Z. Huang, Y. Chen, *et al.*, "Long-Term Lysosomes Tracking with a Water-Soluble Two-Photon Phosphorescent Iridium(III) Complex," *ACS Applied Materials and Interfaces*, 2016.
- [35] S. Moromizato, Y. Hisamatsu, T. Suzuki, Y. Matsuo, R. Abe, and S. Aoki, "Design and synthesis of a luminescent cyclometalated iridium(III) complex having N, N -diethylamino group that stains acidic intracellular organelles and induces cell death by photoirradiation," *Inorganic Chemistry*, 2012.
- [36] Y. Chen, L. Qiao, B. Yu, G. Li, C. Liu, L. Ji, *et al.*, "Mitochondria-specific

- phosphorescent imaging and tracking in living cells with an AIPE-active iridium(III) complex," *Chemical Communications*, vol. 49, 2013.
- [37] A. Nakagawa, Y. Hisamatsu, S. Moromizato, M. Kohno, and S. Aoki, "Synthesis and photochemical properties of pH responsive tris-cyclometalated iridium(III) complexes that contain a pyridine ring on the 2-phenylpyridine ligand," *Inorganic Chemistry*, 2014.
- [38] L. Murphy, A. Congreve, L. O. Pålsson, and J. A. G. Williams, "The time domain in co-stained cell imaging: Time-resolved emission imaging microscopy using a protonatable luminescent iridium complex," *Chemical Communications*, 2010.
- [39] M. H. Chen, F. X. Wang, J. J. Cao, C. P. Tan, L. N. Ji, and Z. W. Mao, "Light-Up Mitophagy in Live Cells with Dual-Functional Theranostic Phosphorescent Iridium(III) Complexes," *ACS Applied Materials and Interfaces*, vol. 9, 2017.
- [40] C. Caporale, C. A. Bader, A. Sorvina, K. D. M. MaGee, B. W. Skelton, T. A. Gillam, *et al.*, "Investigating Intracellular Localisation and Cytotoxicity Trends for Neutral and Cationic Iridium Tetrazolato Complexes in Live Cells," *Chemistry - A European Journal*, vol. 23, 2017.
- [41] K. Yokoi, C. Balachandran, M. Umezawa, K. Tsuchiya, A. Mitrić, and S. Aoki, "Amphiphilic Cationic Triscyclometalated Iridium(III) Complex-Peptide Hybrids Induce Paraptosis-like Cell Death of Cancer Cells via an Intracellular Ca²⁺-Dependent Pathway," *ACS Omega*, 2020.
- [42] A. Sansee, S. Meksawangwong, K. Chainok, K. J. Franz, M. Gál, L. O. Pålsson, *et al.*, "Novel aminoalkyl tris-cyclometalated iridium complexes as cellular stains," *Dalton Transactions*, 2016.
- [43] S. Ding, Y. Xing, M. Radosz, and Y. Shen, "Magnetic nanoparticle supported catalyst for atom transfer radical polymerization," *Macromolecules*, vol. 39, 2006.
- [44] A. H. Lu, E. L. Salabas, and F. Schüth, "Magnetic nanoparticles: Synthesis, protection, functionalization, and application," vol. 46, ed, 2007.
- [45] S. Laurent, D. Forge, M. Port, A. Roch, C. Robic, L. Vander Elst, *et al.*, "Magnetic iron oxide nanoparticles: Synthesis, stabilization, vectorization, physicochemical characterizations and biological applications," *Chemical Reviews*, vol. 108, 2008.
- [46] A. E. Allen and D. W. C. MacMillan, "Synergistic catalysis: A powerful synthetic strategy for new reaction development," vol. 3, ed, 2012.
- [47] R. C. Wende and P. R. Schreiner, "Evolution of asymmetric organocatalysis: Multi- and retrocatalysis," vol. 14, ed, 2012.
- [48] K. Zeitler and M. Neumann, "Synergistic visible light photoredox catalysis," vol. 5, ed, 2020.
- [49] D. M. Hedstrand, W. H. Kruizinga, and R. M. Kellogg, "Light induced and dye accelerated reductions of phenacyl onium salts by 1,4-dihydropyridines," *Tetrahedron Letters*, 1978.
- [50] H. Cano-Yelo and A. Deronzier, "Photo-oxidation of some carbinols by the Ru(II) polypyridyl complex-aryl diazonium salt system," *Tetrahedron Letters*, 1984.
- [51] J. M. Zen, S. L. Liou, A. S. Kumar, and M. S. Hsia, "An efficient and selective photocatalytic system for the oxidation of sulfides to sulfoxides," *Angewandte*

- Chemie - International Edition*, vol. 42, 2003.
- [52] J. Du and T. P. Yoon, "Crossed intermolecular [2+2] cycloadditions of acyclic enones via visible light photocatalysis," *Journal of the American Chemical Society*, vol. 131, 2009.
 - [53] I. M. Dixon, J. P. Collin, J. P. Sauvage, L. Flamigni, S. Encinas Perea, and F. Barigelletti, "A family of luminescent coordination compounds: Iridium(III) polyimine complexes," *Chemical Society Reviews*, 2000.
 - [54] J. D. Slinker, A. A. Gorodetsky, M. S. Lowry, J. Wang, S. Parker, R. Rohl, *et al.*, "Efficient Yellow Electroluminescence from a Single Layer of a Cyclometalated Iridium Complex," *Journal of the American Chemical Society*, vol. 126, 2004.
 - [55] S. S. A. K. J. S. J. Watts, "Photophysical effects of metal-carbon .sigma. bonds in ortho-metalated complexes of iridium(III) and rhodium(III)," *J. Am. Chem. Soc.*, vol. 106, pp. 6647-6653, 1984.
 - [56] A. Juris, V. Balzani, P. Belser, and A. von Zelewsky, "Characterization of the Excited State Properties of Some New Photosensitizers of the Ruthenium (Polypyridine) Family," *Helvetica Chimica Acta*, 1981.
 - [57] J. D. Nguyen, E. M. D'Amato, J. M. R. Narayanam, and C. R. J. Stephenson, "Engaging unactivated alkyl, alkenyl and aryl iodides in visible-light-mediated free radical reactions," *Nature Chemistry*, 2012.
 - [58] C. K. Prier, D. A. Rankic, and D. W. C. MacMillan, "Visible light photoredox catalysis with transition metal complexes: Applications in organic synthesis," ed, 2013.
 - [59] C. L. Joe and A. G. Doyle, "Direct Acylation of C(sp³)-H Bonds Enabled by Nickel and Photoredox Catalysis," *Angewandte Chemie - International Edition*, vol. 55, 2016.
 - [60] R. Fischer, D. Walther, R. Kempe, J. Sieler, and B. Schönecker, "Metallacyclische acyl-carboxylate des nickels: Reaktivität der acylgruppe und synthesespotential bei kreuzkopplungsreaktionen mit alkylhalogeniden," *Journal of Organometallic Chemistry*, vol. 447, 1993.
 - [61] W. Liu, Y. Ma, Y. Yin, and Y. Zhao, "Anodic cyanation of 1-arylpiperidines," *Bulletin of the Chemical Society of Japan*, vol. 79, 2006.
 - [62] K. Muralirajan, R. Kancharla, and M. Rueping, "Dehydrogenative Aromatization and Sulfonylation of Piperidines: Orthogonal Reactivity in Photoredox Catalysis," *Angewandte Chemie - International Edition*, vol. 57, 2018.
 - [63] S. K. Pagire, S. Paria, and O. Reiser, "Synthesis of β -Hydroxysulfones from Sulfonyl Chlorides and Alkenes Utilizing Visible Light Photocatalytic Sequences," *Organic Letters*, vol. 18, 2016.
 - [64] A. McNally, C. K. Prier, and D. W. C. MacMillan, "Discovery of an α -amino C-H arylation reaction using the strategy of accelerated serendipity," *Science*, 2011.
 - [65] M. T. Pirnot, D. A. Rankic, D. B. C. Martin, and D. W. C. MacMillan, "Photoredox activation for the direct β -arylation of ketones and aldehydes," *Science*, 2013.
 - [66] J. D. Cuthbertson and D. W. C. MacMillan, "The direct arylation of allylic sp³ C-H bonds via organic and photoredox catalysis," *Nature*, 2015.
 - [67] J. Yang, M. Jiang, Y. Jin, H. Yang, and H. Fu, "Visible-Light Photoredox

- Difluoromethylation of Phenols and Thiophenols with Commercially Available Difluorobromoacetic Acid," *Organic Letters*, 2017.
- [68] G. Di Marco, M. Lanza, M. Pieruccini, and S. Campagna, "A luminescent iridium(III) cyclometallated complex immobilized in a polymeric matrix as a solid-state oxygen sensor," *Advanced Materials*, vol. 8, 1996.
- [69] F. Wu, Y. Feng, and C. W. Jones, "Recyclable silica-supported iridium bipyridine catalyst for aromatic C-H borylation," *ACS Catalysis*, vol. 4, 2014.
- [70] D. Mazia, G. Schatten, and W. Sale, "Adhesion of cells to surfaces coated with polylysine: Applications to electron microscopy," *Journal of Cell Biology*, vol. 66, 1975.
- [71] T. Moriuchi, K. Yoshii, C. Katano, and T. Hirao, "Poly-L-lysine-induced self-association and luminescence of dicyanoaurate(I)," *Chemistry Letters*, vol. 39, 2010.
- [72] J. R. Bolton, *Ultraviolet Applications Handbook*, 2nd Ed ed., 2001.
- [73] T. Owen, *Principles and applications of UV-visible spectroscopy: a primer*, 1996.
- [74] S. Thermo, "Basic UV-Vis Theory , Concepts and Applications Basic," *ThermoSpectronic*, 2013.
- [75] Clinuvel, "Understanding the Electromagnetic Spectrum," ed, 2019.
- [76] P. W. d. P. J. Atkins, *Physikalische Chemie*, 5. Edition ed., 2013.
- [77] Beer, "Bestimmung der Absorption des rothen Lichts in farbigen Flüssigkeiten," *Annalen der Physik*, 1852.
- [78] Lambert and H. Johann, *Photometria, sive De mensura et gradibus luminis, colorum et umbrae*, First edit ed. Augsburg: Christoph Peter Detleffsen for the widow of Eberhard Klett, 1760.
- [79] R. Gandhimathi, S. Vijayaraj, and M. P. Jyothirmaie, "Analytical Process of Drugs By Ultraviolet (UV) Spectroscopy - A Review," *International Journal of Pharmaceutical Research & Analysis*, 2012.
- [80] P. Worsfold, C. Poole, A. Townshend, M. Miró, P. J. Worsfold, and E. A. G. Zagatto, "Spectrophotometry | Overview," *Encyclopedia of Analytical Science*, pp. 244-248, 2019.
- [81] S. M. Nilapwar, M. Nardelli, H. V. Westerhoff, and M. Verma, "Chapter four - Absorption Spectroscopy." vol. 500, ed, 2011.
- [82] J. R. Lakowicz and B. R. Masters, "Principles of Fluorescence Spectroscopy, Third Edition," *Journal of Biomedical Optics*, 2008.
- [83] J. N. Miller, "Some recent advances in fluorescence spectroscopy," ed, 2006.
- [84] B. Valeur and M. N. Berberan-Santos, *Molecular Fluorescence: Principles and Applications, Second Edition*, 2012.
- [85] S. G. Stanciu, *Micro and Nanotechnologies for Biotechnology*, 2016.
- [86] E. Runge and E. K. U. Gross, "Density-functional theory for time-dependent systems," *Physical Review Letters*, vol. 52, 1984.
- [87] W. Kohn, A. D. Becke, and R. G. Parr, "Density functional theory of electronic structure," *Journal of Physical Chemistry*, vol. 100, 1996.
- [88] W. Koch and M. C. Holthausen, *Wolfram Koch , Max C . Holthausen A Chemist 's Guide to Density Functional Theory* vol. 3, 2001.
- [89] P. Hohenberg and W. Kohn, "Inhomogeneous electron gas," *Physical Review*, 1964.

- [90] W. Kohn and L. J. Sham, "Self-consistent equations including exchange and correlation effects," *Physical Review*, 1965.
- [91] C. J. Cramer and D. G. Truhlar, "Density functional theory for transition metals and transition metal chemistry," *Physical Chemistry Chemical Physics*, vol. 11, 2009.
- [92] !!! INVALID CITATION !!! [91-93].
- [93] P. A. M. Dirac, "Note on Exchange Phenomena in the Thomas Atom," *Mathematical Proceedings of the Cambridge Philosophical Society*, vol. 26, 1930.
- [94] J. C. Slater, "A simplification of the Hartree-Fock method," *Physical Review*, vol. 81, 1951.
- [95] A. D. Becke, "Density-functional exchange-energy approximation with correct asymptotic behavior," *Physical Review A*, vol. 38, 1988.
- [96] J. P. Perdew, "Density-functional approximation for the correlation energy of the inhomogeneous electron gas," *Physical Review B*, vol. 33, 1986.
- [97] C. Lee, W. Yang, and R. G. Parr, "Development of the Colle-Salvetti correlation-energy formula into a functional of the electron density," *Physical Review B*, vol. 37, 1988.
- [98] J. P. Perdew, J. A. Chevary, S. H. Vosko, K. A. Jackson, M. R. Pederson, D. J. Singh, *et al.*, "Atoms, Molecules, Solids, and Surfaces: Applications of the Generalized Gradient Approximation for Exchange and Correlation," *Physical Review B*, vol. 46, pp. 6671-6687, 1992.
- [99] J. P. Perdew, K. Burke, and M. Ernzerhof, "Generalized gradient approximation made simple," *Physical Review Letters*, vol. 77, 1996.
- [100] C. Adamo and V. Barone, "Exchange functionals with improved long-range behavior and adiabatic connection methods without adjustable parameters: The mPW and mPW1PW models," *Journal of Chemical Physics*, vol. 108, 1998.
- [101] !!! INVALID CITATION !!! [101-103].
- [102] A. D. Becke, "Density-functional thermochemistry. III. The role of exact exchange," *The Journal of Chemical Physics*, vol. 98, 1993.
- [103] P. J. Stephens, F. J. Devlin, C. F. Chabalowski, and M. J. Frisch, "Ab Initio calculation of vibrational absorption and circular dichroism spectra using density functional force fields," *Journal of Physical Chemistry®*, vol. 98, 1994.
- [104] G. W. T. H. B. S. G. E. S. M. J. Frisch, J. R. C. J. A. M. M. A. Robb, Jr., K. N. K. J. C. B. J. M. M. T. Vreven, J. T. V. B. B. M. M. C. S. S. Iyengar, N. R. G. A. P. H. N. M. H. G. Scalmani, K. T. R. F. J. H. M. I. M. Ehara, *et al.*, ed: Gaussian, Inc., Wallingford, CT, 2004.
- [105] M. Kimura and Y. Uozumi, "Development of new P-chiral phosphorodiamidite ligands having a pyrrolo[1,2-c]diazaphosphol-1-one unit and their application to regio- and enantioselective iridium-catalyzed allylic etherification," *Journal of Organic Chemistry*, vol. 72, pp. 707-714, 2007.
- [106] E. Calimano and T. D. Tilley, "Alkene hydrosilation by a cationic hydrogen-substituted iridium silylene complex," *Journal of the American Chemical Society*, vol. 130, 2008.
- [107] D. H. Ess, S. M. Bischof, J. Oxgaard, R. A. Periana, and W. A. Goddard, "Transition state energy decomposition study of Acetate-Assisted and internal electrophilic substitution C-H Bond activation by (acac-O,O) 2Ir(X) complexes

- (X = CH₃COO, OH)," *Organometallics*, vol. 27, 2008.
- [108] R. Ghosh, T. J. Emge, K. Krogh-Jespersen, and A. S. Goldman, "Combined experimental and computational studies on carbon-carbon reductive elimination from bis(hydrocarbyl) complexes of (PCP)Ir," *Journal of the American Chemical Society*, vol. 130, 2008.
- [109] W. L. Bragg, "The diffraction of short electromagnetic waves by a crystal," *Proceedings of the Cambridge Philosophical Society*, vol. 17, 1913.
- [110] B. The Editors of Encyclopaedia, "Tetragonal system," ed.
- [111] E. C. Jensen, "Quantitative Analysis of Histological Staining and Fluorescence Using ImageJ," ed, 2013.
- [112] M. Wilson, "Introduction to Widefield Microscopy," ed, 2017.
- [113] E. H. K. Stelzer, "Contrast, resolution, pixelation, dynamic range and signal-to-noise ratio: Fundamental limits to resolution in fluorescence light microscopy," *Journal of Microscopy*, vol. 189, 1998.
- [114] J. B. Pawley, *Handbook of biological confocal microscopy: Third edition*, 2006.
- [115] W. Rebecca Matulka. Daniel, "The History of the Light Bulb," ed.
- [116] M. Izadifard, G. Achari, and C. H. Langford, "Application of photocatalysts and LED light sources in drinking water treatment," *Catalysts*, vol. 3, 2013.
- [117] C. C. Le, M. K. Wismer, Z. C. Shi, R. Zhang, D. V. Conway, G. Li, *et al.*, "A General Small-Scale Reactor to Enable Standardization and Acceleration of Photocatalytic Reactions," *ACS Central Science*, vol. 3, 2017.
- [118] L. Chu, J. M. Lipshultz, and D. W. C. Macmillan, "Merging Photoredox and Nickel Catalysis: The Direct Synthesis of Ketones by the Decarboxylative Arylation of α -Oxo Acids," *Angewandte Chemie - International Edition*, vol. 54, 2015.
- [119] S. Meksawangwong, S. Jiajaroen, K. Chainok, W. Pinyo, and F. Kielar, "Crystal structure of fac -{5-[(hexylazaniumyl)methyl]-2-(pyridin-2-yl)phenyl- κ^2 N,C1 }bis[2-(pyridin-2-yl)phenyl- κ^2 N, C1]iridium(III) chloride," *Acta Crystallographica Section E: Crystallographic Communications*, 2018.
- [120] M. Nonoyama, "Benzo[h]quinolin-10-yl- N Iridium(III) Complexes," *Bulletin of the Chemical Society of Japan*, 1974.
- [121] A. Beeby, S. Bettington, I. D. W. Samuel, and Z. Wang, "Tuning the emission of cyclometalated iridium complexes by simple ligand modification," *Journal of Materials Chemistry*, 2003.
- [122] P. Steunenbergh, A. Ruggi, N. S. Van Den Berg, T. Buckle, J. Kuil, F. W. B. Van Leeuwen, *et al.*, "Phosphorescence imaging of living cells with amino acid-functionalized tris(2-phenylpyridine)iridium(III) complexes," *Inorganic Chemistry*, 2012.
- [123] I. Dance and M. Scudder, "Concerted supramolecular motifs: Linear columns and zigzag chains of multiple phenyl embraces involving Ph₄P⁺ cations in crystals," *Journal of the Chemical Society - Dalton Transactions*, pp. 3755-3769, 1996.
- [124] B. König, "Photocatalysis in Organic Synthesis – Past, Present, and Future," vol. 2017, ed, 2017.
- [125] R. D. Crouch, "Radical Reactions in Organic Synthesis (Oxford Chemistry Masters) (Samir Z. Zard)," *Journal of Chemical Education*, vol. 81, pp. 1718-1718, 2004.

- [126] J. S. Mayell and A. J. Bard, "The Electroreduction of Quaternary Ammonium Compounds," *Journal of the American Chemical Society*, vol. 85, 1963.
- [127] M. P. S. Mousavi, S. Kashefolgheta, A. Stein, and P. Bühlmann, "Electrochemical Stability of Quaternary Ammonium Cations: An Experimental and Computational Study," *Journal of The Electrochemical Society*, vol. 163, 2016.
- [128] Bruker, "APEX3," ed, 2016.
- [129] G. M. Sheldrick, "research papers SHELXT – Integrated space-group and crystal- structure determination research papers," *Acta. Cryst.*, 2015.

